Winter 12-15-2018

Photophysical Characterization and Wavelength Tuning of Natural and Synthetic Oxobacteriochlorins and Biohybrids

Don Hood
Washington University in St. Louis

WASHINGTON UNIVERSITY IN ST. LOUIS

Department of Chemistry

Dissertation Examination Committee:
Dr. Dewey Holten, Chair
Dr. Mikhail Y. Berezin
Dr. Christine Kirmaier
Dr. Jay Ponder
Dr. John Taylor

Photophysical Characterization and Wavelength Tuning of Natural and Synthetic
Oxobacteriochlorins and Biohybrids
by
Donald L. Hood

A dissertation presented to
The Graduate School
of Washington University in
partial fulfillment of the
requirements for the degree
Of Doctor of Philosophy

December 2018
St. Louis, Missouri

Table of Contents

Chapter 1: Background, Overview and Methods

Chapter 4: Biohybrid c-terminal sites

Chapter 5: Synthesis and Photophysical Characterization of Bacteriochlorins

Equipped with Integral Swallowtail Substituents

Chapter 6: Conclusion and Future Direction

List of Figures

Chapter 1

Chapter 2

Chapter 5

List of Tables

List of Charts

List of Synthesis Schemes

Chapter 2

Chapter 5

Acknowledgments

It is important to express how understanding and patient Dr. Dewey Holten has been. Teaching physical chemistry to an older student who has not touched on the subject for many, many years was surely not an easy or pleasant task. His time and instruction was always available. He and Dr. Kirmaier made the lab group a happy and productive place.

My committee members were generous and forthright in their criticism as well in their encouragement. Dr. Ponder and Dr. Taylor were involved in my learning from the very start of my time in the program and I thank them for the knowledge and expertise that pushed my work and understanding further along. Dr. Berezin cheerfully contributed his time and support at essentially the last minute as the fifth member. Thank you all.

The Holten group members provided a sounding board, academic support, experimental assistance, and ongoing feedback. Dr. Kaitlyn Faries was particularly helpful as a classmate. Her work is impressive and it is good that she will continue working with the Holten group.

Outside of the lab and department are the PARC collaborators. Dr.s Paul and Paula Loach for always being encouraging and including me in active discussions of the biohybrid development. Dr. Jon Lindsey and his group for the excellent samples they provided. And far too many other members of the PARC group to try to include here. Superb and helpful chemists and mentors, every one of them. Dr. Darius Niedzwiedzki in the PARC ultrafast laser facility was invaluable for the discussion and help during the TA experiments.

It would be remiss of me to not mention that none of this would have been completed or been half so fruitful without Annie and the children. I dedicate this work to you.

Don Hood
Washington University
December 2018

ABSTRACT OF THE DISSERTATION

Photophysical Characterization and Wavelength Tuning of Natural and Synthetic

Oxobacteriochlorins and Biohybrids

By

Donald L. Hood

Doctor of Philosophy in Chemistry

Washington University in St. Louis, 2018

Dr. Dewey Holten, Chairperson

Herein is discussed the theoretical and practical unpinnings of photophysical behaviors and kinetic constants for tetrapyrrole macrocycles, to wit, porphyrins, chlorins, and bacteriochlorins. Understanding the characteristic photophysical response of tetrapyrroles to changes in environment or substituents is important to designing synthetic chromophores with tunable absorption wavelengths and for preparing useful biohybrids of natural photosynthetic light antennas combined with unnatural chromophores attached to the light antenna oligomers. Synthetic oxobacteriochlorins provide simpler synthetic pathway to the equivalent of highly functionalized natural chlorins while being absorption spectra tunable with the addition of various substituents. Biohybrids of natural light harvesting systems potentially increase the amount of light energy captured and transferred to reaction centers of photosynthetic systems. The studies here directly relate to furthering the increasing organic dye photovoltaic light capture, creation of custom chromophores, and increasing photosynthetic energy transfer.

Chapter 1

Background, Overview and Methods

Overview of the Thesis

The research described herein has a three-fold purpose:

1) To provide photophysical characterizations of natural and artificial chromophores; particularly of porphyrins or porphyrin derivatives,

2) To relate the photophysical properties of said chromophores to design principles for tuning and expanding the spectra from the designed porphyrins,

3) To further understanding of energy transfer from chromophore to oligomer in biohybrid LH1 type systems.

Chapters 2-5 are composed of work published in the scientific literature and contain results from collaborative work with various research laboratories. Details of the collaborative studies will be delineated in the next subsection. The remainder of Chapter 1 will provide an introduction to the principles underlying the electronic behavior of the chromophores, the experimental methods used in the research to obtain the photophysical properties, and the calculations involved in the determination of the photophysical constants of the chromophores.

Chapter 2 describes the photophysical properties of oxo- and dioxo-bacteriochlorins containing only a geminal dimethyl group and either an oxo- or dioxo- substituent attached at the 7th or 7th and 17th positions. This study illustrates the ability to tailor a simple bacteriochlorin to absorb in the spectral region that heretofore had been the realm of extensively modified chlorins.

Chapter 3 is an expansion of the investigation described in Chapter 2 with an emphasis on the photophysical properties of tolyporphin A compared to di- and mon-oxobacteriochlorins specifically regarding their photophysical characteristics in solvents with varying dielectric properties. Within this chapter the influence of the solvent and isoelectric value is applied to the spectral shifts and related changes in the singlet lifetime and triplet yield.

Chapter 4 is a continuation of research performed by previous members of the Holden Group on biohybrid light-harvesting structures. This investigation involved the attachment of a synthetic bacteriochlorin to a Cysteine residue at the +1, +5, and +11 position of a β-peptide and the accompanying energy transfer and efficiency from light capture to LH1 type oligomer.

Chapter 5 is a study of "swallowtail" bacteriochlorins. These compounds have a pair of aryl or alkyl groups at each β-pyrroline unit and illustrate the ability to tailor a molecular design for increased aqueous solubility without altering useful photophysical characteristics.

Collaborations

The following laboratories collaborated in preparation, calculation, and writing for the papers and investigations included in the work for my thesis:

Dr. Jonathan Lindsey Laboratory in the Department of Chemistry at North Carolina State University at Raleigh for the synthetic oxobacteriochlorins and tolyporphin A preparation.

Dr. Philip Williams Laboratory in the Department of Chemistry at University of Hawaii at Manoa for the tolyporphin A samples.

Dr.s Paul and Paula Loach Laboratory in the Department of Molecular Biosciences at Northwestern University in Evanston for the biohybrid conjugates and oligomers preparation.

Dr. David Bocian Laboratory in the Department of Chemistry at University of California, Riverside for the density functional theory calculations of the synthetic bacteriochlorins.

Dr. Darius Niedzwidzki of the Photosynthetic Antenna Research Center (PARC) Ultrafast Laser Facility at Washington University in St. Louis for the transient absorbance data.

General Photophysical Background

The basics of photophysical properties for molecules starts with absorption and emission. A molecule, normally in the ground energy state, absorbs a photon of light. This photon will be a particular energy or frequency / wavelength matched to one of several possible excited vibrational-electronic, or vibronic, states of the molecule. Depending on the molecule's symmetry and electronic state, what happens next depends on the overlap of the vibronic ground and excited state wave functions, the size of the conjugated π-electron system if present, its symmetry, and the local electronic environment; i.e. a solvent. This overlap and the accompanying transitions are illustrated in Figures 1 and 2.
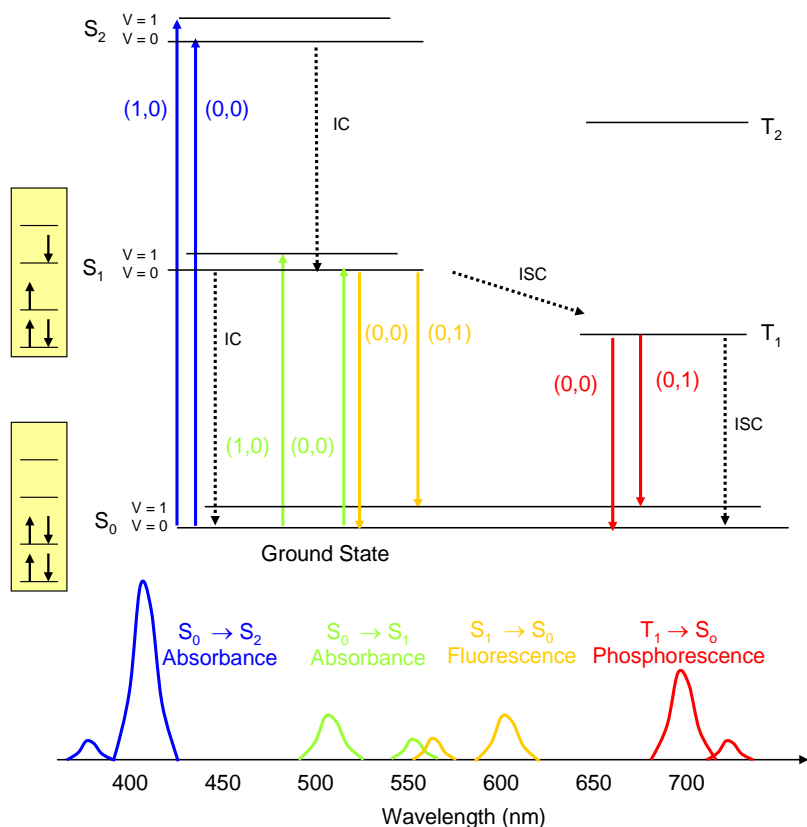
Figure 1. Jablonski Energy Diagram for PdTPP

Figure 2. Franck-Condon diagram showing internuclear distance and wave function overlap between ground and excited electronic states.

Generally, the Jablonski diagram in Figure 1 shows the absorption of a photon, excitation to a higher energy singlet state (S_2), internal conversion (IC) to the lowest excited energy singlet state (S_1), and subsequent IC / fluorescence to ground (S_0) or first vibrational level of the ground state. Further to the right in the same diagram is the intersystem crossing (ISC). This occurs when the excited singlet state undergoes a "forbidden" transition to an excited triplet state (T_1) and subsequently undergoes ISC return to S_0 or phosphorescence to S_0.

At the bottom of the diagram is the spectrum of Palladium tetraphenyl porphyrin (PdTPP) as an illustrator. Here, the consequence of Kasha's Rule and IC on the symmetry of the PdTPP can be seen. From left to right, S_0–S_2 absorption (Soret band / B_y and B_x peaks) and S_0–S_1

absorption (Q_y and Q_x peaks) followed by IC and S_1-S_0 fluorescence (Q_y and Q_x peaks). The shown ISC of the singlet (S_1) excited state energy to excited state triplet energy (T_1) results in phosphorescence (T_1 to S_0). With the appropriate frontier orbital electronic interactions or with a heavy metal central atom the ISC becomes more favorable.

It is important to note the continual red-shifting of the spectrum as the system progresses from absorption to phosphorescence and the mirror symmetry of the absorption and emission peaks. This red-shifting of the absorption peak relative to the fluorescence peak is called the Stoke's Shift and is due to the energy relaxation in S_1 following its formation from S_o due to the change in electron distribution and thus structural changes in the chromophore, the solvent, or both. The mirror symmetry of absorption and emission is related to the comparable shapes of the ground and excited state potential wells.

The violet-blue Soret (B_y and B_x) features may include higher energy transitions than the $S_0 \rightarrow S_3$ and $S_0 \rightarrow S_4$ (for example, for simple metalloporphyrins) which may be close enough in energy as to not show distinctions between the various vibronic levels. The B_x / Q_x and the B_y / Q_y are the transitions from, respectively, the $S_{1(0,0)}$ to $S_{0(0,0)}$ and $S_{1(1,0)}$ to $S_{0(0,1)}$. Peak broadening is an effect of absorption of various vibrational levels between electronic excited state levels.

The Franck-Condon diagram (F-C) in Figure 2 illustrates the relationship between the vibronic wave function overlap of ground and excited electronic energy levels. The essence of the F-C principle lies in the exceptionally fast transition for the electronic state vs. the relatively unchanged nuclear change in position during the same timeframe. In other words, given the timescale and the relative masses of the electrons vs the nuclei the nuclear coordinates of the nuclei are frozen, while the electronic states transition rapidly. The probability of a particular vibronic

state being achieved is proportional to the square of the overlap of the vibrational wave functions of the original and final state, i.e., the intensity of the feature in the spectrum being directly related to the likelihood of a particular transition.

Subsequent to the absorption and accompanying electron density rearrangement, Kasha's Rule states that excited electronic states will quickly relax to the lowest vibrational level of the lowest electronic excitation state. This is due to the F-C principle as the greater the overlap, the faster the transition and at higher vibronic energies where there is a high density of vibrational levels that are typically close in energy (i.e. significant overlap) IC of the energy allows transition relaxation to the lowest excited state, S1 (below which there is a much larger energy difference between levels), before fluorescence occurs. At this S_1 lowest excited state the energy gap from the S_1 to the S_0 is great enough for kinetic competition of fluorescence with IC.

Background, Electronic, and Photophysical Characteristics of Porphyrins, Chlorins, and

Porphyrin	**Chlorin**	**Bacteriochlorin**

22 π e-	20 π e-	18 π e-
Aromatic	Anti-aromatic	Aromatic
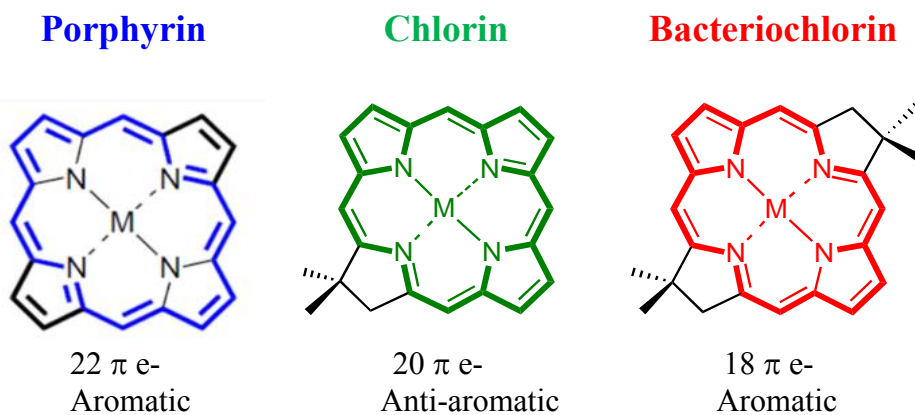
Figure 3. Metallo- form of natural chromophores

Bacteriochlorins

The three 24 member macrocyclic molecules in Figure 3 are often referred to as "Nature's Pigments". These chromophores are found throughout the biological world in a wide range of colors depending on their substituents. Their importance cannot be overstated as they are

responsible for generation of oxygen in the atmosphere, transport of oxygen in the blood, and photosynthesis in plants, just to name a few processes that employ these macrocycles. Each has a 16 member 18 π-electron central aromatic system. In addition, each has either 2 pyrrole rings, two pyrroline (reduced pyrrole) rings, or one pyrrole and one pyrroline rings. The number of each type of ring either increases or decreases the size of the conjugated system.

Porphyrins are abundant as the building blocks of strongly colored compounds and are comprised of a macrocycle consisting of four pyrrole subunits and absorbing in the visible portion of the spectrum. They have a total of 22 π electrons in the conjugated system (two pyrrole rings (4 π-electrons + the basic 16 member aromatic system).

Between the porphyrins and bacteriochlorins are the chlorins which result from the reduction of a pyrrole ring. Also strongly absorbing in the visible range, chlorins are found in plants and bacteria and consist of three pyrroles and one pyrroline unit. They have an asymmetric eighteen member aromatic ring with 20 π electrons in the conjugated system (18 member basic system + 2 π-electrons).

The reduction of one further pyrrole ring on the opposite side of the macrocycle produces the bacteriochlorins that are found in bacteria. Thus, they have two pyrroles and two reduced pyrrole subunits with same sixteen member symmetric aromatic ring as porphyrins. Bacteriochlorins have the minimal 18 π electron aromatic conjugated systems of the three systems. The geminal dimethyl groups used in synthetic constructs prepared in the Lindsey lab stabilize the porphins by reducing the likelihood of the rings deprotonating again and returning to 20 or 22 e-systems.

In nature these macrocycles are often found with a metal ion in the center and coordinated to the nitrogens. A macrocycle without the metal has hydrogen on the nitrogen of the two pyrrole subunits (in chlorins and bacteriochlorins) and is described as "free-base". See Figure 4. Shown are a metallo-porphyrin and the free-base form of chlorin. The x-axis bisects any reduced pyrrole rings and the y-axis is coincident with the hydrogen axis.

A) Metallo   B) Free-Base
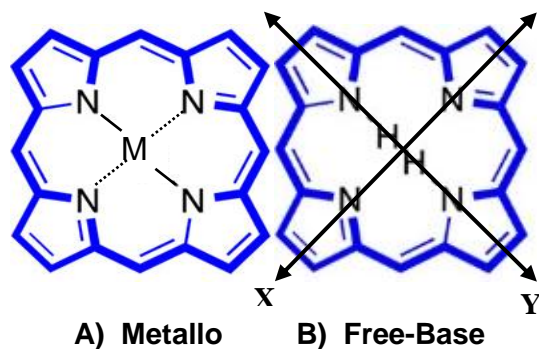
Figure 4. Illustrates the x, y-axis and the changes from n=4 to n=2 with the change from metalloporphyrin (**A**) to free-base (**B**).

Figure 4 also shows the symmetry of the metalloporphyrin compared to the free-base form based on the central rotational axis. In a metalloporphyrin the symmetry is D_{4h} at the central axis. However, in the free-base form the N-H along the y-axis breaks the symmetry giving D_{2h}. This conversion to free-base causes an important change in the absorption spectra. Initially, with the metalloporphyrin symmetry as D_{4h}, the absorption spectrum consists of an absorption in the near-UV (the Soret or B-band) around 400 nm in the near-UV and an absorption in the visible (the Q-band) within the 450-750 nm range in the visible region. For the metalloporphyrin these are two equivalent dipole transitions in the x- and y- directions. Despite the equivalence, the intensity difference of the B-band vs the Q-band
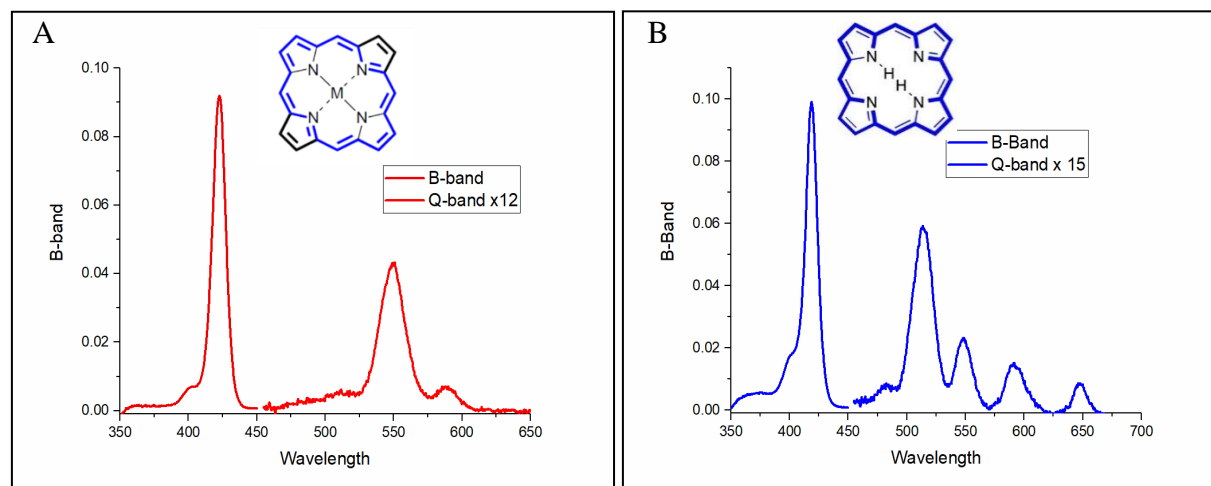
Figure 5. Comparison of ZnTPP (**A**) to FbTPP (**B**). Note that Q-bands in each are magnified for visibility.

(Fig. 5) indicates something more than just a single electron promotion is involved for each molecular transition. With D_{2h} the x- and y- axes of the B-band and Q-band are no longer equivalent. The result of this symmetry break is four long wavelength absorption peaks: $Q_{x\,(1,0),(0,0)}$ $S_0 - S_1$ electronic excitation and $Q_{y\,(1,0),(0,0)}$ $S_0 - S_2$ electronic excitation. And four shorter wavelengths: $B_{x\,(1,0),(0,0)}$ $S_0 - S_3$ and $B_{y\,(1,0),(0,0)}$ $S_0 - S_4$ electronic excitations. With the additional Q-band absorption peaks is an increase in the intensity of those peaks relative to the B-band.

This is not the only change in symmetry. Porphyrin to chlorin to bacteriochlorin also changes the size and shape of the conjugated system with the porphyrin as symmetrical (regarding conjugated system) and the system reducing to chlorin and bacteriochlorin. And with the change from porphyrin to chlorin to bacteriochlorin there is a change in position of the B- and Q-bands. The changes from the above are much like an accordion see-saw. Depending on the size of the conjugated system, the symmetry, and the x- y-axis dipoles, the intensities of the B- and Q-bands will be inversely related while the positions of the bands will either move closer to each other or spread further apart. See Figure 6.
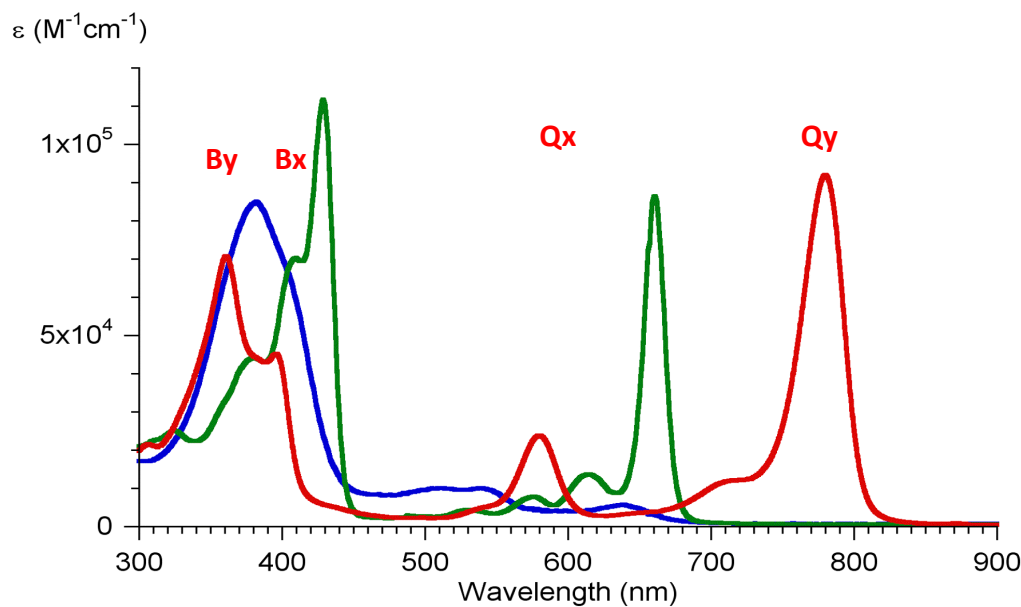
Figure 6. Showing change in intensity of B band vs Q band and compression / expansion of spectral range with change in symmetry.
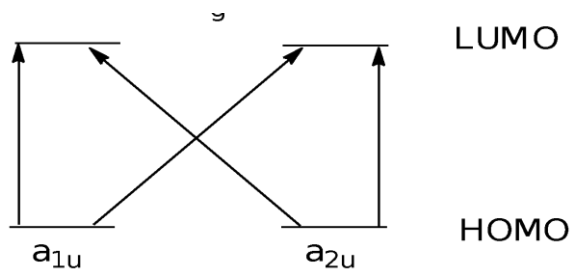
Figure 7. Simplified depiction of Gouterman's Four-Orbital Model with "accidently" degenerate HOMO and HOMO-1.

Figure 7 is a simplified depiction of Gouterman's Four-Orbital Model. Utilizing the Gouterman four-orbital model to explain the shifting and intensity differences for B- and Q-bands, these absorption transitions arise from mixing of the excited state configurations between the two highest HOMOs and the two lowest LUMOs in the π system. The $a_{2u}(\pi)$ and the $a_{1u}(\pi)$ are "accidently" degenerate. The LUMO is a set of rigorously degenerate $e_g(\pi^*)$ orbitals expected from the D_{4h} symmetry. As a result, the excited-state configurations $a_{2u}(\pi) \rightarrow e_{gy}(\pi^*)$ and $a_{1u}(\pi) \rightarrow e_{gx}(\pi^*)$, the two y-polarized configurations, are nearly degenerate as are the two x-polarized configurations $a_{1u}(\pi) \rightarrow e_{gy}(\pi^*)$ and $a_{2u}(\pi) \rightarrow e_{gx}(\pi^*)$. Thus there is pairwise mixing of the excited state configurations and the mixing in each pair is about 50% from each due to the close energies of the configurations. If the a_{2u} and the a_{1u} were not degenerate, then the

relative contributions to the mixing would depend on the energy separation of the $a_{2u}(\pi)$ and the $a_{1u}(\pi)$ orbitals (for a degenerate $e_g(\pi^*)$ pair).

The mixing is the result of linear combinations of the HOMO/HOMO-1 and the LUMO/LUMO+1 orbitals. The HOMOs have different electron densities but are each delocalized around the macrocycle. Due to the similar spatial and energy characteristics, quantum mechanics allows that the orbitals mix. This is called the configuration interaction. Each linear combination gives two electronic states; a constructive and destructive interference of transition dipoles. These two states produce an increase and a decrease in absorption intensity. As the individual orbitals become less similar in energy, there is less mixing. This results in the typical MO theory splitting of the energies of the resultant states.

The following are the linear combinations that describe the above excited states for the $B_{x,y}$ and the $Q_{x,y}$ orbital mixing:

$$\begin{pmatrix} Q_y \\ B_y \end{pmatrix} = \begin{pmatrix} Q_y^0 \\ B_y^0 \end{pmatrix} \cos \eta_y \mp \begin{pmatrix} B_y^0 \\ Q_y^0 \end{pmatrix} \sin \eta_y \qquad\qquad \text{Eqa. (1)}$$

$$\begin{pmatrix} Q_x \\ B_x \end{pmatrix} = \begin{pmatrix} Q_x^0 \\ B_x^0 \end{pmatrix} \cos \eta_x \pm \begin{pmatrix} B_x^0 \\ Q_x^0 \end{pmatrix} \sin \eta_x \qquad\qquad \text{Eqa. (2)}$$

$$\begin{pmatrix} Q_y^0 \\ B_y^0 \end{pmatrix} = \frac{1}{\sqrt{2}} \left[\left(a_{2u}(\pi) \to e_{gy}(\pi^*) \right) \mp \left(a_{1u}(\pi) \to e_{gx}(\pi^*) \right) \right] \qquad\qquad \text{Eqa. (3)}$$

$$\begin{pmatrix} Q_x^0 \\ B_x^0 \end{pmatrix} = \frac{1}{\sqrt{2}} \left[\left(a_{2u}(\pi) \to e_{gx}(\pi^*) \right) \pm \left(a_{1u}(\pi) \to e_{gy}(\pi^*) \right) \right] \qquad\qquad \text{Eqa. (4)}$$

$$\begin{pmatrix} \eta_y \\ \eta_x \end{pmatrix} = \frac{1}{2} \tan^{-1} \left[\frac{1}{2\delta} \left(\frac{\Delta E_{dif,y}}{\Delta E_{dif,x}} \right) \right] \qquad\qquad \text{Eqa. (5)}$$

$$\delta = \int \left(a_{2u}(\pi) \to e_{gx}(\pi^*) \right) H \left(a_{1u}(\pi) \to e_{gy}(\pi^*) \right) dv \qquad\qquad \text{Eqa. (6)}$$

$$\begin{pmatrix} \Delta E_{dif,y} \\ \Delta E_{dif,x} \end{pmatrix} = \frac{1}{2} \begin{pmatrix} E_{a_{2u}(\pi) \to e_{gy}(\pi^*)} - E_{a_{1u}(\pi) \to e_{gx}(\pi^*)} \\ E_{a_{1u}(\pi) \to e_{gy}(\pi^*)} - E_{a_{2u}(\pi) \to e_{gx}(\pi^*)} \end{pmatrix} \qquad\qquad \text{Eqa. (7)}$$

The η_x and η_y mixing coefficients in equations 1 and 2 and the configuration interaction energy in equation 6, δ, for $a_{2u}(\pi) \rightarrow e_{gx}(\pi^*)$ and $a_{1u}(\pi) \rightarrow e_{gy}(\pi^*)$ relationship excited state energies can be rewritten as:

$$\binom{E_{Qy}}{E_{By}} = \Delta E_{avg} \mp \frac{\delta}{\cos 2\eta_y} \qquad \text{Eqa. (8)}$$

$$\binom{E_{Qx}}{E_{Bx}} = \Delta E_{avg} \mp \frac{\delta}{\cos 2\eta_x} \qquad \text{Eqa. (9)}$$

$$\Delta E_{avg} = \frac{1}{2}\left(E_{a_{2u}(\pi) \rightarrow e_{gy}(\pi^*)} + E_{a_{1u}(\pi) \rightarrow e_{gx}(\pi^*)}\right) = \frac{1}{2}\left(E_{a_{1u}(\pi) \rightarrow e_{gy}(\pi^*)} + E_{a_{2u}(\pi) \rightarrow e_{gx}(\pi^*)}\right) \text{ Eqa. (10)}$$

According to Equations 7, 8, and 9 above, the mixing is at a maximum when the contribution from each is 50%. See Figure 8.
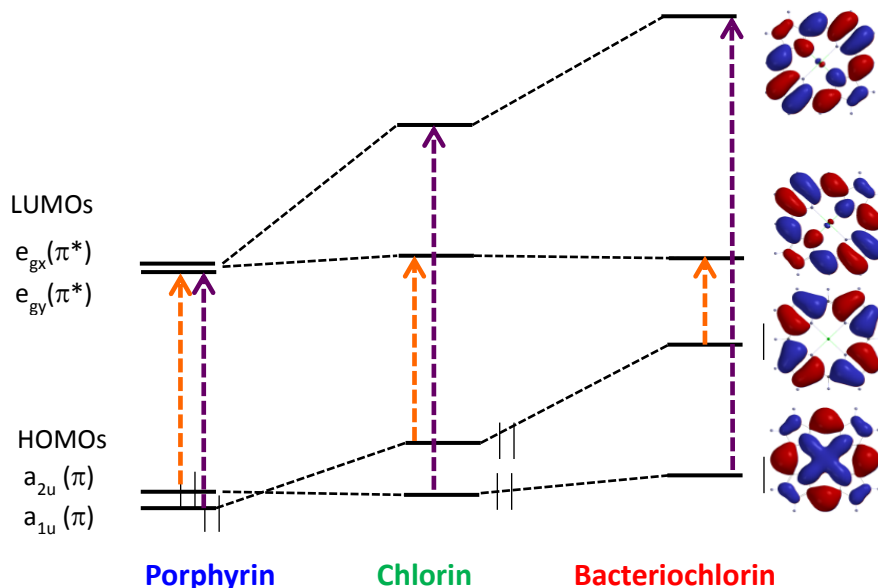
Figure 8. The change in energy gaps for frontier orbital energies vs orbital mixing. Showing only the Y-polarized promotions.

Changes in the mixing leads to the combination see-saw / accordion effect on the B-bands and Q-bands referred to earlier. The see-saw relates to the intensity of the bands and the accordion represents the shifting of the B-band vs the Q-band. Within a given macrocycle (i.e. a fixed

conjugated system) the ΔE_{ave}, the η_x, and η_y values are close to zero. Therefore, with D_{4h} symmetry, all the one electron promotions have almost equal contributions to each state and the B band is the constructively interfered state and the Q band is the destructively interfered state. According to equations 8 & 9, the ΔE_{ave} and the mixing coefficients are the major parameters for the differences in optical transitions in related configurations in the x and y axis.

Here, the extended pi systems are related to the energy gap between linear combinations with the less extended pi system, then the larger the energy gap. From porphyrin to bacteriochlorin the system is decreasing in size and increasing absorption wavelength between the four possible linear combinations. This growing separation in energy levels leads to a decrease in B-band intensity and an increase in Q-band intensity due to less constructive / destructive interference of the transition dipoles. Eventually this leads to unmixing giving four separate absorption peaks with equal intensities.

Thus, if they are not identically symmetrical, then the contribution is not equal, the mixing decreases, and the individual excited states due to one electron promotions increase in intensity with the decrease in mixing (reduced contribution to single transition energy state). Intensities that would add and subtract in an equal manner for degenerate MOs giving two absorptions (one each x and y) will now uncouple and give four absorptions (2 x and 2 y) in relative intensities related to the amount of mixing. Expanding further, if the length of the conjugated system changes, then the size of the energy box changes and the energy/wavelength of the absorbed light changes AND the energy difference between the B and Q bands changes.

Background and Photophysical Characteristics of Oxo- and Dioxobacteriochlorins

Designing, developing, and tailoring synthetic analogues of native hemes, chlorophylls, and bacteriochlorophylls (**BC**) in a manner to introduce or enhance desired characteristics is a major driver in tetrapyrrole research. The ability to adjust solubility to match a local environment and reliably adjust the absorption spectra would greatly benefit applications such as photovoltaic arrays or biological sciences. Near IR and red spectral region investigations have become of increasing interest to obtain suitable chromophores. This work concerns determining the photophysical characteristics of mono-and dioxo-bacteriochlorins (**H₂BC-O⁷** or **H₂BC-O⁷,¹⁷**) lacking any peripheral substituents except for a stabilizing geminal dimethyl group on each pyrroline ring. The oxo- groups are attached to the same pyrroline rings as the dimethyl groups. The mono- and dioxo-bacteriochlorins were compared to **H₂BC**, a bacteriochlorin lacking the oxo-
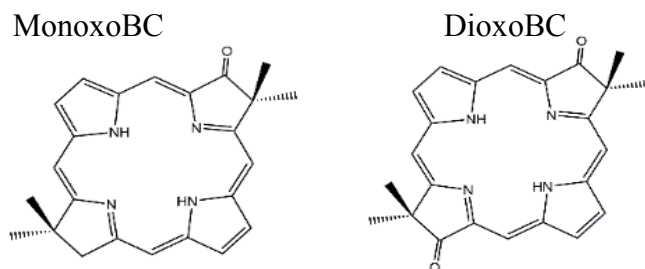
Figure 9. Structures of H₂BC-O⁷ and H₂BC-O⁷,¹⁷.

groups but with the stabilizing geminal dimethyl groups on the pyrroline rings. Without the geminal dimethyl group the pyrroline ring is prone to adventitious dehydrogenation and return to either a chlorin or porphyrin. With this stabilized 'bare bones' bacteriochlorin it was found by collaborators that the position of the long-wavelength absorption Q_y band is capable of being tuned by placement of auxochromes about the perimeter of the macrocycle. Auxochromes on the y-axis give a bathochromic shift versus H₂BC and, as reported above, oxo groups on the x-axis give a hypsochromic shift of the Q-band and a bathochromic shift of the B-band.

In general, relative to **H₂BC**, the oxo groups placed on the x-axis resulted in a hypsochromic effect of 23 nm of the red-region Q_y with the green-region Q_x shifting 23 nm and a bathochromic shift of approximately 45 nm of the violet-blue B-band manifold for **H₂BC-O⁷**. The addition of the second oxo group (**H₂BC-O⁷,¹⁷**) resulted in a further shift (relative to **H₂BC-O⁷**) of 10 nm of the Q_y and a bathochromic shift of 5 nm of the B_y with a 6 nm of the B_x. Along with these shifts was a modest reduction in the intensity of the Q_y band and the Q_x was reduced by approximately seven-fold. The Stokes shift between the Q_y fluorescence and absorption peaks becomes progressively smaller with the addition of each oxo group, suggesting increasing structural rigidity

Here, the accordion-like behavior (compressing or expanding the spectrum) for the B- and Q-bands, combined with the shifting of intensity from the B-band to the Q-band is indicative of progressive reduction of orbital mixing as the symmetry is progressively reduced by the addition of the oxo groups (intensity) and the change in the conjugated system (by shifting the electron density distribution. The latter is evidenced by the results of DFT calculations and the increase in the relative energy differences for the excited-state configurations. The addition of the oxo groups does not cause substantial changes in the Φ_f , Φ_{isc} , or Φ_{ic} .

Further investigations of the photophysical properties for the monoxo- and dioxo-BCs were conducted in concert with tolyporphin-a, as introduced in the following section and in reported in Chapter 3.

Background and Photophysical Characteristics of Naturally Occurring Dioxobacteriochlorin

Tolyporphin and Synthetic Oxobacteriochlorin Analogues
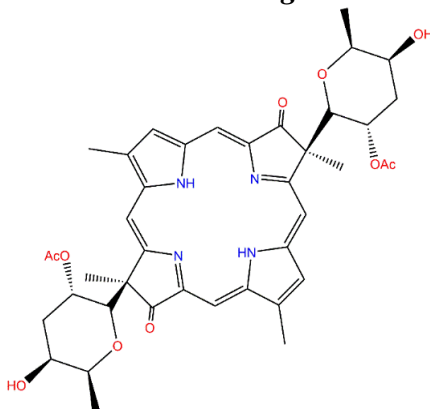
Figure 10. Structure of tolyporphin A, a dioxo-

Tolyporphin A (**TolyP**) (Figure 7) is a novel dioxobacteriochlorin geminally disubstituted with a methyl group and a C-glycoside on each pyrroline ring that partially encumber one tetrapyrrole face and one position in each pyrrole ring is unsubstituted. Several other members of the tolyporphin macrocycles have been identified in the original cyanobacteria, but have not been isolated. **TolyP** may be involved in photoprotection or light-harvesting for the cyanobacteria.

This study included the synthetic mono-and dioxoBCs profiled in the previous section. These experiments were carried out in ten different solvents reflecting a wide range of dielectric properties, as might be found in varying environments. Photophysical characteristics such as fluorescence yield and lifetime, triplet yield, and associated rate constants were obtained in all ten of the solvents. The results (in toluene) were compared to native photosynthetic chlorins and bacteriochlorins.

The absorption spectrum of TolyP (a dioxoBC) resembled $H_2BC\text{-}O$[7,17] more than the monoxo-BC indicating the C-glucoside substituents do not cause major changes in spectral properties. This is reinforced with the similarity to the native chlorins, rather than the native bacteriochlorins. As in the earlier frontier molecular orbital analysis for the "bare bones" oxo-

bacteriochlorins,[ref] the oxo groups stabilize the two highest filled and two lowest empty molecular orbital electron promotions for the near-UV to near-IR spectra. Again, relative to the native bacteriochlorins, TolyP exhibits hypso- and hypochromically shifted Q_y bands and batho- and hyperchromically shifted B_x and B_y bands. While the TolyP has k_f values comparable to the synthetic and native BCs, the k_{isc} values do not appreciably change from the native chlorins and BCs. The dioxo motif of TolyP does not seems to appreciably change the electron density distribution or other factors that control electron spin-orbit coupling, which, in turn, affect the probability of $S_1 \rightarrow T_1$ intersystem crossing. However, the k_{ic} values for TolyP and $H_2BC-O^{7,17}$ are more similar to native chlorins, while reduced from native BCs with generally similar Q_y wavelengths. The S_1-S_0 k_{ic} increases as the S_1 energy decreases. Thus, the slower S_1 k_{ic} parallels the higher S_1 energy reflected in the hypsochromically shifted Q_y band for the TolyP, $H_2BC-O^{7,17}$, and chlorins compared to the native and majority of synthetic BCs.

The spectral and photophysical properties of TolyP were found to be relatively insensitive to solvent characteristics over a large range of polarity. The lack of sensitivity implies TolyP may be active in the cytoplasm as well as more nonpolar membrane environments.

Background and Photophysical Characteristics of Synthetic Biohybrid Light-Harvesting Antennas

The project described in this section requires understanding of a myriad of specialized terms. For convenience and to alleviate potential confusion due to the similarity of several of these terms and the particular concepts they involve the following lexicon is provided:

Lexicon:

Chromophore: **BC1-mal** (synthetic bacteriochlorin) or just **BC1**, **BC0** (bacteriochlorin without maleimido).

Bacteriochlorophyll *a*: **BChl *a***, naturally occurring bacteriochlorin.

Biohybrid: β-peptide analog with BC1 + native α-peptide + BChl *a* self-assemble to form αβ-dyads and LH1-type cyclic (αβ)$_n$ oligomer

Dyad: α- and β-peptides, each with a BChl *a* attached

BChl *a* dimer: **B820** (when in dyad, ≈780 nm unattached), **B875** in oligomer (αβ-dyads in a ring)

Conjugate or BC1 conjugate or bioconjugate or peptide-bacteriochlorin conjugate: involving the synthetic β-peptide with attached **BC1**.

LH1 ring: oligomer, 14-16 αβ-dyads in a ring (**B875**)

One project by a team of investigators (including our group) in the Photosynthetic Antenna Research Center (PARC) has been to investigate the absorption and transfer of energy during photosynthesis and, if possible, to extend the range of the frequencies of light absorbed by the organism.

Photosynthetic organisms utilize light harvesting antennas from chlorins (in plants) and bacteriochlorins (in bacteria). They are made up of 3-D structures of said pigments and their purpose is to absorb energy (as photons) and transfer it to reaction centers. Different antennas absorb various frequencies of light depending on the number and types of pigments present in the antenna. These natural photosynthetic systems absorb in narrow ranges of the solar spectrum

18

leaving gaps that do not make use of these regions of the solar spectrum. One of the difficulties in mimicking the natural antenna systems using organic synthesis is the daunting task of assembling large numbers of chromophores in a large 3D arrangement that affords broad absorption, minimizes self-quenching, and allows efficient delivery of the absorbed energy to a target site.

A successful strategy has been to focus on designs based on the cyclic light-harvesting system one (LH1), but without reaction centers, from photosynthetic purple bacteria. Here, the reaction centers are surrounded by a ring of dyads comprised of α- and β-peptides with each peptide bound to a molecule of bacteriochlorophyll *a* (BCl *a*). See Figures 10A and 10B below.

Figure 11. (A) Native αβ-subunit consisting of the α-peptide (blue), β-peptide (green) and a pair of **BChl *a*** molecules (purple) coordinated via the central magnesium ion to a histidine residue (black) of each peptide (from LH2 of *Phs. Molischianum*22). (B) Theoretical depiction of side and top views of the cyclic oligomeric LH1 complex of *Rb. sphaeroides*;18 some peptides in the side view, and some of the **BChl *a*** molecules in both views are omitted for clarity. (C) Sites for chromophore attachment by replacing the residue with Cys, with numbers corresponding to the position relative to His 0. The sites with negative numbers (toward the *N*-terminus) have been used in prior studies for attachment of bioconjugatable bacteriochlorin **BC1-mal**; the energy transfer efficiencies measured in the resulting cyclic oligomers are shown. The sites with positive numbers were explored herein. (D) The structure of **BC1-mal** and an illustration of the oligomer housing this pigment on all β-peptides (and αβ-dyads).

Biohybrid light-harvesting antennas consist of a maleimido-bearing bacteriochlorin (**BChl *a***) covalently attached to a Cys residue substituted at various positions relative to His of the 48-residue β-peptide of *Rb. Sphaeroides* LH1 (Figure 8C and 8D). The synthetic β-peptides are combined with native α-peptides in a micelle producing αβ-dyads which further self-assemble into cyclic LH1-type $(\alpha\beta)_n$ oligomers. The maleimido terminated tether for bioconjugation with a cysteine sulfhydryl group is located at various positions on the b-peptide for studying energy transfer efficiency (ϕ_{EET}). Previous work examined positions from the histidine reference to the N-terminal (negative numbering) of the β-peptide. This chapter explores the positive or C-

terminal positions. The attachment of BCl-mal to the cysteine results in a peptide-bacteriochlorin conjugate. The dyad itself absorbs at 820 nm and the oligomer at 875 nm. BChl a in the cyclic oligomer has a Q_x at $\approx$ 515 nm and the Q_y at $\approx$875 nm.

The process begins when the BC1-mal absorbs at 515 nm (S_2) or 720 nm (S_1) and undergoes IC to produce S_1 as noted in the general background. This *S"X" state of the chromophore then transfers the energy thru the dyad or directly through space via proximity to the BCl a, and then distributed around the B875 cyclic oligomer (S_1 at 875 nm). One of the goals of this project is to determine how efficiently this transfer occurs and what site along the beta peptide can be used to attach the synthetic BChl for this process to be efficient.

Specifically, photosynthetic purple bacteria cyclic LH1 inner antenna like complexes behave like LH2 accessory antennas, while the BChl a molecules attached to each of the αβ-peptides (dyad) shifts the NIR Q_y absorption band from $\approx$780 nm (isolated pigment) to 820 nm for the dyad. This dyad with two BChl a molecules is now designated B820. By controlling the detergent / water concentration in a B820 solution, the B820 dyads will self-assemble in LH1 style rings with 14-16 αβ-dyads each. Once in a ring oligomer the Qy band again red-shifts to $\approx$875 nm and is designated as B875. Various positions on the α-peptide have been substituted with synthetic chromophores (bioconjugatable bacteriochlorin) at seven different positions as counted from the histidine (position 0) and counting towards the N-terminus of the peptide. These systems have provided energy-transfer efficiencies (Φ_{EET}) from 50 to 90% (Figure 8C negatively numbered positions).

Using the same bioconjugatable bacteriochlorin (**BC1**), three positions toward the C-terminal were investigated here (Figure 8C positive numbers) with the +11 position as an addition to the C-terminal itself.

Experimental Methods

The following methods were generally used to determine the photophysical characteristics for the studies included in this thesis. Specific conditions and results are described in the individual chapters. Spectral and photophysical studies of the molecules were carried out on dilute (mM) argon-purged samples at room temperature.

Static ground state absorption

Absorption spectra were acquired using a Shimadzu UV-1800 spectrometer in 0.2 nm steps from 300 nm to 1100 nm in a quartz 1 cm cuvette and corrected against a solvent blank. A standard was used for relative comparisons and the absorbance was converted to absorptance, which was subsequently utilized to calculate fluorescence quantum yields (Φ_f).

Static fluorescence

Static emission fluorescence spectra were acquired using a Spex-Horiba Nanolog spectrofluorimeter with 2–4 nm excitation and detection bandwidths and corrected for instrument spectral response. Fluorescence quantum yields are the average of values obtained relative to meso-tetraphenylporphyrin ($\Phi_f = 0.070$ in nondegassed toluene and 0.090 in degassed toluene).

Singlet excited-state lifetime

Singlet excited-state lifetimes were determined by using transient absorption (TA) spectroscopy employing ≈100 fs excitation flashes from an ultrafast laser system (Spectra Physics) and acquisition of difference spectra (360–900 nm) using a white-light pulsed laser (≈1 ns rise time) in 100 ps time bins with variable pump–probe spacing up to 0.5 ms (Ultrafast Systems, EOS). Transient absorption measurements employed excitation in the Q_x and Q_y bands. Time profiles of

ΔA at ≈ 1.5 nm spacing across the 380–800 nm region were analyzed at a number of individual wavelengths and also globally.

Measurement of the S_1 lifetime of was also made on a sample degassed by 10 freeze–pump–thaw cycles on a high vacuum line (10^{-5} torr). These studies employed a home-built flash-photolysis set up using 2 μJ 525 nm pulses from a YAG-pumped dye laser (Spectra Physics INDI/Sirah) and a detection system with a 3 μs instrument response function.

Transient absorption

Transient absorption studies were also used to measure the yield of S_1-T_1 intersystem crossing by comparing the extent of bleaching of the ground-state absorption bands due to T_1 at the asymptote of the S_1 decay versus the extent due to S_1 immediately after the excitation flash. Measurements in the Q_y region account for the contribution of both S_0 bleaching and S_1 stimulated emission to the S_1 feature.

Photophysical calculations

Absorbance ($A_{corr+bsln\ adj}$)**:** $A_{corr+bsln\ adj} = (A_{sample} - A_{blank}) \times (\text{baseline factor})$ All measurements taken in the same cuvette on the same day, usually both before and after Argon bubbling.

Absorptance (AbsT)**:** $AbsT = 1 - 10^{(-(A_{corr+bsln\ adj}))}$

Emission, Relative Method (Ems): Ems = Area under peak at B_x, Q_y, Q_x Emission measured for standard at same absorption wavelengths as sample.

Quantum Yield (Φ_f): $\Phi_f = ((Ems/AbsT)_{Sample} / (Ems/AbsT)_{Standard}) \times (\text{Standard reference } Ems) \times (N_{D\ sample}/N_{D\ standard})^2$ At a given excitation wavelength AbsT and Ems wavelength for both sample and standard.

Decay Processes Rate Constants

$$\tau_s = (k_f + k_{ic} + k_{isc})^{-1} \qquad \text{Singlet Lifetime}$$

$$\Phi_f = k_f \,/\, (k_f + k_{ic} + k_{isc}) \qquad \text{Fluorescence Yield}$$

$$\Phi_{isc} = k_{isc} \,/\, (k_f + k_{ic} + k_{isc}) \qquad \text{Triplet Yield}$$

$$\Phi_{ic} = 1 - \Phi_f + \Phi_{isc} \qquad \text{Internal Conversion}$$

$$k_i = \Phi_i \,/\, \tau_s \qquad \text{where } i = f, \text{ isc, or ic}$$

Chapter 2

Synthesis, Photophysics and Electronic Structure of Oxobacteriochlorins

Mengran L, Chih-Yuan C, D Hood, M Taniguchi, J Diers, D Bocian, D Holten and J Lindsey.

Abstract

Synthetic routes are described to access mono- and dioxobacteriochlorins that lack any peripheral substituents, with the exception of a geminal dimethyl group in each pyrroline ring to stabilize the macrocycle towards adventitious oxidation. The introduction of one or two oxo groups on the pyrroline rings results in hypsochromic shifts of the longest wavelength near-infrared absorption band (Q_y) to 690 and 680 nm, respectively, versus the parent bacteriochlorin for which the Q_y band is at 713 nm. The position of the Q_y absorption band of the oxobacteriochlorin is in the range of that of elaborately functionalized chlorin macrocycles (containing one pyrroline ring versus two in a bacteriochlorin), where the elaborate functional groups bathochromically shift the Q_y feature from that of unfunctionalized chlorins (typically in the low 600 nm region). The long-wavelength absorption band of synthetic oxobacteriochlorins thus appears in the window defined by simple chlorins to the red and substituted bacteriochlorins to the near-infrared. The ability to access the deep-red (680–690 nm) region via the relatively simple synthetic modification of oxo-group addition to a bacteriochlorin versus the more complex multifunctionalization of a chlorin is attractive for accessing tetrapyrroles for solar-energy conversion and other applications.

Introduction

A longstanding objective in tetrapyrrole science has been to develop synthetic analogues of the natural chromophores that can be tailored at will for pursuit of diverse applications in solar-energy and life-sciences research. Such tailoring includes the incorporation of functionalities that enhance solubility and stability, facilitate elaboration into multi-chromophore arrays, and allow spectral tuning. The parent synthetic analogues of the native hemes, chlorophylls, and bacteriochlorophylls are respectively porphyrins, chlorins and bacteriochlorins, the long wavelength absorption band of which lies in the visible, red or near infrared (NIR) region, with increasing intensity along the series. All three classes share strong absorption in the near ultraviolet region. In general, the red and NIR spectral regions have been far less explored than the visible region owing chiefly to the availability of suitable chromophores. This situation has improved due to advances in the synthesis of chlorins and bacteriochlorins,[1-9] which together are often referred to as hydroporphyrins. One distinguishing feature of the routes to chlorins and bacteriochlorins that we have developed is the presence of a gem-dimethyl group in each reduced, pyrroline ring thereby stabilizing the macrocycle toward adventitious dehydrogenation.[7]

We have found that the position of the long-wavelength absorption (Q_y) band can be tuned by the placement of auxochromes at distinct sites about the perimeter of the hydroporphyrin macrocycle. The molecular axes and numbering system for the hydroporphyrins are shown in Chart 1. In general, auxochromes located along the axis bisecting the two pyrrole rings (the y axis) result in a bathochromic shift versus that of the unsubstituted bacteriochlorin. The ability to control the position of the long-wavelength absorption band is of utmost importance, not only for the ability to capture light in a given spectral region but also because the band position defines the

maximum energy of the first excited singlet state. The latter places an upper limit on the energetics

of photochemical processes emanating from the hydroporphyrin.
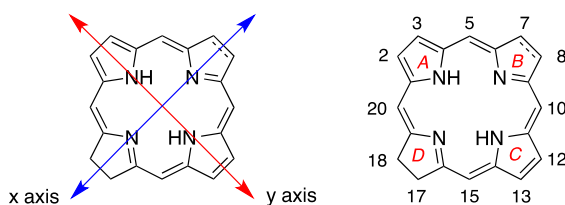
Chart 1 Molecular axes and numbering system for hydroporphyrins.

The Q_y absorption bands are shown in Fig. 1 for representative (bacterio)chlorins (Chart

2). Notable trends are as follows: (1) Chlorins and bacteriochlorins encompass the spectral range

of 602–715 nm and 713–888 nm, respectively. (2) Metalation of a chlorin causes a hypsochromic

shift (compounds *b* vs *a*) whereas metalation of a bacteriochlorin causes a bathochromic shift (*o*

vs *p*). (3) In the bacteriochlorin series, the presence of a 5-methoxy group causes a hypsochromic

shift (*m* vs *n*). (4) The presence of an oxo group in the pyrroline ring causes a significant

hypsochromic shift for bacteriochlorins (*h* and *i* vs *k*) but little or no spectral shift for chlorins (*f*

vs *a* and *g* vs *b*). Additional photophysical trends concerning the effects of substituents have been

described for the compounds shown in Chart 2 and a large number of related macrocycles.[10-15]
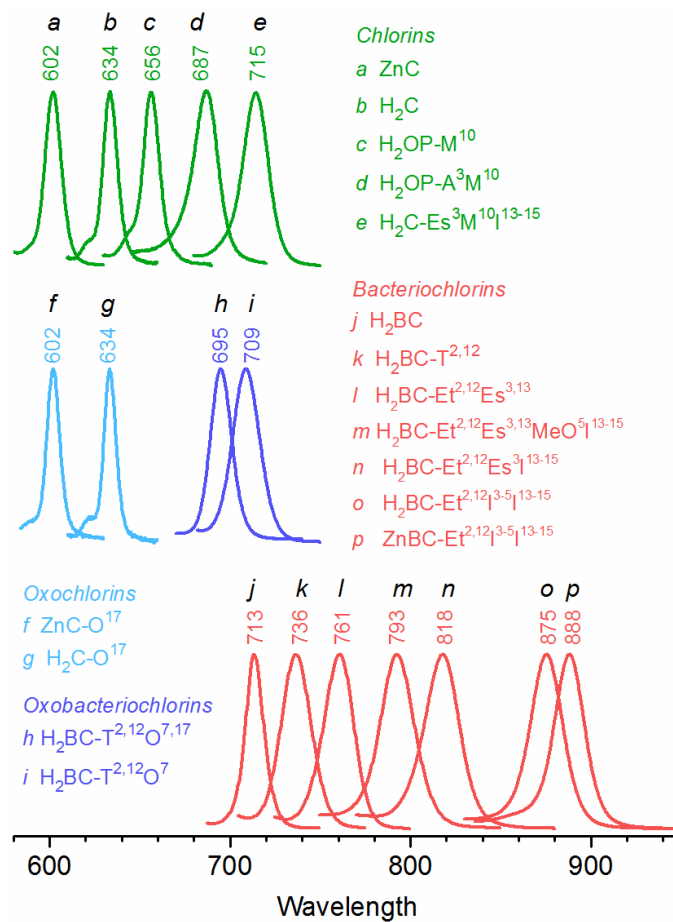
Figure 1. Q_y bands of selected chlorins (green),[16,17] oxochlorins (cyan),[18] oxobacteriochlorins (blue)[13] and bacteriochlorins (red).[10,13] The corresponding structures are shown in Chart 2.

Oxochlorins

Chlorins

X

EtO—O

ZnC-O[17] (M = Zn)
H$_2$C-O[17] (M = H, H)

ZnC (M = Zn)
H$_2$C (M = H, H)

H$_2$OP-M[10] (X = H)
H$_2$OP-A[3]M[10] (X = Ac)

H$_2$C-Es[3]M[10]I[13,15]

Ph

Oxobacteriochlorins

Bacteriochlorins

Y

H$_2$BC-T[2,12]O[7]

H$_2$BC-T[2,12]O[7,17]

H$_2$BC-T[2,12] (Y = H)
H$_2$BC-MeO[5]T[2,12] (Y = OMe)

Ph

Y

EtO—O

EtO—O   Y

O   OEt

Ph

Ph

H$_2$BC (Y = H)
H$_2$BC-MeO[5] (Y = OMe)

H$_2$BC-Et[2,12]Es[3,13]

H$_2$BC-Et[2,12]Es[3]I[13-15] (Y = H)
H$_2$BC-Et[2,12]Es[3]MeO[5]I[13-15] (Y = OMe)

H$_2$BC-Et[2,12] I[3-5]I[13-15] (M = H, H)
ZnBC-Et[2,12] I[3-5]I[13-15] (M = Zn)

Chart 2 Diverse macrocycles: C is chlorin; BC is bacteriochlorin; and OP is 13^1-oxophorbine. Prefixes: H$_2$ is free base; and Zn is zinc chelate. Substituents: A is acetyl; Es is carboethoxy; Et is ethyl; I is *N*-benzylimido; M is mesityl; MeO is methoxy; Oxo is =O; and T is *p*-tolyl.

Given that auxochromes located along the molecular y-axis generally give bathochromic shifts of the Q$_y$ band, noteworthy is the opposite shift observed upon placement of an oxo group along the x-axis of a bacteriochlorin. This hypsochromic effect is demonstrated in Fig. 1 by **H$_2$BC-T^{2,12}O^7** (*i*; 709 nm) versus **H$_2$BC-T^{2,12}** (*k*; 736 nm). This 27-nm shift is followed by a shift of about half that amount (14 nm) upon incorporation of a second oxo group in **H$_2$BC-T^{2,12}O^{7,17}** (*h*;

695 nm). The hypsochromic effect of an oxo group on the spectrum of a bacteriochlorin was intriguing for several reasons. First, the absorption of the resulting structurally simple oxobacteriochlorins appears in the region accessed by elaborately functionalized chlorins, namely the chlorin–imides (e.g., **H₂C-Es³M¹⁰I¹³⁻¹⁵** (*e*); Fig. 1). The ability to access this spectral region merely by installation of an oxo group in the bacteriochlorin is very attractive. Second, in principle, the pyrroline oxo group could serve as a convenient (and little explored) site of further functionalization, with perhaps interesting features for such derivatives in wavelength tuning.

One shortcoming of this initial foray into oxobacteriochlorins is that the synthesis employed at the time also incorporated *p*-tolyl groups at the 2,12-positions of the bacteriochlorin. Fig. 1 shows that these substituents give a 23 nm bathochromic effect on the Q_y band, exemplified by **H₂BC-T²,¹²** (*k*; 736 nm) versus **H₂BC** (*j*; 713 nm). Thus, in **H₂BC-T²,¹²O⁷** the 27-nm hypsochromic effect of the oxo group essentially counterbalances the 23-nm shift in the opposite direction of the two *p*-tolyl substituents, and the second oxo group in **H₂BC-T²,¹²O⁷,¹⁷** then gives a modest shift from that essentially null starting point. To expose the full wavelength shift into the normal chlorin spectral region by oxo substituents on a bacteriochlorin, ideally one would successively incorporate oxo groups on the parent **H₂BC**, unimpeded by potential countering effects of other auxochromes. Such considerations led us to speculate that such a simple dioxobacteriochlorin (**H₂BC-O⁷,¹⁷**) likely would have a Q_y band at 670–675 nm.[13]

In this paper, we report the synthesis and characterization of several oxobacteriochlorins, including **H₂BC-O⁷,¹⁷**. Our objectives were to (1) achieve a rational synthesis of oxobacteriochlorins, (2) use the oxobacteriochlorins as building blocks, and (3) gain a deep understanding of the photophysical features of the oxobacteriochlorins. The absorption spectra of several oxobacteriochlorins have been characterized and analyzed using the results of density

functional theory (DFT) and time-dependent DFT (TDDFT) to gain a deeper understanding of the energetic effects of the oxo group in the pyrroline motif. The rate constants and yields of the three singlet excited-state decay pathways (fluorescence, intersystem crossing, internal conversion) also have been measured using static and time-resolved optical spectroscopy. One oxobacteriochlorin has been elaborated to give a hydrophilic bioconjugatable oxobacteriochlorin.[15] Taken together, the work advances capabilities for tailoring the properties of bacteriochlorins by straightforward synthetic means.

Results and discussion

Reconnaissance

The traditional route for formation of oxobacteriochlorins has relied on treatment of a porphyrin bearing a full complement of β-alkyl substituents with OsO_4 followed by acid-mediated pinacol-like rearrangement.[19-30] An example is shown in Scheme 1 for the reaction with octaethylporphyrin. Even with this symmetrical porphyrin, two dioxobacteriochlorins are produced. The complexity of the reaction mixture often increases with less symmetric porphyrins due to insufficient selectivity of a given pyrrole toward oxidative cycloaddition with OsO_4 as well as the migration preferences of various alkyl groups.[9]
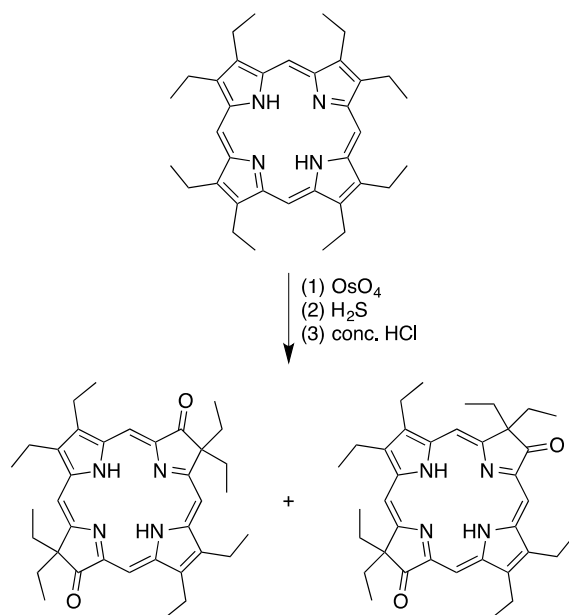
Scheme 1 Traditional route to oxobacteriochlorins.

Rational routes developed more recently for formation of oxobacteriochlorins have relied on preparation of a gem-dialkylbacteriochlorin followed by oxidation of the methylene group of the pyrroline ring. Examples are displayed in Scheme 2. As part of studies related to the synthesis of the natural dioxobacteriochlorin tolyporphin A,[31-37] Minehan and Kishi converted a 3,12-dimethylbacteriochlorin to the corresponding dioxobacteriochlorin through use of CrO_3 and 3,5-dimethylpyrazole (DMP, example 1).[38] Minehan, Wang and Kishi extended this approach to gain access to tolyporphin A *O,O*-diacetate (example 2).[39,40] The same reagent (7 equiv) was used with a 2,12-di-*p*-tolylbacteriochlorin to form the dioxobacteriochlorin **H₂BC-T^{2,12}O^{7,17}** (example 3).[13] Use of only 4 equivalents afforded the mono-oxobacteriochlorin **H₂BC-T^{2,12}O^{7}** (4.1 mg, 72% yield; not shown).[13] We continued examination of $CrO_3 \cdot DMP$ with bacteriochlorins as described in the next section.
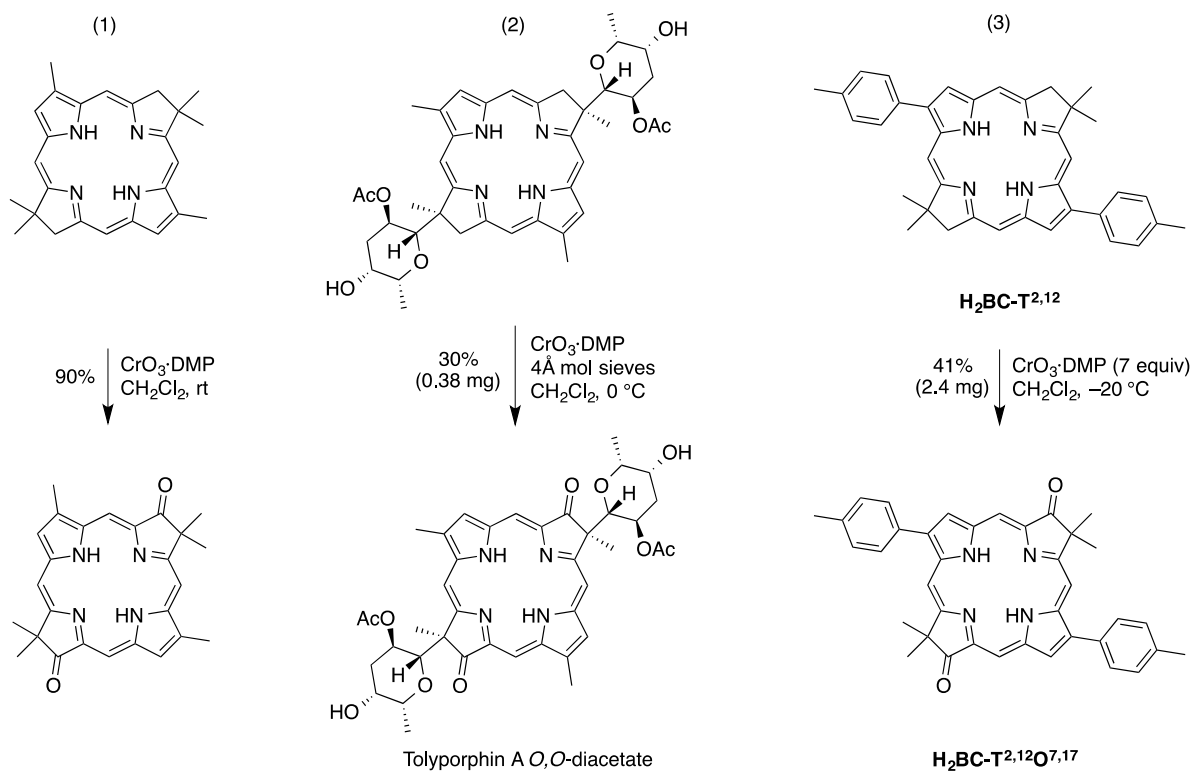
Scheme 2 Rational routes to oxobacteriochlorins.

Synthesis

Survey of Oxidants. Treatment of the 3,13-dibromobacteriochlorin[41] **H₂BC-Br³,¹³** with a CH₂Cl₂ suspension of CrO₃·DMP promptly yielded oxobacteriochlorins. Titration of 5 molar equivalents of CrO₃·DMP to **H₂BC-Br³,¹³** in CH₂Cl₂ at −5 °C gave the mono-oxobacteriochlorin, **H₂BC-Br³,¹³O⁷** in 27% yield. The reaction was readily monitored by absorption spectroscopy, given that the Q_y band at 729 nm (**H₂BC-Br³,¹³**) shifts to 703 nm (**H₂BC-Br³,¹³O⁷**). Upon titration of the bacteriochlorin with 20 molar equivalents of CrO₃·DMP, a more hypsochromically shifted Q_y band at 693 nm was observed, indicating formation of the dioxobacteriochlorin **H₂BC-Br³,¹³O⁷,¹⁷**. Purification of **H₂BC-Br³,¹³O⁷,¹⁷** to homogeneity was thwarted due to poor solubility in various organic solvents (CH₂Cl₂, CHCl₃, ethyl acetate and methanol), yet the partially purified

bacteriochlorin was characterized by matrix-assisted laser desorption ionization mass spectrometry (MALDI-MS) and absorption spectroscopy.

The hygroscopic nature of CrO_3 and the presence of a suspension made handling and quantitative usage rather awkward, particularly at small scale. Therefore, we surveyed other possible oxidizing agents and reaction conditions (Table S1, Supplementary Information). It is noteworthy that Kishi and coworkers arrived at $CrO_3 \cdot DMP$ following examination of a host of other oxidants, including Pt/O_2, 2,3-dichloro-5,6-dicyano-1,4-benzoquinone, *meta*-chloroperoxybenzoic acid/dimethyl dioxirane, and benzoyl peroxide/O_2.[38] The analogous oxidation of gem-dimethylchlorins to form oxochlorins also entailed a lengthy search to identify suitable reagents.[42] Ultimately we found that treatment of **H₂BC-Br**[3,13] with pyridinium dichromate (PDC) in slight excess in CH_2Cl_2 at controlled temperature[43] (–30 °C to room temperature) gave the desired mono-oxobacteriochlorin **H₂BC-Br**[3,13]**O**[7] in 59% yield (Scheme 3).
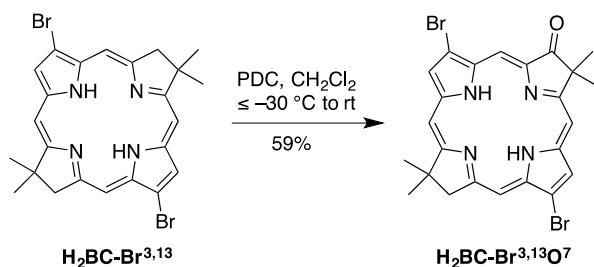
Scheme 3 Synthesis of a monooxobacteriochlorin.

Oxobacteriochlorins without β-pyrrole substituents. Treatment of unsubstituted bacteriochlorin[41] **H₂BC** with 2 equivalents of PDC over 24 h afforded a mixture of **H₂BC-O**[7] and **H₂BC-O**[7,17]. To achieve greater selectivity, we found that excess MnO_2 in CH_2Cl_2 over 24 h afforded mono-oxobacteriochlorin **H₂BC-O**[7] in 70% yield accompanied by a trace amount of unreacted **H₂BC** as well as dioxobacteriochlorin **H₂BC-O**[7,17] (Scheme 4). Treatment of **H₂BC-O**[7]

with MnO$_2$, however, failed to give **H$_2$BC-O^{7,17}**, but reaction with a stoichiometric amount of PDC in CH$_2$Cl$_2$ over 24 h afforded **H$_2$BC-O^{7,17}** in 70% yield.
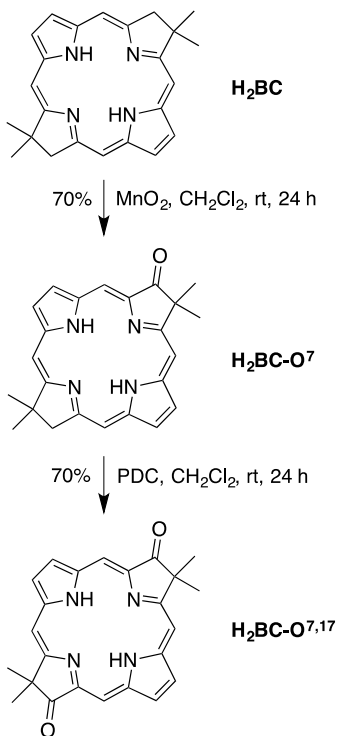
Scheme 4 Synthesis of unsubstituted oxobacteriochlorins.

An alternative route to **H$_2$BC-O^7** entailed hydrodebromination of the dibromooxobacteriochlorin **H$_2$BC-Br^{3,13}O^7** (Scheme 5). Such conditions employ formic acid as the hydrogen-atom donor in the presence of the Pd(0) reagent Pd(PPh$_3$)$_4$ in the presence of hot triethylamine.[44-46] In this manner, **H$_2$BC-Br^{3,13}O^7** afforded the unsubstituted oxobacteriochlorin **H$_2$BC-O^7** in 47% yield. The fully unsubstituted bacteriochlorin, **H$_2$BC**, has been prepared in analogous fashion.[46]
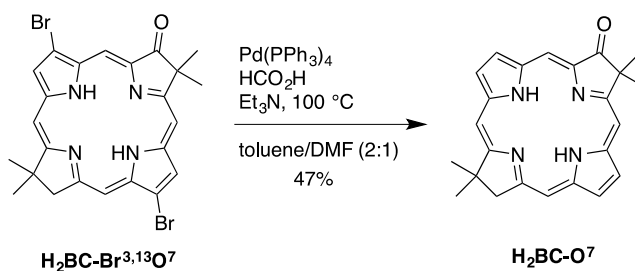
Scheme 5 Hydrodebromination to form the unsubstituted oxobacteriochlorin.

Application to a 5-methoxybacteriochlorin. An oxobacteriochlorin building block derived from **H₂BC-Br³,¹³MeO⁵** was pursued to shift the Q_y band hypsochromically into the red spectral region. Use of PDC afforded two oxobacteriochlorin isomers but also resulted in extensive decomposition of the starting material, whereas MnO_2 gave a conversion yield of only 50% but without obvious decomposition (Scheme 6). Three components were detected upon TLC analysis following MnO_2 treatment: unreacted starting material **H₂BC-Br³,¹³MeO⁵**, minor isomer **H₂BC-Br³,¹³MeO⁵O¹⁷**, and major isomer **H₂BC-Br³,¹³MeO⁵O⁷** (Figure S1, Supplementary Information). The two isomers exhibited distinct chromatographic mobilities and also distinct colors (Fig. 2). Upon column chromatography, the unreacted **H₂BC-Br³,¹³MeO⁵** was recovered, and **H₂BC-Br³,¹³MeO⁵O⁷** and **H₂BC-Br³,¹³MeO⁵O¹⁷** were readily isolated in 27% and 15% yield, respectively (54% and 31% on the basis of 50% conversion). Isomer **H₂BC-Br³,¹³MeO⁵O⁷** was used in the preparation of a hydrophilic, bioconjugatable bacteriochlorin (**I**).[15] Derivatization of **H₂BC-Br³,¹³MeO⁵O¹⁷** with semicarbazide hydrochloride in refluxing ethanol[47] afforded bacteriochlorin–semicarbazone **II** in 78% yield. The latter derivatization was inspired by the analogous derivatization of the formyl group of chlorophyll *b* with a trimethylammonio-substituted semicarbazide (Girard's reagent T).[48] Bacteriochlorin–semicarbazone **II** absorbs at 736 nm, to be compared with 706 nm for the ketone **H₂BC-Br³,¹³MeO⁵O¹⁷**.
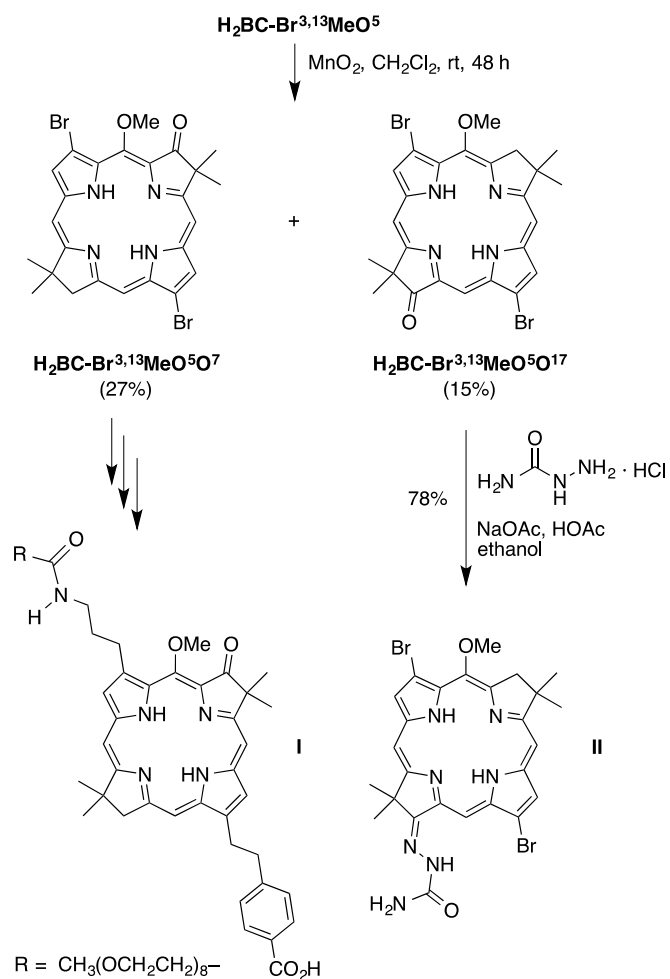
Scheme 6 Oxidation followed by derivatization of a 5-methoxybacteriochlorin.
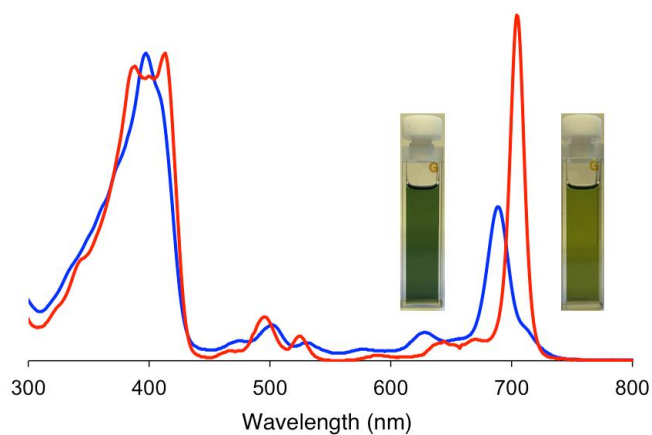
Figure 2. Absorption spectra in toluene of oxobacteriochlorin isomers **H₂BC-Br^{3,13}MeO^{5}O^7** (blue line, Q$_y$ = 692 nm) and **H₂BC-Br^{3,13}MeO^{5}O^{17}** (red line, Q$_y$ = 706 nm).

37

The position of the oxo group in **H₂BC-Br^{3,13}MeO^{5}O^7** and **H₂BC-Br^{3,13}MeO^{5}O^{17}** was determined by analysis of 2D NOESY spectra (Scheme 7). For the major product, the NOE signal between the pyrroline methylene protons and the meso proton at the 15-position establishes the oxo group at the 7-position **(H₂BC-Br^{3,13}MeO^{5}O^7)**. For the minor product, the NOE signal between the pyrroline methylene protons and the protons of the 5-methoxy group imply the oxo group at the 17-position (**H₂BC-Br^{3,13}MeO^{5}O^{17}**). The observed selectivity for oxidation of the 7-methylene site, adjacent to the 5-methoxy group, versus that at the 17-position, is somewhat surprising. One interpretation is that the 7-methylene site is more susceptible to oxidation due to electronic stabilization of the putative incipient radical. A second interpretation is that the methoxy group provides some coordination of the incoming MnO_2 oxidant. The data are insufficient to provide any insight into these distinct possibilities. It warrants mention, however, that reaction at the bromine sites can be affected by the neighboring 5-methoxy group. The Pd-mediated coupling reaction of **H₂BC-Br^{3,13}MeO^5** to install an ethynyl group (Sonogashira reaction)[49] or aryl group (Suzuki reaction)[50] proceeds selectively at the 13-position rather than the 3-position. The differential reactivity enables successive coupling reactions at both sites, and has been deftly exploited to create bacteriochlorin-containing arrays.[50,51] Thus, the regioselectivity for Pd-coupling at the pyrrole positions is quite different from that for oxidation at the pyrroline positions of the 5-methoxybacteriochlorin.
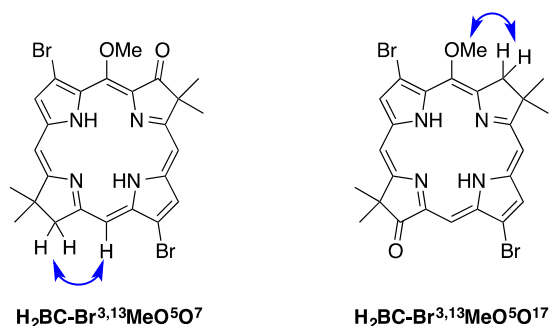
Scheme 7 NOEs observed in identification of oxobacteriochlorin isomers.

To seek further consistency with these NMR assignments and with the relative positions of the NIR Q_y bands of 7-oxo versus 17-oxo bacteriochlorins (Fig. 2), TDDFT calculations were carried out on the analogues of the two isomers shown in Scheme 7 that lack the 3,13-bromine atoms (for ease of calculation). The calculations for the fictive **H2BC-MeO^{5}O^7** and **H2BC-MeO^{5}O^{17}** give Q_y bands at 631 and 668 nm with oscillator strengths of 0.24 and 0.26, respectively. The B_x/B_y bands for the two isomers have positions (and oscillator strengths) of 373/344 nm (1.55/0.825) and 373/348 nm (1.56/1.05), respectively. The calculations are thus consistent with (1) the Q_y band of **H2BC-Br^{3,13}MeO^{5}O^7** at shorter wavelength than that for **H2BC-Br^{3,13}MeO^{5}O^{17}**, and (2) the Soret features (B_x/B_y) at comparable positions for the two isomers (Fig. 2).

Spectral properties

The absorption spectra of the unsubstituted oxobacteriochlorin **H2BC-O^7** and dioxobacteriochlorin **H2BC-O^{7,17}** are shown in Fig. 3A, along with that of the benchmark bacteriochlorin **H2BC**. The spectra are normalized to the total absorption intensity (300−1000 nm) obtained by integration of spectra plotted versus wavenumbers (linear in energy). This presentation is useful for comparing spectra of related tetrapyrroles with each other and with calculations and spectral simulations (vide infra), and complements other methods such as normalization at the Q_y or Soret maximum.[13]
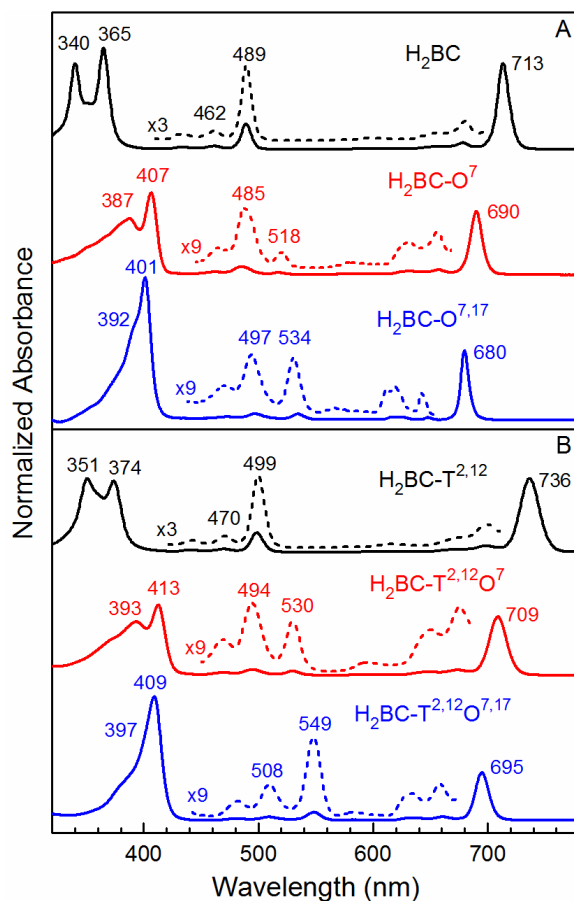
Figure 3. Absorption spectra in toluene at room temperature of (A) **H₂BC** (black), **H₂BC-O^7** (red), and **H₂BC-O^{7,17}** (blue) and (B) **H₂BC-T^{2,12}** (black), **H₂BC-T^{2,12}O^7** (red), and **H₂BC-T^{2,12}O^{7,17}** (blue). The spectra are normalized to the total intensity obtained by integration of the spectra when plotted versus wavenumbers. The ~440–680 nm region (dashed) is expanded vertically (x3 for black and x9 for red and blue spectra).

The presence of the single oxo group in **H₂BC-O^7** causes a significant (23 nm) hypsochromic shift in the position of the Q_y band versus **H₂BC** (690 versus 713 nm); conversely, the B-band manifold (comprised of B_x and B_y transitions) undergoes an even more substantial (42–47 nm) bathochromic shift (387/407 nm) versus (340/365 nm). There is also an apparent modest reduction in the relative intensity of the Q_y band. The addition of the single oxo group also results in significant change in the Q_x manifold, which is shown on an expanded vertical scale along with the Q_y vibronic satellite features in Fig. 3A. The $Q_x(0,0)$ band undergoes a 29-nm bathochromic shift from 489 nm for **H₂BC** to 518 nm for **H₂BC-O^7** and is diminished in intensity

by about 7-fold. The $Q_x(1,0)$ band similarly shifts by 23 nm from 462 to 485 nm, but increases more modestly (2.7-fold) in relative intensity. Collectively, the hypsochromic effect on Q_y and bathochromic effect on $B_{x,y}$ accompany an overall bathochromic shift of the wavelength (and energy) center of gravity of the spectrum. These effects will be discussed below in the context of the MO characteristics that underpin the spectral properties.

The addition of the second oxo group in **H₂BC-O[7,17]** engenders various changes in spectral properties relative to those for **H₂BC-O[7]** (Fig. 3A). The addition of the second oxo group (**H₂BC-O[7,17]** vs **H₂BC-O[7]**) results in a 10 nm hypsochromic shift of Q_y (680 vs 690 nm) and a 5 nm bathochromic shift of B_y (392 vs 387 nm). These shifts are in a similar direction but smaller in magnitude to those found for **H₂BC-O[7]** vs **H₂BC**. The addition of the second oxo group causes a 6 nm hypsochromic shift in B_x (401 to 407 nm), which is opposite in direction and smaller in magnitude than found upon incorporation of the first oxo group. The $Q_x(0,0)$ band of **H₂BC-O[7,17]** (534 nm) is bathochromically shifted from that for **H₂BC-O[7]** (518) nm, which follows the trend from **H₂BC** (489 nm). However, the $Q_x(0,0)$ band for **H₂BC-O[7,17]** gains intensity relative to that for **H₂BC-O[7]**, thus increasing back toward that for **H₂BC**. The $Q_x(1,0)$ feature for **H₂BC-O[7,17]** also shifts to longer wavelength than (and has comparable intensity to) that for **H₂BC-O[7]** (497 versus 485 nm). Collectively, although the Q_x bands of these bacteriochlorins are weak and do not contribute significantly to overall light absorption, the above-noted effects are insightful regarding the electronic-structure perturbation of the oxo groups, which are located along the x-axis of the molecule (Chart 1).

The spectral consequences of incorporation of one and then two oxo groups in the parent bacteriochlorin (**H₂BC, H₂BC-O[7]**, **H₂BC-O[7,17]**; Fig. 3A) are generally similar to those found previously[13] for the analogous set with 2,12-di-*p*-tolyl groups (**H₂BC-T[2,12]**, **H₂BC-T[2,12]O[7]**, **H₂BC-**

41

T^{2,12}O^{7,17}; Fig. 3B), yet there are differences in detail. For the new set that lacks the 2,12-di-*p*-tolyl groups, the Q$_y$ band lies at shorter wavelength (by 23, 19, and 15 nm) and the B$_x$/B$_y$ bands are at shorter wavelength (by 9/11, 6/6 and 8/5 nm) for the benchmark, mono-oxo derivative, and di-oxo derivative, respectively. The Q$_x$(1,0) and Q$_x$(0,0) bands of **H₂BC** are also hypsochromically shifted from those of **H₂BC-T^{2,12}**, **H₂BC-O^7** and **H₂BC-O^{7,17}** along with a changing ratio of the two bands along the series. In general the spectral features (and notably the Q$_y$ band) are broader for the bacteriochlorins that contain the 2,12-di-*p*-tolyl groups (Fig. 3B versus 3A).

Fig. 4 shows the S$_1$ → S$_0$ fluorescence spectra of **H₂BC**, **H₂BC-O^7** and **H₂BC-O^{7,17}** along with the corresponding Q$_y$ region (S$_0$ → S$_1$) of the absorption spectrum. The fluorescence spectrum of each bacteriochlorin is dominated by the Q$_y$(0,0) band, with at least one weak vibronic satellite band to longer wavelength. Thus the emission spectrum is roughly the mirror image to the Q$_y$ absorption manifold. The (Stokes) shift between the Q$_y$ fluorescence and absorption peaks is <100 cm^{-1} for all three bacteriochlorins, and becomes progressively smaller upon addition of oxo groups, suggesting diminished changes in molecular and solvent coordinates in the Q$_y$ excited state (S$_1$) versus the ground state (S$_0$).
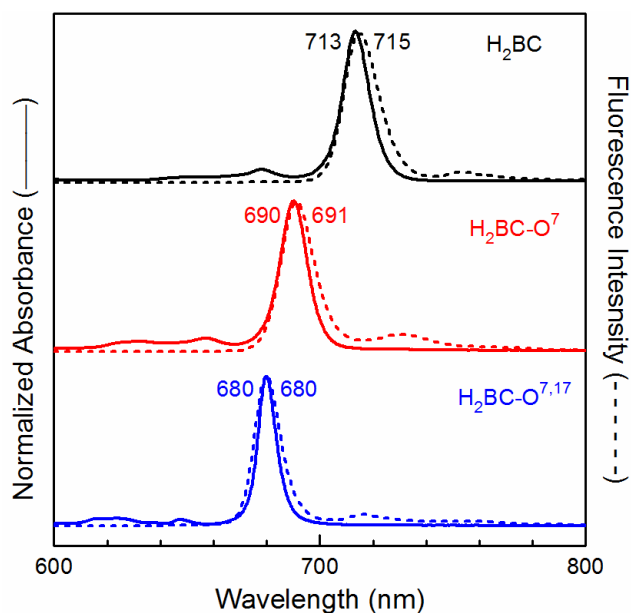
Figure 4. Q_y-region absorption (solid) and fluorescence (dashed) spectra in toluene at room temperature of **H₂BC** (black), **H₂BC-O⁷** (red), and **H₂BC-O⁷,¹⁷** (blue). The excitation wavelengths used for the emission spectra are 356, 485, and 497 nm. The same spectra were obtained for a number of different excitation wavelengths.

Excited-state properties

The excited-state properties of the two new oxobacteriochlorins along with those for the benchmark **H₂BC** are given in Table 1. The measured quantities are the lifetime (τ_S) of the lowest singlet excited state (S_1), the $S_1 \rightarrow S_0$ fluorescence quantum yield (Φ_f), and the yield of $S_1 \rightarrow T_1$ intersystem crossing (Φ_{isc}). The yield of $S_1 \rightarrow S_0$ internal conversion is obtained by the difference $\Phi_{ic} = 1 - \Phi_f - \Phi_{isc}$. The fluorescence ($k_f$), intersystem crossing (k_{isc}), and internal conversion (k_{ic}) rate constants are obtained from these data via the calculation $k_x = \Phi_x/\tau_S$, where x = f, isc or ic. The τ_S values for all three bacteriochlorins are in the range 3.6–4.0 ns and the Φ_f values are in the range 0.14–0.16. These values are comparable to the ranges observed previously for the three analogues that bear 2,12-di-*p*-tolyl groups.[13] Thus, the addition of oxo groups does not appreciably change the yield or rate constant for the fluorescence decay pathway of the S_1 excited state. The

data in Table 1 also show that addition of oxo groups does not cause substantial changes in the yields or rate constants for intersystem crossing or internal conversion.

Table 1 Photophysical properties of bacteriochlorins[a]

Cmpd	S_1 λ_{abs} (nm)	S_1 λ_{em} (nm)	S_1 energy (eV)[b]	τ_s (ns)	Φ_f	Φ_{isc}	Φ_{ic}	k_f^{-1} (ns)	k_{isc}^{-1} (ns)	k_{ic}^{-1} (ns)
H₂BC	713	715	1.74	4.0	0.14	0.62	0.24	29	7	17
H₂BC-O⁷	690	691	1.80	3.6	0.16	0.73	0.11	23	5	33
H₂BC-O⁷,¹⁷	680	680	1.82	3.8	0.16	0.72	0.12	24	5	32

[a] All data were acquired on Ar-purged toluene solutions at room temperature. [b] Average energy of the $Q_y(0,0)$ absorption and emission maxima.

Molecular-orbital characteristics

DFT calculations were performed to gain insights into the spectral effects of the addition of oxo groups to the parent bacteriochlorin. Fig. 5 shows the variations in the electron density distributions and the energies of the four frontier MOs along this series (**H₂BC**, **H₂BC-O⁷**, **H₂BC-O⁷,¹⁷**). These orbitals are the highest occupied MO (HOMO), the lowest unoccupied MO (LUMO) and the HOMO-1 and LUMO+1. The energies of these orbitals are listed in the first four columns in Table 2. To elucidate the effects of the addition of oxo groups, each MO energy for **H₂BC-O⁷** and **H₂BC-O⁷,¹⁷** is accompanied (in italics) by the shift in energy from the same MO for the parent **H₂BC**.
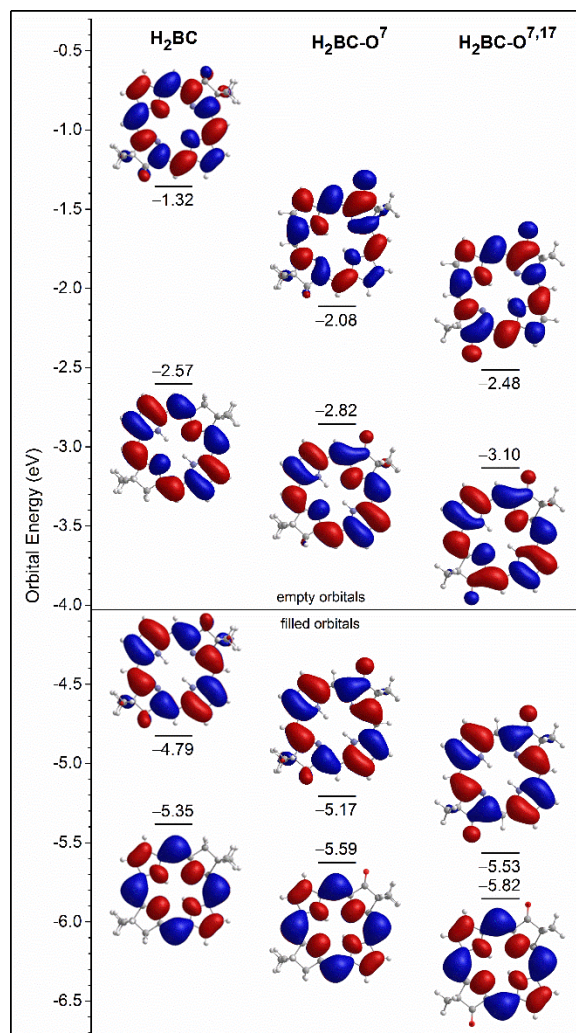
Figure 5. MO correlation diagram from DFT calculations.

Table 2A. MO properties from DFT calculations (eV)[a]

Compound	H-1	H	L	L+1	L − H
H₂BC	−5.35	−4.79	−2.57	−1.32	2.22
H₂BC-O⁷	−5.59	−5.17	−2.82	−2.08	2.35
	−0.24	*−0.38*	*−0.25*	*−0.76*	*0.13*
H₂BC-O⁷,¹⁷	−5.82	−5.53	−3.1	−2.48	2.43
	−0.47	*−0.74*	*−0.53*	*−1.16*	*0.21*

Table 2B. MO properties from DFT calculations (eV)[a]

Compound	(L+1) − (H-1)	L − (H-1)	(L+1) − H	$\Delta E_{\alpha\varpi\gamma}$	$\Delta E_{\delta\iota\phi\psi}$	$\Delta E_{\delta\iota\phi\xi}$
H₂BC	4.03	2.78	3.47	3.13	1.81	−0.69
H₂BC-O⁷	3.51	2.77	3.09	2.93	1.16	−0.32
	−0.52	*−0.01*	*−0.38*	*−0.2*	*−0.65*	*0.37*
H₂BC-O⁷,¹⁷	3.34	2.72	3.05	2.89	0.91	−0.33
	−0.69	*−0.06*	*−0.42*	*−0.24*	*−0.9*	*0.36*

[a] The MOs are abbreviated as HOMO-1 (H-1), HOMO (H), LUMO (L), and LUMO+1 (L+1). The last three columns are defined for use in the four-orbital model as follows: $DE_{avg} = (E_L - E_H) + (E_{L+1} - E_{H-1})/2 = (E_{L+1} - E_H) + (E_L - E_{H-1})/2$; $DE_{dify} = (E_{L+1} - E_{H-1}) - (E_L - E_H)$; $DE_{difx} = (E_L - E_{H-1}) - (E_{L+1} - E_H)$. For **H₂BC-O⁷** and **H₂BC-O⁷,¹⁷**, the first number is the orbital energy or energy gap. The second value (in italics) is the difference in the value from that for the parent **H₂BC**

Inspection of Fig. 5 and Table 2 A&B shows that the successive addition of oxo groups has an additive effect on the energies of the HOMO-1 and LUMO. For example, compared to **H₂BC** (−5.35 eV) the HOMO-1 is stabilized by 0.24 eV for **H₂BC-O⁷** (−5.59 eV) and by 0.47 eV for **H₂BC-O⁷,¹⁷** (−5.82 eV). Similarly, the LUMO is stabilized by 0.25 eV for **H₂BC-O⁷** and by 0.53 eV for **H₂BC-O⁷,¹⁷** relative to **H₂BC**. On the other hand, the HOMO for **H₂BC-O⁷** and **H₂BC-O⁷,¹⁷** is stabilized by 0.38 and 0.74 eV, respectively, versus that for **H₂BC**, whereas the LUMO+1 is stabilized by an additional ~50% (0.76 and 1.16 eV) rather than being doubled. Thus, the orbital primarily affected by the addition of oxo groups is the LUMO+1, followed by the HOMO, with still smaller yet significant effects on the HOMO-1 and LUMO.

These relative effects of oxo groups on the different MOs can be understood to a first approximation by the observation that the 7- and 17-positions of attachment on **H₂BC** (on the x-axis; Chart 1) have a fair amount of electron density in the LUMO+1 and HOMO but virtually none in the LUMO and HOMO-1 (Fig. 5). These different effects on the four orbitals give rise to changes in the energy/wavelength center of gravity of the absorption spectrum and to the spacing

and relative intensities of the absorption bands. To gain more insight into how the effects of oxo groups on the MOs translate into changes in the optical spectrum, in the following we first examine the MO-energy shifts within the context of the Gouterman four-orbital model.[52-54] We then turn to the results of TDDFT calculations, which utilize the same MOs to deduce the nature and absorption properties of the excited states.

Within the four-orbital model, one-electron promotions among the four frontier MOs give rise to the four excited states. Transitions from the ground state to these excited states dominate the absorption spectrum across the near-ultraviolet to NIR spectral regions. In particular, constructive and destructive linear combinations of the HOMO $\rightarrow$ LUMO and HOMO-1 $\rightarrow$ LUMO+1 excited-state configurations give, respectively the B_y and Q_y bands, which generally are of comparable intensity for bacteriochlorins. Analogous combinations of the HOMO-1 $\rightarrow$ LUMO and HOMO $\rightarrow$ LUMO+1 configurations afford a strong B_x band and weaker Q_x band. As the relative energies of two excited-state configurations that are mixing split farther apart, the energy (and wavelength) separation of the B and Q components increases and intensity is shifted from B to Q, and vice versa. These configurational energy differences, governed by the MO energy gaps, are denoted ΔE_{dify} (for HOMO $\rightarrow$ LUMO vs HOMO-1 $\rightarrow$ LUMO+1) and ΔE_{dify} (for HOMO-1 $\rightarrow$ LUMO and HOMO $\rightarrow$ LUMO+1). The energy/wavelength center of gravity of the spectrum shifts with the average energy of the configurations, and thus the average energy of the associated MOs (denoted ΔE_{avg}). The last three columns of Table 2 list the orbital parameters of the four-orbital model. The table reproduces the energies of the four frontier MOs from Fig. 5 (first four columns) and relevant MO energy gaps (middle columns) for the three bacteriochlorins.

Fig. 6 compares the measured absorption spectra (solid lines; from Fig. 3) with spectra simulated using the four-orbital model (dashed spectra) for the three bacteriochlorins. The vertical

47

arrows are the results of TDDFT calculations described below. The simulations utilize values for

the configuration-interaction energy of 0.5 eV for the y-polarized configurations and 0.3 for the x-

polarized configurations, and an energy shift of 0.35 eV from the MO to the spectral domain.

These values are similar to those we have used previously.[16,55] The only values that differ between

the three bacteriochlorins are the MO energies that are set by the DFT calculations (Fig. 5).
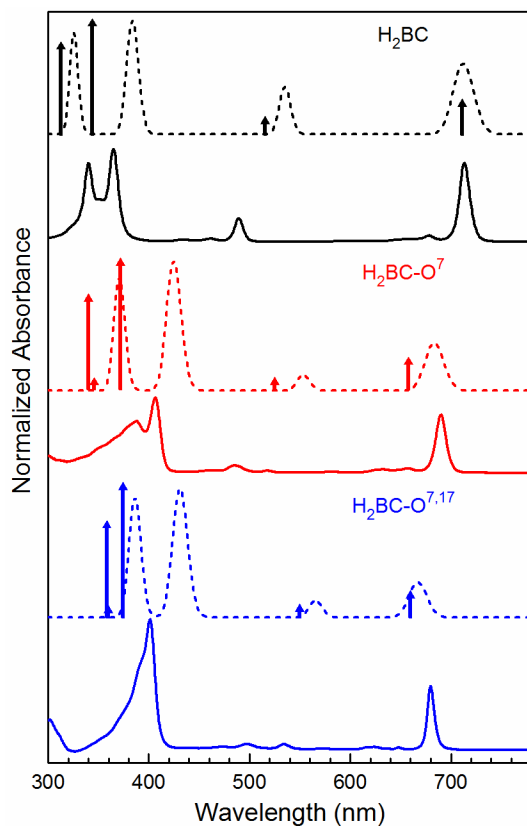
Figure 6. Comparison of spectra of the benchmark, oxo- and dioxo-bacteriochlorins that are
measured (solid), simulated using the four-orbital model (dashed) or calculated using TDDFT
(vertical arrows).

The four-orbital simulations reproduce the main spectral changes that occur upon addition

of the first oxo group to **H₂BC** (black spectra) to give **H₂BC-O⁷** (red spectra), as shown in Fig. 6.

The strong NIR Q_y band and the much weaker blue-green Q_x band both shift hypsochromically,

and the two near-ultraviolet B_y and B_x bands shift bathochromically, giving the appearance of an

overall contraction of the spectrum. Close examination shows that there are hypsochromic effects on the Q_y and Q_x band intensities counterbalanced by hyperchromic effects on the B_x and B_y bands. These coupled changes in spectral positions and intensities are understood within the four-orbital model as arising from decreased excited-state configurational energy gaps (ΔE_{dify} and ΔE_{difx}; Table 2) for both the y-polarized configurations (HOMO $\rightarrow$ LUMO and HOMO-1 $\rightarrow$ LUMO+1) and the x-polarized configurations (HOMO-1 $\rightarrow$ LUMO and HOMO $\rightarrow$ LUMO+1). The consequent increased configurational mixing (due to a smaller energy denominator in the mixing coefficient) shifts intensity into the B band at the expense of the Q bands upon the addition of the first oxo group (**H₂BC-O⁷**) to the parent bacteriochlorin (**H₂BC**).

The four-orbital simulations produce an additional hypsochromic shift in the Q_y band and additional bathochromic shifts in the B_x and B_y bands upon addition of the second oxo group to **H₂BC-O⁷** to give **H₂BC-O⁷,¹⁷**. These shifts are smaller than those predicted (and found) for incorporation of the first oxo group to **H₂BC** to give **H₂BC-O⁷**. The simulations reproduce the small bathochromic shift in the Q_x band upon addition of the second oxo group, but not the small increase in intensity (**H₂BC-O⁷,¹⁷** vs **H₂BC-O⁷**).

Comparisons also can be made between the measured spectra and those calculated by TDFFT. Stick spectra showing the calculated spectral positions and relative oscillator strengths are shown in Fig. 6 alongside the simulations from the four-orbital model. These calculated parameters and other results from the calculations are listed in Table S2 (Supplementary Information). The TDDFT calculations predict a hypsochromic effect on the Q_y band of **H₂BC-O⁷** versus **H₂BC**, but the shift is larger than measured, and the intensity (relative to the B_y intensity) is much smaller than measured. The TDDFT calculations also afford a hypsochromic shift of the Q_y band for the dioxo analogue **H₂BC-O⁷,¹⁷** relative to the parent **H₂BC** that is closer to the

measured but still too large. In turn this means that the calculated Q_y band positions of **H$_2$BC-O^{7,17}** and **H$_2$BC-O^7** are about the same, which is not in accord with observation. The TDDFT calculations reproduce the progressive bathochromic shifts in the B_x and B_y bands, but the magnitudes of the shifts are smaller than observed. The TDDFT calculations also show the diminution in Q_x intensity for **H$_2$BC-O^7** vs **H$_2$BC**, but (like the simulations using the four-orbital model) do not show the increase in Q_x intensity for **H$_2$BC-O^{7,17}** vs **H$_2$BC-O^7**.

Those aspects of the experimental trends for the addition of the first and second oxo group to the parent bacteriochlorin that are not reproduced by the TDDFT calculations or four-orbital-model simulations must arise from factors that are not accounted for by these methods. For example, TDDFT typically does not correctly predict the energies of charge-transfer-like states.[56] In this regard, the HOMO-2 of these systems (not shown) has substantial electron density on the oxo group(s) and far less on the macrocycle. Electron promotions from such an orbital to the normal LUMO or LUMO+1 would give rise to an excited-state configuration with charge-transfer character. The calculations may not predict the true involvement of such configurations in the optical characteristics of the oxo-containing bacteriochlorins. The calculations are also at the single-configuration level, and do not include contributions of multiple (e.g., double and triple) excitations.

One motivation of this study was to evaluate the extent to which a bacteriochlorin with one or two oxo groups but no other auxochromes would have a Q_y band that penetrates into the 670–700 nm spectral region normally accessed by elaborately functionalized and thus red-shifted chlorins. We had hypothesized on the basis of prior work on analogues bearing 2,12-di-*p*-tolyl groups (which cause a bathochromic effect) that an otherwise naked dioxobacteriochlorin would absorb in the 670–675 nm range. The current results on **H$_2$BC-O^{7,17}** show a Q_y band at 680 nm,

close to the predictions. The monooxo-analogue **H₂BC-O**[7] absorbs at 690 nm. The ability to tailor a simple bacteriochlorin in relatively simple fashion to absorb in the spectral region normally accessed by extensive modification of chlorins is attractive for tuning hydroporphyrin macrocycles for red absorption in solar-energy and other applications.

Other structural modifications that impart spectral shifts of bacteriochlorin-like molecules warrant comment. The *cis*-porphodilactone **III** or *trans*-porphodilactone **IV** exhibits a long-wavelength absorption at 657 or 676 nm (in dichloromethane),[57] each of which is bathochromic and intensely hyperchromic compared with that of the parent *meso*-tetrakis(pentafluorophenyl)porphyrin (635 nm in dichloromethane[58]). Alternatively, the morpholinobacteriochlorin **V** exhibits the Q_y band at 790 nm, to be compared with the parent tetrahydroxybacteriochlorin **VI** at 707 nm.[59] The structures are shown in Chart 3. The constrasting spectral shifts among **III-VI** and the various oxobacteriochlorins described herein highlight the points[10-18] that (1) the more conjugated tetrapyrrole macrocycle does not necessarily absorb at longer wavelength, and (2) there are diverse structural modifications available for tuning the position of the long-wavelength absorption band of hydroporphyrins.
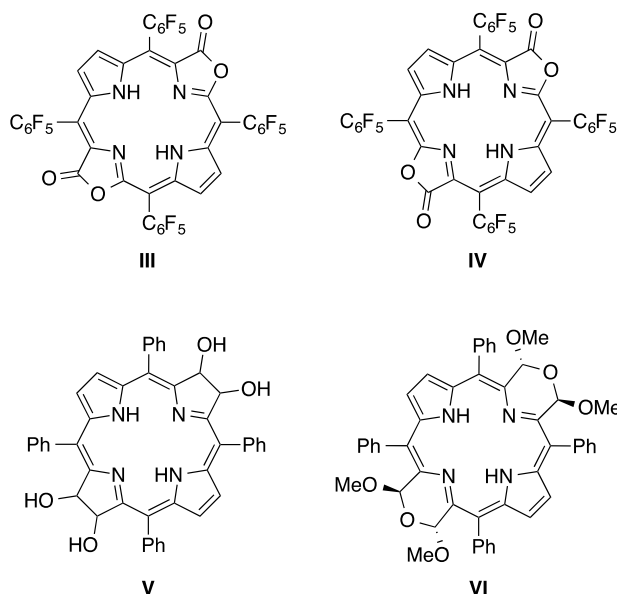
Chart 3 Diverse pyrroline-modified tetrapyrrole macrocycles.

Experimental Section

General methods

^{1}H NMR (300 MHz) and ^{13}C NMR (100 MHz) were collected at room temperature in CDCl$_3$ unless noted otherwise. Each distinct β-pyrrole proton of the bacteriochlorins typically appeared as a doublet in the ^{1}H NMR spectrum due to coupling with the pyrrolic N–H unit. Matrix-assisted laser-desorption mass spectrometry (MALDI-MS) was performed with the matrix 1,4-bis(5-phenyl-2-oxazol-2-yl)benzene.[60] Electrospray ionization mass spectrometry (ESI-MS) data are reported for the molecular ion. Silica gel (40 μm average particle size) was used for column chromatography. All solvents were reagent grade and were used as received unless noted otherwise. THF was freshly distilled from sodium/benzophenone ketyl. Sonication was carried out with a benchtop open-bath sonicator. Compounds **H₂BC-Br^{3,13}** and **H₂BC-MeO^{5}Br^{3,13}** were prepared following reported procedures.[41] The oxidations of **H₂BC** and **H₂BC-Br^{3,13}MeO^5** have been reported in part previously.[61]

Synthesis

3,13-Dibromo-8,8,18,18-tetramethyl-7-oxobacteriochlorin (H₂BC-Br^{3,13}O^7). A solution of **H₂BC-Br^{3,13}** (15.0 mg, 28.4 μmol) in freshly distilled CH_2Cl_2 (3 mL) at ≤ -30 °C (bath of dry ice in 1:1 EtOH/ethylene glycol)[43] was treated with PDC (22.1 mg, 58.7 μmol). The mixture was allowed to warm to room temperature. After 48 h, the reaction mixture was diluted with CH_2Cl_2 (~1 mL) and chromatographed silica, CH_2Cl_2 to afford a green solid (9.1 mg, 59%): ^{1}H NMR δ − 2.00 (brs, 1H), −1.90 (brs, 1H), 1.95 (s, 6H), 1.99 (s, 6H), 4.52 (s, 2H), 8.70 (s, 1H), 8.79 (s, 1H), 8.81 (d, $J = 2.2$ Hz, 1H), 8.97 (s, 1H), 8.99 (d, $J = 2.1$ Hz, 1H), 9.70 (s, 1H); ESI-MS obsd 541.0224, calcd 541.0233 (M + H)$^+$, M = $C_{24}H_{22}Br_2N_4O$; λ_{abs} (CH_2Cl_2) 391, 410, 488, 703 nm.

8,8,18,18-Tetramethyl-7-oxobacteriochlorin (H₂BC-O^7). Following a procedure for hydrodebromination of bacteriochlorins,[46] a mixture of **H₂BC-Br^{3,13}O^7** (10.8 mg, 19.9 μmol), Pd(PPh₃)₄ (29.5 mg, 25.5 μmol), formic acid (15 μL, 0.40 mmol), and TEA (55 μL, 0.40 mmol) was heated in toluene (20 mL) at 100 °C in a Schlenk flask. After 16 h, Pd(PPh₃)₄ (29.5 mg, 25.5 μmol), formic acid (15 μL, 0.40 mmol), and TEA (55 μL, 0.40 mmol) were added. After 16 h, the reaction mixture was concentrated and chromatographed silica, CH_2Cl_2 to afford a green solid (3.6 mg, 47%): ^{1}H NMR δ −2.18 (brs, 1H), −2.08 (brs, 1H), 1.97 (s, 6H), 2.01 (s, 6H), 4.53 (s, 2H), 8.81 (dd, $J = 4.4, 2.0$ Hz, 1H), 8.82 (s, 1H), 8.85 (dd, $J = 4.7, 1.9$ Hz, 1H), 8.89 (s, 1H), 8.91 (s, 1H), 8.97 (dd, $J = 4.7, 1.8$ Hz, 1H), 9.03 (dd, $J = 4.4, 2.0$ Hz, 1H), 9.64 (s, 1H); ^{13}C NMR δ 23.5, 31.4, 45.8, 50.3, 52.5, 96.8, 97.5, 98.5, 99.8, 121.6, 125.1, 125.5, 126.9, 132.8, 137.7, 137.9, 139.2, 142.4, 163.0, 165.3, 171.4, 210.0; MALDI-MS obsd 384.4, calcd 384.19 (M$^+$); ESI-MS obsd 385.2019, calcd 385.2023 (M + H)$^+$, M = $C_{24}H_{24}N_4O$; λ_{abs} (CH_2Cl_2) 390, 408, 488, 688 nm.

3,13-Dibromo-5-methoxy-8,8,18,18-tetramethyl-7-oxobacteriochlorin (**H₂BC-**

Br^{3,13}MeO^{5}O^7). A solution of **H₂BC-Br^{3,13}MeO^5** (100. mg, 0.179 mmol) in CH_2Cl_2 (6 mL) was treated with MnO_2 (300. mg, 3.45 mmol) at room temperature. After 48 h, the reaction mixture was filtered through a Celite pad. The pad containing the filtered material was rinsed with CH_2Cl_2. The filtrate was concentrated and chromatographed. TLC analysis silica, hexanes/CH_2Cl_2 (1:1) showed three distinct components: unreacted starting material (R_f = 0.82), a minor product (brownish, R_f = 0.46), and a major product (green, R_f = 0.17). Column chromatography silica, hexanes/CH_2Cl_2 (1:1) afforded unreacted starting material **H₂BC-Br^{3,13}MeO^5** (50. mg), the minor product (**H₂BC-Br^{3,13}MeO^{5}O^{17}**, 16 mg, 16%) and the major product (the title compound, 28 mg, 27%). Data for the title compound: ^{1}H NMR (400 MHz) δ –1.00 (s, 1H), –0.97 (s, 1H), 1.87 (s, 6H), 1.89 (s, 6H), 4.32 (s, 2H), 4.49 (s, 3H), 8.40 (s, 1H), 8.48 (s, 1H), 8.59 (s, 1H), 8.60 (d, J = 2.8 Hz, 1H), 8.80 (d, J = 2.4 Hz, 1H); ^{13}C NMR δ 23.6, 31.3, 45.3, 51.8, 52.5, 66.5, 96.2, 96.9, 98.0, 110.1, 115.8, 124.4, 125.3, 129.0, 135.8, 136.98, 137.08, 138.9, 141.8, 165.6, 166.2, 171.0, 206.6; MALDI-MS obsd 570.0, calcd 570.0; ESI-MS obsd 571.0331, calcd 571.0339 (M + H)$^+$, M = $C_{25}H_{24}Br_2N_4O_2$; λ_{abs} (toluene) 396, 504, 692 nm.

Data for **3,13-Dibromo-5-methoxy-8,8,18,18-tetramethyl-17-oxobacteriochlorin (H₂BC-Br^{3,13}MeO^{5}O^{17}**): ^{1}H NMR (400 MHz, CDCl₃) δ –2.45 (s, 1H), –2.09 (s, 1H), 1.95 (s, 6H), 1.98 (s, 6H), 4.39 (s, 3H), 4.53 (s, 2H), 8.75 (s, 1H), 8.83 (s, 1H), 8.85 (d, J = 2.0 Hz, 1H), 9.02 (d, J = 2.8 Hz, 1H), 9.63 (s, 1H); ^{13}C NMR δ 23.7, 31.3, 45.6, 48.6, 50.0, 65.1, 96.4, 97.2, 98.1, 109.1, 115.1, 124.1, 129.3, 130.1, 132.4, 135.1, 135.2, 136.0, 145.0, 160.5, 165.2, 171.3, 209.4; MALDI-MS obsd 570.0, calcd 570.0; ESI-MS obsd 571.0331, calcd 571.0339 (M + H)$^+$, M = $C_{25}H_{24}Br_2N_4O_2$; λ_{abs} (toluene) 386, 412, 494, 524, 706 nm.

8,8,18,18-Tetramethyl-7-oxobacteriochlorin (H₂BC-O⁷). A solution of **H₂BC** (8.0 mg, 0.022 mmol) in CH_2Cl_2 (4.5 mL) was treated with MnO_2 (56.3 mg, 0.648 mmol) at room temperature. After 24 h, the reaction mixture was filtered through a Celite pad. The pad containing the filtered material was rinsed with CH_2Cl_2. The filtrate was concentrated and chromatographed (silica, hexanes/CH_2Cl_2 = 1:2) to afford the title compound as a green solid (5.8 mg, 70%). Starting material **H₂BC** was recovered (0.5 mg), and dioxobacteriochlorin **H₂BC-O⁷,¹⁷** was also isolated (0.5 mg). Data for the title compound: ¹H NMR (400 MHz) δ –2.19 (s, 1H), –2.08 (s, 1H), 1.97 (s, 6H), 2.00 (s, 6H), 4.51 (s, 2H), 8.79 (dd, J = 2.0 Hz, J = 4.4 Hz, 1H), 8.81 (s, 1H), 8.83 (dd, J = 2.0 Hz, J = 4.8 Hz, 1H), 8.87 (s, 1H), 8.90 (s, 1H), 8.96 (dd, J = 2.0 Hz, J = 4.8 Hz, 1H), 9.02 (dd, J = 2.0 Hz, J = 4.4 Hz, 1H), 9.65 (s, 1H); ¹³C NMR δ 23.6, 29.9, 31.5, 45.9, 50.4, 52.6, 96.9, 97.6, 98.6, 99.9, 121.7, 125.2, 125.6, 127.0, 132.9, 137.8, 138.0, 139.2, 142.5, 163.1, 165.4, 171.5; MALDI-MS obsd 384.9742, calcd 385.2023 $(M + H)^+$, M = $C_{24}H_{24}N_4O$; ESI-MS obsd 384.19446, calcd 384.19417 M^+, M = $C_{24}H_{24}N_4O$; λ_{abs} (toluene) 388, 407, 485, 690 nm.

8,8,18,18-Tetramethyl-7,17-dioxobacteriochlorin (H₂BC-O⁷,¹⁷). A solution of **H₂BC-O⁷** (5.6 mg, 0.015 mmol) in CH_2Cl_2 (3.0 mL) was treated with PDC (5.6 mg, 0.015 mmol) at room temperature. After 24 h, the reaction mixture was filtered through a Celite pad. The pad containing the filtered material was rinsed with CH_2Cl_2. The filtrate was concentrated and chromatographed (silica, hexanes/CH_2Cl_2 = 1:2) to afford a purple solid (4.2 mg, 70%): ¹H NMR (400 MHz) δ –2.77 (s, 2H), 2.05 (s, 12H), 9.15 (dd, J = 2.0 Hz, J = 4.4 Hz, 2H), 9.22–9.24 (m, 4H), 9.82 (s, 2H); ¹³C NMR δ 23.9, 29.6, 29.9, 50.1, 97.9, 98.5, 126.3, 127.2, 136.8, 138.0; MALDI-MS obsd 398.9602, calcd 399.1816 $(M + H)^+$, M = $C_{24}H_{24}N_4O_2$; ESI-MS obsd 398.17341, calcd 398.17373 M^+, M = $C_{24}H_{22}N_4O_2$; λ_{abs} (toluene) 401, 680 nm.

2-(3,13-Dibromo-5-methoxy-8,8,18,18-tetramethylbacteriochlorin-17-ylidene)hydrazine-1-carboxamide (II). A solution of **H$_2$BC-Br^{3,13}MeO^{5}O^{17}** (11.0 mg, 0.0200 mmol) in ethanol (5 mL) at reflux was treated with sodium acetate (164 mg, 2.00 mmol), semicarbazide hydrochloride (223 mg, 2.00 mmol), and several drops of acetic acid. After 24 h, the reaction mixture was filtered through a Celite pad. The pad containing the filtered material was rinsed with CH$_2$Cl$_2$. The filtrate was concentrated and chromatographed (silica, CH$_2$Cl$_2$/CH$_3$OH = 100:1) to afford a green solid (9.8 mg, 78%): ^{1}H NMR (400 MHz, CDCl$_3$, CD$_3$OD) δ −2.15 (s, 1H), −1.91 (s, 1H), 1.96 (s, 6H), 2.31 (s, 6H), 4.36 (s, 3H), 4.45 (s, 2H), 8.62 (s, 1H), 8.64 (s, 1H), 8.82 (d, *J* = 2.0 Hz, 1H), 8.84 (d, *J* = 2.0 Hz, 1H), 9.42 (s, 1H); ^{13}C NMR (CDCl$_3$, CD$_3$OD, the three amide protons were not observed) δ 22.8, 24.4, 31.1, 31.8, 45.9, 47.8, 47.9, 64.8, 93.2, 96.0, 97.6, 106.7, 114.3, 125.0, 126.6, 128.1, 134.0, 134.1, 135.6, 136.1, 136.3, 150.5, 157.0, 157.8, 164.8, 171.4; MALDI-MS obsd 628.6707, calcd 628.0666 (M + H)$^+$, M = C$_{26}$H$_{27}$Br$_2$N$_7$O$_2$; ESI-MS obsd 627.05848, calcd 627.05875 M$^+$, M = C$_{26}$H$_{27}$Br$_2$N$_7$O$_2$; λ$_{abs}$ (toluene) 387, 416, 486, 515, 736 nm.

Photophysical measurements

Spectral and photophysical studies of the three bacteriochlorins were carried out on dilute (μM) argon-purged samples. Absorption spectra were acquired using a Shimadzu UV-1800 spectrometer. Static emission spectra were acquired using a Spex-Horiba Nanolog spectrofluorimeter with 2–4 nm excitation and detection bandwidths and corrected for instrument spectral response. Fluorescence quantum yields were obtained relative to *meso*-tetraphenylporphyrin (Φ$_f$ = 0.070 in nondegassed toluene).[55] The value for **H$_2$BC** is the same as that obtained by absolute measurement using an integrating sphere (Quanti-Phi, Horiba). Singlet excited-state lifetimes were determined by using transient absorption (TA) spectroscopy employing ~100 fs excitation flashes from an ultrafast laser system (Spectra Physics) and

acquisition of difference spectra (360–900 nm) using a white-light pulsed laser (~1 ns rise time) in 100-ps time bins with variable pump-probe spacing up to 0.5 ms (Ultrafast Systems, EOS). Transient absorption measurements employed excitation both on the long-wavelength side of the Soret absorption (400–420 nm) and in the Q-band region (485–535 nm). Time profiles of ΔA at ~1.5 nm spacing across the 380–750 nm region were analyzed at a number of individual wavelengths and also globally. Transient absorption studies were also used to measure the yield of $S_1 \rightarrow T_1$ intersystem crossing by comparing the extent of bleaching of the ground-state absorption bands due to T_1 at the asymptote of the S_1 decay versus the extent due to S_1 immediately after the excitation flash.

Density functional theory calculations

DFT calculations were performed with Gaussian 09 version D.01. All calculations were in toluene using the polarizable continuum model (PCM). Molecular geometries were fully optimized using the hybrid B3LYP functional and basis set 6-31++G**.[62] Ground-state MOs were calculated at the optimized geometry using the B3LYP functional and basis set 6-31++G**. Single point TDDFT calculations were performed at the B3LYP/6-31++G** optimized geometry using the long range corrected wB97XD functional and basis set 6-31++G**. These calculations used Gaussian defaults with the exception of the keywords SCF=(NoVarAcc, NoIntFock), GFInput POP=(Full, NBO) and TD(nStates=16). MO images were generated from Gaussian outputs using the Chemcraft program (http://www.chemcraftprog.com).

† **Electronic supplementary information (ESI) available:** Results from the survey of oxidants for **H$_2$BC-Br^{3,13}**, chromatographic results upon oxidation of **H$_2$BC-Br^{3,13}MeO^5**, and results of TDDFT calculations. See DOI:10.1039/XX

Acknowledgments

References

1   P. H. Hynninen, in *Chlorophylls*, ed. H. Scheer, CRC Press, Boca Raton, FL, USA 1991, pp. 145–209.

2   V. Y. Pavlov and G. V. Ponomarev, *Chem. Heterocyclic Compds.* 2004, **40**, 393–425.

3   Y. Chen, G. Li and R. K. Pandey, *Curr. Org. Chem.*, 2004, **8**, 1105–1134.

4   M. Galezowski and D. T. Gryko, *Curr. Org. Chem.,* 2007, **11**, 1310–1338.

5   M. A. Grin, A. F. Mironov and A. A. Shtil, *Anti-Cancer Agents Med. Chem.*, 2008, **8**, 683–697.

6   C. Brückner, L. Samankumara and J. Ogikubo, in *Handbook of Porphyrin Science*, ed. K. M. Kadish, K. M. Smith and R. Guilard, World Scientific, Singapore, 2012, Vol. 17, pp. 1–112.

7   J. S. Lindsey, *Chem. Rev.,* 2015, **115**, 6534–6620.

8   C. Brückner, *Acc. Chem. Res.*, 2016, **49**, 1080–1092.

9   M. Taniguchi and J. S. Lindsey, *Chem. Rev.*, 2017, **117**, 344–535.

10   E. Yang, C. Kirmaier, M. Krayer, M. Taniguchi, H.-J. Kim, J. R. Diers, D. F. Bocian, J. S. Lindsey and D. Holten, *J. Phys. Chem. B*, 2011, **115**, 10801–10816.

11   C.-Y. Chen, E. Sun, D. Fan, M. Taniguchi, B. E. McDowell, E. Yang, J. R. Diers, D. F. Bocian, D. Holten and J. S. Lindsey, *Inorg. Chem.*, 2012, **51***,* 9443–9464.

12   E. Yang, C. Ruzié, M. Krayer, J. R. Diers, D. M. Niedzwiedzki, J. S. Lindsey, D. F. Bocian and D. Holten, *Photochem. Photobiol.*, 2013, **89**, 586–604.

13   P. Vairaprakash, E. Yang, T. Sahin, M. Taniguchi, M. Krayer, J. R. Diers, A. Wang, D. M. Niedzwiedzki, C. Kirmaier, J. S. Lindsey, D. F. Bocian and D. Holten, *J. Phys. Chem. B*, 2015*,* **119**, 4382–4395.

14   E. Yang, N. Zhang, M. Krayer, M. Taniguchi, J. R. Diers, C. Kirmaier, J. S. Lindsey, D. F. Bocian and D. Holten, *Photochem. Photobiol.*, 2016, **92**, 111–125.

15   N. Zhang, J. Jiang, M. Liu, M. Taniguchi, A. K. Mandal, R. B. Evans-Storms, J. B. Pitner, D. F. Bocian, D. Holten and J. S. Lindsey, *New J. Chem.*, 2016, **40**, 7750–7767.

16   J. W. Springer, K. M. Faries, J. R. Diers, C. Muthiah, O. Mass, H. L. Kee, C. Kirmaier, J. S. Lindsey, D. F. Bocian and D. Holten, *Photochem. Photobiol.,* 2012, **88**, 651–674.

17   K. M. Faries, J. R. Diers, J. W. Springer, E. Yang, M. Ptaszek, D. Lahaye, M. Krayer, M. Taniguchi, C. Kirmaier, J. S. Lindsey, D. F. Bocian and D. Holten, *J. Phys. Chem. B,* 2015*,* **119***,* 7503–7515.

18   O. Mass, M. Taniguchi, M. Ptaszek, J. W. Springer, K. M. Faries, J. R. Diers, D. F. Bocian, D. Holten and J. S. Lindsey, *New J. Chem.*, 2011, **35**, 76–88.

19   H. H. Inhoffen and W. Nolte, *Tetrahedron Lett.*, 1967, **8**, 2185–2187.

20   H. H. Inhoffen and W. Nolte, *Liebigs Ann. Chem.,* 1969, **725**, 167–176.

21   C. K. Chang, *Biochemistry,* 1980, **19**, 1971–1976.

22   C. K. Chang and W. Wu, *J. Org. Chem.*, 1986, **51**, 2134–2137.

23   A. M. Stolzenberg, P. A. Glazer and B. M. Foxman, *Inorg. Chem.,* 1986, **25**, 983–991.

24   A. R. Morgan, G. M. Garbo, R. W. Keck, D. Skalkos and S. H. Selman, *J. Photochem. Photobiol. B: Biol.,* 1990, **6**, 133–141.

25   P. A. Connick and K. A. Macor, *Inorg. Chem.,* 1991, **30**, 4654–4663.

26   A. R. Morgan, D. Skalkos, G. M. Garbo, R. W. Keck and S. H. Selman, *J. Med. Chem.,* 1991, **34**, 2126–2133.

27   C. K. Chang and W. Wu, US patent, 1991, US 5064952.

28   D. Kessel, K. M. Smith, R. K. Pandey, F.-Y. Shiau and B. Henderson, *Photochem. Photobiol.,* 1993, **58**, 200–203.

29   R. K. Pandey, M. Isaac, I. MacDonald, C. J. Medforth, M. O. Senge, T. J. Dougherty and K. M. Smith, *J. Org. Chem.,* 1997, **62**, 1463–1472.

30   Y. Chen, C. J. Medforth, K. M. Smith, J. Alderfer, T. J. Dougherty and R. K. Pandey, *J. Org. Chem.,* 2001, **66**, 3930–3939.

31   M. R. Prinsep, F. R. Caplan, R. E. Moore, G. M. L. Patterson and C. D. Smith, *J. Am. Chem. Soc.*, 1992, **114**, 385–387.

32   C. D. Smith, M. R. Prinsep, F. R. Caplan, R. E. Moore and G. M. L. Patterson, *Oncol. Res.*, 1994, **6**, 211–218.

33   M. R. Prinsep, G. M. L. Patterson, L. K. Larsen and C. D. Smith, *Tetrahedron*, 1995, **51**, 10523–10530.

34   P. Morlière, J.-C. Mazière, R. Santus, C. D. Smith, M. R. Prinsep, C. C. Stobbe, M. C. Fenning, J. L. Golberg and J. D. Chapman, *Cancer Res.*, 1998, **58**, 3571–3578.

35   M. R. Prinsep, G. M. L. Patterson, L. K. Larsen and C. D. Smith, *J. Nat. Prod.*, 1998, **61**, 1133–1136.

36   T. G. Minehan, L. Cook-Blumberg, Y. Kishi, M. R. Prinsep and R. E. Moore, *Angew. Chem. Int. Ed.*, 1999, **38**, 926–928.

37   M. R. Prinsep and J. Puddick, *Phytochem. Anal.*, 2011, **22**, 285–290.

38   T. G. Minehan and Y. Kishi, *Tetrahedron Lett.*, 1997, **38**, 6811–6814.

39   T. G. Minehan and Y. Kishi, *Angew. Chem. Int. Ed.*, 1999, **38**, 923–925.

40   W. Wang and Y. Kishi, *Org. Lett.*, 1999, **1**, 1129–1132.

41   M. Krayer, M. Ptaszek, H.-J. Kim, K. R. Meneely, D. Fan, K. Secor and J. S. Lindsey, *J. Org. Chem.*, 2010, **75**, 1016–1039.

42   M. Taniguchi, H.-J. Kim, D. Ra, J. K. Schwartz, C. Kirmaier, E. Hindin, J. R. Diers, S. Prathapan, D. F. Bocian, D. Holten and J. S. Lindsey, *J. Org. Chem.*, 2002, **67**, 7329–7342.

43   D. W. Lee and C. M. Jensen, *J. Chem. Educ.*, 2000, **77**, 629.

44   A. K. Sahoo, Y. Nakamura, N. Aratani, K. S. Kim, S. B. Noh, H. Shinokubo, D. Kim and A. Osuka, *Org. Lett.,* 2006, **8**, 4141–4144.

45   A. Kato, R. D. Hartnell, M. Yamashita, H. Miyasaka, K.-i. Sugiura and D. P. Arnold, *J. Porphyrins Phthalocyanines,* 2004, **8**, 1222–1227.

46   M. Taniguchi, D. L. Cramer, A. D. Bhise, H. L. Kee, D. F. Bocian, D. Holten and J. S. Lindsey, *New J. Chem.*, 2008, **32**, 947–958.

47   R. L. Shriner, R. C. Fuson and D. Y. Curtin, *The Systematic Identification of Organic Compounds*, John Wiley & Sons, Inc., New York, Fifth Ed., 1964, p. 253.

48   A. Losev and D. Mauzerall, *Photochem. Photobiol.*, 1983, **38**, 355−361.

49   Z. Yu and M. Ptaszek, *Org. Lett.*, 2012, **14***, 3708–3711.

50   Z. Yu and M. Ptaszek, *J. Org. Chem.*, 2013, **78**, 10678–10691.

51   Z. Yu, C. Pancholi, G. V. Bhagavathy, H. S. Kang, J. K. Nguyen and M. Ptaszek, *J. Org. Chem.*, 2014, **79**, 7910–7925.

52   M. Gouterman, *J. Chem. Phys.* 1959, **30**, 1139–1161.

53   M. Gouterman, *J. Mol. Spectrosc.*1961, **6**, 138–163.

54   M. Gouterman, in *The Porphyrins*, ed. D. Dolphin, Academic Press, New York, 1978, vol. 3, pp. 1−165.

55   A. K. Mandal, M. Taniguchi, J. R. Diers, D. M. Niedzwiedzki, C. Kirmaier, J. S. Lindsey, D. F. Bocian and D. Holten, *J. Phys. Chem. A,* 2016, **120**, 9719–9731.

56   A. Dreuw and M. Head-Gordon, *J. Am. Chem. Soc.*, 2004, **126**, 4007–4016.

57   X.-S. Ke, Y. Chang, J.-Z. Chen, J. Tian, J. Mack, X. Cheng, Z. Shen and J.-L. Zhang, *J. Am. Chem. Soc.*, 2014, **136**, 9598–9607.

58   M. Gouterman, R. J. Hall, G.-E. Khalil, P. C. Martin, E. G. Shankland and R. L. Cerny, *J. Am. Chem. Soc.*, 1989, **111**, 3702–3707.

59   M. J. Guberman-Pfeffer, J. A. Greco, L. P. Samankumara, M. Zeller, R. R. Birge, J. A. Gascón and C. Brückner, *J. Am. Chem. Soc.*, 2017, **139**, 548–560.

60   N. Srinivasan, C. A. Haney, J. S. Lindsey, W. Zhang and B. T. Chait, *J. Porphyrins Phthalocyanines*, 1999, **3**, 283–291.

61   M. Liu, PhD thesis, NC State University, 2016.

62   M. J. Frisch, G. W. Trucks, H. B. Schlegel, G. E. Scuseria, M. A. Robb, J. R. Cheeseman, G. Scalmani, V. Barone, B. Mennucci, G. A. Petersson, H. Nakatsuji, M. Caricato, X. Li, H. P. Hratchian, A. F. Izmaylov, J. Bloino, G. Zheng, J. L. Sonnenberg, M. Hada, M. Ehara, K. Toyota, R. Fukuda, J. Hasegawa, M. Ishida, T. Nakajima, Y. Honda, O. Kitao, H. Nakai, T. Vreven, J. A. Montgomery Jr., J. E. Peralta, F. Ogliaro, M. Bearpark, J. J. Heyd, E. Brothers, K. N. Kudin, V. N. Staroverov, R. Kobayashi, J. Normand, K. Raghavachari, A. Rendell, J. C. Burant, S. S. Iyengar, J. Tomasi, M. Cossi, N. Rega, J. M. Millam, M. Klene, J. E. Knox, J. B. Cross, V. Bakken, C. Adamo, J. Jaramillo, R. Gomperts, R. E. Stratmann, O. Yazyev, A. J. Austin, R. Cammi, C. Pomelli, J. W. Ochterski, R. L. Martin, K. Morokuma, V. G. Zakrzewski, G. A. Voth, P. Salvador, J. J. Dannenberg, S. Dapprich, A. D. Daniels, Ö. Farkas, J. B. Foresman, J. V. Ortiz, J. Cioslowski and D. J. Fox, Gaussian, Inc., Wallingford CT, 2009.

Chapter 3

Photophysical Characterization of Tolyporphin A, a Naturally Occurring Dioxobacteriochlorin, and Synthetic Oxobacteriochlorin Analogues

Abstract

Tolyporphins are tetrapyrrole macrocycles produced by a cyanobacterium-containing culture known as HT-58-2. Tolyporphins A–J are free base dioxobacteriochlorins whereas tolyporphin K is an oxochlorin. Here, the photophysical characterization is reported of tolyporphin A and two synthetic analogues, an oxobacteriochlorin and a dioxobacteriochlorin. The characterization (in toluene, diethyl ether, ethyl acetate, dichloromethane, 1-pentanol, 2-butanone, ethanol, methanol, *N,N*-dimethylformamide, and dimethylsulfoxide) includes static absorption and fluorescence spectra, fluorescence quantum yields, and time-resolved data. The data afford the lifetime of the lowest singlet excited state and the yields of the nonradiative decay pathways (intersystem crossing and internal conversion). The three macrocycles exhibit only modest variation in spectroscopic and excited-state photophysical parameters across the solvents. The long-wavelength (Q_y) absorption band of tolyporphin A appears at ~680 nm and is remarkably narrow (full-width-at-half-maximum ~7 nm). The position of the long-wavelength (Q_y) absorption band of tolyporphin A (~680 nm) more closely resembles that of chlorophyll *a* (662 nm) than bacteriochlorophyll *a* (772 nm). The absorption spectra of tolyporphins B–I, K (which were available in minute quantities) are also reported in methanol; the spectra of B–I closely resemble that of tolyporphin A. Taken together, tolyporphin A generally exhibits spectral and photophysical features resembling those of chlorophyll *a*.

Introduction

In the late 1980s, a team of scientists at University of Hawaii collected several thousand cyanobacteria in a worldwide search for strains that produce bioactive compounds.[1] In 1992, Moore, Patterson and coworkers reported that a strain from Nan Madol, Pohnpei (Micronesia) produced a compound with activity as an efflux pump inhibitor against human cancer cell lines.[2] The strain, HT-58-2, was classified on the basis of morphology as *Tolypothrix nodosa*, given the clumping tendency of the filamentous cyanobacteria. The compound proved to be a novel tetrapyrrole macrocycle dubbed a tolyporphin – a portmanteau of the genus name and the generic porphyrin term. The structure of the first tolyporphin discovered (tolyporphin A) was identified by total synthesis of the derivative tolyporphin A diacetate.[3-5] Tolyporphin A also was found to reverse multidrug resistance in cancer cell lines[6], and exhibit photoactivity in studies of photodynamic therapy of mouse tumor cells.[7]

Tolyporphin A, while not a porphyrin, differs in three remarkable ways from any previously known tetrapyrrole (Chart 1). First, the macrocycle is a dioxobacteriochlorin. Second, the site flanking the oxo group in the pyrroline ring is geminally disubstituted with a methyl group and a *C*-glycoside. Third, one position in each pyrrole ring is unsubstituted. Since the discovery of tolyporphin A, other members of the family of tolyporphin macrocycles have been identified in the HT-58-2 strain, including B-I[8]; J, K[9]; and L, M[10] (Chart 2). Except for tolyporphin A, knowledge concerning the tolyporphin structures is somewhat incomplete: tolyporphins B and C have not been isolated in pure form and hence the structural assignments are provisional, as is also the case for tolyporphins G and H; the structures of tolyporphins L and M have not been fully characterized; and in general, the stereochemistry in the pyrroline moieties of tolyporphins B–M

has not been fully defined. Tolyporphin A has distinct tetrapyrrole faces, one partially encumbered

by the two *C*-glycosides and the other relatively unshielded altogether.
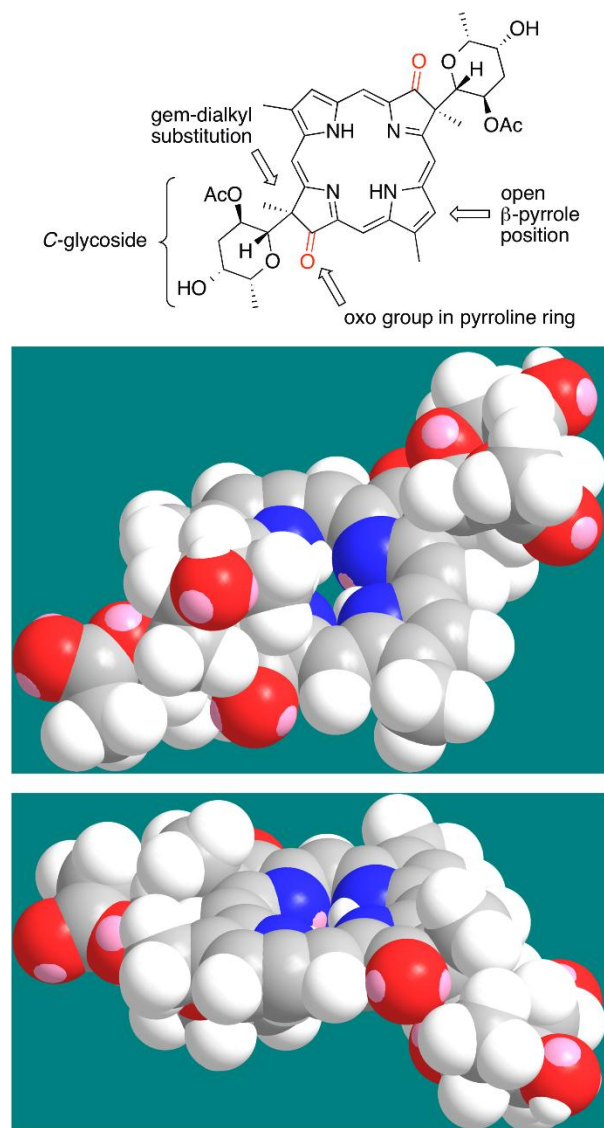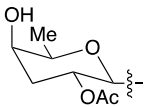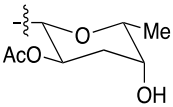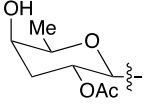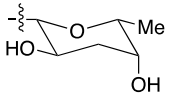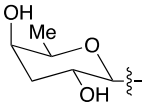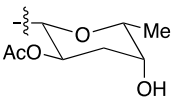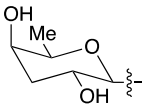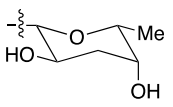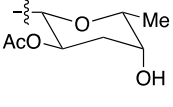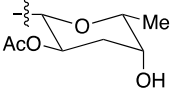
Chart 1. Structure of tolyporphin A (top) and CPK diagrams showing the top face (middle) and bottom face (lower, upon 180° rotation about the horizontal axis).
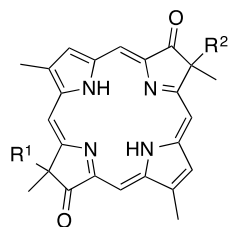
Tolyporphin (general structure)

Tolyporphin	R^1	R^2
A	sugar: OH, Me, O, OAc	sugar: AcO, O, Me, OH
B+C	sugar: OH, Me, O, OAc	sugar: HO, O, Me, OH
	sugar: OH, Me, O, OH	sugar: AcO, O, Me, OH
D	sugar: OH, Me, O, OH	sugar: HO, O, Me, OH
E	AcO–	sugar: AcO, O, Me, OH
F	HO–	sugar: AcO, O, Me, OH
G+H	AcO–	–OH
	HO–	–OAc
I	AcO–	–OAc

65
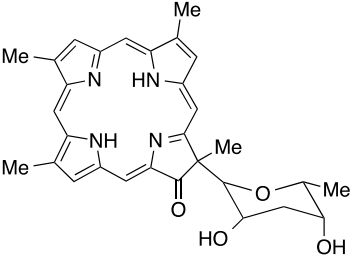
J	HO–	–OH
K		

Chart 2. Structures of tolyporphins A–K.

Our interests in tolyporphins initially were to obtain the enzymes employed in the biosynthesis for use in chemoenzymatic syntheses of designer tetrapyrrole macrocycles. The tolyporphin biosynthetic pathway is of particular interest owing to the gem-dialkyl groups in the pyrroline motif and the unsubstituted pyrrole sites, which together afford an oxidation-resistant macrocycle and opportunities for installation of pyrrole substituents, respectively. More broadly, we are interested in identifying the unknown issues of biosynthesis and biological function of tolyporphins.

One interpretation concerning function is that tolyporphins are photochemically active and thereby serve in light-harvesting or photoprotection phenomena. In this regard, it is surprising that the spectroscopic and photophysical features of tolyporphins have heretofore not been reported (other than photoactivity in a single PDT study[7]). A very recent paper reports the electron paramagnetic properties of the silver and copper chelate of tolyporphin A[11]. The characterization of the photochemical features of the native, free base macrocycles is essential for addressing issues of possible function as well as searching for tolyporphins in other cellular samples. Accordingly, in this paper we report an in-depth study of tolyporphin A, which as the most abundant tolyporphin was available in sufficient quantity. The study includes examination in 10 different solvents of

the static absorption spectra, static fluorescence spectra, and excited-state spectra and lifetimes; such data enable determination of photophysical parameters including the yields and rate constants of the fluorescence, internal-conversion, and intersystem-crossing decay pathways of the lowest singlet excited state. The solvent variation study is meant to simulate the wide range of environments – from membranous to hydrophilic – that tolyporphins might encounter *in vivo*. In addition, the absorption spectra of tolyporphins B-I and K are reported. The studies are complemented by similar examination of two synthetic macrocycles[12], an oxobacteriochlorin and a dioxobacteriochlorin, both of which contain a geminal-dimethyl group flanking each oxo moiety (Chart 3). Together, the studies provide the foundation for understanding the spectroscopic and photochemical features of tolyporphins.
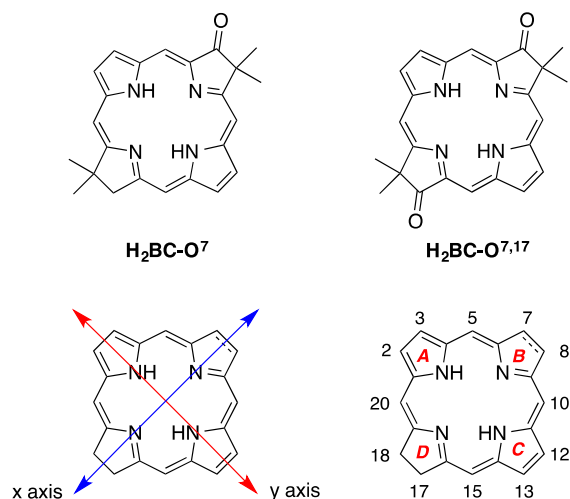
Chart 3. Two synthetic oxobacteriochlorin analogues along with the molecular axes and numbering system for chlorins and bacteriochlorins.

Experimental Section

Samples of tolyporphins were isolated from large-scale cultures at University of Hawaii. Oxobacteriochlorin **H₂BC-O⁷** and dioxobacteriochlorin **H₂BC-O⁷,¹⁷** were synthesized as described recently[12].

Spectral and photophysical studies were carried out on dilute (μM) argon-purged samples at room temperature. Absorption spectra were acquired using a Shimadzu UV-1800 spectrometer using 0.2-nm spacing. Static emission spectra were acquired using a Spex-Horiba Nanolog spectrofluorimeter with 2–4 nm excitation and detection bandwidths and corrected for instrument spectral response. Fluorescence quantum yields were obtained relative to *meso*-tetraphenylporphyrin ($\Phi_f = 0.070$ in nondegassed toluene)[13]. The Φ_f value for tolyporphin A was also obtained by absolute measurement and was found to be the same as the value from the relative measurement (Quanta-ϕ, Horiba). Singlet excited-state lifetimes were determined by using transient absorption (TA) spectroscopy employing ~100 fs excitation flashes from an ultrafast laser system (Spectra Physics) and acquisition of difference spectra (360–900 nm) using a white-light pulsed laser (~1 ns rise time) in 100-ps time bins with variable pump-probe spacing up to 0.5 ms (EOS, Ultrafast Systems). Transient absorption measurements employed excitation both on the long-wavelength side of the Soret absorption (400–420 nm) and in the Q-band region (485–535 nm). Time profiles of ΔA at ~1.5 nm spacing across the 380–750 nm region were analyzed at a number of individual wavelengths and also globally. Transient absorption studies were also used to measure the yield of $S_1 \rightarrow T_1$ intersystem crossing by comparing the extent of bleaching of the ground-state absorption bands due to T_1 at the asymptote of the S_1 decay versus the extent due to S_1 immediately after the excitation flash. Measurements in the Q_y region account for the contribution of both S_0 bleaching and S_1 stimulation emission to the S_1 feature. Measurement of

the S_1 lifetime of tolyporphyin was also made on a sample degassed by 10 freeze-pump-thaw cycles on a high vacuum line (10^{-5} torr).

Results

Absorption spectral properties of tolyporphin A. The electronic ground-state absorption spectra for tolyporphin A in 10 solvents that encompass a wide polarity range ($\varepsilon = 2.38-46.7$) are shown in Figure 1. Peak wavelengths are listed in Table 1. Each spectrum consists of the $Q_y(0,0)$ band in the far-red region (678 nm) that reflects absorption from the ground state (S_0) to the lowest singlet excited state (S_1). A series of much weaker Q_y vibronic-satellite features reside in the 600–650 nm region. The feature in the green region (538–551 nm) is the $Q_x(0,0)$ band, and the band of comparable intensity at shorter wavelength by ~40 nm (~1400 cm^{-1}) is the $Q_x(1,0)$ band, which together reflect $S_0 \rightarrow S_2$ absorption. Progressing to still higher energy are the strong $B_x(0,0)$ band ($S_0 \rightarrow S_3$) that affords the near-UV absorption maximum, and the $B_y(0,0)$ shoulder ($S_0 \rightarrow S_4$) that has roughly 0.6–0.7 of the peak intensity.

As a point of reference, the molar absorption coefficient data of tolyporphin A in ethanol are reported as follows: 148,000 M^{-1}cm^{-1} (402 nm) and 68,500 M^{-1}cm^{-1} (676 nm)[7]. The molar absorption coefficient data for other dioxobacteriochlorins include the following: 2,6-mesoporphyrindione dimethyl ester, $\varepsilon = 187,000$ M^{-1}cm^{-1} (411 nm) and 95,000 M^{-1}cm^{-1} (685 nm) in CH_2Cl_2[14]; 8,18-dioxo derivative of etioporphyrin II, $\varepsilon = 197,700$ M^{-1}cm^{-1} (408 nm) and 104,300 M^{-1}cm^{-1} (684 nm; solvent not stated)[15]. The variation observed is typical in the tetrapyrrole field and likely reflects experimental error rather than intrinsic differences in the strength of absorption.
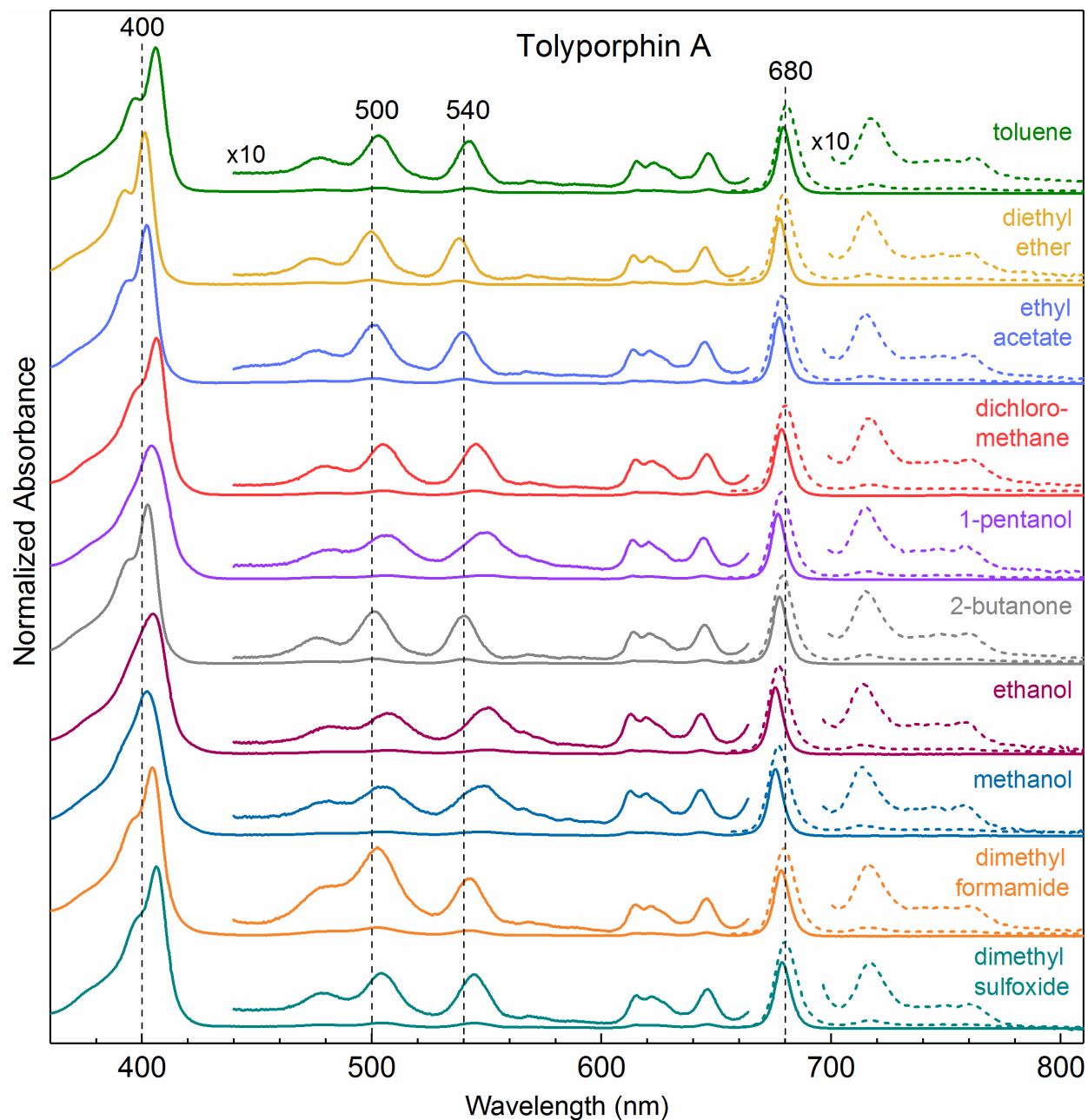
Figure 1. Absorption (solid) and fluorescence (dashed) spectra of tolyporphin A in 10 solvents. The absorption spectra are normalized to the maximum of the $Q_y(0,0)$ band (~690 nm) and the fluorescence spectra to 1.3 times that value. The insets show regions of the spectra expanded vertically by 10× the main traces.

Table 1. Photophysical properties of tolyporphin A.[a]

solvent	ε	B_y [b] λ_{abs} (nm)	B_x λ_{abs} (nm)	Q_x λ_{abs} (nm)	Q_y λ_{abs} (nm)	Q_y λ_{em} (nm)	τ_s (ns)	Φ_f	Φ_{isc}	Φ_{ic}
toluene	2.4	397	406	543	679	681	3.9	0.14	0.77	0.09
diethyl ether	4.3	393	401	538	678	679	4.2	0.11	0.81	0.08
ethyl acetate	6.1	394	402	540	677	678	3.9	0.12	0.80	0.08
dichloromethane	8.9	398	406	545	679	680	3.7	0.11	0.83	0.06
1-pentanol	13	394	404	551	677	678	4.4	0.11	0.82	0.07
2-butanone	18.5	394	402	540	677	682	4.1	0.13	0.82	0.05
ethanol	24.6	396	405	551	676	677	4.1	0.12	0.81	0.07
methanol	32.7	393	402	550	676	677	4.3	0.11	0.85	0.04
dimethylformamide	36.7	397	404	543	678	680	3.8	0.11	0.79	0.10
dimethylsulfoxide	46.7	398	406	545	679	680	3.9	0.11	0.79	0.10
average		*395*	*404*	*545*	*678*	*679*	*4.0*	*0.12*	*0.81*	*0.07*

[a]All values were measured using Ar-purged samples at room temperature. The four absorption wavelengths listed are for the origin, or (0,0), band in the associated manifold. Similarly, the emission wavelength is for Q_y(0,0) fluorescence. [b]This absorption feature is a shoulder on the larger B_x band and thus the precise wavelength is uncertain (see Figure 1).

Figure 1 and Table 1 show that the Q_y(0,0) band varies only from 676 nm to 679 nm across the solvents. The B_x(0,0) near-UV maximum varies by only 5 nm (401−406 nm). The Q_x(0,0) band typically rests in a narrow range (540−545 nm) except for the alcohols methanol, ethanol and 1-pentanol, for which the band lies at 550−551 nm. The bathochromic shift of the Q_x(0,0) band and the Q_y(1,0) satellite feature likely result from hydrogen bonding to the 7,17-oxo groups of tolyporphin A (Chart 1), which are located along the x-molecular axis (Chart 3). Close examination of Table 1 shows that the Q_y(0,0) band of the compound in these alcohols also lies at the shorter-wavelength end of the (narrow) span of wavelengths for this feature.

To explore the effects of increasing aqueous content of the environment, the absorption spectrum of tolyporphin A was also acquired in methanol−water mixtures. A concentrated

methanol solution was added to a series of methanol–water mixtures to attain percent methanol as low as 2.5% and thus water percent as high as 97.5%. The results are shown in Figure 2. As the percent water increases to 75%, the near-UV Soret band undergoes a small bathochromic shift while the red-region Q_y band retains the same position, and the absorption intensity of both bands remains relatively constant. At even greater water content, both bands broaden and decrease in intensity suggestive of aggregation. These results complement those described above for tolyporphin A in a variety of organic solvents in showing that this native dioxobacteriochlorin tolerates a wide span of environment polarity, which may be relevant to the environments accessed *in vivo*.
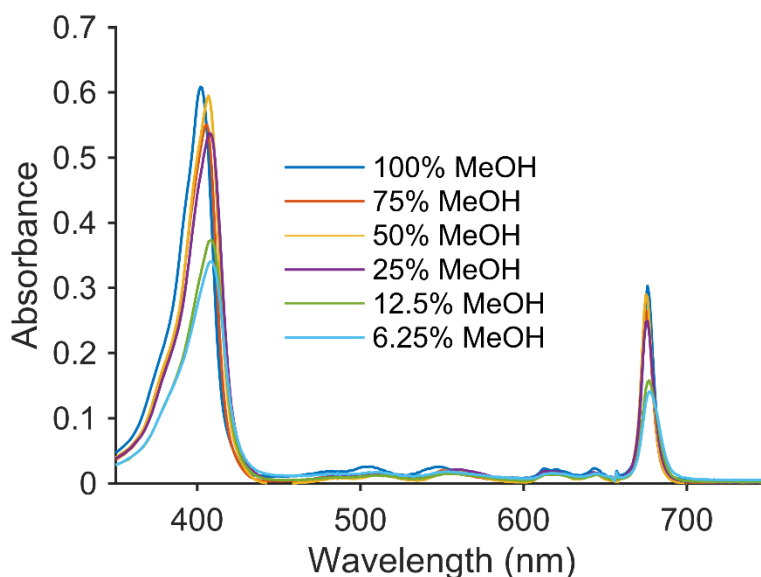
Figure 2. Absorption spectra of tolyporphin A in methanol–water solutions having the percent methanol indicated.

For comparison with the absorption properties of tolyporphin A, the spectra of tolyporphins A–I, K in methanol are shown in Figure 3. Tolyporphins A–I are dioxobacteriochlorins, and exhibit spectral properties that are quite similar to one another. Tolyporphin K is an oxochlorin and lacks the intense long-wavelength band characteristic of the dioxobacteriochlorins.
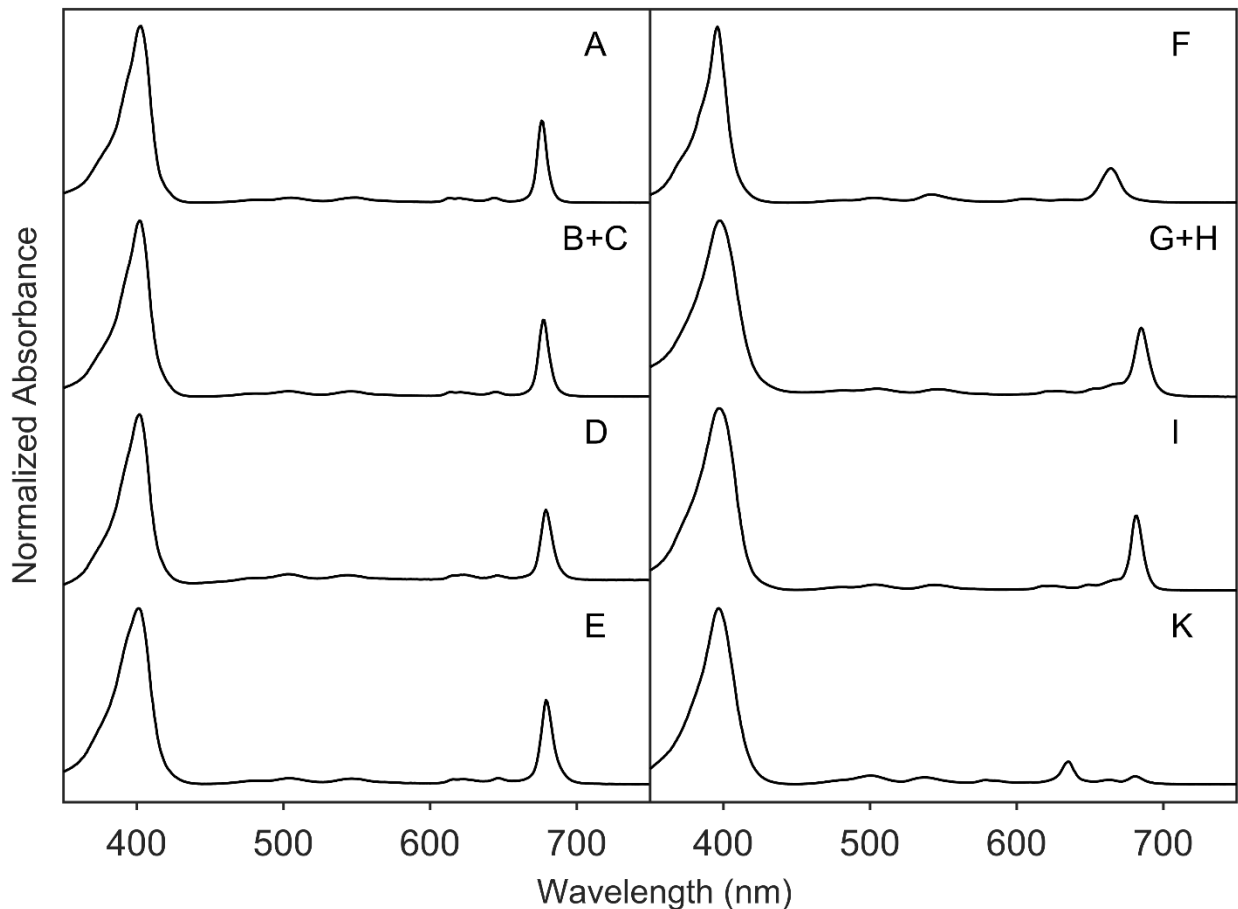
Figure 3. Absorption spectra of tolyporphins in methanol at room temperature.

Fluorescence spectral properties of tolyporphin A. The fluorescence spectrum of tolyporphin A in the 10 solvents is shown in Figure 1 (dashed lines). The spectrum is dominated by the $Q_y(0,0)$ band (679 nm), with a number of vibronic overtone features, including $Q_y(0,1)$, to longer wavelengths. The fluorescence manifold has approximate mirror symmetry to the Q_y absorption manifold. The $Q_y(0,0)$ fluorescence peak for tolyporphin A in all solvents is shifted from the $Q_y(0,0)$ absorption peak by ~1-2 nm (~20–40 cm^{-1}). These very small Stokes shifts correspond to minimal changes in molecular and solvent nuclear coordinates in the S_1 vs S_0 states. The structural rigidity implied is consistent with the rather narrow full-width-at-half-maxima of

the Q_y absorption band (~7 nm) and fluorescence band (~10 nm) of tolyporphin A across the solvents.

Excited-state properties of tolyporphin A. The measured excited-state properties are the lifetime (τ_S) of the lowest singlet excited state (S_1), the $S_1 \rightarrow S_0$ fluorescence quantum yield (Φ_f), and the yield of $S_1 \rightarrow T_1$ intersystem crossing (Φ_{isc}). The yield of $S_1 \rightarrow S_0$ internal conversion is obtained by the difference $\Phi_{ic} = 1 - \Phi_f - \Phi_{isc}$. These data are collected for tolyporphin A in Table 1. The last row of the table gives the average values.

The Φ_f value for tolyporphin A across the 10 solvents ranges from 0.11–0.14, with an average of 0.12. Figure 4 shows representative TA difference spectra and kinetic traces for tolyporphin A in toluene (obtained using 100-fs excitation flashes at 680 nm) that illustrate the measurements of τ_S and Φ_{isc}. The spectrum at 0.7 ns is due to the lowest singlet excited state (S_1 or Q_y). The spectrum is dominated by bleaching of the near-UV Soret ground-state absorption (B_x and B_y features) centered at 405 nm and a feature at 680 nm comprised of bleaching of the Q_y ground-state absorption band plus the Q_y excited-state stimulated emission. In between are small features at approximately 505 and 545 nm due to bleaching of the weaker $Q_x(1,0)$ and $Q_x(0,0)$ absorption bands. The spectrum at 35 ns is due to the lowest triplet excited state (T_1). The bleaching of each ground-state absorption feature is somewhat diminished and the S_1 stimulated emission has disappeared. Based on the diminution of the features at 405 and 680 nm, a yield of $S_1 \rightarrow T_1$ internal conversion of 0.80 is obtained for tolyporphin A in toluene. Similar values are found in the other solvents (Table 1). The inset to Figure 3 shows a representative kinetic profile for decay of the S_1 excited state of tolyporphin A in toluene. The average value from such measurements at 680 and 405 nm (and all wavelengths across the spectrum analyzed globally) is

3.9 ns. Similar τ_S values are found for tolyporphin A in the other 9 solvents, with an average of 4.1 ns (Table 1).
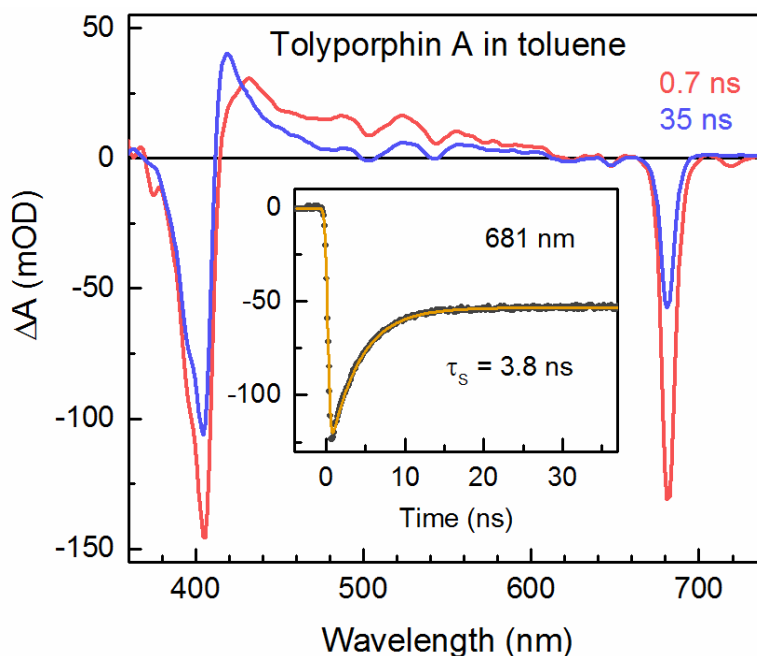
Figure 4. Representative transient absorption data for tolyporphin A in toluene obtained using 100 fs excitation flashes at 680 nm.

Triplet excited-state lifetime of tolyporphin A and quenching by O_2. The lifetime of the lowest triplet excited state (τ_T) was measured for tolyporphin A in *N,N*-dimethylformamide in ambient O_2 (air), purged with argon to remove the bulk of the dissolved O_2 (Figure 5),or degassed by repeated freeze-pump-thaw cycles. The lifetime of 100 µs in Ar-purged (or degassed) DMF is reduced to 0.6 µs in air. These values in conjunction with the typical 1–3 mM concentration of O_2 in organic solvents[16–19] and the typical factor-of-9 spin restriction on the rate of quenching of triplet excited states of chromophores by triplet ground state O_2 ($^3O_2$) suggests that the bimolecular process is basically diffusion controlled. The quenching by energy transfer causes formation of the singlet excited state of O_2 ($^1O_2$) and the singlet ground state of the chromophore[16,20,21]. Thus, the triplet excited state of tolyporphin A has generally similar photochemical activity toward forming such reactive oxygen species as many other tetrapyrrole chromophores[19,22].
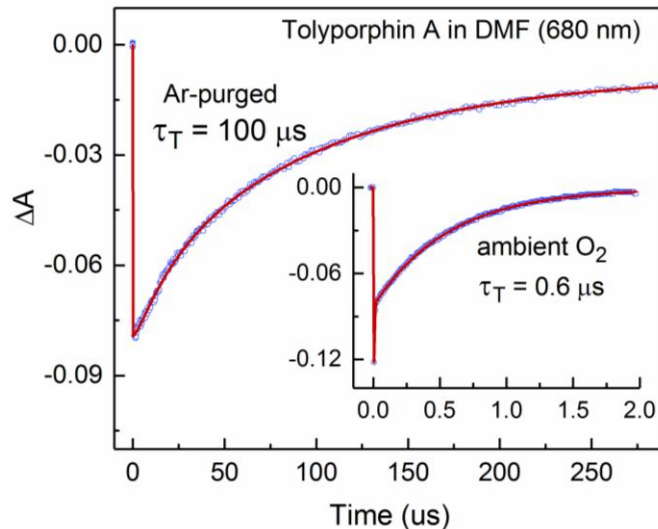
Figure 5. Representative transient absorption lifetime data for tolyporphin A in DMF with and without dissolved oxygen.

Spectral and photophysical properties of synthetic oxobacteriochlorins. Figure 6 and

Table 2 give the absorption and fluorescence spectra and photophysical data for

monoxobacteriochlorin **H₂BC-O⁷**, in analogy to Figure 1 and Table 1 for tolyporphin A. Figure 7

and Table 3 give the corresponding data for dioxobacteriochlorin and **H₂BC-O⁷,¹⁷**. The excited-

state properties (τ_S, Φ_f, Φ_{isc} Φ_{ic}) were determined similarly to those described above for

tolyporphin A, including from transient absorption measurements analogous to those shown in

Figure 4. The properties for **H₂BC-O⁷** and **H₂BC-O⁷,¹⁷** in toluene have been described recently

along with the synthesis of the compounds[12]. The findings for both bacteriochlorins in the nine

other solvents are similar to the results in toluene.
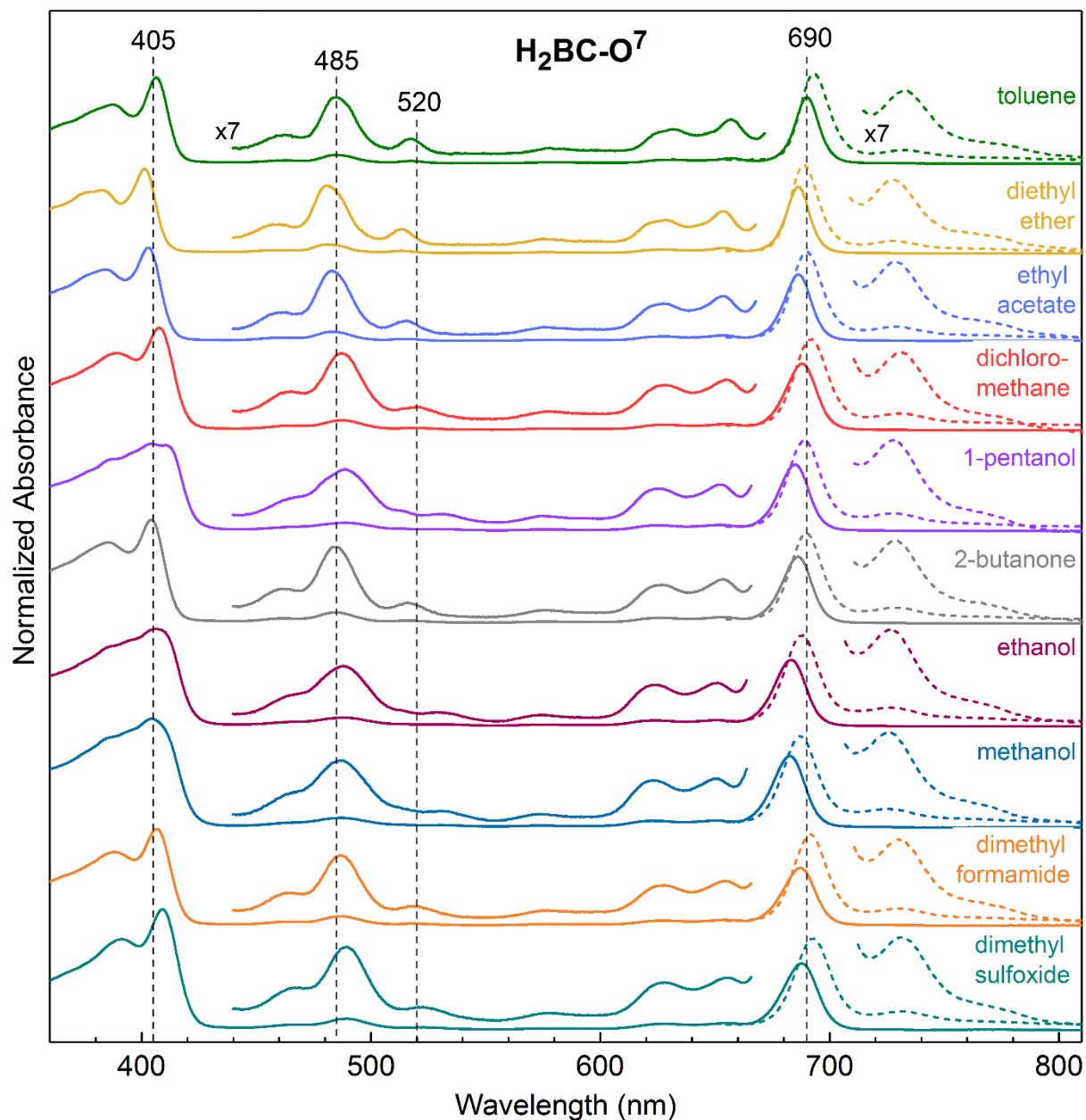
Figure 6. Absorption (solid) and fluorescence (dashed) spectra of **H₂BC-O⁷** in 10 solvents. The absorption spectra are normalized to the maximum of the $Q_y(0,0)$ band (~690 nm) and the fluorescence spectra to 1.3 times that value. The insets show regions of the spectra expanded vertically by 7× the main traces.

Table 2. Photophysical properties of oxobacteriochlorin **H₂BC-O⁷**.[a]

solvent	ε	B_y λ_{abs} (nm)	B_x λ_{abs} (nm)	Q_x λ_{abs} (nm)	Q_y λ_{abs} (nm)	Q_y λ_{em} (nm)	τ_s (ns)	Φ_f	Φ_{isc}	Φ_{ic}
Toluene	2.4	388	407	517	690	693	3.5	0.16	0.72	0.12
diethyl ether	4.3	383	401	514	686	688	3.4	0.12	0.73	0.15
ethyl acetate	6.1	385	403	515	686	690	3.5	0.14	0.75	0.11
dichloromethane	8.9	389	408	521	688	692	3	0.12	0.79	0.09
1-pentanol	13	389	411	531	685	689	3.4	0.14	0.76	0.1
2-butanone	18.5	386	404	517	686	690	3.4	0.1	0.76	0.14
Ethanol	24.6	388	406	532	683	688	3.2	0.13	0.78	0.09
Methanol	32.7	387	404	531	683	686	3.5	0.13	0.77	0.1
dimethylformamide	36.7	388	407	520	687	693	3.3	0.15	0.77	0.08
dimethylsulfoxide	46.7	391	409	523	688	693	3.4	0.14	0.8	0.06
Average		*387*	*406*	*522*	*686*	*690*	*3.4*	*0.13*	*0.76*	*0.10*

[a]All values were measured using Ar-purged samples at room temperature.

Table 3. Photophysical properties of dioxobacteriochlorin **H₂BC-O⁷,¹⁷**.[a]

solvent	ε	B_y[b] λ_{abs} (nm)	B_x λ_{abs} (nm)	Q_x λ_{abs} (nm)	Q_y λ_{abs} (nm)	Q_y λ_{em} (nm)	τ_s (ns)	Φ_f	Φ_{isc}	Φ_{ic}
Toluene	2.4	391	401	534	680	682	3.8	0.16	0.77	0.07
diethyl ether	4.3	385	395	529	677	679	3.9	0.13	0.74	0.13
ethyl acetate	6.1	387	396	532	677	678	3.9	0.11	0.77	0.12
dichloromethane	8.9	391	400	535	678	681	3.3	0.09	0.74	0.17
1-pentanol	13	390	398	540	677	677	4.0	0.13	0.75	0.12
2-butanone	18.5	389	397	533	676	677	4.0	0.11	0.76	0.13
Ethanol	24.6	387	397	541	675	678	4.1	0.10	0.74	0.16
Methanol	32.7	386	396	540	674	676	4.1	0.12	0.73	0.15
dimethylformamide	36.7	391	400	536	677	678	3.9	0.13	0.79	0.08
dimethylsulfoxide	46.7	394	402	540	678	679	3.5	0.12	0.75	0.13
Average		*389*	*398*	*536*	*677*	*679*	*3.8*	*0.12*	*0.75*	*0.13*

[a]All values were measured using Ar-purged samples at room temperature. [b]This feature is a shoulder on the larger B_x band, and thus the precise wavelength is uncertain.
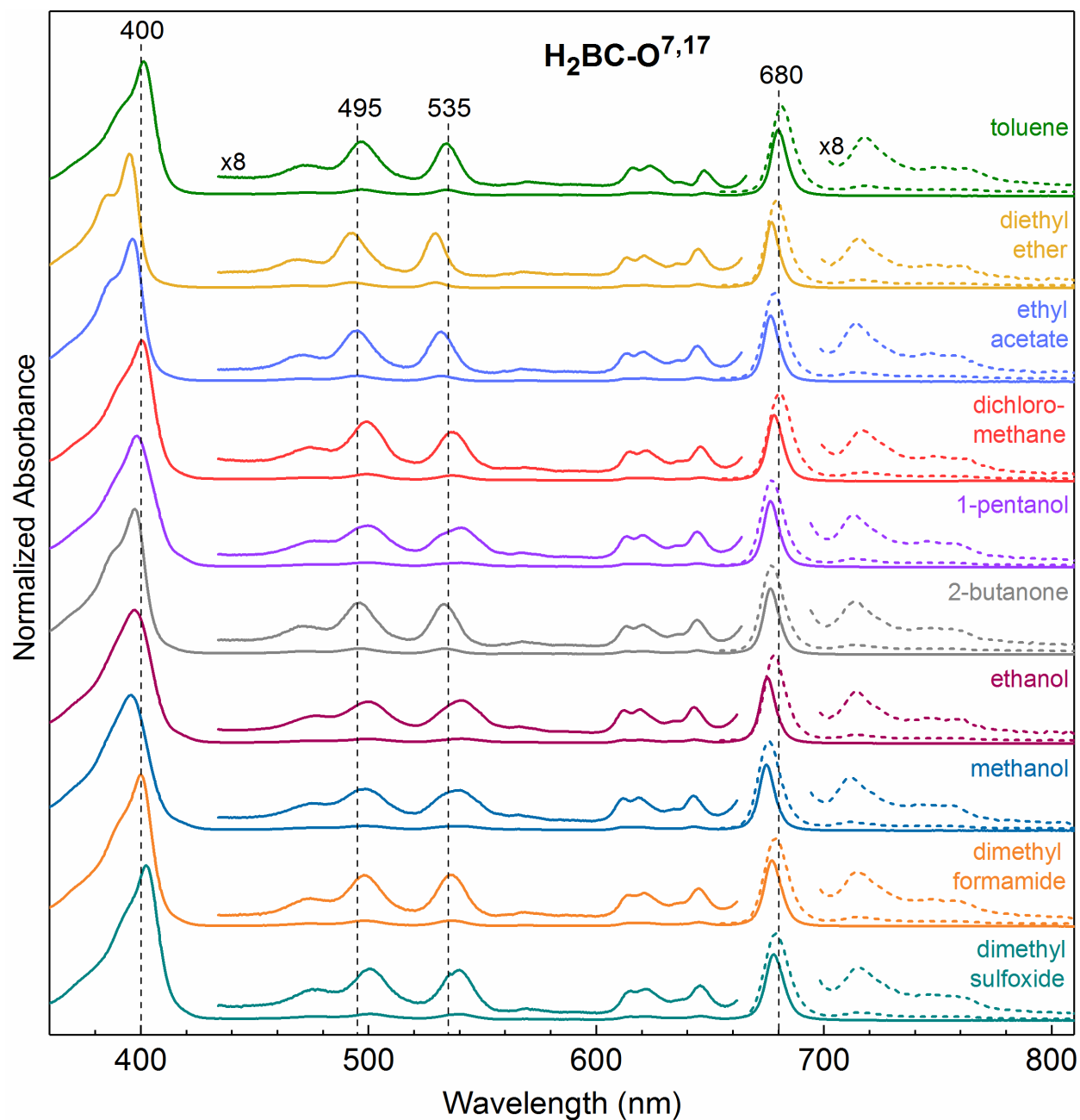
Figure 7. Absorption (solid) and fluorescence (dashed) spectra of **H$_2$BC-O^{7,17}** in 10 solvents. The absorption spectra are normalized to the maximum of the Q$_y$(0,0) band (~680 nm) and the fluorescence spectra to 1.3 times that value. The insets show regions of the spectra expanded vertically by 8× the main traces.

In general, the spectral properties of tolyporphin A and the synthetic analogues **H$_2$BC-O^7** and **H$_2$BC-O^{7,17}** are quite similar among the 10 solvents, which vary widely in properties such as dielectric constant (Tables 1−3). Perhaps the most notable difference is that the Q$_x$(0,0) band of

tolyporphin A is bathochromically shifted by ~5 nm in the alcoholic media (1-pentanol, ethanol, methanol) and to a lesser extent in a few other solvents (e.g., dimethylsulfoxide). In this regard, the $Q_x(0,0)$ band for both synthetic bacteriochlorins **H₂BC-O⁷** (Figure 6) and **H₂BC-O⁷,¹⁷** (Figure 7) in the alcohols is broad with contributions of components near the same wavelengths as found in the other solvents and at least one other component that is bathochromically shifted by up to ~15 nm. These data suggest that structures may be present for the synthetic bacteriochlorins with and without hydrogen bonds from the alcohol solvent molecules to the keto group(s) of these bacteriochlorins.

The above-noted effect is more pronounced for **H₂BC-O⁷** than **H₂BC-O⁷,¹⁷** and lesser still for tolyporphin A (Figure 1). Along the same series, the B_y-region of the spectrum for **H₂BC-O⁷** is broad (with several underlying components), a phenomenon that is again most pronounced in the alcohols. This breadth decreases for **H₂BC-O⁷,¹⁷** and perhaps still more for tolyporphin A, accompanying the general bathochromic shift of $B_y(0,0)$ such that for tolyporphin A the feature begins to coalesce with $B_x(0,0)$. Perhaps along this series the presence of two versus one oxo group and then the other macrocycle substituents in tolyporphin A (not present in the synthetic analogues) facilitates the hydrogen-bonding interactions and thus progressively reduces the contribution of species in the alcoholic solutions that lack such interactions. One can only speculate that such hydrogen-bonding interactions may be present and play some structural (or electronic) role for tolyporphin A *in vivo*.

Tables 1–3 give the values of the S_1 (Q_y) excited-state lifetime (τ_S) and the yields of the three decay pathways (Φ_f, Φ_{isc}, Φ_{ic}) for **H₂BC-O⁷**, **H₂BC-O⁷,¹⁷** and tolyporphin A in 10 solvents spanning a wide polarity range. The values of the parameters are not particularly sensitive to medium. The results spanning all solvents indicate that $S_1 \rightarrow T_1$ intersystem crossing dominates

the excited-state decay of all three molecules. This pathway accounts for an average of 75–80%

of the S_1 decay. The $S_1 \rightarrow S_0$ fluorescence-emission route accounts for 12–13% and $S_1 \rightarrow S_0$

nonradiative internal conversion the remaining ~10%.

Photophysical data for photosynthetic pigments. Comparison of the properties of

tolyporphin A with those of natural chlorins (chlorophyll *a* and pheophytin *a*) and bacteriochlorins

(bacteriochlorophyll *a* and bacteriopheophytin *a*) is best done in a common solvent, and for this

purpose we chose toluene. The τ_S, Φ_f and Φ_{isc} values for bacteriochlorophyll *a* and

bacteriopheophytin *a* in toluene have been reported[23,24]. The Φ_f values for pheophytin *a* and

chlorophyll *a* in toluene have been reported[25]. Here we measured the τ_S and Φ_{isc} values for

pheophytin *a* in toluene and chlorophyll *a* in toluene (and in toluene with ~5% pyridine) that are

near the mean of literature values in a variety media[22,26–33]. The values are listed in Table 4 along

with those for tolyporphin A and the two synthetic bacteriochlorins from Tables 1-3.   The

structures of the native pigments are provided in Chart 4.

Table 4. Photophysical properties of tolyporphin A, synthetic oxobacteriochlorins, and photosynthetic pigments.[a]

Compound	B_y λ_{abs} (nm)	B_x λ_{abs} (nm)	Q_x λ_{abs} (nm)	Q_y λ_{abs} (nm)	Q_y λ_{em} (nm)	τ_S (ns)	Φ_f	Φ_{isc}	Φ_{ic}	k_f^{-1} (ns)	k_{isc}^{-1} (ns)	k_{ic}^{-1} (ns)
tolyporphin A	397	406	543	679	681	3.9	0.14	0.77	0.09	28	5.1	43
H₂BC-O[7]	388	407	517	690	69	3.5	0.16	0.72	0.12	22	4.9	29
H₂BC-O[7,17]	391	401	534	680	682	3.8	0.16	0.77	0.07	24	4.9	54
pheophytin *a* [b]	400	415	538	671	676	6.7	0.24	0.60	0.16	28	11	42
chlorophyll *a* [b]	413	432	532	665	671	6.4	0.33	0.55	0.12	19	12	53
bacteriopheophytin *a* [c]	363	389	532	758	768	2.7	0.1	0.57	0.33	27	4.7	8
bacteriochlorophyll *a* [d]	363	396	581	781	789	3.1	0.12	0.30	0.58	26	10	5.3

[a]All values were measured using Ar-purged toluene samples at room temperature. [b] Wavelengths and Φ_f from ref 25. [c] From ref 23. [d] From ref 24.
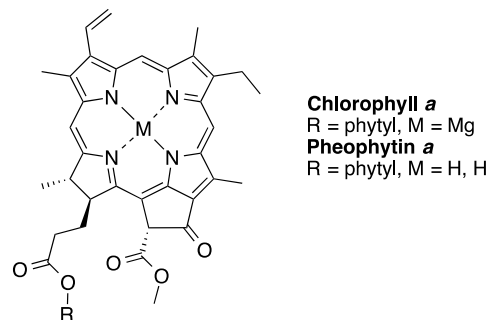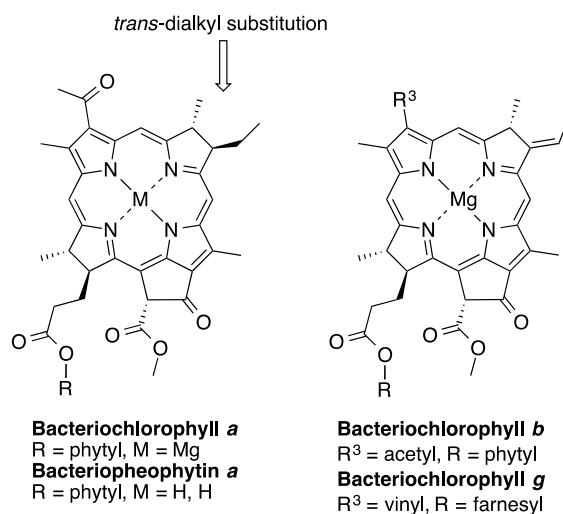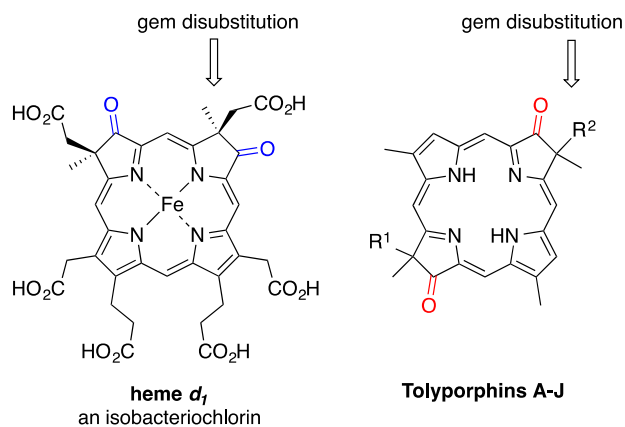
Chart 4. Hydroporphyrins with distinct pyrroline ring substitutions.

Discussion

In this section, we first summarize the spectral and photophysical features of tolyporphins, and compare the observed results with the typical features of the chief tetrapyrrole pigments of photosynthesis, namely the native chlorins (chlorophyll *a* and the free base analogue pheophytin

a) of plant and cyanobacterial photosynthesis, and the native bacteriochlorins (bacteriochlorophyll *a* and the free base analogue bacteriopheophytin *a*) of anoxygenic bacterial photosynthesis. Second, we contrast the unusual structural features of tolyporphins with those of the known family of tetrapyrroles. Third, in the context of the photophysical data collected herein, we speculate briefly on possible *in vivo* functional roles of tolyporphins.

Spectral characteristics. Figure 8 compares the absorption spectra in toluene of tolyporphin A (and synthetic bacteriochlorins **H₂BC-O⁷,¹⁷** and **H₂BCO⁷**) with those for native photosynthetic chlorins and bacteriochlorins. Table 4 lists the peak wavelengths, with those for tolyporphin A and the two synthetic bacteriochlorins reproduced from Tables 1–3 to facilitate comparisons.

Compared with the two synthetic bacteriochlorins, the spectrum of tolyporphin A resembles that of **H₂BC-O⁷,¹⁷** more closely than that of **H₂BC-O⁷** as expected because tolyporphin A is a dioxobacteriochlorin. Thus, the *C*-glycoside substituents of tolyporphin A do not cause major changes in spectral properties from bacteriochlorin **H₂BC-O⁷,¹⁷**. The spectrum of tolyporphin A more closely resembles those of the native chlorins (chlorophyll *a* and pheophytin *a*) than the native bacteriochlorins[34] (bacteriochlorophyll *a* and bacteriopheophytin *a*). In short, the 7,17-oxo groups of tolyporphin A are the source of the differences in spectra from those of bacteriochlorins (native and synthetic) that lack such substituents.
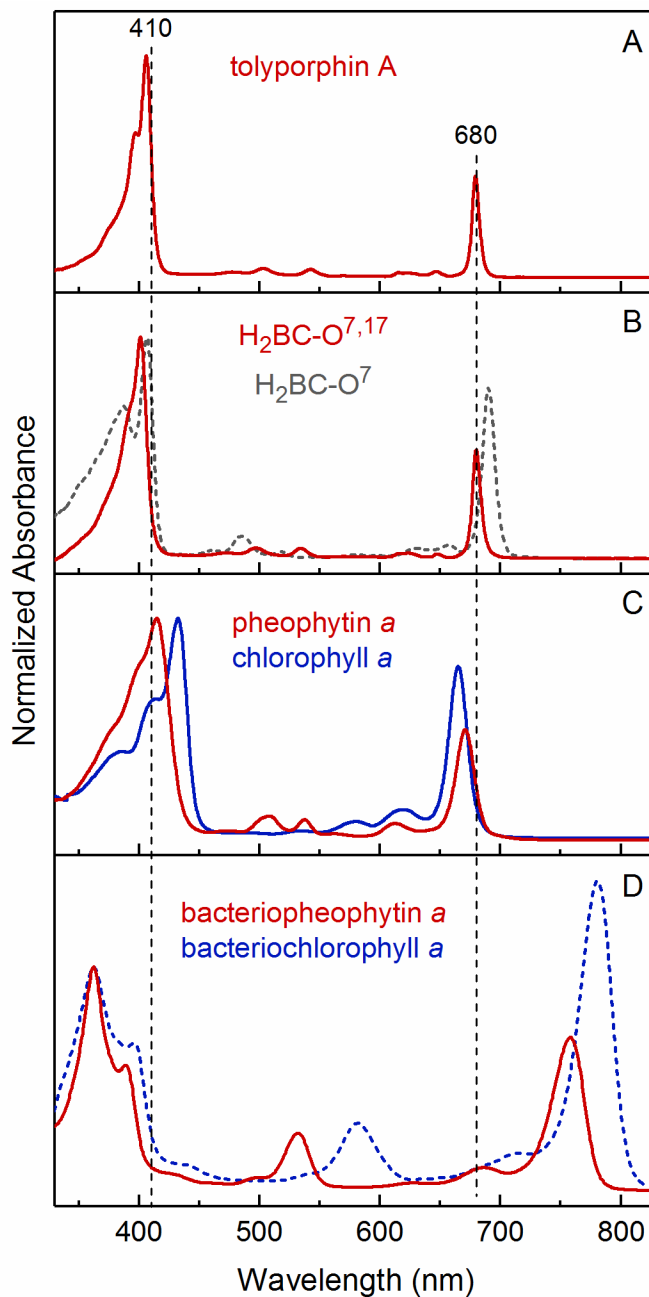
Figure 8. Absorption spectra (normalized at the B band) in toluene for tolyporphin A (A), synthetic bacteriochlorins (B), native chlorins (C), and native bacteriochlorins (D).

We have previously examined the molecular-electronic origins of the spectral consequences of 7,17-oxo groups on the bacteriochlorin macrocycle in terms of the effects on the energies (and electron distributions) of the frontier molecular orbitals[12,35]. The oxo groups stabilize, but unequally, the two highest filled and two lowest empty molecular orbitals, electron

promotions between which dominate the near-UV to near-infrared spectra of tetrapyrroles within the four-orbital model[36-38]. Relative to more traditional native or synthetic bacteriochlorins, dioxobacteriochlorins such as tolyporphin A exhibit hypsochromically and hypochromically shifted Q_y bands and bathochromically and hyperchromically shifted B_x and B_y bands (Figure 8).

Excited-state properties. Table 4 gives the values of the S_1 (Q_y) excited-state lifetime (τ_S) and the yields of the three decay pathways (Φ_f, Φ_{isc}, Φ_{ic}) determined in toluene for tolyporphin A, **H$_2$BC-O[7]**, **H$_2$BC-O[7,17]** and the chlorin and bacteriochlorin photosynthetic pigments. The τ_S, Φ_{isc}, and Φ_{ic} values of tolyporphin A in toluene (3.9 ns, 0.77, 0.09) are generally closer to those of the native chlorins (6.4–6.7 ns, 0.55–0.60, 0.12–0.16) than native bacteriochlorins (2.7–3.1 ns, 0.30–0.57, 0.33–0.58). On the other hand, the Φ_f of tolyporphin A (0.14) is closer to the values for native bacteriochlorins (0.10–0.12) than native chlorins (0.24–0.33).

The values of τ_S, Φ_f, Φ_{isc}, and Φ_{ic} can be used to obtain the rate constants for the fluorescence (k_f), intersystem-crossing (k_{isc}), and internal-conversion (k_{ic}) decay pathways of the S_1 excited state via the calculation $k_x = \Phi_x/\tau_S$, where x = f, isc or ic. The values are listed in the last three columns of Table 4 as the associated time constants (with units of nanoseconds). These rate constants are the most fundamental factors that govern the behavior of the S_1 excited state and associated photophysical/photochemical functional characteristics. Comparison of excited-state decay rate constants for tolyporphin A and **H$_2$BC-O[7,17]** with those for native chlorins (chlorophyll *a* and pheophytin *a*) and native bacteriochlorins (bacteriochlorophyll *a* and bacteriopheophytin *a*) in toluene lead to the following conclusions.

(1) The k_f values for tolyporphin A and **H$_2$BC-O[7,17]** (24–28 ns)$^{-1}$ are comparable to that for native bacteriochlorins (26–27 ns)$^{-1}$ and a variety of synthetic bacteriochlorins (20–30 ns)$^{-1}$[23,24], and intermediate between native chlorins (19–28 ns)$^{-1}$ and a variety of synthetic chlorins

(40–50 ns)$^{-1}$[139]. Thus, the tolyporphin A (and synthetic analogue **H$_2$BC-O^{7,17}**) largely retains the $S_1 \leftrightarrow S_0$ radiative (emission and absorption) probabilities of native and simple synthetic bacteriochlorins.

(2) The k_{isc} values for tolyporphin A, **H$_2$BC-O^{7,17}** and the native chlorins and bacteriochlorins are in the range of $(4.7–12 \text{ ns})^{-1}$, like a variety of synthetic bacteriochlorins[23,24]. Thus, the 7,17-dioxo motif of tolyporphin A does not appreciably change the electron density distribution or other factors that control electron spin-orbit coupling and in turn the probability of $S_1 \rightarrow T_1$ intersystem crossing.

(3) The k_{ic} values for tolyporphin A and **H$_2$BC-O^{7,17}** $(43–54 \text{ ns})^{-1}$ are generally similar to that for native chlorins $(42–53 \text{ ns})^{-1}$ but much reduced from native bacteriochlorins $(5–8 \text{ ns})^{-1}$ and a host of synthetic bacteriochlorins typically $(5–15 \text{ ns})^{-1}$ with generally similar Q_y wavelengths[23]. According to the energy-gap law for nonradiative decay[16], the rate constant for $S_1 \rightarrow S_0$ internal conversion increases as the S_1 energy decreases. Thus, slower S_1 nonradiative deactivation to the ground state parallels the higher S_1 energy reflected in the hypsochromically shifted Q_y band (Figure 8 and Table 4) for tolyporphin, **H$_2$BC-O^{7,17}** and chlorins compared to the native (and most synthetic) bacteriochlorins. In short, the 7,17-dioxo motif of tolyporphin A makes the Q_y energy/wavelength and k_{ic} values more like those of the native chlorins than the native bacteriochlorins.

Tolyporphins – distinct structures in the family of tetrapyrroles. The characterization of naturally occurring tetrapyrroles over more than a century has led to a number of broad observations, with which tolyporphins appear to be at odds. The observations are as follows:

First, in the main, tetrapyrroles are found in nature as the metal chelate: heme contains Fe(II), chlorophylls and bacteriochlorophylls contain Mg(II), cobalamin contains Co(I), and F$_{430}$

contains Ni(I). Free base macrocycles are found as electron-acceptors in photosynthetic reaction centers (pheophytin, bacteriopheophytin) albeit in minute quantities relative to the much larger amount of chlorophylls and bacteriochlorophylls in the antenna complexes as well as the remainder of the pigments of the reaction centers. The only other significant provenance of free base tetrapyrroles is as biosynthetic intermediates and as products of metabolic pathologies. The presence in HT-58-2 of tolyporphins[2,8-10], which are free base macrocycles, is at odds with this phenomenon.

Second, other than tolyporphins, the only natural occurrence of bacteriochlorins is in bacteriochlorophylls, which contain a *trans*-dialkyl configuration in each pyrroline ring (bacteriochlorophyll *a*), or a *trans*-dialkyl configuration in one pyrroline ring and one exocyclic double bond and a single flanking methyl group in the other pyrroline ring (bacteriochlorophylls *b* and *g*)[40]. By contrast, tolyporphins contain a gem-disubstituted group in each pyrroline ring[2-5,8,9]. The only other known dioxobacteriochlorins appear in the dioxo*iso*bacteriochlorin ligand of heme *d₁* (Chart 4), which contains adjacent rather than opposing pyrroline rings as in tolyporphins. Heme *d₁* contains oxo groups with flanking gem-dialkyl groups[41]. Knowledge about the biosynthetic pathways for formation of tolyporphins and heme *d₁* remains unknown and incomplete, respectively. In brief, gem-disubstitution occurs in the hydroporphyrin family of enzymatic cofactors such as heme d_1, cobalamin, and F_{430} (and their biosynthetic precursors) but not among known photosynthetic pigments. The evolutionary origin of this dichotomy remains obscure.

Third, tetrapyrroles generally contain a full complement of substituents at the β-pyrrole positions. The substituents include methyl, ethyl, acetic acid, propionic acid, vinyl, acetyl and

formyl. The presence of an unsubstituted pyrrole site (i.e., a C–H bond) is rare – to our knowledge one other example is the pigment bonellin, a chlorin found in the marine worm *Bonellia viridis*[42,43].

Speculation on physiological roles. The chief physiological roles of cyclic tetrapyrroles include cofactors in enzymatic catalysis, light-harvesting and electron-transfer processes in photosynthesis, and transmission of cellular or physiological information (i.e., signaling molecules); photoreception is achieved with linear tetrapyrroles, namely bilins. While the *in vivo* function of tolyporphins remains unknown, the data reported herein show that tolyporphin A retains photoactivity across a wide range of solvent polarities. Illumination of tolyporphin A in aerated ethanol is known to yield singlet oxygen[7], and the data presented here suggest that such photoactivity is expected in diverse solvent environments. The known tetrapyrrole signaling molecules (heme and cobalamin) are both photochemically inactive, thus a role for tolyporphins as signaling molecules seems unlikely.

Cyanobacteria are known to produce pigments for photo-protection[44,45], particularly for those terrestrial species found on surfaces exposed to prolonged intense sunlight. A representative class of such pigments is the scytonemins, which absorb in the UV and into the visible region[44,45]. The close resemblance of the absorption spectra of tolyporphins A–J with that of chlorophyll *a* suggests a possible role as a photoprotective agent (by absorption) or as a photo-toxin (by generation of $^1O_2$ or other reactive oxygen species such as hydroxyl radicals). Cyanobacteria also are known to produce myriad natural products (46–48), which in fact prompted the survey by the University of Hawaii team >25 years ago that led to the discovery, inter alia, of HT-58-2 and tolyporphins[1]. Roles for tolyporphins as supporting metabolites[49,50] that do not derive from light absorption are also possible, such as efflux pump inhibition of the cyanobacterium or of associated bacteria. While the *in vivo* function of tolyporphins remains unknown, the results reported herein

concerning photoactivity of tolyporphin A across diverse solvents, and similar spectral features (where available) for the other dioxobacteriochlorin tolyporphins (B-I) establish a framework for informed consideration of possible physiological functions in photic environments.

Conclusions

Tolyporphin A is a free base dioxobacteriochlorin that is found in the cyanobacterium-containing sample HT-58-2. Each reduced, pyrroline ring contains geminal disubstitution at the 8,18-positions (*C*-glycoside and methyl) adjacent to the 7,17-oxo groups. Comparative studies of tolyporphin A and synthetic monooxo- and dioxo-bacteriochlorins show that the 7,17-dioxo motif underlies the spectral distinctions of tolyporphin A from native bacteriochlorins (bacteriochlorophyll *a* and pheophytin *a*) and spectral similarities to native chlorins (chlorophyll *a* and pheophytin *a*). One such characteristic is that the long-wavelength (Q_y) absorption band of tolyporphin A is shifted hypsochromically relative to native bacteriochlorins and into the wavelength regime of native chlorins. This higher energy of the S_1 excited state also results in the yield and rate constant for $S_1 \rightarrow S_0$ internal conversion being more similar to those of native and synthetic chlorins than native and synthetic bacteriochlorins. Tolyporphin A has a yield and rate constant for $S_1 \rightarrow S_0$ fluorescence similar to those of bacteriochlorins. The 7,17-dioxo motif of tolyporphin A does not significantly alter the rate constant for $S_1 \rightarrow T_1$ intersystem crossing compared to native or synthetic metal-free chlorins or bacteriochlorins, a process that comprises roughly 80% of the decay of the S_1 excited state for tolyporphin A, which is significantly greater than for native and synthetic bacteriochlorins. This high triplet yield along with strong absorption in the red (versus near infrared) spectral region may underlie possible functional roles of tolyporphin A *in vivo*. The spectral and photophysical properties of tolyporphin A (and synthetic oxobacteriochlorins) were found to be relatively insensitive to solvent characteristics

encompassing a large range of polarity, thus mimicking potential environments for the pigment *in vivo*. The lack of sensitivity of such properties to environmental polarity implies that tolyporphins may be active in the cytoplasm as well as more non-polar membrane environments.

Acknowledgments

References

1.	Patterson, G. M. L., C. L. Baldwin, C. M. Bolis, F. R. Caplan, H. Karuso, L. K. Larsen, I. A. Levine, R. E. Moore, C. S. Nelson, K. D. Tschappat, G. D. Tuang, E. Furusawa, S. Furusawa, T. R. Norton and R. B. Raybourne (1991) Antineoplastic activity of cultured blue-green algae (cyanophyta). *J. Phycol.* **27**, 530–536.

2.	Prinsep, M. R., F. R. Caplan, R. E. Moore, G. M. L. Patterson and C. D. Smith (1992) Tolyporphin, a novel multidrug resistance reversing agent from the blue-green alga *Tolypothrix nodosa*. *J. Am. Chem. Soc.* **114**, 385–387.

3.	Minehan, T. G. and Y. Kishi (1999) Total synthesis of the proposed structure of (+)-tolyporphin A *O,O*-diacetate. *Angew. Chem. Int. Ed.* **38**, 923–925.

4.	Minehan, T. G., L. Cook-Blumberg, Y. Kishi, M. R. Prinsep and R. E. Moore (1999) Revised structure of tolyporphin A. *Angew. Chem. Int. Ed.* **38**, 926–928.

5.	Wang, W. and Y. Kishi (1999) Synthesis and structure of tolyporphin A *O,O*-diacetate. *Org. Lett.* **1**, 1129–1132.

6.	Smith, C. D., M. R. Prinsep, F. R. Caplan, R. E. Moore and G. M. L. Patterson (1994) Reversal of multiple drug resistance by tolyporphin, a novel cyanobacterial natural product. *Oncol. Res.* **6**, 211–218.

7.	Morlière, P., J.-C. Mazière, R. Santus, C. D. Smith, M. R. Prinsep, C. C. Stobbe, M. C. Fenning, J. L. Golberg and J. D. Chapman (1998) Tolyporphin: a natural product from cyanobacteria with potent photosensitizing activity against tumor cells *in vitro* and *in vivo*. *Cancer Res.* **58**, 3571–3578.

8.   Prinsep, M. R., G. M. L. Patterson, L. K. Larsen and C. D. Smith (1995) Further tolyporphins from the blue-green alga *Tolypothrix nodosa*. *Tetrahedron* **51**, 10523–10530.

9.   Prinsep, M. R., G. M. L. Patterson, L. K. Larsen and C. D. Smith (1998) Tolyporphins J and K, two further porphinoid metabolites from the cyanobacterium *Tolypothrix nodosa*. *J. Nat. Prod.* **61**, 1133–1136.

10.   Prinsep, M. R. and J. Puddick (2011) Laser desorption ionization–time of flight mass spectrometry of the tolyporphins, bioactive metabolites from the cyanobacterium *Tolypothrix nodosa*. *Phytochem. Anal.* **22**, 285–290.

11.   Prinsep, M. R., T. G. Appleton, G. R. Hanson, I. Lane, C. D. Smith, J. Puddick and D. P. Fairlie (2017) Tolyporphin macrocycles from the cyanobacterium *Tolypothrix nodosa* selectively bind copper and silver and reverse multidrug resistance. *Inorg. Chem.* **2017**, XX, DOI:10.1021/acs.inorgchem.6b03000.

12.   Liu, M., C.-Y. Chen, D. Hood, M. Taniguchi, J. R. Diers, D. F. Bocian, D. Holten and J. S. Lindsey (2017) Synthesis, photophysics and electronic structure of oxobacteriochlorins. *New J. Chem.* **41**, DOI:10.1039/c6nj04135c.

13.   Mandal, A. K., M. Taniguchi, J. R. Diers, D. M. Niedzwiedzki, C. Kirmaier, J. S. Lindsey, D. F. Bocian and D. Holten (2016) Photophysical properties and electronic structure of porphyrins bearing zero to four *meso*-phenyl substituents: new insights into seemingly well understood tetrapyrroles. *J. Phys. Chem. A* **120**, 9719–9731.

14.   Chang, C. K. and W. Wu (1986) On the hydrogen peroxide/sulfuric acid oxidation of mesoporphyrin. Synthesis of mesoporphyrindiones. *J. Org. Chem.* **51**, 2134–2137.

15.   Pandey, R. K., M. Isaac, I. MacDonald, C. J. Medforth, M. O. Senge, T. J. Dougherty and K. M. Smith (1997) Pinacol–pinacolone rearrangements in *vic*-dihydroxychlorins and bacteriochlorins: effect of substituents at the peripheral positions. *J. Org. Chem.* **62,** 1463–1472.

16.   Birks, J. B. (1970) Photophysics of aromatic molecules. Wiley-Interscience: pp. 142–192. London.

17.   Achord, J. M. and C. L. Hussey (1980) Determination of dissolved oxygen in nonaqueous electrochemical solvents. *Anal. Chem.* **52**, 601–602.

18.   Bonnett, R., D. J. McGarvey, A. Harriman, E. J. Land, T. G. Truscott and U.-J. Winfield (1988) Photophysical properties of *meso*-tetraphenylporphyrin and some *meso*-tetra(hydroxyphenyl)porphyrins. *Photochem. Photobiol.* **48**, 271–276.

19.   Wilkinson, W., W. P. Helman and A. B. Ross (1993) Quantum yields for the photosensitized formation of the lowest electronically excited singlet state of molecular oxygen in solution. *J. Phys. Chem. Ref. Data* **22**, 113–262.

20.   Gijzeman, O. L. J., F. Kaufman and G. Porter (1973) Oxygen quenching of aromatic triplet states in solution. Part 1. *J. Chem. Soc., Faraday Trans. 2* **69**, 708–720.

21.	Demas, J. N., E. W. Harris and R. P. McBride (1977) Energy transfer from luminescent transition metal complexes to oxygen. *J. Am. Chem. Soc.* **99**, 3547–3551.

22.	Redmond, R. W. and J. N. Gamlin (1999) A compilation of singlet oxygen yields from biologically relevant molecules. *Photochem. Photobiol.* **70**, 391–475.

23.	Yang, E., C. Kirmaier, M. Krayer, M. Taniguchi, H.-J. Kim, J. R. Diers, D. F. Bocian, J. S. Lindsey and D. Holten (2011) Photophysical properties and electronic structure of stable, tunable synthetic bacteriochlorins: extending the features of native photosynthetic pigments. *J. Phys. Chem. B* **115**, 10801–10816.

24.	Chen, C.-Y., E. Sun, D. Fan, M. Taniguchi, B. E. McDowell, E. Yang, J. R. Diers, D. F. Bocian, D. Holten and J. S. Lindsey (2012) Synthesis and physicochemical properties of metallobacteriochlorins. *Inorg. Chem.* **51***, 9443–9464.

25.	Springer, J. W., K. M. Faries, J. R. Diers, C. Muthiah, O. Mass, H. L. Kee, C. Kirmaier, J. S. Lindsey, D. F. Bocian and D. Holten (2012) Effects of substituents on synthetic analogs of chlorophylls. Part 3: The distinctive impact of auxochromes at the 7- *versus* 3-positions. *Photochem. Photobiol.* **88**, 651–674.

26.	Livingston, R. and E. Fujimori (1958) Some properties of the ground triplet state of chlorophyll and related compounds. *J. Am. Chem. Soc.* **80**, 5610–5613.

27.	Bowers, P. G. and G. Porter (1967) Quantum yields of triplet formation in solutions of chlorophyll. *Proc. R. Soc. London A* **296**, 435–441.

28.	Gradyushko, A. T., A. N. Sevchenko, K. N. Solovyov and M P. Tsvirko (1970) Energetics of photophysical processes in chlorophyll-like molecules. *Photochem. Photobiol.* **11**, 387–400.

29.	Gurinovich, G. P., O. M. Petsol'd and I. M. Byteva (1974) Mechanism of pigment-photosensitized oxidation of thiourea by oxygen. *Biophysics (Engl. Transl.)* **19**, 249–253.

30.	Krasnovsky, Jr. A. A. (1979) Photoluminescence of singlet oxygen in pigment solutions. *Photochem. Photobiol.* **29**, 29–36.

31.	Connolly, J. S., A. F. Janzen and E. B. Samuel (1982) Fluorescence lifetimes of chlorophyll *a*: solvent, concentration and oxygen dependence. *Photochem. Photobiol*. **36**, 559–563.

32.	Tanielian, C. and C. Wolff (1995) Porphyrin-sensitized generation of singlet molecular oxygen: comparison of steady-state and time-resolved methods. *J. Phys. Chem.* **99**, 9825–9830.

33.	Niedzweidzki, D. M. and R. E. Blankenship (2010) Singlet and triplet excited state properties of natural chlorophylls and bacteriochlorophylls. *Photosynth. Res.* **106**, 227–238.

34.	Kobayashi, M., M. Akiyama, H. Kano and H. Kise (2006) Spectroscopy and structure determination. In *Chlorophylls and Bacteriochlorophylls: Biochemistry, Biophysics,*

Functions and Applications, (Edited by B. Grimm, R. J. Porra, W. Rüdiger, H. Scheer), pp. 79–94. Springer, Dordrecht, The Netherlands.

35. Vairaprakash, P., E. Yang, T. Sahin, M. Taniguchi, M. Krayer, J. R. Diers, A. Wang, D. M. Niedzwiedzki, C. Kirmaier, J. S. Lindsey, D. F. Bocian and D. Holten (2015) Extending the short and long wavelength limits of bacteriochlorin near-infrared absorption via dioxo- and bisimide-functionalization. *J. Phys. Chem. B* **119**, 4382–4395.

36. Gouterman, M. (1959) Study of the effects of substitution on the absorption spectra of porphin. *J. Chem. Phys.* **30**, 1139–1161.

37. Gouterman, M. (1961) Spectra of porphyrins. *J. Mol. Spectroscopy* **6**, 138–163.

38. Gouterman, M. (1978) Optical spectra and electronic structure of porphyrins and related rings. In *The Porphyrins* (Edited by D. Dolphin), pp. 1−165. Volume 3, Academic Press, New York.

39. Kee, H. L., C. Kirmaier, Q. Tang, J. R. Diers, C. Muthiah, M. Taniguchi, J. K. Laha, M. Ptaszek, J. S. Lindsey, D. F. Bocian and D. Holten (2007) Effects of substituents on synthetic analogs of chlorophylls. Part 1: synthesis, vibrational properties and excited-state decay characteristics. *Photochem. Photobiol.* **83**, 1110–1124.

40. Scheer, H. (2006) An overview of chlorophylls and bacteriochlorophylls: biochemistry, biophysics, functions and applications. In *Chlorophylls and Bacteriochlorophylls: Biochemistry, Biophysics, Functions and Applications,* (Edited by B. Grimm, R. J. Porra, W. Rüdiger, H. Scheer), pp. 1–26. Vol. 25, Springer, Dordrecht, The Netherlands.

41. Bali, S., D. J. Palmer, S. Schroeder, S. J. Ferguson and M. J. Warren (2014) Recent advances in the biosynthesis of modified tetrapyrroles: the discovery of an alternative pathway for the formation of heme and heme d_1. *Cell. Mol. Life Sci.* **71**, 2837–2863.

42. Agius, L., J. A. Ballantine, V. Ferrito, V. Jaccarini, P. Murray-Rust, A. Pelter, A. F. Psaila and P. J. Schembri (1979) The structure and physiological activity of bonellin − a unique chlorin derived from *Bonellia viridis*. *Pure Appl. Chem.* **51**, 1847−1864.

43. Lindsey, J. S. (2015) *De novo* synthesis of gem-dialkyl chlorophyll analogues for probing and emulating our green world. *Chem. Rev.* **115**, 6534–6620.

44. Sinha, R. P. and D.-P. Häder (2008) UV-protectants in cyanobacteria. *Plant Sci.* **174**, 278–289.

45. Gröniger, A., R. P. Sinha, M. Klisch and D.-P. Häder (2000) Photoprotective compounds in cyanobacteria, phytoplankton and macroalgae – a database. *J. Photochem. Photobiol. B: Biol.* **58**, 115–122.

46. Tan, L. T. (2010) Filamentous tropical marine cyanobacteria: a rich source of natural products for anticancer drug discovery. *J. Appl. Phycol.* **22**, 659–676.

47. Tidgewell, K., B. R. Clark and W. H. Gerwick (2010) The natural products chemistry of cyanobacteria. In *Comprehensive Natural Products II Chemistry and Biology,* (Edited by L. Mander, H.-W. Liu), pp. 141–188. Volume 2, Elsevier, Oxford.

48.   Singh, R. K., S. P. Tiwari, A. K. Rai and T. M. Mohapatra (2011) Cyanobacteria: an emerging source for drug discovery. *J. Antibiotics* **64**, 401–412.

49.   Firn, R. D., and C. G. Jones (2003) Natural products – a simple model to explain chemical diversity. *Nat. Prod. Rep.* **20**, 382–391.

50.   Firn, R. D., and C. G. Jones (2009) A Darwinian view of metabolism: molecular properties determine fitness. *J. Exp. Bot.* **60**, 719–726.

Chapter 4

Expanding Covalent Attachment Sites of Nonnative Chromophores to Encompass the *C*-terminal Hydrophilic Domain in Biohybrid Light-Harvesting Architectures

D Hood, T Sahin, P Parkes-Loach, Jieying J, M Harris, P Dilbeck, D Niedzwiedzki, C Kirmaier, P Loach, D Bocian, D Holten J Lindsey.

Abstract

Increasing the solar spectral coverage of native photosynthetic antennas can be achieved using biohybrid light-harvesting (LH) structures comprised of native-like bacterial photosynthetic peptides and synthetic bacteriochlorins with strong near-infrared absorption. Four such biohybrids have been prepared wherein synthetic maleimido-bearing bacteriochlorin **BC1-mal** is covalently attached to a Cys residue substituted at either the +1, +5 or +11 position (relative to His-0) of the 48-residue β-peptide of *Rb. sphaeroides* LH1. In addition, a β-peptide with Phe substituted for Tyr at the +4 position along with +1Cys was used to examine possible quenching of the excited **BC1** by the Tyr. The β-peptide analogs, as well as their peptide−**BC1** conjugates when combined with native α-peptide, and bacteriochlorophyll *a* (**BChl *a***) self-assemble to form αβ-dyads and therefrom LH1-type cyclic (αβ)$_n$ oligomers. Static and time-resolved optical studies show that all of the oligomeric assemblies transfer excitation energy from the appended **BC1** to the **BChl *a*** array (**B875**) with an average efficiency of 85%.

INTRODUCTION

Photosynthesis provides the ultimate source of energy for almost all forms of life. Photosynthetic organisms have light-harvesting (LH) antennas made of highly organized, three dimensional systems of pigments – primarily chlorins for plants and bacteriochlorins for photosynthetic bacteria – that absorb light and funnel the excitation energy to reaction centers.[1-5] To adapt to their habitat, photosynthetic organisms differ in the regions of the solar spectrum from which they absorb light,[6] largely due to differences in their antennas,[5] which in turn differ in the number and types of pigments present. No single class of pigments offers broad-band solar coverage. Synthetic light-harvesting systems have been studied extensively to gain insights into mechanisms of electronic energy migration among pigments;[7,8] however, preparation of synthetic antenna systems is challenging given the requirement to arrange a large number of pigments in close proximity and in well-defined 3-dimensional architectures.[9-11]

Building on the antenna designs that nature has developed, enhanced solar coverage has been achieved in biohybrid LH systems. Our work in this area[12-15] has focused on designs inspired by the cyclic LH1 inner antenna from photosynthetic purple bacteria. These complexes, like LH2 accessory antennas, contain dyads comprised of α- and β-peptides,[16,17] where each peptide is bound to a molecule of bacteriochlorophyll *a* (**BChl *a***) (Figure 1A). Interaction between the two **BChl *a*** molecules in the dyad shifts the near-infrared (NIR) Q_y absorption band from ~780 nm for the isolated pigment to 820 nm for the αβ-dyad; the **BChl *a*** dimer is designated **B820**. Native LH1 rings are comprised of 14–16 αβ-dyads (Figure 1B) depending on bacterial species.[18-22] Interactions among the larger number of **BChl *a*** molecules in the rings shift the Q_y band to ~875 nm; the **BChl *a*** array is designated **B875**.

The biohybrid approach entails coupling of a synthetic β-peptide having a single Cys residue at a predetermined position with a maleimido-terminated chromophore having desired absorption characteristics. Biohybrid antennas have been previously prepared with synthetic chromophores at seven different positions from the His at the 0 position towards the *N*-terminus of the β-peptide, namely at −34, −21, −17, −14, −10, −6, −2 (Figure 1C).[12-15] The chromophores include a bioconjugatable bacteriochlorin that decorates the outside of the LH1-like cyclic architecture (Figure 1D), affording energy-transfer efficiencies (Φ_{EET}) to **B875** ranging from 50 to 95% (Figure 1C). In addition to determination of Φ_{EET}, these studies have addressed the photophysical and helical properties of the chromophore–peptide conjugates; self-assembly of the conjugates, α-peptide and **BChl *a*** into αβ-dyads and from them $(\alpha\beta)_n$ oligomeric rings; and expanding the number and spectral coverage of the appended chromophores in a given LH1-like antenna.[12-15]

Figure 1. (A) Native αβ-subunit consisting of the α-peptide (blue), β-peptide (green) and a pair of **BChl *a*** molecules (purple) coordinated via the central magnesium ion to a histidine residue (black) of each peptide (from LH2 of *Phs. Molischianum*[22]). (B) Theoretical depiction of side and top views of the cyclic oligomeric LH1 complex of *Rb. sphaeroides*;[18] some peptides in the side view, and some of the **BChl *a*** molecules in both views are omitted for clarity. (C) Sites for chromophore attachment by replacing the residue with Cys, with numbers corresponding to the position relative to His 0. The sites with negative numbers (toward the *N*-terminus) have been used in prior studies for attachment of bioconjugatable bacteriochlorin **BC1-mal**; the energy transfer efficiencies measured in the resulting cyclic oligomers are shown. The sites with positive numbers were explored herein. (D) The structure of **BC1-mal** and an illustration of the oligomer housing this pigment on all β-peptides (and αβ-dyads).

The design of the biohybrid antennas is aided by the helical wheel for the β-peptide displayed in Figure 2A. Figure 2B shows the sequence of the native β-peptide (with an additional Cys at the *C*-terminus) and the hydropathicity values of amino acid side-chains of the β-peptide of *Rb. sphaeroides* LH1, with the most hydrophobic at +4.5 and the least hydrophobic at –4.5.[23] In both panels, sites previously replaced with Cys are encircled in red, and sites studied here are encircled in green. The positions utilized to substitute a Cys residue for this study are the +1, +5 and +11 positions. The latter site, labeled as C11 circled with dotted green in Figure 2B, is an addition to the *C*-terminus of the native peptide. Locations for conjugation of chromophores were

chosen so that they would not interfere with the binding of **BChl** *a* to form a subunit or the subsequent association of subunits to form LH1-type complexes (as illustrated in Figure 1D).
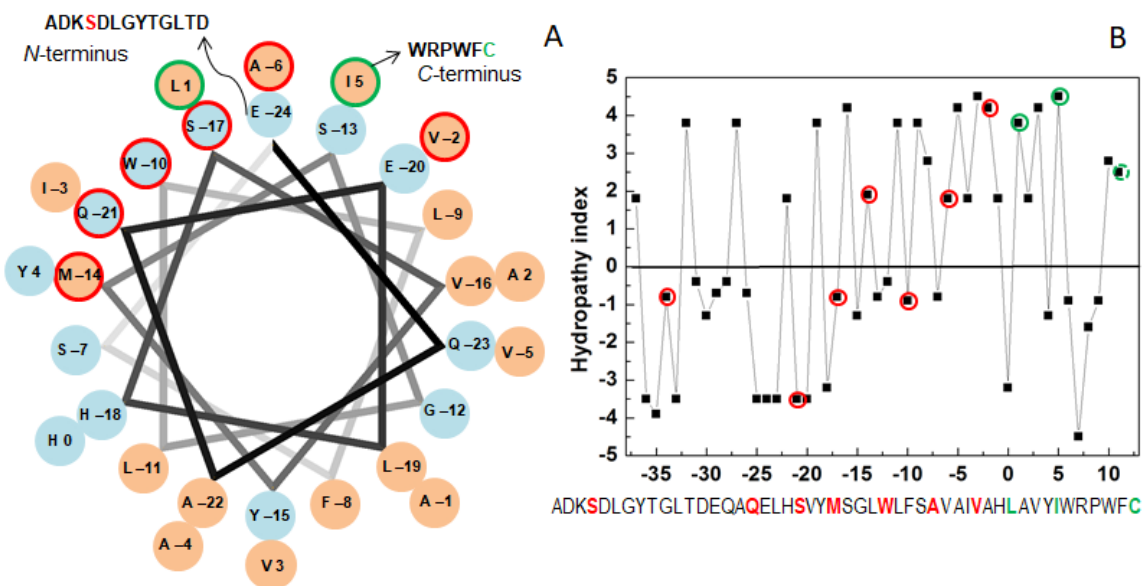
Figure 2. (A) The helical wheel display of the β-peptide from *Rb. sphaeroides* LH1. The hydrophilic residues are presented in cyan and hydrophobic residues in salmon. The helical wheel presentation is only valid for the α-helical region of the β peptide, roughly from the –24 to +6 positions. (B) The sequence (with an additional Cys at the *N*-terminus) and the hydropathicity values of amino acid side-chains of *Rb. sphaeroides* LH1 β-peptide: most hydrophobic, +4.5; least hydrophobic, –4.5.[23] In both panels, sites previously replaced with Cys are encircled (or typed) in red, and sites studied here are encircled (or typed) in green. The site labeled as C11 circled with dotted green is an addition to the native peptide.

Assembly of the biohybrid antennas is accomplished in an aqueous detergent solution. The detergent concentration is controlled to allow formation of micelles consisting of hydrophobic native α-peptides with synthetic β-peptides to give αβ-dyads, which then further assemble into the cyclic LH1-type $(\alpha\beta)_n$ oligomers. The average ring size of the biohybrid oligomers is comparable to that of native LH1 as indicated by electron microscopy, and the Q_y absorption feature is close to the 875 nm peak for native complexes.[12-15] Despite no reaction center (as in LH2), ring size and spectral behavior indicate that the biohybrids – which utilized the *Rb. sphaeroides* LH1 sequence as a template – are more like LH1 than LH2. The variations in the Φ_{EET} from 50% to 95% may

originate in the distance of the chromophore from the **BChl *a*** array and potential involvement of amino acids along or near the energy-transfer pathway.

The self-assembled light-harvesting architectures prepared from synthetic hydrophobic bacteriochlorins present difficulties when working in aqueous media. Amphiphilic bacteriochlorins appear to provide greater ease of assembly, handling, and energy-transfer studies than hydrophilic or hydrophobic designs alone.[24] Figure 2 shows the relationship between the attachment positions and the degree of hydrophobicity or hydrophilicity. Investigating positions near the *C*-terminus of the peptide (+ positions) was the logical extension of prior studies on variants at the (−) positions.

In this paper, we describe the preparation and photophysical characterization of biohybrid systems having the same synthetic bacteriochlorin (**BC1-mal**, Figure 1D) utilized previously at the (−) position on the β-peptide of *Rb. sphaeroides*, but at three additional (+) positions near the *C*-terminus of the β-peptide (Figure 2). The synthetic bacteriochlorin bears a maleimide-terminated tether for bioconjugation with a cysteine sulfhydryl group. The structure of **BC1-mal** is reproduced in Figure 3 along with that of bacteriochlorin **BC0**, which is an analog lacking the maleimide group for photophysical comparison. The two synthetic bacteriochlorins contain a gem-dimethyl group in each reduced ring, to be compared with the *trans*-dialkyl configuration in **BChl *a*** (Figure 3). Attachment of **BC1-mal** to the cysteine of a peptide results in a peptide–bacteriochlorin conjugate; we term the bioconjugated bacteriochlorin **BC1**. The results complement the previous studies and extend our knowledge of useful sites for chromophore/cofactor attachment. The study also included a biohybrid with +4Tyr replaced by Phe to determine what effect, if any, the Tyr has on the excited-state properties of **BC1** (attached at nearby (+) positions) and the Φ_{EET} for energy flow to the **BChl *a*** array of the LH1-type cyclic

oligomer. The +4Tyr was targeted because Tyr (and Trp) residues are known to quench the excited states of nearby dye molecules.[25]
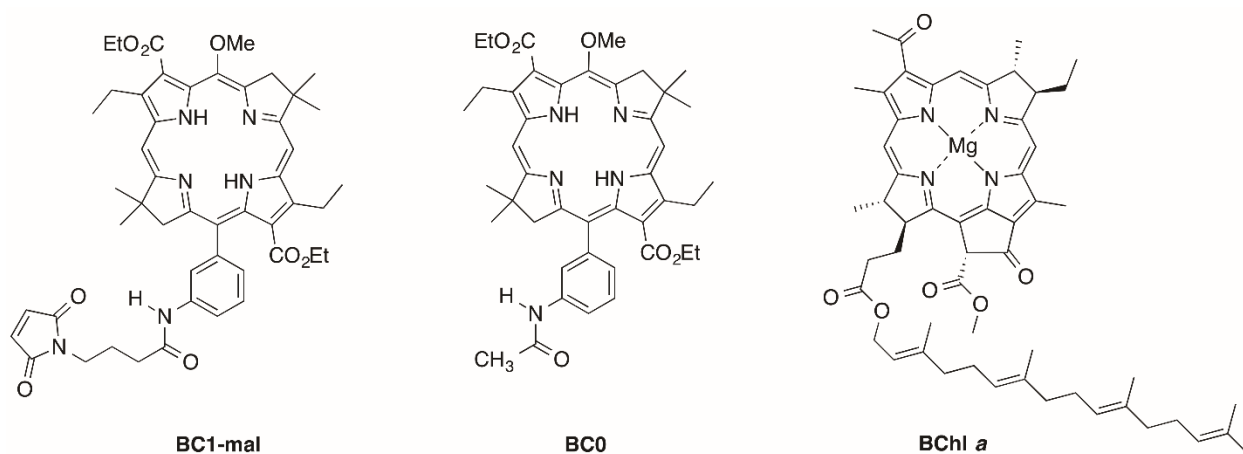
Figure 3. Structures of **BC1-mal**, **BC0** and **BChl** *a*.

RESULTS

Formation of the Conjugates

The structure of **BC1-mal**, chosen for covalent attachment, is shown in Figure 1D.[13] Previously this bacteriochlorin has been used for attachment at the (−) positions in other biohybrid constructs to evaluate the formation of αβ-subunits and oligomers in energy-transfer studies.[12,15] Using the same chromophore as in the (−)-position studies allows a relevant comparison of parameters important in energy transfer; i.e., the distance of the donor from the attachment site and the electronic environments in these sites.

BC1-mal was conjugated to each peptide individually in aqueous *N,N*-dimethylformamide (DMF) solution containing Tris buffer (pH 8.6) using previously established methods[13,15] to afford peptide–**BC1** conjugates **β(+1Cys)BC1**, **β(+5Cys)BC1**, **β(+11Cys)BC1** and **β(+1)BC1(+4Phe)**. The crude reaction mixtures were purified using reverse-phase HPLC and the total (isolated) yields were determined on the basis of the absorption spectrum of the **BC1-mal** in the starting sample versus that of the product using an extinction coefficient of 120,000 M^{-1} cm^{-1} for the Q_y absorption

band of the synthetic bacteriochlorin. (See the Supporting Information for experimental procedures and HPLC conditions.) As an example, the overlay of absorption spectra of **BC1-mal** and conjugate **β(+1Cys)BC1** in Figure 4 shows an absorption band in the ultraviolet region (nonexistent in the free **BC1-mal**) that is due to the peptide. Each conjugate was characterized by HPLC, absorption spectroscopy and ESI-MS.
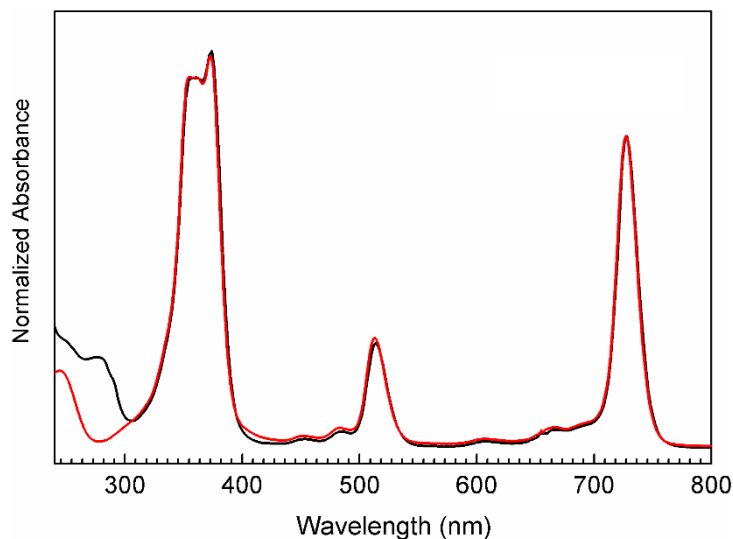
Figure 4. Absorption spectra of the conjugate **β(+1Cys)BC1** (black) and **BC1-mal** (red) normalized at Q_y absorption band.

There are three issues that affect the compositional and stereochemical purity of the conjugates. (1) The starting synthetic peptides are not 100% pure but are typically >85% (see Experimental Section). (2) The generation of a stereocenter upon reaction of the Cys residue with the maleimido-terminated **BC1-mal** gives rise to a pair of diastereomers. (3) Oxidation of the methionine at the −14 position to methionine sulfoxide can easily occur during routine handling of the peptides in air (see Supporting Information).[26,27] Sulfoxide formation creates a stereocenter as well, hence another source of diastereomerism of the peptides. Therefore, forming both of the possible configurations of these two new stereocenters in each conjugate would yield a total of 4 diastereomers. Given the locations of the stereocenters, the resulting stereochemically impure

sample is not expected to interfere with dyad and oligomer assembly processes leading to viable light-harvesting architectures.

FTIR Studies

Synthetic β-peptides **β(+1Cys)**, **β(+5Cys)**, **β(+11Cys),** and **β(+1Cys)(+4Phe)** and **BC1** conjugates were examined by single-reflection FTIR spectroscopy to verify that the α-helical nature of the peptides was not compromised by either addition/substitution of a Cys residue (or Phe in the case of **β(+1Cys)(+4Phe)**) or bioconjugation. Figure 5 shows FTIR spectra of the peptides of the four synthetic β-peptides and a representative conjugate **β(+1Cys)BC1(+4Phe)**, all of which display characteristic bands at 1664 and 1546 cm^{-1} assignable to the Amide I and Amide II vibrations. These signatures confirm that the α-helical character of the peptides is retained, as is evidenced by comparison with the spectrum of myoglobin, which has extensive α-helical structure.
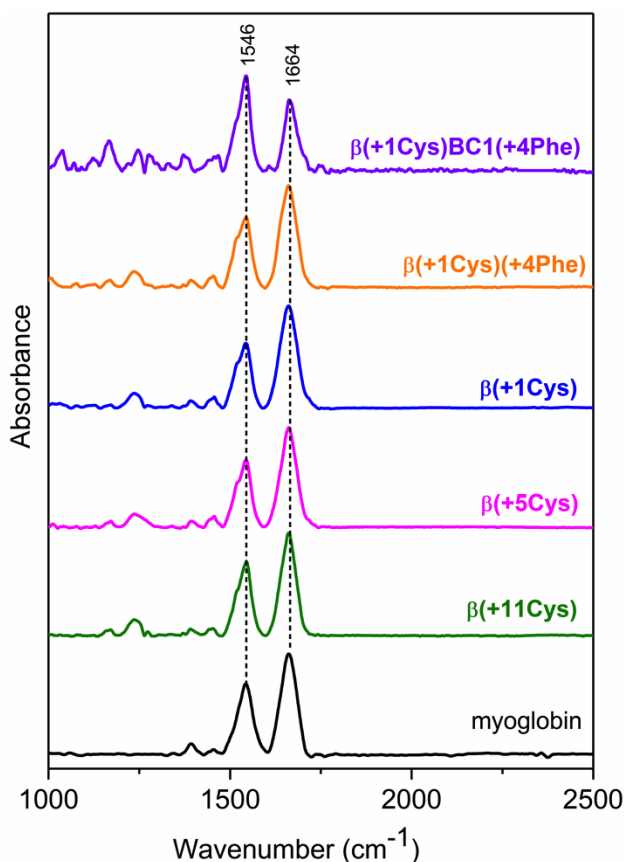
Figure 5. Single-reflection FTIR spectra of synthetic β-peptides on gold substrates show that amino acid replacements or **BC1** attachment does not affect α-helicity, as evidenced by Amide I and II resonances.

Formation of Biohybrid Antennas

All four synthetic peptides (having a substitution or addition of a Cys residue without attachment of **BC1**) were evaluated for their ability to support formation of B820- and LH1-type complexes with the native α-peptide and **BChl *a***. In each case, substitution or addition of a single residue or two in the case of **β(+1Cys)(+4Phe)** at these locations does not inhibit the formation of dimers and oligomers.

Each peptide–**BC1** conjugate was subjected to reconstitution conditions using the native α-peptide and **BChl *a*** as described in the literature.[12,14] To briefly exemplify using **β(+1Cys)BC1**, 0.05 mg of peptide–bacteriochlorin conjugate and 0.08 mg of native α-peptide were each dissolved

in separate 10 µL hexafluoroacetone trihydrate (HFA) solutions and sonicated. Then, 0.5 mL of 4.5% *n*-octyl β-D-glucopyranoside (OctG) was added to the **β(+1Cys)BC1** sample, which was subsequently mixed with the α-peptide sample. After diluting to 0.90% OctG, **BChl *a*** was added to initiate formation of the αβ-dyad **αβ(+1Cys)BC1**; the dyad formation is evidenced by the growth of a bathochromically shifted Q_y absorption feature at 825 nm (Figure 6A). Upon decreasing the OctG concentration, the equilibrium shifts toward the dyad; the K_{assoc} value approaches that for formation of the native αβ-dyad (Figure 6B) and formation of the oligomer **αβ(+1Cys)BCn** commences, as evidenced by a further bathochromic shift in absorption to 842 nm. The LH1-type oligomers are formed by chilling the sample overnight at 4–6 °C. Once formed, these complexes are generally stable in the cold for months. Figure 6C shows the spectrum of **αβ(+1Cys)BCn,** having the Q_y band of the **BChl *a*** array at 870 nm, a wavelength similar to that found in native LH1 complexes. The LH1-type oligomer was then used for energy-transfer studies. The ability to form dimers and oligomers with the conjugates shows that the presence of the appended chromophores does not interfere with either the dimerization or oligomerization process.
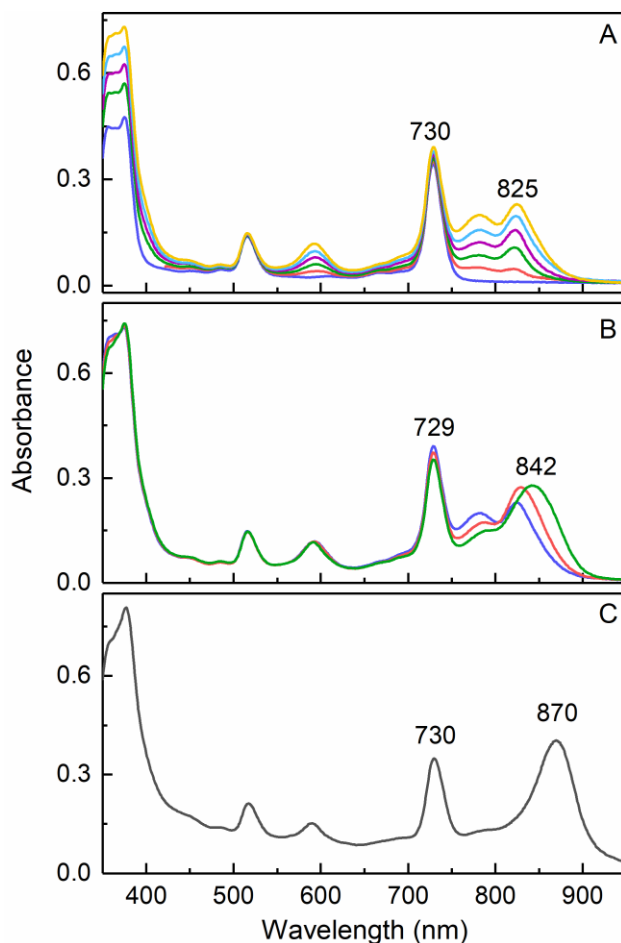
Figure 6. Absorption spectra. (A) Addition of 0 (blue), 5 (red), 10 (green), 15 (mauve), 20 (cyan) and 25 (gold) μL of **BChl *a*** to mixture of α-peptide and **β(+1Cys)BC1** to form the dyad **αβ(+1Cys)BC1**. (B) Dilution to decrease the concentration of OctG from 0.90% (blue) to 0.75% (red) and to 0.64% (green) drives formation of the αβ-dyad and shifts the equilibrium toward the **αβ(+1Cys)BC1$_n$** oligomer (LH1-type complex). (C) Completely formed **αβ(+1Cys)BC1$_n$** oligomer after storage at 4–6 °C for 18 days. Note the extent of bathochromic shift for the Q_y band.

Absorption Spectra

Figure 7 shows absorption spectra of the LH1-type cyclic oligomers **αβ(+1Cys)BC1$_n$**, **αβ(+1Cys)BC1(+4Phe)$_n$**, **αβ(+5Cys)BC1$_n$**, and **αβ(+11Cys)BC1$_n$**. Each spectrum is compared with that of the related peptide–chromophore conjugate (n = 1). The **BC1** constituent of the cyclic oligomers displays a Q_x band at ~515 nm and the Q_y band at ~730 nm. The **BChl *a*** array **B875** of the cyclic oligomers has Q_x absorption at ~595 nm and a pronounced Q_y feature at ~875 nm. Also

seen in oligomers is a feature near 785 nm due to **BChl _a_** that is not incorporated into the αβ-dyad and thence into the oligomeric array. The broad weak absorption near 690 nm is due to a combination of a vibronic satellite of **BC1** and trace oxidation product of **BChl _a_** (a chlorin).
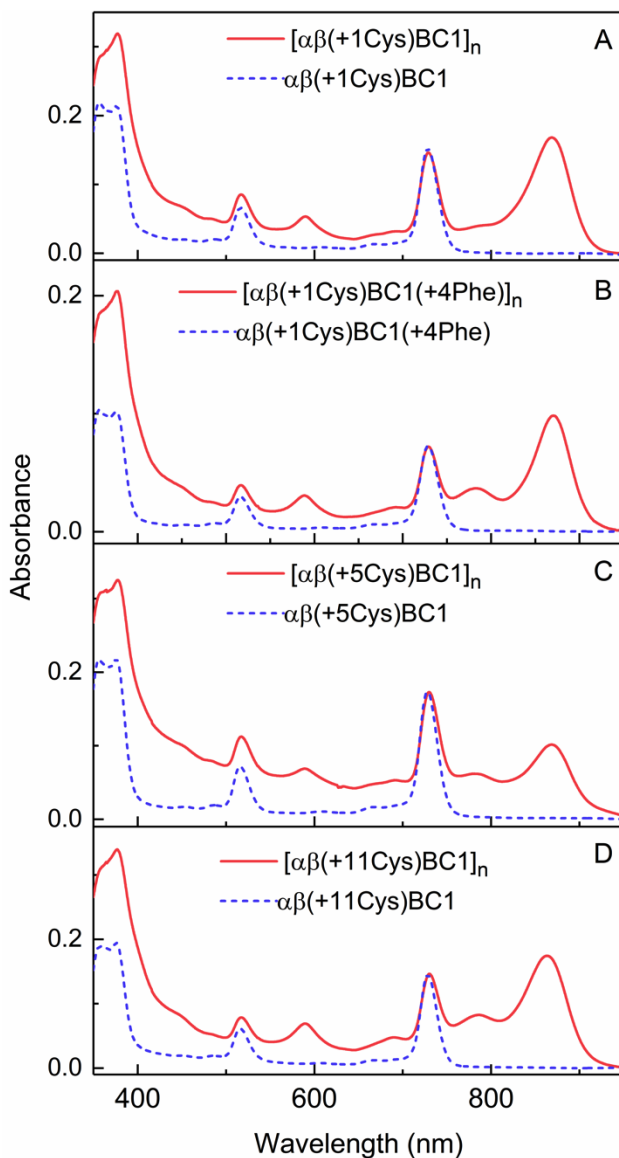
Figure 7. Absorption spectra of the (+) position oligomers and the peptide–**BC1** conjugates.

Fluorescence Spectra

Figure 8 shows the emission spectra for the oligomers that resulted from exciting **BC1** directly in its Q_x band at 516 nm and exciting **B875** directly in its Q_x band at 590 nm. The spectra

were divided by their respective absorbance at the excitation wavelength to facilitate comparisons of relative amplitudes; fluorescence yields are described below. The finding that the **B875** emission band (λ_{max} = 885 nm) is present when exciting **BC1** at 516 nm indicates that energy flows from **BC1*** to **B875**. The emission feature at 730 nm represents some **BC1** emission, and that near 800 nm is due to some free **BChl *a***; the latter must be sufficiently far removed (e.g., in a separate micelle) to not be entirely quenched by energy transfer to **B875**. The minor emission near 690 nm is due to trace **BChl *a*** oxidation product (a chlorin).
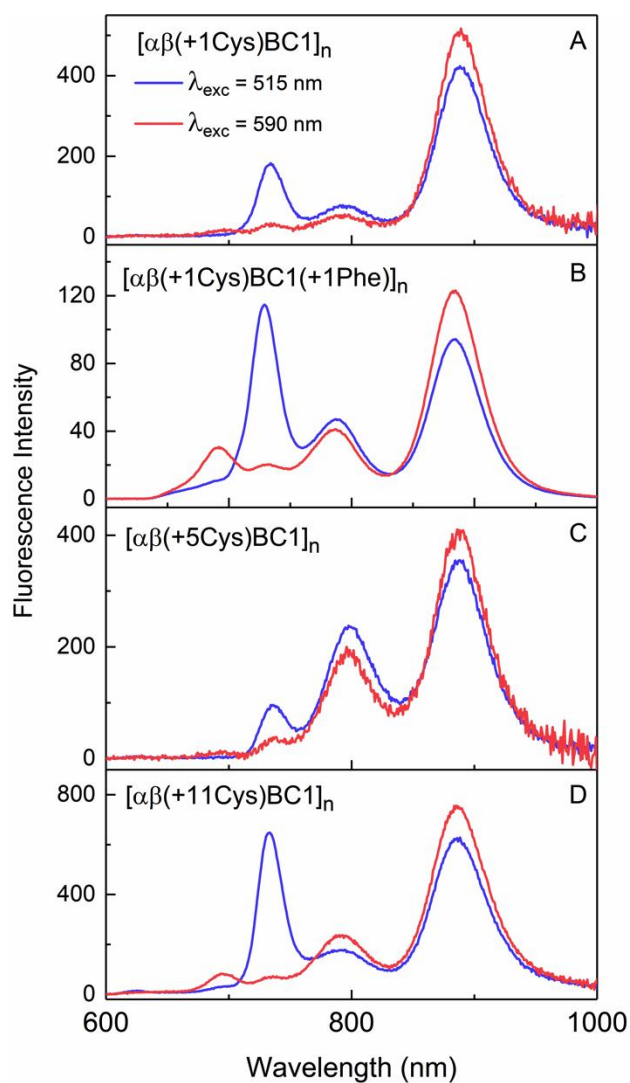
Figure 8. Fluorescence spectra obtained by excitation at 515 nm (blue) and 590 nm (red) for oligomers. The emission intensities were divided by the absorbance at the excitation wavelength.

Energy-Transfer Efficiency

The Φ_{EET} value for energy transfer from **BC1*** to **B875** in the LH1-type oligomers was determined from a series of complementary static and time-resolved measurements. Each measurement has distinct scope and limitations given the nature of the experiment and the composition of the oligomeric assemblies.[14] These studies include the following: (1) comparison of the **B875** fluorescence excitation spectra and absorptance (1 − transmittance) spectra of the oligomeric assembly, (2) the fluorescence yield (Φ_f) of **B875*** using excitation of **BC1** versus **B875** directly, (3) the **BC1*** fluorescence quantum yield in the oligomer versus that in the peptide– **BC1** conjugate (using direct excitation of **BC1**), and (4) the amplitude-weighted (from multiexponential fits) **BC1*** lifetime in the oligomeric assembly compared to that of the peptide– **BC1** conjugate. The various measurements and results are described in the following subsections.

Absorptance vs Fluorescence-Excitation Spectra

For each oligomer, the absorptance (1 − transmittance, 1 − T) spectrum was compared with the excitation spectrum of **B875** fluorescence (Figure 9) when detecting the **B875** emission at 930 nm (on the long-wavelength side of the band; Figure 8) . The absorptance and excitation spectra were normalized at the **B875** Q_x maximum (590 nm). The areas under the Q_x and Q_y features of the absorptance and excitation spectra were compared to determine Φ_{EET}. The average yields are 0.75, 0.67, 0.72, 0.62 for the oligomers with **BC1** attached at the +11, +5, +1, and +1 (with +4Phe) positions, respectively.
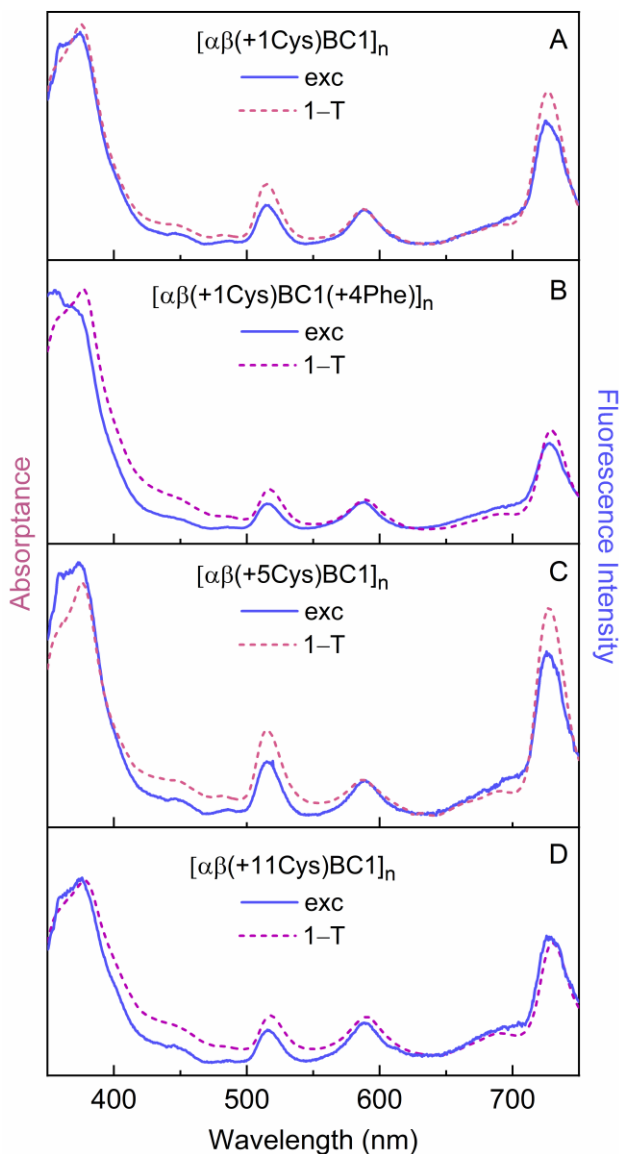
Figure 9. Comparison of absorptance (1−T) (magenta) and fluorescence excitation spectra (black) for oligomers normalized at 590 nm. A small light-scattering correction was applied to the absorptance spectra.

Fluorescence Quantum Yield of B875 Exciting B875 vs BC1

Table 1 lists the fluorescence yields of **BChl** *a* array **B875** obtained upon excitation of **BC1** at 516 nm or of **B875** directly at 590 nm, in the Q_x bands of the respective units. Comparison of these two values allows a measure of Φ_{EET} for transfer of energy from **BC1*** to **B875** (Table 1).

Table 1. B875 photophysical properties in cyclic oligomers.[a]

Oligomer	Φ_f ($\lambda_{516\,nm}^{exc\,BC1}$)	Φ_f ($\lambda_{590\,nm}^{exc\,B875}$)	Φ_{EET}
[αβ(+11Cys)BC1ₙ	0.0029	0.0031	0.94
[αβ(+5Cys)BC1ₙ	0.0065	0.0076	0.86
[αβ(+1Cys)BC1ₙ	0.0068	0.0096	0.71
[αβ(+1Cys)BC1(+4Phe)ₙ	0.0047	0.0058	0.81

[a] Fluorescence yield of **B875** obtained by integrating its emission feature (λ_{max} = 885 nm) using excitation of **BC1** at 516 nm or of **B875** directly at 590 nm. The energy transfer efficiency is obtained from the ratio of the B875 Φ_f exciting **BC1** at 516 nm and **B875** at 590 nm.

Fluorescence Quantum Yield of BC1 in Oligomers vs Conjugates

The emission of **BC1** at 730 nm upon excitation at 516 nm is compared between conjugate and oligomer to determine the amount of energy that is transferred from **BC1*** to **B875** in the oligomer (Figure 10). The emission areas were determined after adjusting for the absorptance at the excitation wavelength. Comparison of each value with that of a fluorescence standard gives the **BC1** fluorescence yields (Table 2). The ratio of the **BC1** fluorescence yield for the **αβ-BC1ₙ** oligomer versus the peptide–**BC1** conjugate (or fluorescence intensities in Figure 10) affords another measure of Φ_{EET} for energy transfer from **BC1*** to **B875** in the oligomer. The results are listed in the rightmost column of Table 2.
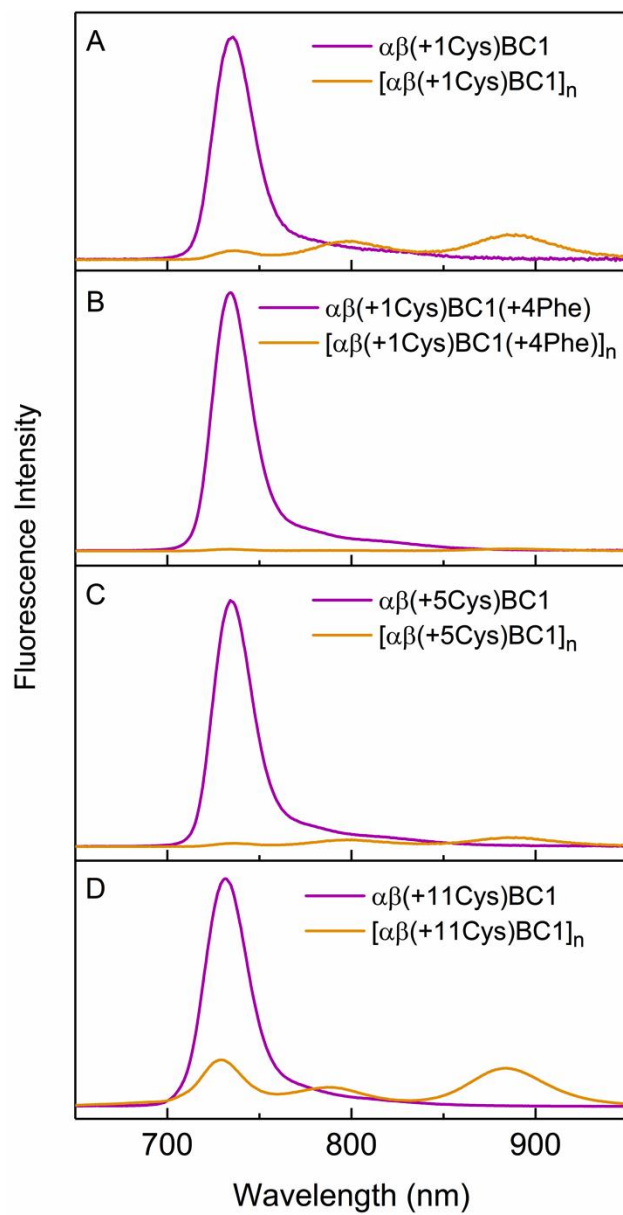
Figure 10. Comparsion of **BC1** fluorescence for peptide–**BC1** conjugate vs oligomer upon excitation at 516 nm and adjusted for absorptance.

Table 2. Fluorescence yields of **BC1** in conjugates and oligomers.[a]

Conjugate	Φ_f conjugate	Oligomer	Φ_f oligomer	Φ_{EET} [b]
β(+11Cys)BC1	0.18	**[αβ(+11Cys)BC1$_n$**	0.0028	0.98
β(+5Cys)BC1	0.083	**[αβ(+5Cys)BC1$_n$**	0.0044	0.95
β(+1Cys)BC1	0.027	**[αβ(+1Cys)BC1$_n$**	0.0016	0.94
β(+1Cys)BC1(+4Phe)	0.022	**[αβ(+1Cys)BC1(+4Phe)$_n$**	0.00022	0.99

[a] λ_{exc} = 530 nm. and λ_{det} = 730 nm. [b] Efficiency of energy transfer from **BC1** to **B875** calculated from the formula $\Phi_{EET} = 1 - \Phi_{f\text{-}O} / \Phi_{f\text{-}C}$, where $\Phi_{f\text{-}O}$ and $\Phi_{f\text{-}C}$ are fluorescence yields of **BC1** of the oligomer and conjugate, respectively.

Fluorescence Decay Profiles for Conjugates

Figure 11 shows **BC1** fluorescence decay traces (and fits) for peptide–chromophore **β(+1Cys)BC**1, **β(+5Cys)BC1**, and **β(+11Cys)BC1** obtained on an apparatus with ~1 ns time resolution. In Panel A, the emission intensity was divided by the sample absorbance at the 530 nm excitation wavelength. Panel B shows the same traces normalized at the maximum intensity to better compare the decay profiles. The caveat with Figure 11A is that given the ~1 ns time response, **BC1*** decay components that decay at earlier times will result in a smaller initial fluorescence amplitude. Therefore the decrease in the initial amplitude in the order **β(+1Cys)BC1** ~ **β(+1Cys)BC1(+4Phe)** > **β(+5Cys)BC1** > **β(+11Cys)BC1** shows that the extent of fast (<0.5 ns undetectable) components to the **BC1*** decay increases in the same order. The amplitude-weighted lifetimes from dual-exponential fits to the data in Figure 11 are as follows: **β(+1Cys)BC1** (2.4 ns), **β(+1Cys)BC1(+4Phe)** (2.1 ns), **β(+5Cys)BC1** (4.0 ns) and **β(+11Cys)BC1** (4.5 ns). These findings are consistent with the relative Φ_f values for these conjugates (Table 2) and the results of the ultrafast transient absorption (TA) measurements, which are described next.
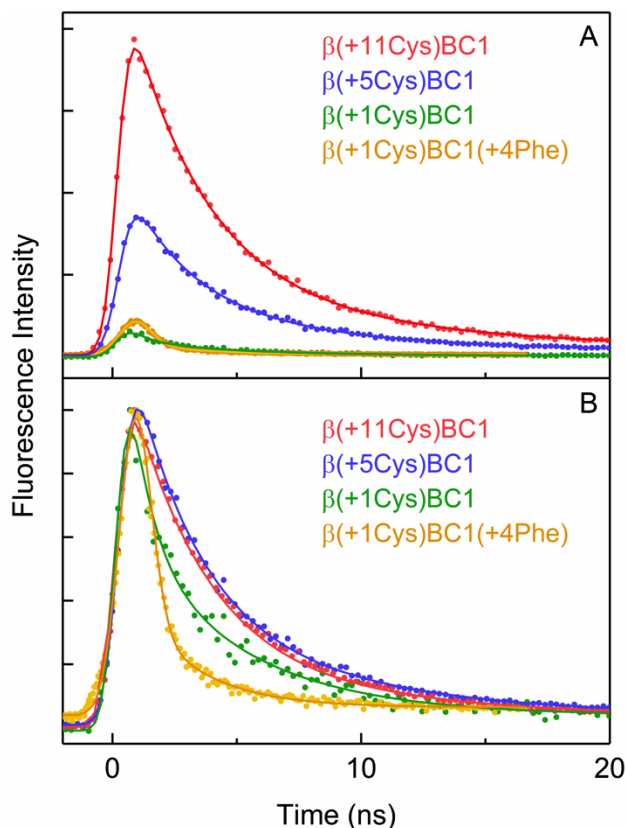
Figure 11. Decay of **BC1** fluorescence at 730 nm for conjugates **β(+1Cys)BC1**, **β(+5Cys)BC1**, and **β(+11Cys)BC1** divided by the absorbance at the 530 nm excitation wavelength (A) or normalized at the initial peak intensity (B).

Transient Absorption Studies

TA data were acquired for the various samples using excitation of **BC1** in its Q_y band at 730 nm. Figure 12 presents data in the 440−680 nm region for peptide–**BC1** conjugate **β(+1Cys)BC1** (panels A−C) and for oligomer **[αβ(+1Cys)BC1$_n$** (panels D−F). Data for the oligomer in the NIR region are presented in Figure 13. Figure 14 shows representative time profiles for **β(+1Cys)BC1** at 480 nm, **[αβ(+1Cys)BC1$_n$** at 480 nm and **[αβ(+1Cys)BC1$_n$** at 890 nm. The time profiles at 480, 520 and 600 nm were fit with a function consisting of three exponentials (plus a constant) convolved with the instrument response. (The time constants derived from the fits at these three wavelengths are in good agreement with those obtained by global fits of the time profiles for the whole data set spanning 440−680 nm). The average of the

amplitude-weighted time constants from the fits of the decay profiles at 480, 520 and 600 nm, which reflect the **BC1*** decay, are given in Table 3. TA data were collected for the other three conjugates and oligomers, which have **BC1** attached at the +5, +11, or +1 (with +4Phe) positions. The spectral shapes are quite similar to those analogous to those shown for conjugate **β(+1Cys)BC1** and oligomer **[αβ(+1Cys)BC1ₙ** in Figures 11−13; the main difference are the time constants for the **BC1*** decay profiles. The amplitude-weighted time constants for **BC1*** decay for those six samples are given in Table 3. The main features of the TA data and the key findings are described next.
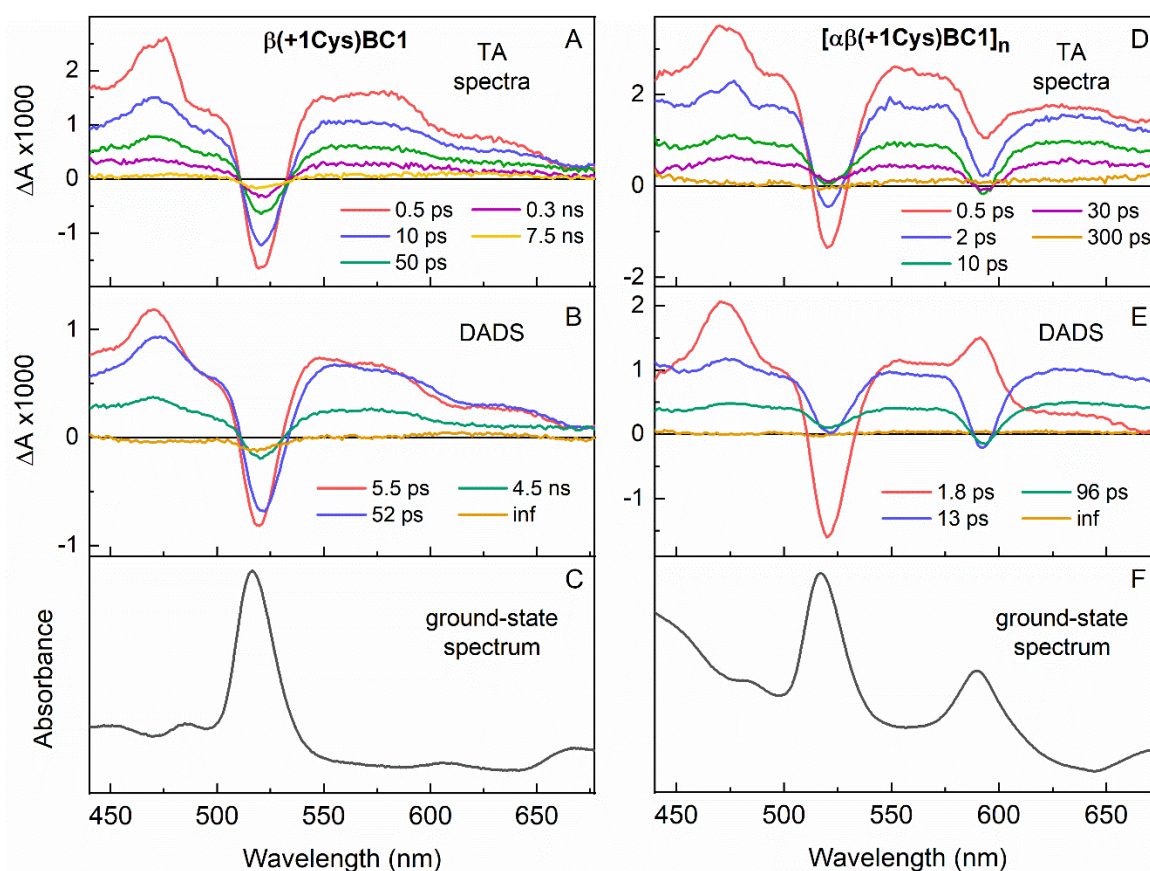
Figure 12. TA difference spectra in the visible region at representative times following excitation with 100 fs flashes at 730 nm (A,C), decay associated difference spectra (DADS) from global analysis (B,E) and ground-state absorption spectra (C,F) for peptide–**BC1** conjugate **β(+1Cys)BC1** (A−C) and oligomer **αβ(+1Cys)BC1ₙ** (D−F).
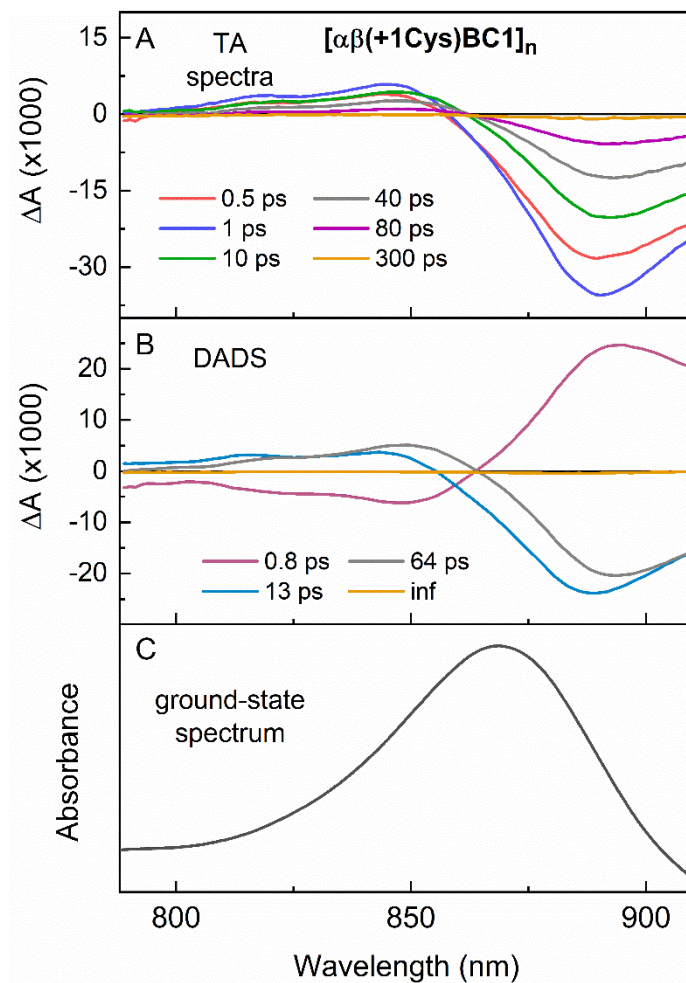
Figure 13. TA difference spectra in the NIR region at representative times following excitation with 100 fs flashes at 730 nm (A), decay associated difference spectra (DADS) from global analysis (B) and ground-state absorption spectrum (C) for oligomer $\alpha\beta(+1Cys)BC1_n$ (D−F).
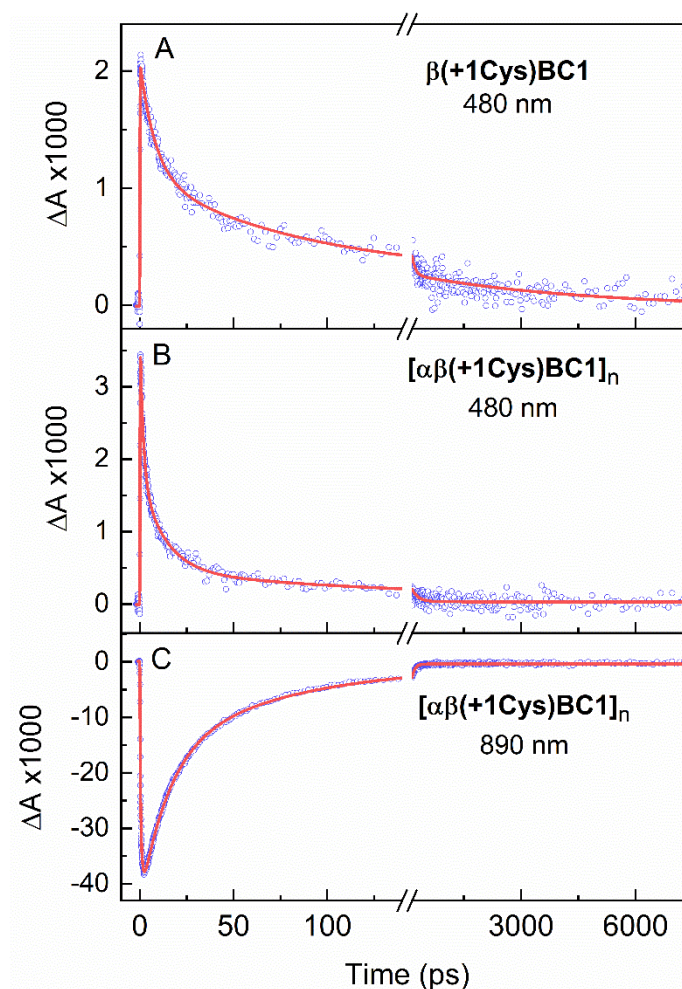
Figure 14. Representative TA time profiles for peptide–**BC1** conjugate β(**+1Cys)BC1** and for oligomer αβ(**+1Cys)BC1ₙ** obtained using 100 fs excitation flashes at 730 nm.

Table 3. Amplitude-weighted **BC1*** lifetimes.[a]

Conjugate	τ_S (ns) conjugate	Oligomer	τ_S (ps) oligomer	Φ_{EET} [b]	$(k_{ET})^{-1}$ (ps)
β(**+11Cys)BC1**	3.0	[αβ(**+11Cys)BC1ₙ**	20	0.99	20
β(**+5Cys)BC1**	1.6	[αβ(**+5Cys)BC1ₙ**	40	0.98	41
β(**+1Cys)BC1**	0.62	[αβ(**+1Cys)BC1ₙ**	20	0.97	21
β(**+1Cys)BC1(+4Phe)**	0.48	[αβ(**+1Cys)BC1(+4Phe)ₙ**	46	0.90	51

[a]Amplitude-weighted **BC1*** lifetime obtained from triple-exponential fits of the TA profiles at 480, 520 and 600 nm. [b]Efficiency of energy transfer from **BC1*** to **B875** calculated from the formula $\Phi_{EET} = 1 - \tau_{Swtd-O} / \tau_{Swtd-C}$, where τ_{Swtd-O} and τ_{Swtd-C} are amplitude-weighted **BC1*** lifetimes of the oligomer and conjugate, respectively.

The TA difference spectra in Figure 12A for conjugate β(+1Cys)BC1, acquired using excitation into the $S_0 \rightarrow S_1$ band of **BC1** (730 nm), are dominated by bleaching of the Q_x ($S_0 \rightarrow S_2$) ground-state absorption of **BC1** at 520 nm, which is shown in Figure 12C. This bleaching rests on a relatively featureless **BC1*** absorption ($S_1 \rightarrow S_n$) spanning the 440–680 nm region displayed. The bleaching and excited-state absorption features have essentially decayed to zero by the 7.5 ns time limit of the measurements. The decay is multi-exponential and was analyzed using a triple-exponential fit with time constants of ~5 ps, ~50 ps and ~4.5 ns, the latter being fixed at the value found in the **BC1*** fluorescence decays, which span a much longer time scale (Figure 11). The profiles of the pre-exponential factors of the decay components, known as decay associated difference spectra (DADS), are given in Figure 12B. A positive feature in the DADS indicates that the time-constant associated with the DADS involves a decay of excited-state absorption or growth of ground-state bleaching at that wavelength; similarly a negative feature represents formation of excited-state absorption or decay of ground-state bleaching. The various DADS β(+1Cys)BC1 resemble each other and the raw data, reflecting the fact that decay components all reflect **BC1*** decay, but with different time constants. Each time constant, and the amplitude-weighted average in Table 3, are much shorter than the lifetime of 3.7 ns found for the excited state of **BC1-mal** in toluene. Given the range of values, a likely contributor involves motions of **BC1** about the linker and thus different distances from the attached peptide backbone and/or different distances from (and quenching by) other peptide–bacteriochlorin conjugates in solution.

The TA data in Figure 12D for oligomer [$\alpha\beta$(+1Cys)BC1$_n$ also show bleaching of the 520 nm Q_x band of **BC1**, along with bleaching of the Q_x band of the **BChl** *a* array **B875**. The amplitude of the former is greater than the latter at 0.5 ps but the ratio reverses as time proceeds. This behavior reflects (1) predominant direct excitation of **BC1** with the 730 nm flashes, (2) some direct

excitation of **B875**, (3) energy transfer from **BC1*** to **B875**, and (4) decay of **BC1*** and **B875***, each of which is multi-exponential with time constants spanning ~1 ps to >100 ps. The DADS in Figure 12E show the expected dip at 520 nm that reflects decay of **BC1** Q_x bleaching (as **BC1*** decays) and a positive-going feature at 590 nm that reflects formation of **B875** Q_x bleaching (as **B875** receives energy from **BC1***). The 13 ps and 96 ps DADS both show dips at 520 nm (decay of **BC1***) and 590 nm (decay of **B875***). The situation is complicated by the facts that the various **BC1*** decay components do not reflect the same yield of energy transfer to **B875**, some components of **BC1*** decay may be unproductive in energy transfer, and some components of **B875** decay may be limited by the lifetime components of **BC1*** decay (for fractions in which **B875*** has a shorter lifetime than **BC1***).

The above points and the fact that energy rapidly flows from **BC1*** to **B875** are reflected in the NIR TA data in Figure 13, which focus on the Q_y region of **B875**. The 0.8 ps DADS in Figure 13B has a positive feature at 890 nm that reflects growth of (1) bleaching of the Q_y band **B875** and (2) **B875*** stimulated emission to longer wavelengths, giving a peak at an average wavelength of 890 nm. Both contributions develop as energy flows from **BC1*** to **B875**. The 1.8 ps time constant of the NIR DADS is comparable to the 0.8 ps value for the visible DADS, reflecting **BC1*** decay. **B875*** in turn decays with 13 and 64 ps components, with an amplitude-weighted value of 35 ps at 890 nm (Figure 14C). This time is much shorter than the **B875*** lifetime of 300–750 ps for native LH1.[28,29] We have discussed such an observation previously concerning oligomers with **BC1** or other bacteriochlorins attached at a variety of positions on the β-peptide.[12,15] The comparison may be due to the difference in interactions among the **BChl** *a* of the reconstituted biohybrid oligomers compared to the native antenna, interactions between rings in the reconstituted systems, exciton annihilation effects, or some combination thereof.

The amplitude-weighted **BC1*** lifetime of 20 ps determined from the fit to the time profiles at 480, 520 and 600 nm for the oligomer $\alpha\beta$(**+1Cys)BC1$_n$** is significantly shorter than the value of 620 ps obtained for the conjugate β(**+1Cys)BC1**. This difference can be seen visually by comparing the traces at 480 nm for the two samples (Figures 14A and 14B). The shorter average **BC1*** lifetime in the oligomer versus the conjugate is due to **BC1* B875** $\rightarrow$ **BC1 B875*** energy transfer in the oligomer. The efficiency of energy transfer obtained from these data is $\Phi_{EET} = 1 -$ 20 ps / 620 ps = 0.97 (Table 3).

The same data sets were acquired and analyzed for the samples in which **BC1** was attached at the +5 and +11 positions, namely $\alpha\beta$(**+5Cys)BC1$_n$** vs β(**+5Cys)BC1** and $\alpha\beta$(**+11Cys)BC1$_n$** vs β(**+11Cys)BC1**. The amplitude-weighted **BC1*** lifetimes are 40 ps vs 1.6 ns for the +5 conjugates and 20 ps vs 3.0 ns for the +11 conjugates, affording Φ_{EET} values of 0.98 and 0.99 (Table 3). The system in which **BC1** was attached at the +1 position along with replacement of +4Tyr with Phe was examined to determine any potential excited-state quenching contribution. The amplitude-weighted **BC1*** lifetimes are 46 ps for $\alpha\beta$(**+1Cys)BC1(+4Phe)$_n$** and 0.48 ns for β(**+1Cys)BC1(+4Phe)** giving a Φ_{EET} of 0.9. Thus, replacement of the native Tyr with Phe at the +4 position does not significantly impact the lifetime or energy-transfer efficiency involving **BC1** attached at the +1 position.

Measured Versus Calculated Energy-Transfer Efficiencies

Static and time-resolved measurements described above were undertaken to obtain the efficiency of energy transfer to **B875** from excited **BC1** attached at the (+) positions toward the *C*-terminus of the β-peptide (Figure 1C). Two of the measurements probe the emission amplitude of the **B875** energy acceptor (versus light absorbed by **B875** directly or by the **BC1** energy donor) and two probe the properties of **BC1** (Φ_f or τ_S) in the presence or absence of **B875**. In principle

all four measurements should give the same energy-transfer efficiency because all fundamentally depend on the decay properties of the **BC1** energy donor, namely the rate constant for energy transfer relative to the sum of the rate constants for all the **BC1*** decay routes. However, each measurement has different sources of error associated with the biohybrid assemblies including trace **BChl** *a* or **BC1** (free or attached to protein) that are not assembled into oligomers; some may bias the result to higher values and vice versa for others, as we have discussed previously.[12,15] The values from the four measurements are collected in Table S1 (Supporting Information). The average values (typically ± 0.14) for the biohybrid oligomers are given in Table 4. The latter table also gives the results from prior measurements for attachment of the same bacteriochlorin at other ($-$) positions (Figure 1C).

Table 4. Measured and calculated Φ_{EET} values for **BC1*** to **B875** in oligomers.

Oligomers	Measured[a]	Förster Theory	Reference
[αβ(+11Cys)BC1$_n$	0.92	0.84–0.98	This study
[αβ(+5Cys)BC1$_n$	0.87	0.82–0.94	This study
[αβ(+1Cys)BC1$_n$	0.84	0.90–0.93	This study
[αβ(+1Cys)BC1(+4Phe)$_n$	0.83	0.90–0.93	This study
[αβ(–2Cys)BC1$_n$	0.80	0.93–0.96	15
[αβ(–6Cys)BC1$_n$	0.85	0.89–0.96	15
[αβ(–10Cys)BC1(–21Cys)$_n$	0.85	0.73–0.96	15
[αβ(–14Cys)BC1$_n$	0.95	0.64–0.93	15
[αβ(–10PGly)(–17Cys)BC1$_n$	0.80	0.50–0.89	15
[αβ(–10Cys)(–21Cys)BC1$_n$	0.50	0.35–0.84	15
[αβ(–34Cys)BC1$_n$	0.60	0.25–0.64	15

[a]Average Φ_{EET} value from the four measurements given in the text and Tables 1 and 3. The measured values and the average for the four *N*-terminal region biohybrid antennas studied here are given in Table S1 of the Supporting Information.

Table 4 also lists the Φ_{EET} value calculated using Förster theory, with the range for each system spanning the estimated closest and farthest approach of **BC1** to the **BChl** *a* array given flexibility of the linker (Figure 1D).[15] Using crystallographic data for native LH2[30,31] (and thus of

the β-peptide) and the structure of the synthetic bacteriochlorin, models of the αβ-dyad with extreme positions of **BC1** via its linker to the Cys site were found, and center-to-center distances (R) between **BC1** and the **BChl *a***-containing dyad were estimated. The ranges of values for the three attachment positions are 29–31 Å (+1), 28–35 Å (+5) and 23–34 Å (+11). As described previously,[15] the R values were input into PhotochemCAD[32] to perform the Förster calculation, $\Phi_{EET} = 1/1+(R/R_0)^6$. The Förster radius R_0 (45 Å; distance for $\Phi_{EET} = 0.5$) was obtained from (1) spectral data and photophysical parameters for **BC1** and **B875** (including the molar absorptivity of the Q_y band of **B875** of 236,000 $M^{-1}cm^{-1}$) to obtain the spectral overlap integral (4.54 x 10^{-13} cm^6mmol^{-1}), (2) the refractive index (n = 1.33) and (3) the orientation factor ($\kappa^2 = 0.667$; dynamically averaged value).[15] The spectral overlap is between the **BC1** fluorescence (Figure 10) and the **B875** absorption (Figure 7), which includes vibronic satellite features which carry significant oscillator strength in proportion to the large **B875** peak extinction coefficient. This extinction coefficient is consistent with an exciton diffusion length of 2–3 bacteriochlorins in the **BChl *a*** array.[15] The results in Table 4 show that at the distances involved, the spectral overlap is sufficient to support rapid and efficient energy transfer, with good agreement between the measured values and those predicted by Förster theory. The calculated maximum and minimum values of Φ_{EET} are compiled in Table 4 for the four new oligomers as well as those studied previously.

Discussion

The development of tailorable antennas requires organization of a large number of chromophores into an architecture of nanoscale or even mesoscale dimensions. The biohybrid approach utilized herein blends designer synthetic chromophores with a scaffold derived from natural photosynthetic systems. A key feature of the biohybrid approach is synthetic modification

122

of the relatively short α- and β-peptides (~50 amino acids in length). A dyad forms from an α- and a β-peptide and two **BChl a** molecules; the dyad then self-associates to give oligomers with a supramolecular LH1-type ring containing roughly 30 **BChl a** molecules (for rings with an average of 14–16 dyad subunits). The two-tiered assembly process affords incorporation of an average of 15 synthetic chromophores (in the case of one attached to each β-peptide) to complement the absorption provided by the ring of native **BChl a** molecules. Thus, the biohybrid approach provides one solution to the challenges of 3-dimensional organization of large numbers of chromophores in a viable light-harvesting system.

In prior studies using this approach, we have (1) found efficient energy transfer from an attached bacteriochlorin (including **BC1** in Figure 1D) at a range of sites (−2, −6, −10, −14, −17, −21, −34) toward the *N*-terminus of the β-peptide from the His (position 0) that coordinates **BChl a** (Figure 1C and Table 4),[12,14,15] (2) attached two **BC1** to two sites per β-peptide to give an average of 30 synthetic chromophores per ring to increase absorptivity,[15] (3) incorporated three different peptide–bacteriochlorin conjugates per ring with different spectral properties to increase solar coverage, making use of a palette of synthetic bacteriochlorins designed for such purposes,[15] (4) demonstrated relay energy transfer using different chromophores and attachment sites to increase the efficiency of energy transfer from distant sites,[14] (5) explored bacteriochlorins with different photophysical and physicochemical properties (hydrophobic, hydrophilic, amphiphilic),[13,24] and (6) demonstrated effective energy transfer from nonattached chromophores to the **BChl a** complex in the LH1-type rings, and enhancement of this process by the attachment of bacteriochlorins with spectral properties complementary to those free in solution.[33]

In all of these prior studies, one or more chromophores was attached at positions (−2, −6, −10, −14, −17, −21, −34) toward the *N*-terminus of the β-peptide. In the present study, we have

extended this approach by incorporating a chromophore at three different positions (+1, +5, +11) toward the *C*-terminus of the β-peptide. We utilized the same bacteriochlorin (**BC1-mal** in Figure 3) that had been explored in prior studies at the seven (−) positions toward the *N*-terminus. The results, summarized in Table 4, show that energy transfer from the **BC1** at the +1, +5 or +11 positions to **B875** has Φ_{EET} values comparable to those found for attachment of **BC1-mal** along the central α-helical region of the β-peptide. The average Φ_{EET} for the 10 sites now explored from one end of the β-peptide to the other is 0.80. Given that **BC1-mal** is relatively hydrophobic, and that the *C*-terminal domain is likely more exposed to the aqueous interface at the detergent belt, the results open the door to further studies making use of hydrophilic and amphiphilic bacteriochlorins that have been prepared as part of this project.[12,24]

The biohybrid antennas studied here, like many biological systems, are not necessarily homogeneous in terms of cofactor-protein characteristics that influence functional properties. For example, at the instant of photoexcitation, there may exist populations of antennas with a range of distances and orientations involving the attached **BC1** and the **BChl *a*** array **B875** due to motions about the flexible linker. Electron microscopy studies suggest that biohybrid oligomers with more than one ring size (and thus the number of αβ-dyad subunits) exist in solution.[14] Ring-size variations could give rise to differing extents of interactions between the subunits and thus altered electronic properties. The combination of such factors no doubt underlies the observed multi-exponential excited-state lifetimes, for both **BC1** and **B875**. The multi-exponentiality of the **BC1*** decay for the biohybrid oligomers may reflect, at least in part, differing rate constants and yields of energy transfer from **BC1*** to **B875**. However, multi-exponential **BC1*** decays are also observed for the peptide–**BC1** conjugates (Figure 13). This means that the static properties, such as fluorescence yields, also represent average values. We have analyzed the multi-exponential

BC1* decays using three exponentials as the minimum number of parameters to obtain good fits of the time profiles spanning picoseconds to several nanoseconds. The resulting amplitude-weighted **BC1*** lifetimes then provide convenient comparisons of excited-state characteristics among the conjugates with attachment of **BC1** at different sites (+1, +5, +11 here) and between the conjugate and oligomer for a given attachment motif, the latter affording one of the four measures from static and time-resolved studies that we employed to obtain Φ_{EET} in the oligomeric antenna.

Although the focus of the studies has been on energy transfer in the biohybrid antennas, the properties of the peptide–**BC1** conjugates were analyzed in detail because these systems represent the necessary benchmarks. Table 5 lists the amplitude-weighted **BC1*** lifetime along with the corresponding **BC1** fluorescence yields, reproduced from Table 2. These values afford the **BC1** natural radiative rate constant via the expression $k_f = \Phi_f / \tau_S$. The results for the four conjugates are given in the last column of Table 5, expressed as the time constant (k_f^{-1}) in units of nanoseconds. The values are in the range 17–23 ns for the four conjugates, being comparable to the value of 22 ns for **BC1** in toluene, 22 ns for analog **BC0** that lacks the maleimide-terminated tether, and 26 ns for **BChl** *a* (Figure 3). These values are generally comparable to the radiative time constants for a host of synthetic bacteriochlorins.[34,35]

Table 5. Excited-state properties of peptide–**BC1** conjugates and benchmarks.[a]

System	τ_{Swtd} [b] (ns)	Φ_f [c]	k_f^{-1} [d] (ns)
Conjugates			
β(+1Cys)BC1	0.62	0.027	23
β(+1Cys) BC 1(+4Phe)	0.48	0.022	22
β(+5Cys)BC1	1.6	0.083	19
β(+11Cys)BC1	3.0	0.18	17
Benchmarks			
BC1-mal in toluene	3.7	0.17	22
BC0 in toluene	4.3	0.20	22
BChl *a* in toluene	3.1	0.12	26

[a]Photophysical properties of the peptide–**BC1** conjugates in buffer (0.9% OctG, 0.05 mM potassium phosphate, pH 7.6) and of bacteriochlorins in buffer or toluene at room temperature. [b]Amplitude-weighted **BC1*** lifetime from Table 3. [c]**BC1*** fluorescence yield from Table 2. [d] **BC1** natural radiative lifetime calculated from the expression $k_f = \Phi_f / \tau_{Swtd}$.

The similarity of the radiative lifetimes for the different conjugates indicates the consistency of the time-resolved and static measurements in spite of the complexity of the systems (e.g., multi-exponential **BC1*** decay profiles). An interesting aspect of these comparisons is that the amplitude-weighted **BC1*** lifetime in the three conjugates that differ only in **BC1** attachment site decreases in the order β(+11Cys)BC1 (3.0 ns) > β(+5Cys)BC1 (1.6 ns) > β(+1Cys)BC1 (0.62 ns). The lifetime for **BC1** changes with attachment position: (1) at the +11 position the lifetime is comparable to that for free **BC1-mal** in toluene (3.7 ns), and (2) with attachment closer to the *C*-terminus of the peptide, the lifetime becomes progressively longer. This finding led us to ask whether there may be specific quenching of **BC1*** by an amino acid residue. The Tyr at the +4 position was a logical target, given the fact that Tyr and Trp residues are known to quench excited dyes.[25] Thus, we prepared the conjugate β(+1Cys)BC1(+4Phe) wherein **BC1** is attached at the +1 position but with +4Tyr replaced by Phe. The amplitude-weighted lifetime of 0.48 ns is comparable to the value of 0.62 ns for β(+1Cys)BC1, indicating that the +4Tyr is not the source

of **BC1*** quenching, at least with **BC1** attached at the +1 position. The lifetime of **BC1*** in the corresponding oligomer $[\alpha\beta(+1Cys)BC1(+4Phe)_n$ is 46 ps, giving $\Phi_{EET} = 0.90$ (Table 3).

The results in Table 5 indicate that the substantial shortening of the **BC1*** lifetime in the conjugate $\beta(+1Cys)BC1$ compared to unattached **BC1-mal** (and to a lesser degree in $\beta(+5Cys)BC1$ and $\beta(+11Cys)BC1$) derives from enhanced non-radiative decay. Possibilities include some electron-transfer quenching, but the most likely source in that regard was removed when +4Tyr was replaced by Phe. Another possibility is interaction of adjacent conjugates and thus adjacent **BC1**s, leading to a form of concentration quenching. Perhaps greater freedom of motion of **BC1** attached at the *C*-terminus (+11 position) does not bring **BC1** as closely into contact with another **BC1** or the peptide. Regardless, the shortening of the **BC1*** lifetime to 0.48–0.62 ns for $\beta(+1Cys)BC1$ and $\beta(+1Cys)BC1(+4Phe)$ does not significantly impact Φ_{EET}, which remains >0.9 in the corresponding oligomers. The high efficiency accrues because energy transfer is sufficiently rapid to outpace other routes of **BC1*** decay (which afford a **BC1*** lifetime much shorter than that of 3.6 ns for nonattached **BC1**).

Conclusions and Outlook

Biohybrid antennas have been constructed starting with four new bacteriochlorin–peptide conjugates $\beta(+1Cys)BC1$, $\beta(+5Cys)BC1$, $\beta(+11Cys)BC1$ and $\beta(+1Cys)BC1(+4Phe)$. The peptide analogs retain their α-helicity regardless of substitution by Cys at a single site as judged by FTIR studies. The conjugates are combined with native *Rb. sphaeroides* α-peptide and **BChl** *a* to first form $\alpha\beta$-dyads and then cyclic $(\alpha\beta)_n$ oligomers in which the outside of the rings are decorated with **BC1**. Neither replacement of the native amino acid at each position with Cys or attachment of **BC1** compromised formation of the biohybrid antennas. Energy transfer from excited **BC1** to the **BChl** *a* array **B875** was measured by four complementary static and time-

resolved optical techniques and was found to have an efficiency of 0.83–0.92. Exploration of these three sites near the *C*-terminus of the β-peptide complements prior studies with chromophore attachment at seven sites toward the *N*-terminus of the peptide. In total, 10 different positions (−34, −21, −17, −14, −10, −6, −2, +1, +5 and +11) along the β-peptide have been utilized for preparation of biohybrid antenna systems with an average Φ_{EET} of 80%. The examination of sites along the β-peptide, including the more flexible and hydrophilic terminal regions and the central α-helical and more hydrophobic regions allows potential incorporation of chromophores with hydrophobic, hydrophilic or amphiphilic character and complementary spectral properties for the preparation of biohybrid antennas. These studies further exemplify the versatility of the biohybrid approach for incorporating larger numbers of chromophores in antenna systems that combine native and tailorable synthetic constituents.

Experimental Section

BC0 and **BC1-mal** were prepared according to literature procedure.[13] Native LH1 α- and β-peptides were isolated from an *Rb. sphaeroides* LH2-less mutant, *puc*705BA, as previously described.[14] *n*-Octyl β-D-glucopyranoside (octG) was used as received from Sigma. **BChl** *a* with a phytol esterifying alcohol was purchased from Sigma-Aldrich.

Four synthetic peptides (Bio-Synthesis, Lewisville, TX) were used in these studies. Each of the peptides **β(+1Cys)**, **β(+5Cys)** and **β(+1Cys)(+4Phe)** contains 48 amino acids with a sequence identical to that of the β-peptide of LH1 of *Rb. sphaeroides* except for the substitution of a Cys in place of either Leu +1, Ile +5, or Leu +1, respectively. The latter also has a Phe in place of Tyr. The peptide **β(+11Cys)** contains 49 amino acids with a sequence identical to that of the β-peptide of LH1 of *Rb. sphaeroides* except for addition of a Cys residue at the *C*-terminus (denoted as +11). The sequences of the peptides are as follows:

β(Cys+1): ADKSDLGYTGLTDEQAQELHSVYMSGLWLFSAVAIVAH^0C^1AVYIWRPWF

β(Cys+5): ADKSDLGYTGLTDEQAQELHSVYMSGLWLFSAVAIVAH^0LAVYC^5WRPWF

β(Cys+1)(+4Phe): ADKSDLGYTGLTDEQAQELHSVYMSGLWLFSAVAIVAH^0C^1AVF^4IWRPWF

β(+11Cys): ADKSDLGYTGLTDEQAQELHSVYMSGLWLFSAVAIVAH^0LAVYIWRPWFC^{11}

In these sequences, the His residue, to which **BChl *a*** is coordinated, is position 0, and the residues substituted (or added) with Cys are designated by emboldened font and their corresponding positions are superscripted. Purity was >87%, >98%, >91% and >97% for **β(+1Cys)**, **β(+5Cys),** **β(+11Cys)**, and **β(+1Cys)(+4Phe)**, respectively, according to HPLC data (from the company). Each peptide gave the expected peak upon mass spectrometry (see Supporting Information). FTIR studies of the peptides and static and time-resolved optical studies on the conjugates and oligomers (in 0.9% octG, 0.05 mM potassium phosphate, pH 7.6) were performed as described previously.[13]

Acknowledgments

References

1   C. N. Hunter, R. van Grondelle, J. D. Olsen, *Trends Biochem. Sci.* **1989**, *14*, 72–76.

2   R. E. Blankenship, D. M. Tiede, J. Barber, G. W. Brudvig, G. Fleming, M. Ghirardi, M. R. Gunner, W. Junge, D. M. Kramer, A. Melis, T. A. Moore, C. C. Moser, D. G. Nocera, A. J. Nozik, D. R. Ort, W. W. Parson, R. C. Prince, R. T. Sayre, *Science* **2011**, *332*, 805–809.

3   D. Gust, T. A. Moore, A. L. Moore, *Acc. Chem. Res.* **2001**, *34*, 40–48.

4   B. R. Green, J. M. Anderson, W. W. Parson in *Light-Harvesting Antennas in Photosynthesis* (Eds.: B. R. Green, W. W. Parson), Kluwer Academic Publishers, Dordrecht, The Netherlands, **2003**, pp. 1–28.

5   R. E. Blankenship in *Molecular Mechanisms of Photosynthesis*, Blackwell Science, Oxford, **2002**, pp. 61–67.

6   D. Buczynska, Ł. Bujak, M. A. Loi, T. H. P. Brotosudarmo, R. Cogdell, S. Mackowski, *Appl. Phys. Lett.* **2012**, *101*, 173703(1–4).

7   D. Holten, D. F. Bocian, J. S. Lindsey, *Acc. Chem. Res.* **2002**, *35*, 57–69.

8   P. D. Harvey in *The Porphyrin Handbook* (Eds.: K. M. Kadish, K. M. Smith, R. Guilard), Academic Press, San Diego, CA, **2003**, Vol. 18, pp. 63–250.

9   N. Aratani, A. Osuka in *Handbook of Porphyrin Science* (Eds.: K. M. Kadish, K. M. Smith, R. Guilard), World Scientific Publishing Co., Singapore, Vol. 1, **2010**, pp. 1–132.

10   Z. S. Yoon, J. Yang, H. Yoo, S. Cho, D. Kim, in *Handbook of Porphyrin Science* (Eds.: K. M. Kadish, K. M. Smith, R. Guilard), World Scientific Publishing Co., Singapore, Vol. 1, **2010**, pp. 439–505.

11   P. D. Harvey, C. Stern, R. Guilard in *Handbook of Porphyrin Science* (Eds.: K. M. Kadish, K. M. Smith, R. Guilard), World Scientific Publishing Co., Singapore, Vol. 11, **2011**, pp. 1–179.

12   J. W. Springer, P. S. Parkes-Loach, K. R. Reddy, M. Krayer, J. Jiao, G. M. Lee, D. M. Niedzwiedzki, M. A. Harris, C. Kirmaier, D. F. Bocian, J. S. Lindsey, D. Holten, P. A. Loach, *J. Am. Chem. Soc.* **2012**, *134*, 4589–4599.

13   K. R. Reddy, J. Jiang, M. Krayer, M. A. Harris, J. W. Springer, E. Yang, J. Jiao, D. M. Niedzwiedzki, D. Pandithavidana, P. S. Parkes-Loach, C. Kirmaier, P. A. Loach, D. F. Bocian, D. Holten, J. S. Lindsey, *Chem. Sci.* **2013**, *4*, 2036–2053.

14   M. A. Harris, P. S. Parkes-Loach, J. W. Springer, J. Jiang, E. C. Martin, P. Qian, J. Jiao, D. M. Niedzwiedzki, C. Kirmaier, J. D. Olsen, D. F. Bocian, D. Holten, C. N. Hunter, J. S. Lindsey, P. A. Loach, *Chem. Sci.* **2013**, *4*, 3924–3933.

15   M. A. Harris, J. Jiang, D. M. Niedzwiedzki, J. Jiao, M. Taniguchi, C. Kirmaier, P. A. Loach, D. F. Bocian, J. S. Lindsey, D. Holten, P. S. Parkes-Loach, *Photosynth. Res.* **2014**, *121*, 35–48.

16   M. Gabrielsen, A. T. Gardiner, R. J. Cogdell in *The Purple Phototrophic Bacteria* (Eds.: C. N. Hunter, F. Daldal, M. C. Thurnauer, J. T. Beatty), Springer, Dordrecht, The Netherlands, **2009**, pp. 135–153.

17   P. A. Loach, P. S. Parkes-Loach in *The Purple Phototrophic Bacteria* (Eds.: C. N. Hunter, F. Daldal, M. C. Thurnauer, J. T. Beatty), Springer, Dordrecht, The Netherlands, **2009**, pp. 181–198.

18   X. Hu, K. Schulten, *Biophys. J.* **1998**, *75*, 683–694.

19   A. W. Roszak, T. D. Howard, J. Southall, A. T. Gardiner, C. J. Law, N. W. Isaacs, R. J. Cogdell, *Science* **2003**, *302*, 1969–1972.

20   P. Qian, C. N. Hunter, P. A. Bullough, *J. Mol. Biol.* **2005**, *349*, 948–960.

21   M. K. Şener, K. Schulten in *The Purple Phototrophic Bacteria* (Eds.: C. N. Hunter, F. Daldal, M. C. Thurnauer, J. T. Beatty), **2009**, pp. 275–294.

22   J. Koepke, X. C. Hu, C. Muenke, K. Schulten, H. Michel, *Structure* **1996**, *4*, 581–597.

22   P. Qian, M. Z. Papiz, P. J. Jackson, A. A. Brindley, I. W. Ng, J. D. Olsen, M. J. Dickman, P. A. Bullough, C. N. Hunter, *Biochemistry USA* **2013**, *52*, 7575–7585.

23   J. Kyte, R. F. Doolittle, *J. Mol. Biol.* **1982**, *157*, 105–132.

24   J. Jiang, K. R. Reddy, M. P. Pavan, E. Lubian, M. A. Harris, J. Jiao, D. M. Niedzwiedzki, C. Kirmaier, P. S. Parkes-Loach, P. A. Loach, D. F. Bocian, D. Holten, J. S. Lindsey, *Photosynth. Res.* **2014**, *122*, 187–202.

25   N. Marmé, J.-P. Knemeyer, M. Sauer, J. Wolfrum, *Bioconjugate Chem.* **2003**, *14*, 1133–1139.

26   Z.-Y. Wang, M. Shimonaga, Y. Muraoka, M. Kobayashi, T. Nozawa, *Eur. J. Biochem.* **2001**, *268*, 3375–3382.

27   J. Holzmann, A. Hausberger, A. Rupprechter, H. Toll, *Anal. Bioanal. Chem.* **2013**, *405*, 6667–6674.

28   C. N. Hunter, H. Bergström, R. van Grondelle, V. Sundström, *Biochemistry USA* **1990**, *29*, 3203–3207.

29   A. Freiberg, J. P. Allen, J. C. Williams, N. W. Woodbury, *Photosyn. Res.* **1996**, *48*, 309–319.

30   G. McDermott, S. M. Prince, A. A. Freer, A. M. Hawthornthwaite-Lawless, M. Z. Papiz, R. J. Cogdell, N. W. Isaacs, *Nature* **1995**, *374*, 517–521.

31   M. Z. Papiz, S. M. Prince, T. Howard, R. J. Cogdell, N. W. Isaacs, *J. Mol. Biol.* **2003**, *326*, 1523–1538.

32   H. Du, R.-C. A. Fuh, J. Li, L. A. Corkan, J. S. Lindsey, *Photochem. Photobiol.* **1998**, *68*, 141–142.

33   M. A. Harris, T. Sahin, J. Jiang, P. Vairaprakash, P. S. Parkes-Loach, D. M. Niedzwiedzki, C. Kirmaier, P. A. Loach, D. F. Bocian, D. Holten, J. S. Lindsey, *Photochem. Photobiol.* **2014**, *90*, 1264–1276.

34   E. Yang, C. Kirmaier, M. Krayer, M. Taniguchi, H.-J. Kim, J. R. Diers, D. F. Bocian, J. S. Lindsey, D. Holten, *J. Phys. Chem. B* **2011**, *115*, 10801–10816.

35   P. Vairaprakash, E. Yang, T. Sahin, M. Taniguchi, M. Krayer, J. R. Diers, A. Wang, D. M. Niedzwiedzki, C. Kirmaier, J. S. Lindsey, D. F. Bocian, D. Holten, *J. Phys. Chem. B* **2015**, *119*, 4382–4395.

Chapter 5

Synthesis and Photophysical Characterization of Bacteriochlorins Equipped with Integral Swallowtail Substituents

Y Liu, S Allu, M Reddy, D Hood, J Diers, D Bocian, D Holten and J Lindsey. Synthesis and Photophysical Characterization of Bacteriochlorins Equipped with Integral Swallowtail Substituents. Reproduced from *New J. Chem.,* 2017, 41, 4360—4376 with permission from the Centre National de la Recherche Scientifique (CNRS) and the Royal Society of Chemistry.

ABSTRACT

Bacteriochlorins such as bacteriochlorophyll *a* absorb strongly in the near-infrared spectral region and are potentially useful in a variety of photochemical fields. *De novo* syntheses of bacteriochlorins entail self-condensation of a dihydrodipyrrin–acetal (containing one pyrrole and one pyrroline joined via a methylidene bridge) either via a largely studied Eastern-Western (E-W) route or a recently reported Northern-Southern (N-S) route. The Michael addition to form the dihydrodipyrrin–acetal for the E-W approach has limited scope for the installation of substituents on the pyrroline units. By use of the N-S route, new bacteriochlorins have been prepared that bear symmetrically branched alkyl or aryl groups, termed "swallowtail" substituents, at the □-pyrroline units, a previously inaccessible design. Single-crystal X-ray structures of three intermediates were determined. Bacteriochlorins synthesized herein exhibit characteristic bacteriochlorophyll-like absorption spectra, including a Q_y band in the region of 730–758 nm. The swallowtail groups have little impact on the excited-state properties of the bacteriochlorins, and the slight changes of spectral properties that are observed stem from substituent electronic effects rather than changes in structure. In summary, introduction of an integral swallowtail unit on the pyrroline ring opens new sites for manipulation without altering the attractive photophysical features of the synthetic bacteriochlorins.

INTRODUCTION

Bacteriochlorins are the chromophoric cores of bacteriochlorophylls, the chief pigments of anoxygenic bacterial photosynthesis.[1] The characteristic strong absorption of bacteriochlorins in the near-infrared (NIR) spectral region[2] (Q_y band, 700–900 nm) offers diverse photochemical opportunities. Many studies require bacteriochlorins tailored with respect to the position of the absorption/emission wavelengths, polarity ranging from lipophilic to hydrophilic, and features for bioconjugation. Routes to bacteriochlorins include semisynthesis from bacteriochorophylls,[3,4] reduction or cycloaddition of porphyrins,[5,6] and *de novo* syntheses. Four *de novo* syntheses have been developed: (1) the Kishi route[7-11] to tolyporphin A diacetate, a derivative of an architecturally complex natural bacteriochlorin; (2) an Eastern-Western (E-W) self-condensation of dihydrodipyrrin–acetals to form non-natural bacteriochlorins;[12] (3) a Northern-Southern (N-S) self-condensation of dihydrodipyrrin–acetals to form non-natural bacteriochlorins;[13] and (4) a directed route to form non-natural bacterio-13^1-oxophorbines.[14] In all four synthetic routes, each pyrroline ring contains a gem-dialkyl group versus the *trans*-dialkyl configuration in bacteriochlorophyll *a* (Chart 1); the gem-dialkyl group stabilizes the chromophore toward aerobic environments by blocking adventitious dehydrogenation that would lead to the chlorin and porphyrin.
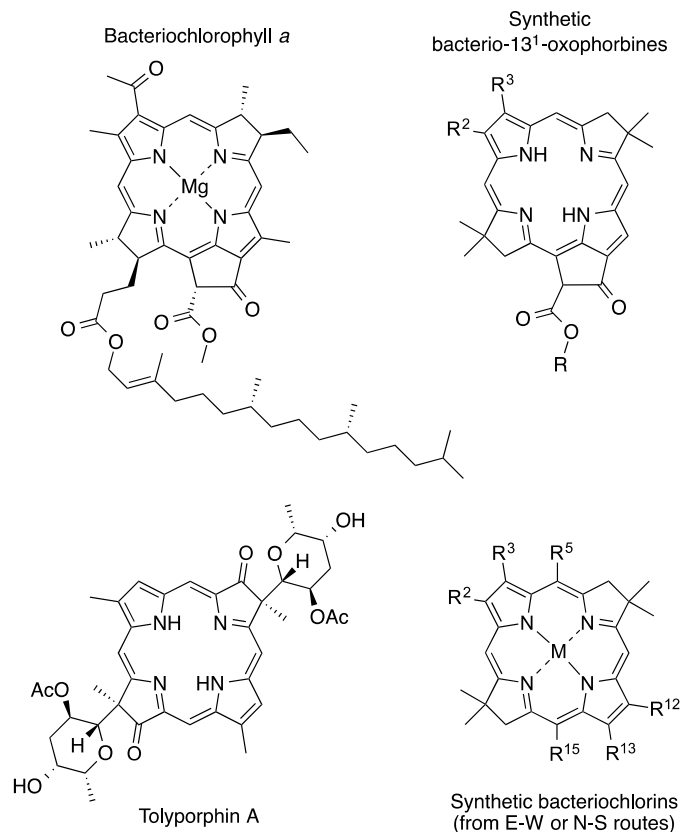
Chart 1. Bacteriochlorophyll *a*, tolyporphin A, and synthetic macrocycles.

The E-W route has been developed and exploited over the past decade to prepare bacteriochlorins tailored with diverse substituents at the β-pyrrole and meso-positions,[12,15-21] whereas the N-S and directed routes were only reported in the past year. Regardless, the functionalization of β-pyrroline units has been far less explored owing to synthetic difficulties. Indeed, the gem-dimethyl unit has been employed as the stabilizing group in the pyrroline ring (with only one exception[22]) in the E-W, N-S, and directed route. Tolyporphins − naturally occurring dioxobacteriochlorins that contain a *C*-glycoside in each pyrroline unit - have been the object of total synthesis. The route reported by Wang and Kishi was lengthy (>20 steps) and in the only instantiation afforded a tiny amount (0.38 mg) of tolyporphin A diacetate, a derivative of the natural tolyporphin A.[11] Substituents in the pyrroline ring project above and below the plane

134

of the macrocycle, and manipulation of such substituents in hydroporphyrins represent an opportunity to address a longstanding problem in the tetrapyrrole field – accessing 3-dimensional designs with a 2-dimensional (i.e., planar) macrocycle. The problem has largely been addressed with *porphyrins* rather than hydroporphyrins. Designs dating to the 1970s with iron porphyrins were aimed at creating a sterically protected pocket for binding of O_2 to suppress μ-oxo dimer formation, thereby mimicking hemoglobins and myoglobins.[23] From these objectives emerged the "picket-fence porphyrins" built around the atropisomeric *meso*-tetrakis(*o*-aminophenyl)porphyrins (Chart 2, top), wherein the amino groups project above and/or below the plane of the macrocycle.[24] Numerous designs for creation of steric bulk in the *z*-direction relative to the *xy*-plane of the macrocycle have emerged since then, chiefly for porphyrins,[25] but more recently for chlorins[26,27] and bacteriochlorins.[28,29]
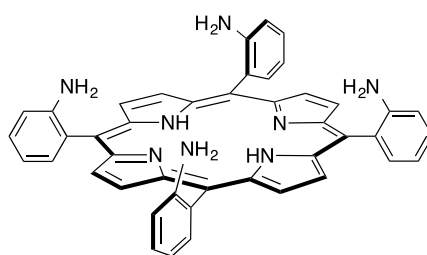
meso-tetrakis(*o*-aminophenyl)porphyrin
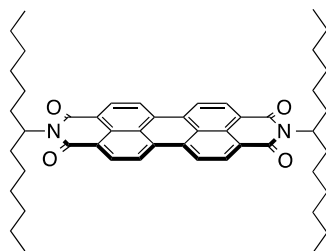
swallowtail perylene-diimide

Chart 2. Picket-fence porphyrin (top) and swallowtail perylene derivative (bottom).

Among possible geminal substituents in the pyrroline ring, we are especially interested in integrating aryl or longer alkyl groups, which can be regarded as "swallowtail" groups. The use

of alkyl swallowtail groups with organic chromophores was pioneered by Langhals and coworkers[30-34] in the synthesis of perylene–imides; enhanced solubility[35] was reported compared to simple (non-swallowtail) aryl or alkyl groups (Chart 2, bottom).

Swallowtail porphyrin (water-soluble, bioconjugatable)

A

Swallowtail chlorin (water-soluble)

B

Swallowtail bacteriochlorin (lipophilic)

C

Chlorin with integral spirohexyl motif

D

Bacteriochlorin with integral spiro-piperidine motifs

E
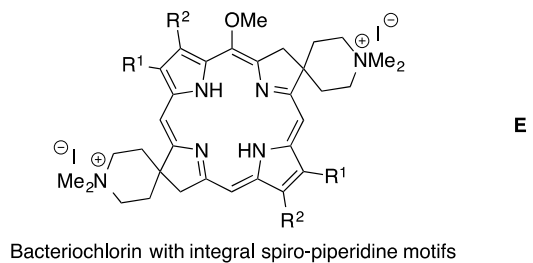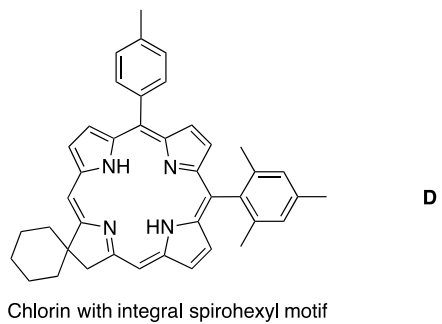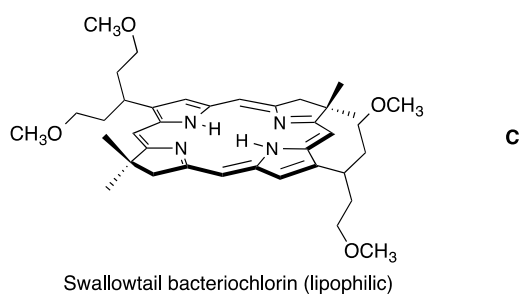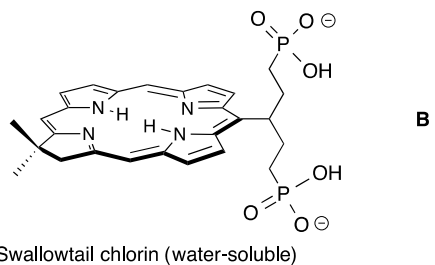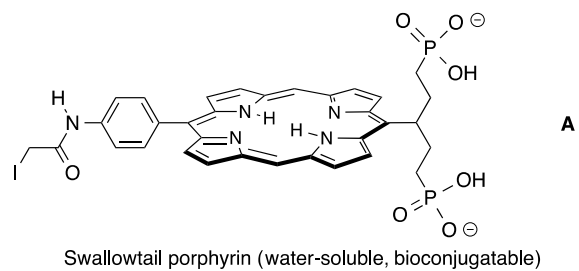
Chart 3. Swallowtail tetrapyrroles (top) and spirohexyl analogues (bottom).

We have previously prepared a number of tetrapyrrole macrocycles containing *appended* – not integrated – swallowtail substituents for photophysical studies[36] or photomedical applications. Molecules for photomedicine include hydrophilic, wavelength-tunable, bioconjugatable porphyrins[37-39] (e.g., **A**), a swallowtail-containing hydrophilic chlorin[26] (**B**), and a β-pyrrole-substituted swallowtail–bacteriochlorin[28] (**C**) (Chart 3, top). A number of other symmetrically branched alkyl groups have been appended at porphyrin meso-positions.[40] The attachment of swallowtail units at the bacteriochlorin β-pyrrole positions blocked one of the key sites typically employed to tune the location of the long-wavelength absorption band. The only cases where substituents other than the gem-dimethyl groups have been employed include a lipophilic chlorin with a spirohexyl motif[41] (**D**) and a bacteriochlorin with 4-aza-spirohexyl (a piperidine-like) motifs[22] (**E**) (Chart 3, bottom). Molecular designs other than the spirohexyl groups either were not explored (chlorins) or were not accessible (bacteriochlorins).

Herein, we describe the integration of swallowtail alkyl and aryl groups on the β-pyrroline units of bacteriochlorins. The synthesis makes use of a recent advance in methodology for construction of the dihydrodipyrrin–acetals. One resulting synthesis afforded a bacteriochlorin bearing 2-benzoxyethyl groups as swallowtail substituents, which upon deprotection has given a bacteriochlorin bearing 2-hydroxyethoxy groups. A second synthesis has afforded two bacteriochlorins each bearing pairs phenyl groups as swallowtail substituents and the presence or absence of a 10-methoxy group. The four bacteriochlorins have been characterized by static and time-resolved optical spectroscopy, along with molecular orbital calculations to address spectral shifts observed with the aryl swallowtail motifs. Two analogues prepared recently using the N-S route were also photophysically characterized for comparison with the properties of the swallowtail bacteriochlorins.

RESULTS AND DISCUSSION

Reconnaissance. The challenge to elaborate the β-pyrroline rings of bacteriochlorins (**I**) via the E-W synthesis resides in the Michael addition in the preparation of the 3,3-disubstituted dihydrodipyrrin (**II**) (Scheme 1, left). The Michael addition relies on reaction of a 2-(2-nitroethyl)pyrrole (**III**) and an α,β-unsaturated ketone (**IV**). With various Michael acceptors (**IV**) examined, only the substituents L = Me or L, L = spirohexyl[41] or spiro-piperidine[22] (poor yield) gave a successful reaction. The failure where L is a long-chain alkyl unit – a highly sought design – may stem in part from base-mediated isomerization of the Michael acceptor in the presence of the carbon nucleophile **III**.[22]
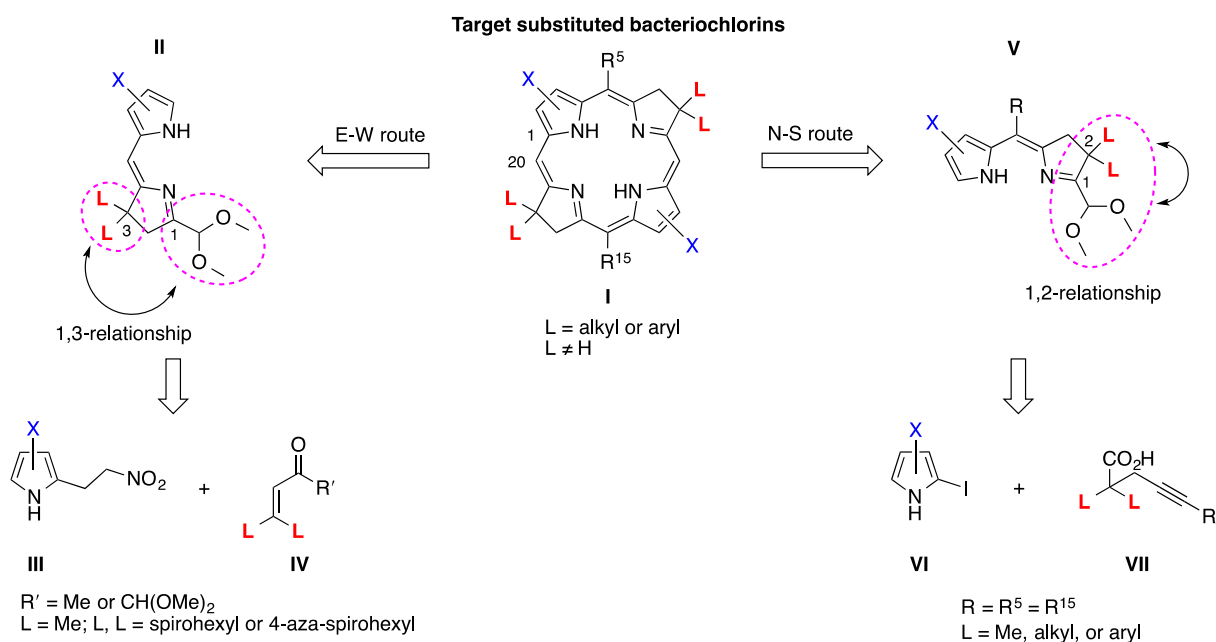
Scheme 1. Retrosynthetic scheme for the target bacteriochlorins.

The new N-S route to synthetic bacteriochlorins[13] complements the existing E-W route in the means by which the dihydrodipyrrin–acetals are prepared. The dihydrodipyrrin–acetal precursor (**V**) in the N-S route, which is 2,2-disubstituted versus 3,3-disubstituted dihydrodipyrrin in the E-W route, is prepared via methodology developed by Jacobi:[42-52] a Pd-catalyzed coupling of an iodopyrrole (**VI**) and a substituted pentynoic acid (**VII**) is followed by Petasis reagent treatment, acid-catalyzed hydrolysis and Paal-Knorr-like ring closure (Scheme 1, right). This route to the N-S dihydrodipyrrin–acetals sidesteps the problematic Michael addition in the synthesis of E-W dihydrodipyrrin–acetals. On the other hand, the substituted pentynoic acid in the N-S route provides the swallowtail units. The swallowtail units must survive the conditions along the N-S route[13] to dihydrodipyrrin–acetals and bacteriochlorins, which include treatment with a strong base, metal reagents (Pd catalyst and Petasis reagent), SeO_2, and a Lewis acid. Our initial designs focused on swallowtails composed of two- or three-carbon alkyl chains with various terminal functional groups (amino, hydroxy) in protected form (see Section I of the Supplementary Information). The alkylations (chiefly of *tert*-butyl acetate) leading to the required quaternary carbon encountered substantial problems. Successful alkylation was ultimately achieved of acetonitrile in THF containing a large quantity of HMPA; the reaction was carried out with 2-(benzoxy)ethyl iodide, and we did not return to examine any prior substrates or alkyl entities under these conditions.

Synthesis of bacteriochlorins bearing open-chain alkyl groups as swallowtail units. Acetonitrile was subjected to alkylation in THF/HMPA (2:1) at –78 °C. The alkylating agent ((2-iodoethoxy)methyl)benzene was employed in two portions followed by 1-bromo-2-butyne to obtain nitrile **1** in 46% yield. The direct hydrolysis of nitrile **1** to carboxylic acid **3a** was not successful. Nitrile **1** was converted to aldehyde **2** by treatment with DIBAL-H, whereupon

oxidation with Jones reagent gave the desired **3a** (Scheme 2). The palladium-coupling reaction of alkynoic acid **3a** and iodopyrrole **4** gave the anticipated lactone–pyrrole **5a** in 52% yield. The structure of **5a** (including the expected *E* configuration)[13,46,47] was confirmed by single-crystal X-ray analysis (Figure 1).
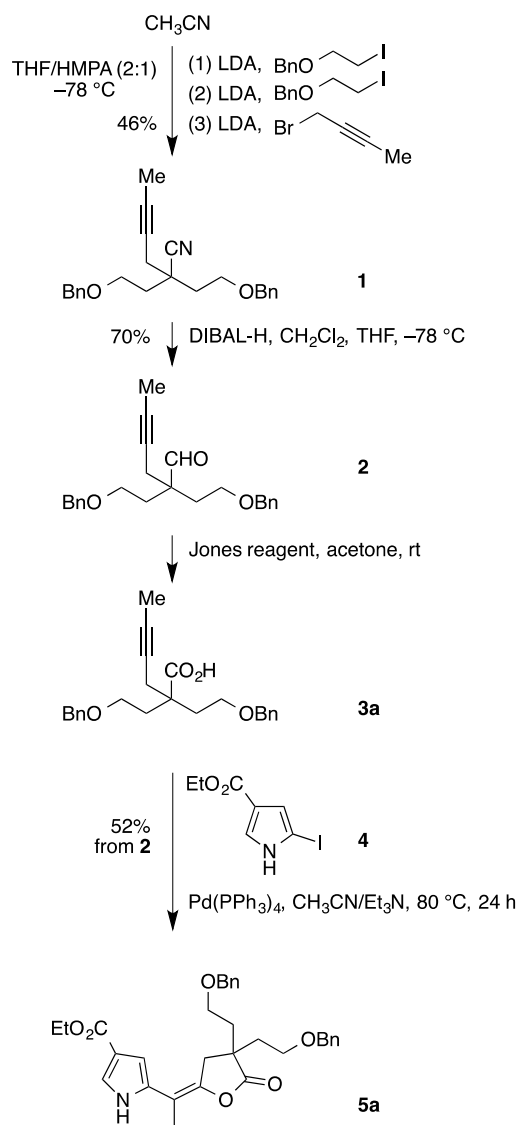
Scheme 2. Synthesis of swallowtail bacteriochlorin precursor.

141
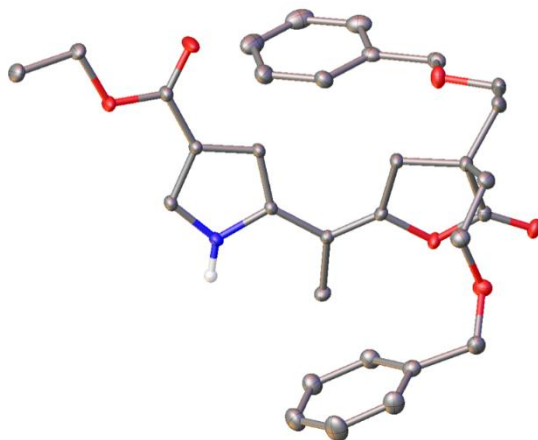
Figure 1. ORTEP diagram of lactone–pyrrole **5a** showing the *E* configuration. Ellipsoids are at the 50% probability level, and hydrogen atoms (except N–H) are omitted for clarity.

Treatment of **5a** with the Petasis reagent afforded **6a** in 55% yield. Hydrolysis of **6a** and subsequent Paal-Knorr-like ring closure gave 1-methyldihydrodipyrrin **7a** as a mixture of *Z* (50%) and *E* (30%) isomers. The two isomers were readily separated by column chromatography. In prior studies with substrates containing gem-dimethyl groups, the *Z*-isomer was generally formed exclusively, an outcome attributed to the existence of the NH–N intramolecular hydrogen bond.[13,47] In this case, prolonged reaction (24 h) and higher temperature (80 °C) also gave the *Z*-isomer exclusively. However, no increase in yield was observed, perhaps due to parallel decomposition of the dihydrodipyrrin isomers. Treatment of **7a-Z** with SeO$_2$ followed by trimethyl orthoformate[13,22] gave the corresponding dihydrodipyrrin–acetal **8a-Z** (57%). Similar treatment of **7a-E**, however, gave both **8a-Z** (51%) and **8a-E** (12%).
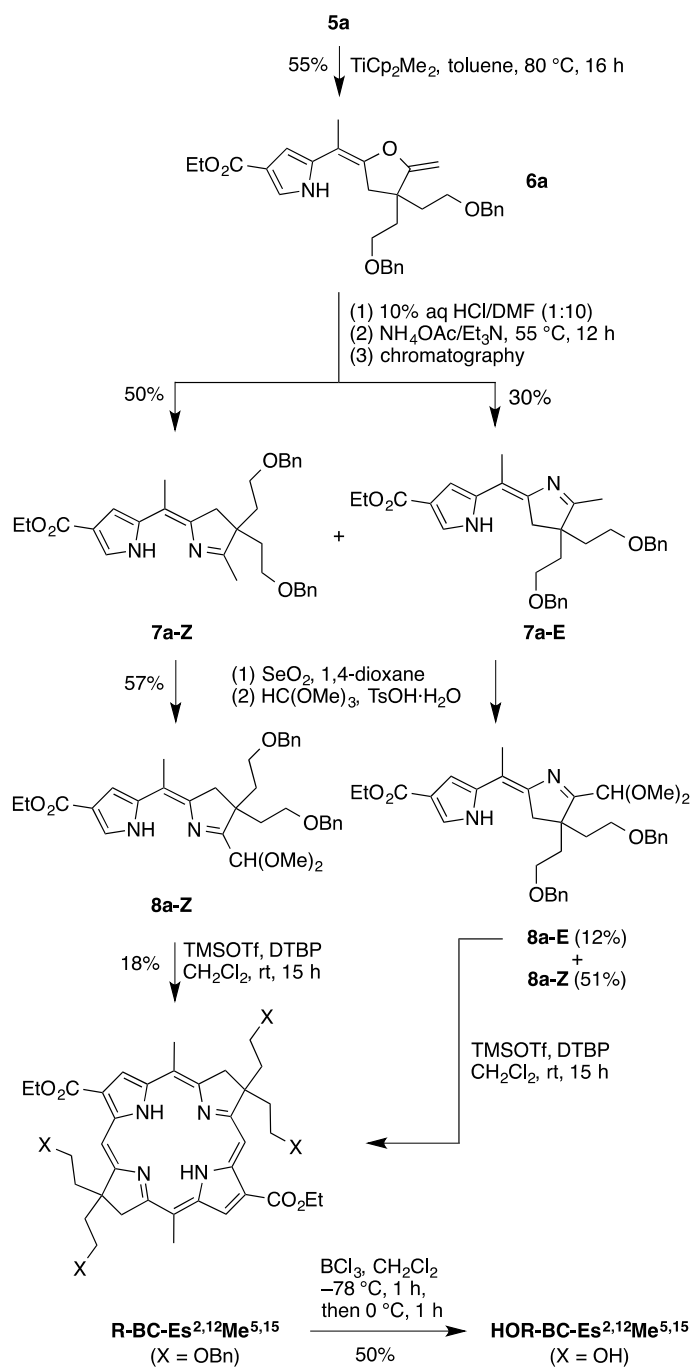
Scheme 3. Synthesis of a swallowtail bacteriochlorin.

The *Z* and *E* isomers of dihydrodipyrrins (compounds **7** and **8**) were assigned by the characteristic N–H chemical shifts upon ^{1}H NMR spectroscopy. In this regard, the Z isomer typically resonates downfield ($\geq$10.5 ppm) due to intramolecular NH hydrogen bonding, whereas the E isomer, which lacks such a feature, resonates in the ~8–9 ppm region for gem-dialkyl-

substituted compounds.[13,47] Representative ^{1}H NMR spectra of dihydrodipyrrins **8a-Z** and **8a-E**, showing the diagnostic NH chemical shift, are displayed in Figure 2.
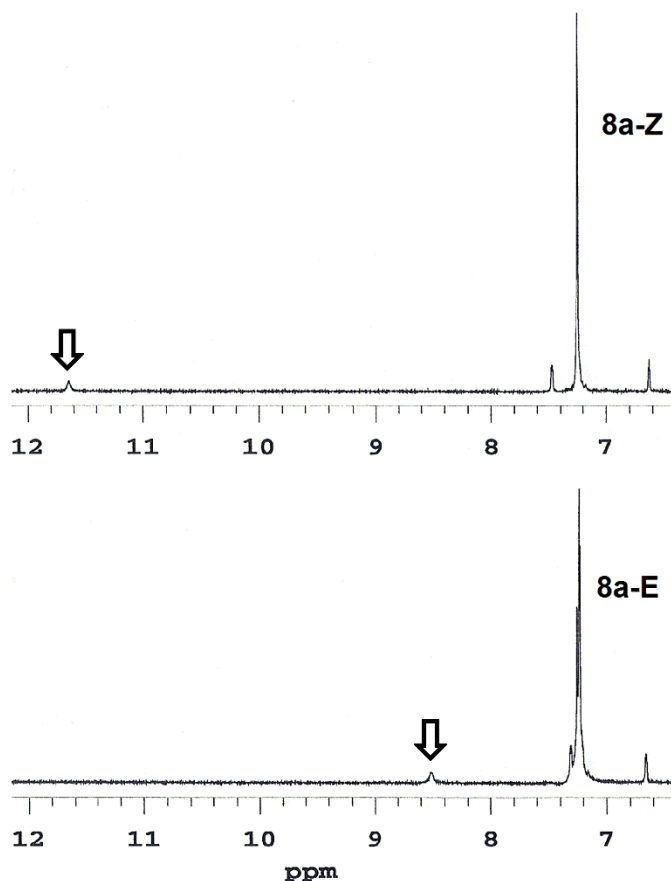
Figure 2. ^{1}H NMR spectra of dihydrodipyrrins **8a-Z** and **8a-E** showing the characteristic chemical shift of the NH proton depending on the presence/absence of intramolecular hydrogen bonding, respectively.

Treatment of dihydrodipyrrin–acetal **8a-Z** with the standard conditions for bacteriochlorin formation [TMSOTf and 2,6-di-*tert*-butylpyridine (DTBP) in dichloromethane at room temperature][15] afforded the meso-dimethylbacteriochlorin **R-BC-Es^{2,12}Me^{5,15}** in 18% yield, wherein the terminus of each swallowtail substituent bears an OBn group (Scheme 3). Compound **8a-E** was also subjected to the same conditions, whereupon the bacteriochlorin **R-BC-Es^{2,12}Me^{5,15}** was observed by absorption spectroscopy and matrix-assisted laser desorption ionization mass spectrometry (MALDI-MS) but not isolated. Isomerization of the dihydrodipyrrin–acetal **8a-E**

144

must occur during the course of the reaction. The terminology here employs "8,8,18,18-substituents"–"bacteriochlorin"–"substituents with position denoted by superscripts", wherein "R" denotes the 2-benzyloxyethyl group of the alkyl swallowtail motif at the 8,8,18,18 positions.

Attempted debenzylation upon hydrogenolysis[53,54] [H_2 and Pd/C or Pd(OH)$_2$/C] proved sluggish and gave incomplete deprotection (as determined by MALDI-MS, Experimental section). Partially de-protected products were also observed upon treatment[55] with TiCl$_4$. Quick debenzylation was observed upon treatment of **R-BC-Es^{2,12}Me^{5,15}** with 1 M BCl$_3$ solution in CH$_2$Cl$_2$[56] to afford the tetrahydroxy-terminated swallowtail–bacteriochlorin **HOR-BC-Es^{2,12}Me^{5,15}** in 50% yield.

Synthesis of bacteriochlorins bearing aryl groups as swallowtail units. Propargylation of methyl diphenylacetate followed by base hydrolysis afforded 2,2-diphenylpent-4-ynoic acid (**3b**).[57] Reaction of **3b** with iodopyrrole **4** in the presence of Pd(PPh$_3$)$_4$ afforded lactone **5b** in 57% yield. Subsequent treatment with the Petasis reagent gave **6b** in 71% yield (Scheme 4). Acid-catalyzed hydrolysis of **6b** followed by Paal-Knorr-like ring closure afforded 1-methyldihydrodipyrrin **7b** as a mixture of *Z* (36%) and *E* (55%) isomers. In contrast to a previous study with simple gem-dimethyl substituents,[13] in this case with the swallowtail units on the β-pyrroline ring the *E*-isomer was formed preferentially. Treatment of **7b-E/Z** with SeO$_2$ followed by CH(OMe)$_3$ gave the isomeric dihydrodipyrrin–acetals **8b-Z** and **8b-E**, which were separated and isolated. A single-crystal X-ray structure of ene–lactone–pyrrole **6b** and of dihydrodipyrrin–acetal **8b-E** confirmed the respective *E* and *Z* configurations (Figure 3).

With the dihydrodipyrrin–acetals in hand, we attempted to synthesize bacteriochlorin **Ph-BC-Es^{2,12}**. An initial microscale reaction revealed a poor yield upon treatment with TMSOTf and DTBP in dichloromethane at room temperature. Therefore, a screen of several acid catalysts and

reaction concentration was carried out (see Supplementary Information, Section II), but satisfactory results were not observed. Under the established TMSOTf/DTBP conditions, dihydrodipyrrin–acetal **8b-Z** (1.38 mmol) afforded bacteriochlorin **Ph-BC-Es[2,12]** and 10-methoxybacteriochlorin **Ph-BC-Es[2,12]MeO[10]** in 1.3 and 0.46% yield, respectively (estimated total yield 2.6% by absorption spectroscopy). Bacteriochlorin formation with dihydrodipyrrin–acetal **8b-E** under the above conditions gave an estimated yield of 0.7% by absorption spectroscopy; the bacteriochlorins were not isolated.
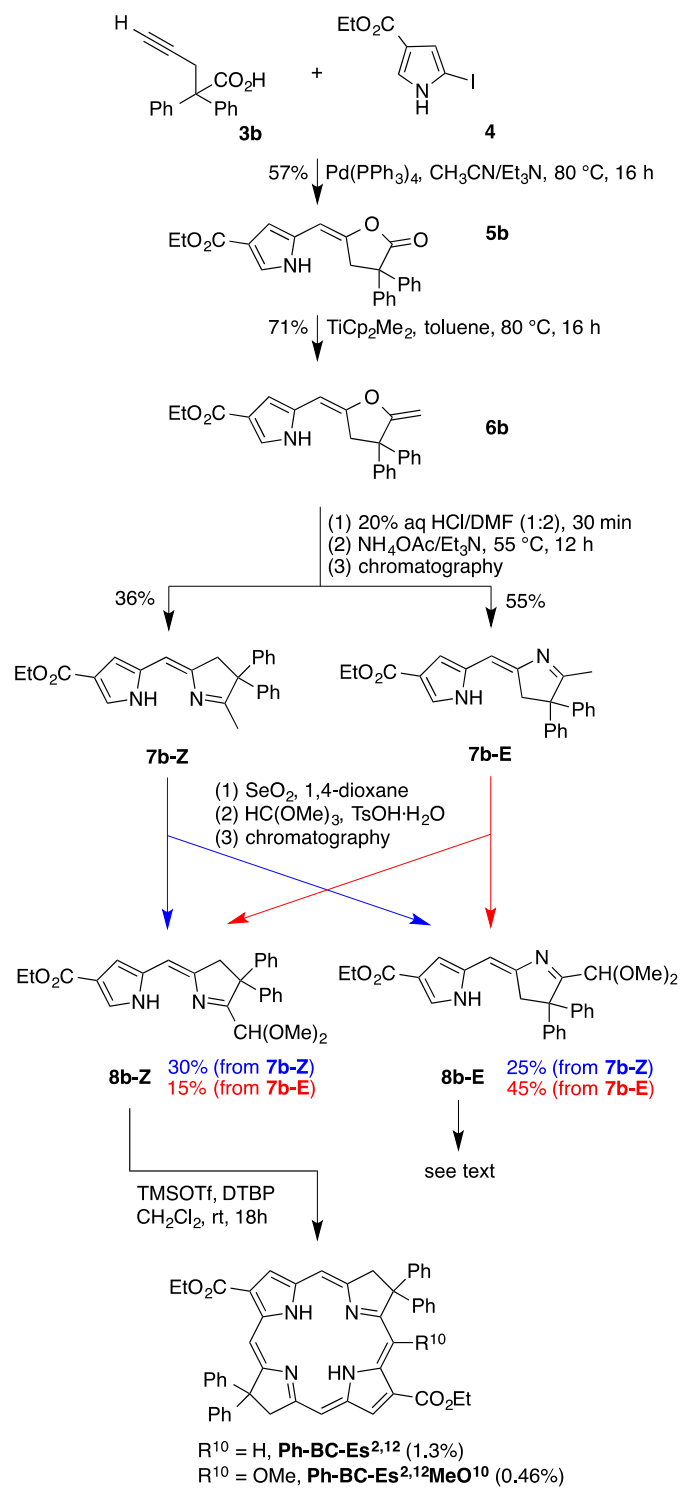
Scheme 4. Synthesis of 8,8,18,18-tetraphenylbacteriochlorins.

6b

8b-E
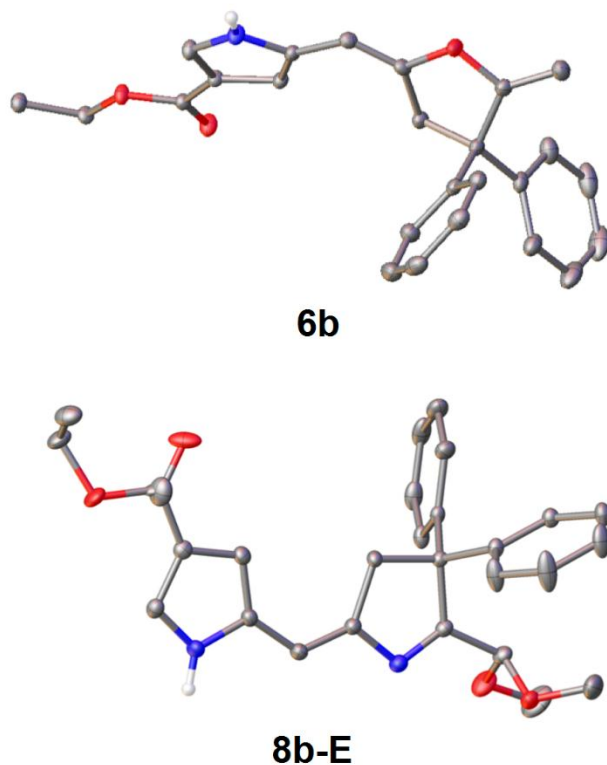
Figure 3. ORTEP diagrams of ene–lactone–pyrrole **6b** (top) and dihydrodipyrrin–acetal **8b-E** (bottom). Ellipsoids are at the 50% probability level, and hydrogen atoms (except N-H) are omitted for clarity. The bridging C=C bond is 134.7 pm (**6b**) and 133.0 pm (**8b-E**) (to be compared with 134.6 pm for **5a**). The non-bridging exocyclic C=C bond of **6b** exhibited a length of 131.8 pm. For compound **6b**, the dihedral angle between the gem-diphenyl planes was 72.05°, and the Ph–C–Ph bond angle was 112.27°. For compound **8b-E**, the corresponding dihedral angle was 60.26°, and the Ph–C–Ph bond angle was 114.25°.

In summary, the long-sought bacteriochlorin architecture bearing geminal substituents other than methyl or spirohexyl units has been achieved, albeit *via* lengthy synthesis (alkyl groups) or in very low yield (phenyl substituents). One distinction in the comparison of the two types of swallowtail bacteriochlorins is that the former also are equipped with two meso-methyl groups whereas the latter lack meso substituents, hence a direct comparison is not possible of the effect of different swallowtail moieties on the yield of bacteriochlorin formation. The presence of mixtures of *E/Z* isomers of dihydrodipyrrin on the path to bacteriochlorins is undesirable, yet in each reaction (of 6a, 6b, 7a-E and 7b-Z) the resulting mixture of E/Z isomers was readily separated.

While it may be possible to carry the mixture through to the bacteriochlorin-forming step, to date such macro-cyclizations have only been performed with dihydrodipyrrin–acetals in pure form.

Chemical Characterization. All new precursors to bacteriochlorins (including known compounds synthesized via new pathways) were characterized by ^{1}H NMR spectroscopy, ^{13}C NMR spectroscopy, and electrospray ionization mass spectrometry (ESI-MS). The *Z* and *E* isomers of dihydrodipyrrins, which were assigned by the characteristic N–H chemical shifts[13,46,47] upon ^{1}H NMR spectroscopy, found unambiguous confirmation in one case, the single-crystal X-ray structure of dihydrodipyrrin–acetal **8b-E** (Figure 3). Compound **8b-E** is a new member of the very small family (currently 4 in total) of 2,3-dihydrodipyrrins validated by X-ray analysis,[46,58] and only the second *E*-dihydrodipyrrin analyzed. The bacteriochlorins were characterized by ^{1}H NMR spectroscopy, ^{13}C NMR spectroscopy (if accessible), ESI-MS and MALDI-MS. Further characterization by absorption and fluorescence spectroscopy is described in the following sections.

Absorption and fluorescence spectra. Chart 4 shows structures of four swallowtail bacteriochlorins (**Ph-BC-Es^{2,12}**, **Ph-BC-Es^{2,12}MeO^{10}**, **R-BC-Es^{2,12}Me^{5,15}**, **HOR-BC-Es^{2,12}Me^{5,15}**) and two benchmark, gem-dimethyl-substituted bacteriochlorins prepared previously via the N-S route[13] (**Me-BC-Es^{2,12}**, **Me-BC-Es^{2,12}Et^{5,15}**) for which full photophysical characterization was performed here. The spectrum of the parent bacteriochlorin (**Me-BC**) that is unsubstituted except for the 8,8,18,18-tetramethyl substituents is also shown and serves as the ultimate reference for delineation of substituent effects. The absorption spectrum of each bacteriochlorin exhibits features characteristic of known synthetic and natural bacteriochlorins (Figure 4).[2] Each spectrum includes strong bands in the near-UV region (B_y, B_x), a strong band in the NIR region (Q_y) and a weaker feature in between (Q_x). Spectral parameters are collected in Table 1.
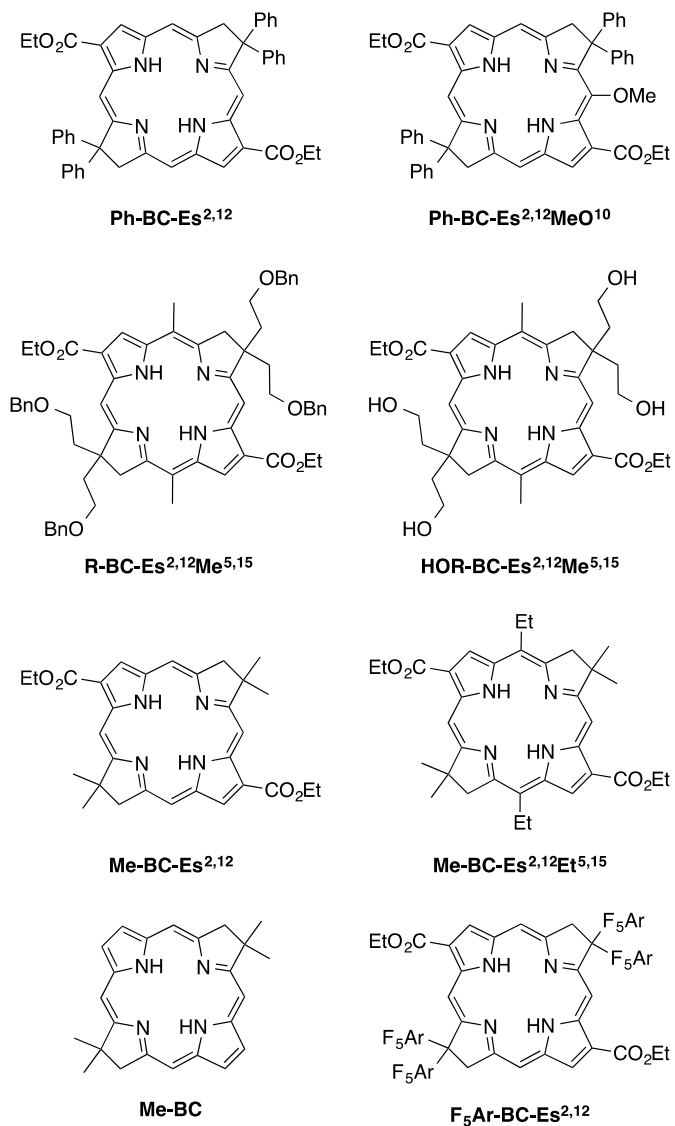
Chart 4. Compounds synthesized here (top four) and previously (**Me-BC-Es^{2,12}** and **Me-BC-Es^{2,12}Et^{5,15}**).[13] MO calculations were performed on fictive compound **F$_5$Ar-BC-Es^{2,12}**, which is the analogue of **Ph-BC-Es^{2,12}** bearing fluorinated (versus non-fluorinated) phenyl substituents.
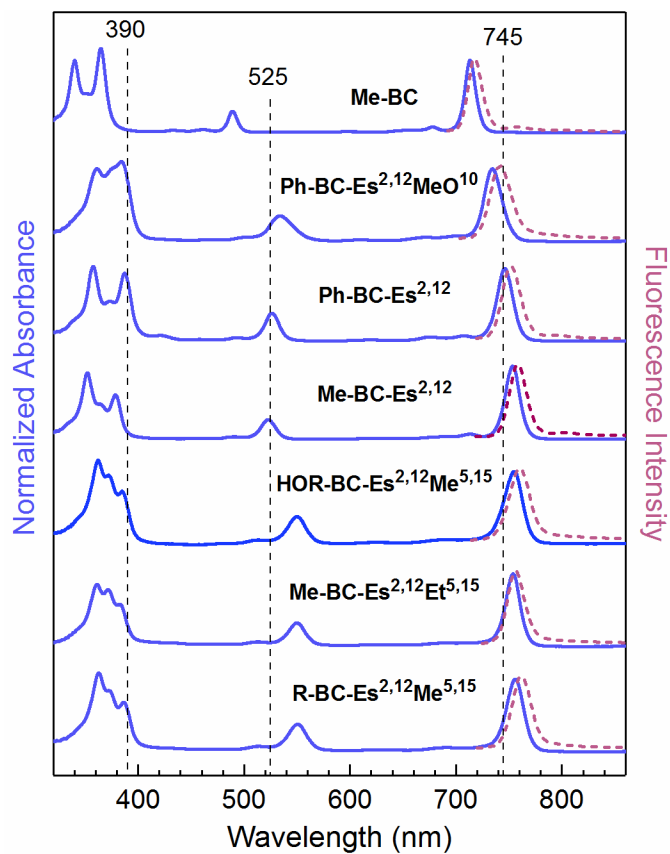
Figure 4. Absorption (solid blue) and fluorescence (dashed red) spectra of bacteriochlorins in toluene at room temperature, normalized at the Q_y band. The dashed vertical lines serve as a reference and mark the approximate positions of key features for phenyl-swallowtail bacteriochlorin **Ph-BC-Es^{2,12}**.

Table 1. Spectral properties of bacteriochlorins.[a]

Compound	B_y λ_{abs} (nm)	B_x λ_{abs} (nm)	Q_x λ_{abs} (nm)	Q_y λ_{abs} (nm)	$Q_{y\,abs}$ fwhm (nm)	Q_y λ_{em} (nm)	$Q_{y\,abs}$ fwhm (nm)	$\Delta_{ab\text{-}em}$ [b] (cm^{-1})
Me-BC	340	365	490	714	12	718	16	78
Ph-BC-Es[2,12]MeO[10]	361	384	534	734	20	742	23	147
Ph-BC-Es[2,12]	357	387	526	746	18	751	20	89
Me-BC-Es[2,12]	352	379	523	753	16	758	19	88
HOR-BC-Es[2,12]Me[5,15]	363	385	550	755	21	761	23	104
Me-BC-Es[2,12]Et[5,15]	361	382	550	754	16	759	19	87
R-BC-Es[2,12]Me[5,15]	362	386	550	756	19	762	21	104

[a] All values were measured using Ar-purged samples in toluene at room temperature. The four absorption wavelengths listed are for the origin, or (0,0), band in the associated manifold. Similarly, the emission wavelength is for Q_y(0,0) fluorescence. [b] Shift between the Q_y absorption and fluorescence maxima.

The presence of phenyl groups at the 8,8,18,18-positions of **Ph-BC-Es[2,12]** compared to the 8,8,18,18-methyl groups of **Me-BC-Es[2,12]** results in a moderate 7 nm hypsochromic effect on the Q_y position (746 vs 753 nm) and little change in the Q_x wavelength. The Q_y shift most likely derives from an electronic effect on the MO energies because there is essentially no change in structure, and the phenyl groups are more potent auxochromes than methyls (*vide infra*). The minimal conformational distortion imparted by the presence of the four phenyl groups on the β-pyrroline units is consistent with the sharpness of the Q_y absorption band, which exhibits a full-width-at-half-maximum (fwhm) of 18 nm for **Ph-BC-Es[2,12]**, which is marginally greater than 16 nm for **Me-BC-Es[2,12]**.

The extended alkyl swallowtail groups of **R-BC-Es[2,12]Me[5,15]** and **HOR-BC-Es[2,12]Me[5,15]** have virtually no effect on the spectral positions compared to non-swallowtail analogue **Me-BC-Es[2,12]Et[5,15]** that bears the simpler 8,8,18,18-tetramethyl substituents. The spectra of all three of these compounds display bathochromic Q_x and Q_y positions relative to benchmark **Me-BC-Es[2,12]**,

indicating that these shifts derive from the effects of the two meso-alkyl groups (methyl or ethyl) that **Me-BC-Es^{2,12}** lacks. In a similar vein, the presence of a single meso substituent (methoxy) in **Ph-BC-Es^{2,12}MeO^{10}** causes an intermediate bathochromic shift of Q_x, along with the hypsochromic effect on the Q_y band. The latter effect of a meso-methoxy groups on the Q_y position of synthetic bacteriochlorins is well known, and the magnitude depends on the other substituents present.[16,59]

In addition to the effects of one or two meso-groups, and differences due to tetraphenyl versus tetraalkyl substitution in the pyrroline rings, the four swallowtail bacteriochlorins and the two benchmark bacteriochlorins all have significant bathochromic shifts of the Q_x and Q_y bands along with greater fwhm of these features compared to parent bacteriochlorin **Me-BC** (Figure 4 and Table 1). These differences arise from the presence of the 2,12-dicarbethoxy groups that the parent compound lacks. The magnitudes of the bathochromic shifts are in keeping with those observed previously for such ester substituents in other synthetic bacteriochlorins.[59,60]

Excited-state properties. The measured excited-state properties of tetrapyrroles are the lifetime (τ_S) of the lowest singlet excited state (S_1), the $S_1 \rightarrow S_0$ fluorescence quantum yield (Φ_f), and the yield of $S_1 \rightarrow T_1$ intersystem crossing (Φ_{isc}). The yield of $S_1 \rightarrow S_0$ internal conversion is obtained by the difference $\Phi_{ic} = 1 - \Phi_f - \Phi_{isc}$. These data for the bacteriochlorins are collected in Table 2.

The Φ_f values of all the bacteriochlorins are in the range 0.13 to 0.19. The effect of 8,8,18,18-phenyl versus 8,8,18,18-methyl groups in the reduced (pyrroline) rings is found by comparing **Ph-BC-Es^{2,12}** and **Me-BC-Es^{2,12}**. The two compounds have otherwise the same

substituent pattern (Chart 4). The Φ_f value is about 30% smaller for **Ph-BC-Es[2,12]** (0.13) than **Me-BC-Es[2,12]** (0.19) (Table 2).

Table 2. Excited-state properties of bacteriochlorins.[a]

Compound	S_1[b] (eV)	τ_s (ns)	Φ_f	Φ_{isc}	Φ_{ic}	k_f^{-1} (ns)	k_{isc}^{-1} (ns)	k_{ic}^{-1} (ns)
Me-BC	1.73	3.8	0.14	0.63	0.23	27	6	17
Ph-BC-Es[2,12]MeO[10]	1.68	4.1	0.18	0.51	0.31	23	8	13
Ph-BC-Es[2,12]	1.66	3.3	0.13	0.56	0.31	25	6	11
Me-BC-Es[2,12]	1.64	3.2	0.19	0.47	0.34	17	7	9
Me-BC-Es[2,12]Et[5,15]	1.64	4.2	0.19	0.33	0.48	22	13	9
R-BC-Es[2,12]Me[5,15]	1.63	4.3	0.15	0.32	0.53	29	13	8

[a] All values were measured using Ar-purged samples in toluene at room temperature. [b] Energy of the S_1 (Q_y) excited state defined by the average energies of the Q_y absorption and fluorescence wavelengths in Table 1.

The Φ_f for **R-BC-Es[2,12]Me[5,15]** with alkyl swallowtails terminated by benzyloxy groups has a fluorescence yield of 0.15 in toluene. The value appears to increase moderately to 0.18 upon debenzylation to give the terminal OH groups of **HOR-BC-Es[2,12]Me[5,15]**. However, the latter compound is only sparingly soluble in toluene. Attempts to make more concentrated solutions for time-resolved studies in DMF or DMF/water showed a gradual decrease in the entire absorption spectrum with time after preparation. Photo-enhanced aggregation or other photochemical processes can occur during time-resolved spectroscopy experiments, so characterization of other excited-state properties of **HOR-BC-Es[2,12]Me[5,15]** could not be pursued. However, the benzyloxy-terminated analogue **R-BC-Es[2,12]Me[5,15]** in toluene could be fully characterized.

Figure 5 shows representative TA difference spectra and kinetic traces for **Ph-BC-Es[2,12]** (panel A) and **Me-BC-Es[2,12]** (panel B) in toluene (obtained using 100-fs excitation flashes near the Q_y wavelength) that illustrate the measurements of τ_S and Φ_{isc}. For both compounds, the

spectrum at 0.7 ns is due to the lowest singlet excited state (S_1 or Q_y). The spectrum is dominated by a NIR feature that consists of bleaching of the Q_y ground-state absorption band plus the Q_y excited-state stimulated emission. Bleaching of the visible-region ground-state Q_x band and the near-UV B_x Soret component is also apparent. The spectrum at 35 ns is due to the lowest triplet excited state (T_1). The bleaching of each ground-state absorption feature is somewhat diminished, and the S_1 stimulated emission has disappeared. On the basis of the diminution of the bleaching/stimulated-emission features, the yield of $S_1 \rightarrow T_1$ intersystem crossing is 0.56 for **Ph-BC-Es[2,12]** and 0.47 for **Me-BC-Es[2,12]** in toluene. These Φ_{isc} values and those for the other bacteriochlorins are listed in Table 2. The $S_1 \rightarrow S_0$ internal-conversion yields ($\Phi_{ic} = 1 - \Phi_f - \Phi_{isc}$) are in the range (0.23–0.53) for all the bacteriochlorins studied and are comparable for **Ph-BC-Es[2,12]** (0.31) and **Me-BC-Es[2,12]** (0.34).
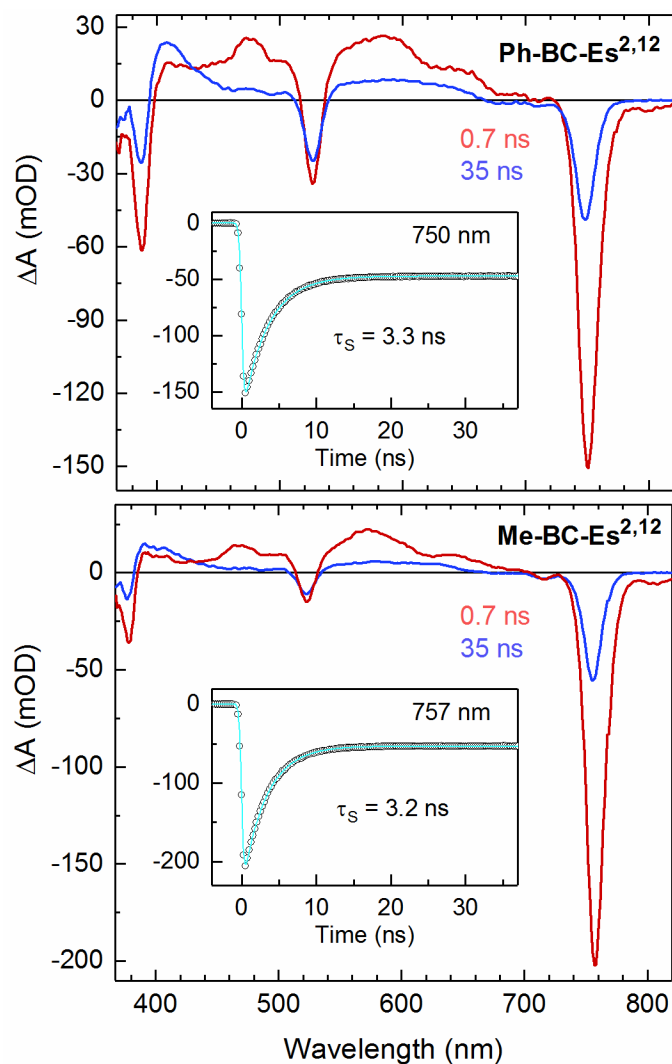
Figure 5. Representative transient absorption data for bacteriochlorins **Ph-BC-Es^{2,12}** and **Me-BC-Es^{2,12}** in toluene obtained using 100 fs excitation flashes at 680 nm. The insets show time profiles (open black circles) and single-exponential fits (cyan line) of the time profiles for decay of the Q_y bleach and stimulated emission.

The insets to Figure 5 show representative kinetic profiles for decay of the S_1 excited state monitored at the Q_y bleaching/stimulated-emission feature. The average value from such measurements at a number of wavelengths (and across the spectrum analyzed globally) is 3.3 ns for **Ph-BC-Es^{2,12}** and 3.2 ns for **Me-BC-Es^{2,12}** in toluene. Thus, tetraphenyl versus tetramethyl substitution in the reduced ring has basically no effect on the lifetime of the S_1 excited state. These

τ_S values and those for the other bacteriochlorins are given in Table 2. The values range from 3.2 to 4.3 ns.

The values of τ_S, Φ_f, Φ_{isc}, and Φ_{ic} can be used to obtain the rate constants for the fluorescence (k_f), intersystem-crossing (k_{isc}), and internal-conversion (k_{ic}) decay pathways of the S_1 excited state via the calculation $k_x = \Phi_x/\tau_S$, where x = f, isc or ic. The results are listed in the last three columns of Table 2 as the associated time constants (with units of nanoseconds). These rate constants are the most fundamental measures of the effects of substituents (e.g., the nature of the 8,8,18,18-groups) on the characteristics of the S_1 excited state and thus on photophysical/photochemical properties.

There is no systematic trend in k_f values depending on swallowtail (or other) substituents. The range of values and the average of $(24 \text{ ns})^{-1}$ are in line with findings on a variety of synthetic bacteriochlorins.[59,60] The k_{isc} values are also in the range of values for synthetic free base bacteriochlorins bearing diverse substituent patterns. Among the compounds studied here, the two that bear two meso-alkyl groups (**R-BC-Es^{2,12}Me^{5,15}** and **Me-BC-Es^{2,12}Et^{5,15}**) exhibit a roughly two-fold lower k_{isc} than the others, contributing to the longer singlet lifetime than for all the others except the methoxy-substituted **Ph-BC-Es^{2,12}MeO^{10}**. The rate constants for $S_1 \rightarrow S_0$ internal conversion in Table 2 follow a general trend of an increase in k_{ic} with a decrease in S_1 energy, consistent with the energy-gap law for nonradiative decay.[61] In particular, k_{ic} is smallest (as is Φ_{ic}) for the parent **Me-BC**, which contains no substituents other than 8,8,18,18-methyl groups. The reverse is true for **R-BC-Es^{2,12}Me^{5,15}**, which is more highly substituted, contains mobile alkyl chains at the 8,18-positions, and has the longest Q_y wavelength and lowest S_1 energy of the set. The 8,8,18,18-phenyl groups of **Ph-BC-Es^{2,12}** make k_{ic} about 30% smaller than analogue **Me-BC-Es^{2,12}** that bears 8,8,18,18-methyl groups, again consistent with the hypsochromic effect of the

phenyl versus methyl motif on the Q_y band to give a higher energy S_1 excited state (Table 2 and Figure 4).

Molecular orbital calculations. Density functional theory (DFT) calculations were performed to gain insight into the spectral differences (Figure 6 and Table 1) among the bacteriochlorins studied (Chart 4), including the moderate effects of phenyl versus alkyl substituents at the 8,8,18,18-positions. The results described below will show that these and other differences among the compounds and spectra are fully consistent with electronic rather than structural effects of the substituents. In this regard, the calculated energy-minimized structure for **Ph-BC-Es^{2,12}** shows a C_{Ph}-C_{Ph}-C_7-C_8-C_{Ph}'-C_{Ph}' dihedral angle of 65° that is comparable to the angle of 62° for precursor **6b** (Figure 3). Thus, formation of the bacteriochlorin macrocycle with the 8,8,18,18-phenyl groups does not alter the relationship of the phenyl groups with respect to each other or with the pyrroline ring to which they are attached. Moreover, the calculated structure for **Ph-BC-Es^{2,12}** like all the other bacteriochlorins shows that the macrocycle is essentially planar, including the reduced (pyrroline) rings, with all dihedral angles that would reflect nonplanarity typically being <5°. Additionally, the same situation applies to a fictive analogue of **Ph-BC-Es^{2,12}** in which the phenyl groups are replaced by pentafluorophenyl groups, which should have minimal structural perturbation but have notable electronic effects on the spectra, as is observed (*vide infra*). For both **Ph-BC-Es^{2,12}** and the fictive pentafluorophenyl analogue **F₅Ar-BC-Es^{2,12}**, the two aryl rings tend toward a T-shaped arrangement, which is the known energy minimized configuration for benzene and hexafluorobenzene dimers in the gas phase.[62] Collectively, these considerations and those presented below indicate that the modest effects of phenyl versus alkyl groups at the 8,8,18,18-positions are electronic and not structural in origin.

Figure 6 shows the electron-density distributions and energies of the frontier molecular orbitals (MOs) of four selected bacteriochlorins to illustrate the origins of the main (yet moderate) spectral differences that are observed among the compounds. Bacteriochlorin **F₅Ar-BC-Es**[2,12] is the fictive pentafluorophenyl analogue of **Ph-BC-Es**[2,12]. The key frontier orbitals are the highest occupied MO (HOMO), the lowest unoccupied MO (LUMO), along with the HOMO-1 and LUMO+1. In Gouterman's four-orbital model,[63-65] the near-UV to NIR spectra of tetrapyrroles are due to transitions to excited states that arise from linear combinations of one-electron promotions among the four orbitals. In particular, B_y and Q_y are comprised of constructive (+) and destructive (−) linear combinations of the HOMO → LUMO and HOMO-1 → LUMO+1 configurations, and B_x and Q_x are composed of the analogous linear combinations of the HOMO-1 → LUMO and HOMO → LUMO+1 configurations. The extent of mixing and thus, the wavelength positions and relative intensities of B_y versus Q_y and of B_x versus Q_x depend on the relative energies of the contributing excited-state configurations, which in turn depend on the relative energies of the four frontier MOs. The focus here is how the different substituent patterns on the representative bacteriochlorins shown at the top of Figure 6 affect the MO energies and thus, the positions of the two longest wavelength absorption transitions/bands (Q_x and Q_y) and the energies of the two corresponding lowest singlet excited states (S_2 and S_1). In this regard, the S_1 (Q_y) excited state of bacteriochlorins is typically comprised of roughly 90% HOMO→ LUMO configuration because the presence of two pyrroline rings shifts the energy of this configuration far below that of the HOMO-1 → LUMO+1 configuration.
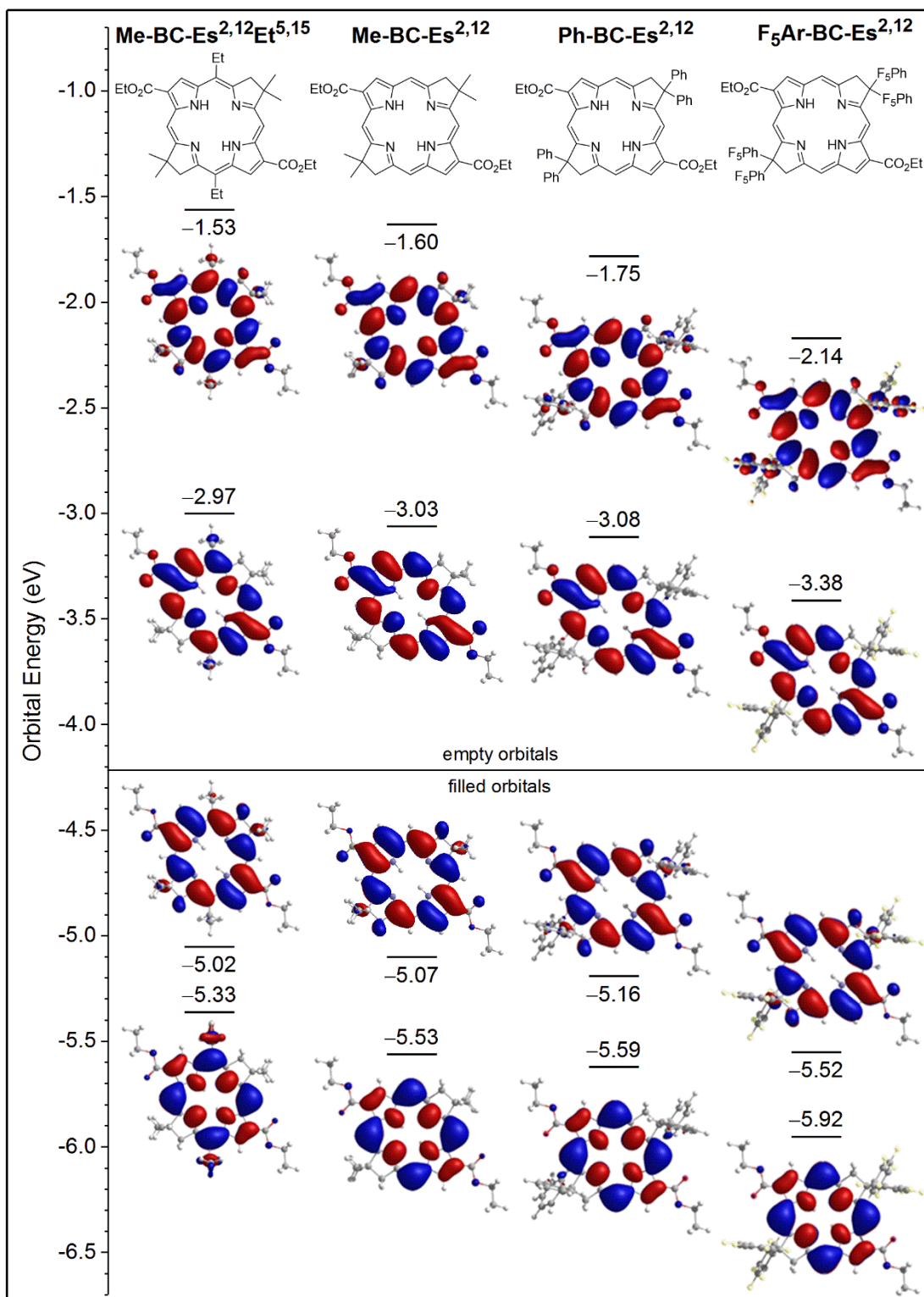
Figure 6. MO diagram for bacteriochlorins bearing methyl (**Me-BC-Es^{2,12}Et^{5,15}**), methyl (**Me-BC-Es^{2,12}**), phenyl (**Ph-BC-Es^{2,12}**) and pentafluorophenyl (fictive compound **F$_5$Ar-BC-Es^{2,12}**) groups at the 8,8,18,18-positions. **Me-BC-Es^{2,12}Et^{5,15}** also contains 5,15-ethyl groups that are not present in the other three bacteriochlorins.

Figure 7 is helpful in understanding how substituent effects on certain MOs are directly manifested in the absorption spectra. The figure compares spectra that were measured (solid), simulated using the four-orbital model in which the only variables among the compounds are the MO energies obtained from DFT (dashed), and calculated using time-dependent DFT (TDDFT) (vertical arrows). The focus of comparisons is the trends, and not precise positions, of the absorption features.
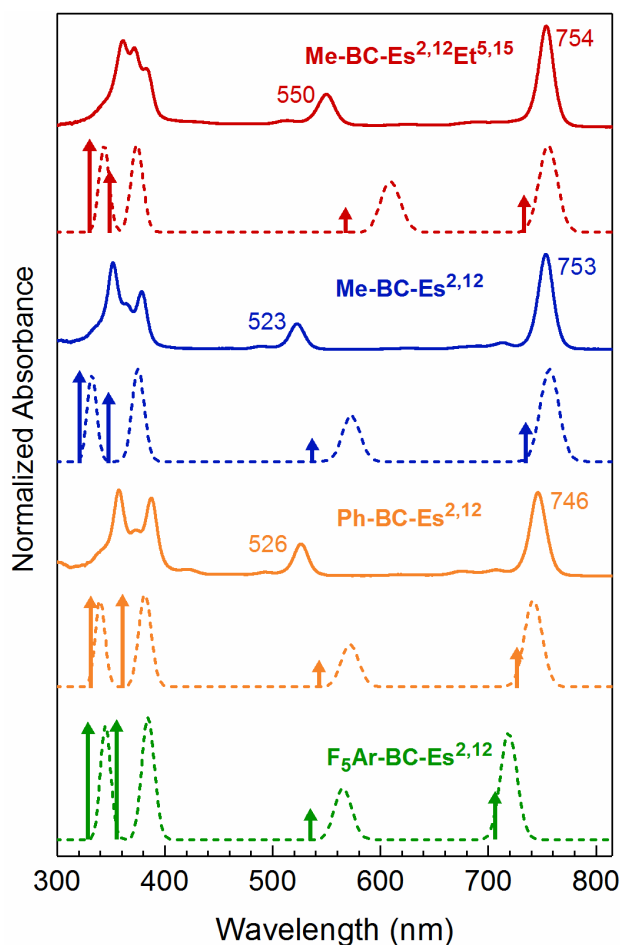
Figure 7. Absorption spectra of bacteriochlorins measured (solid), simulated using the four-orbital model (dashed), and calculated with TDDFT (vertical arrows). The four-orbital simulations used configuration interaction energies of 0.45 and 0.30 for the y- and x-polarized configurations and an energy shift of 0.30 eV from the MO to spectral domain.

Figure 7 reveals that the four-orbital-model simulations and TDDFT calculations both reproduce a small (~7 nm observed) bathochromic shift in Q_y wavelength upon replacement of the

8,8,18,18-methyl groups of **Me-BC-Es**[2,12] with the phenyl substituents of **Ph-BC-Es**[2,12]. Furthermore, this trend continues when the phenyl rings are fluorinated in fictive analogue **F₅Ar-BC-Es**[2,12]. As noted above, replacement of hydrogens with fluorines is not expected to have significant structural consequences, but have significant electronic effects. This can be seen in Figure 6 wherein the electron density on the 8,8,18,18-groups in certain MOs increases along the following series: methyl < phenyl < pentafluorophenyl. It is also seen that although both the energies of both the HOMO and LUMO change along this series, it is the preferential stabilization of the HOMO and consequent increase in the energy gap between these two orbitals that drives the shift of the Q_y band to shorter wavelengths and the associated increase in S_1 energy. As noted above, this change has some, albeit quite modest, photophysical consequences, namely a small decrease in the rate constant for $S_1 \rightarrow S_0$ internal conversion.

The four-orbital-model simulations and TDDFT calculations are also consistent with the measured spectra in showing that replacement of the 8,8,18,18-methyl groups of **Me-BC-Es**[2,12] with phenyl groups of **Ph-BC-Es**[2,12] has little consequence on the Q_x wavelength (and S_2 energy). However, a substantial (~25 nm) bathochromic effect on Q_x position is observed upon addition of 5,15-ethyl groups to **Me-BC-Es**[2,12] to make **Me-BC-Es**[2,12]**Et**[5,15], and this effect is also reproduced by both simulations and calculations. Similar shifts are also observed for **R-BC-Es**[2,12]**Me**[5,15] and **HOR-BC-Es**[2,12]**Me**[5,15], which contain 5,15-methyl groups (Chart 4 and Figure 4). Examination of Figure 6 shows that this effect on the Q_x band arises in large measure from energetic destabilization of the HOMO-1 (which exhibits considerable electron density at the meso positions) and consequent decreased energy of the HOMO-1 $\rightarrow$ LUMO excited-state configuration which (along with HOMO $\rightarrow$ LUMO+1 configuration) defines the Q_x state and its spectral characteristics within the four-orbital model.

CONCLUSIONS

An approach for elaborating the β-pyrroline units of bacteriochlorins has been developed through use of a new Northern-Southern pathway for constructing the macrocycle, which makes use of dihydrodipyrrin–acetals. Swallowtail alkyl and phenyl groups were introduced as the □-pyrroline substituents. Such integral swallowtail motifs provide a means for tailoring the 3-dimensional environment of the planar tetrapyrrole macrocycle, complementing the existing approaches for modification of the β-pyrrole and meso-positions. The swallowtail bacteriochlorins exhibit strong absorption in the near-infrared (NIR) spectral region characteristic of natural and other synthetic bacteriochlorins. The swallowtails have little impact on the excited-state properties of the bacteriochlorins and the small observed changes in spectral properties can be understood in terms of substituent electronic effects and not changes in structure.

Regardless of the attractive attributes of the swallowtail bacteriochlorins, the overall yield and tiny quantities of materials obtained remain limitations. The alkyl swallowtail design requires a lengthy synthesis yet the yield of macrocyclization is reasonable, whereas the phenyl swallowtail design affords a concise synthesis but the macrocyclization yield is abysmal. The presence of *E/Z* isomers of the dihydrodipyrrins also is undesirable, although separation of the isomeric mixture is facile. For swallowtail designs to reach practical levels, an alternative route to dihydrodipyrrins bearing alkyl swallowtail groups is required, as are studies of reaction conditions for the self-condensation of dihydrodipyrrin–acetals containing aryl swallowtail groups.

EXPERIMENTAL SECTION

General methods. ^{1}H NMR (300 MHz) and ^{13}C NMR (75 MHz) spectra were collected at room temperature in $CDCl_3$ unless noted otherwise. Silica gel (40 μm average particle

size) was used for column chromatography. All solvents were reagent grade and were used as received unless noted otherwise. THF was freshly distilled from sodium/benzophenone ketyl. ESI-MS data are reported for the molecular ion or protonated molecular ion. MALDI-MS was performed with the matrix 1,4-bis(5-phenyl-2-oxazol-2-yl)benzene (POPOP)[66] for bacteriochlorins. Commercial compounds were used as received. The known compounds **3b**[57] and **4**[13] were prepared as described in the literature. X-ray crystallographic data for compounds **5a**, **6b** and **8b-E** are provided in the Supplementary Information (Section III).

2,2-Bis(2-(benzyloxy)ethyl)hex-4-ynenitrile (**1**). A stirred solution of anhydrous acetonitrile (840 mg, 20.0 mmol) in THF (40 mL) and HMPA (20 mL) was cooled to −78 °C under argon, whereupon the solution became a partially frozen slush. The mixture was treated with LDA solution (2.0 M, 10 mL in THF/heptane/ethylbenzene, 20 mmol) at −78 °C under argon. After 30 min, [(2-iodoethoxy)methyl]benzene (5.24 g, 20.0 mmol) was added dropwise, and the reaction mixture was allowed to warm to room temperature. After 1 h at room temperature, the solution was cooled to −78 °C and another portion of LDA (2.0 M, 10 mL in THF/heptane/ethylbenzene, 20 mmol) was added dropwise. After 30 min, another portion of [(2-iodoethoxy)methyl]benzene (5.24 g, 20 mmol) was added dropwise, and the reaction mixture was allowed to warm to room temperature. After 1 h at room temperature, the solution was cooled to −78 °C again, and another portion of LDA (2.0 M, 10 mL in THF/heptane/ethylbenzene, 20 mmol) was added dropwise. After 30 min, 1-bromobut-2-yne (2.66 g, 20.0 mmol) was added dropwise, and the reaction mixture was allowed to warm to room temperature. After 30 min, the reaction mixture was quenched by the addition of saturated aqueous NH$_4$Cl solution. Dichloromethane (200 mL) was added. The mixture was washed with water and brine. The organic layer was dried (Na$_2$SO$_4$), concentrated and chromatographed [silica, hexanes/ethyl acetate (10:1)] to afford a colorless liquid

(3.33 g, 46%): ^{1}H NMR δ 1.80 (t, J = 2.4 Hz, 3H), 2.01–2.14 (m, 4H), 2.62 (q, J = 2.4 Hz, 2H), 3.70 (t, J = 6.9 Hz, 4H), 4.52 (s, 4H), 7.25–7.35 (m, 10H); ^{13}C NMR δ 3.83, 28.3, 36.3, 38.5, 66.9, 73.1, 73.4, 80.3, 122.7, 127.8, 127.9, 128.6, 138.2; ESI-MS obsd 362.2117, calcd 362.2120 [(M + H)$^{+}$, M = C$_{24}$H$_{27}$NO$_2$].

2,2-Bis(2-(benzyloxy)ethyl)hex-4-ynal (**2**). A stirred solution of **1** (3.33 g, 9.22 mmol) in dichloromethane (70 mL) was treated with DIBAL-H solution (1.0 M, 23 mL in THF, 23 mmol) at –78 °C under argon. After 1 h at –78 °C, water (3.2 mL) was added, and the reaction mixture was allowed to warm to room temperature. After 30 min at room temperature, aqueous NaOH solution (2.5 M, 3.2 mL, 8.0 mmol) was added, and the reaction mixture was stirred for another 15 min. A large portion of Na$_2$SO$_4$ was added, and the resulting mixture was filtered. The filtrate was concentrated and chromatographed [silica, hexanes/ethyl acetate (10:1)] to afford a colorless liquid (2.35 g, 70%): ^{1}H NMR δ 1.75 (t, J = 2.4 Hz, 3H), 1.82–2.10 (m, 4H), 2.40 (q, J = 2.4 Hz, 2H), 3.39–3.58 (m, 4H), 4.42 (s, 4H), 7.26–7.34 (m, 10H), 9.57 (s, 1H); ^{13}C NMR δ 3.82, 21.1, 34.4, 49.8, 66.1, 73.3, 74.4, 78.2, 127.8, 128.6, 138.3, 204.2; ESI-MS obsd 365.2121, calcd 365.2117 [(M + H)$^{+}$, M = C$_{24}$H$_{28}$O$_3$].

2,2-Bis(2-(benzyloxy)ethyl)hex-4-ynoic acid (**3a**). A stirred solution of **2** (900 mg, 2.49 mmol) in acetone (30 mL) was treated with Jones reagent [prepared from CrO$_3$ (1.65 g, 16.5 mmol) in 1.3 mL of concentrated H$_2$SO$_4$ and 10 mL of water] at room temperature under nitrogen. After 1 h, water (100 mL) was added, and the reaction mixture was extracted with dichloromethane. The organic layer was dried (Na$_2$SO$_4$) and concentrated. The resulting viscous liquid was used directly in the next step without purification due to limited stability.

Ethyl   (E)-5-(1-(4,4-bis(2-(benzyloxy)ethyl)-5-oxodihydrofuran-2(3H)-ylidene)ethyl)-1H-pyrrole-3-carboxylate (**5a**). Following an established procedure,[13,47] a solution of **3a**

(prepared from 900 mg of **2**) in dry acetonitrile (7.0 mL) in a Schlenk flask was treated with **4** (690 mg, 2.60 mmol), BnNEt$_3$Cl (658 mg, 2.37 mmol) and Et$_3$N (3.0 mL). The mixture was deaerated by three freeze–pump–thaw cycles. A sample of Pd(PPh$_3$)$_4$ (137 mg, 0.118 mmol) was then added, and the resulting mixture was further deaerated. The reaction mixture was heated at 80 °C for 24 h, and then CH$_2$Cl$_2$ and water were added. The organic layer was dried (Na$_2$SO$_4$), concentrated and chromatographed [silica, hexanes/ethyl acetate (3:2)] to afford a light yellow solid (672 mg, 52%): mp 114–116 °C; ^{1}H NMR δ 1.35 (t, $J = 7.2$ Hz, 3H), 1.87–2.12 (m, 7H), 3.08 (s, 2H), 3.54–3.59 (m, 4H), 4.30 (q, $J = 7.2$ Hz, 2H), 4.41 (ABq, $\Delta\delta_{AB} = 0.3$ Hz, $J = 12.0$ Hz, 4H), 6.42 (s, 1H), 7.22–7.33 (m, 11H), 8.65 (br, 1H); ^{13}C NMR δ 14.3, 14.6, 35.5, 37.6, 45.2, 59.9, 66.3, 73.4, 103.8, 107.7, 117.2, 123.2, 127.7, 128.5, 131.0, 137.9, 144.6, 165.2, 178.9; ESI-MS obsd 518.2540, calcd 518.2537 [(M + H)$^+$, M = C$_{31}$H$_{35}$NO$_6$].

(E)-Ethyl 5-((5-oxo-4,4-diphenyldihydrofuran-2(3H)-ylidene)methyl)-1H-pyrrole-3-carboxylate) (**5b**). Following an established procedure,[13,47] a solution of **4** (5.30 g, 20.0 mmol) in dry acetonitrile (80.0 mL) in a Schlenk flask was treated with **3b** (7.50 g, 30.0 mmol), BnNEt$_3$Cl (4.56 g, 20.0 mmol), and Et$_3$N (20.0 mL). The mixture was deaerated by three freeze–pump–thaw cycles. A sample of Pd(PPh$_3$)$_4$ (1.16 g, 1.00 mmol) was then added, and the resulting mixture was further deaerated. The reaction mixture was heated at 80 °C for 24 h, and then CH$_2$Cl$_2$ and water were added. The organic layer was dried (Na$_2$SO$_4$), concentrated and chromatographed [silica, hexanes/ethyl acetate (4:1)] to afford a white solid (4.42 g, 57%): mp 62–64 °C; ^{1}H NMR δ 1.34 (t, $J = 7.2$ Hz, 3H), 3.79 (d, $J = 2.1$ Hz, 2H), 4.29 (q, $J = 7.2$ Hz, 2H), 6.17 (s, 1H), 6.50 (s, 1H), 7.30–7.39 (m, 11H), 8.94 (br, 1H); ^{13}C NMR δ 14.5, 41.3, 41.4, 56.9, 60.1, 97.5, 107.3, 117.7, 123.8, 127.0, 127.4, 127.9, 128.9, 140.9, 147.4, 165.2, 175.0; ESI-MS obsd 388.1544, calcd 388.1543 [(M + H)$^+$, M = C$_{24}$H$_{21}$NO$_4$].

***Ethyl (E)-5-(1-(4,4-bis(2-(benzyloxy)ethyl)-5-methylenedihydrofuran-2(3H)-ylidene)ethyl)-1H-pyrrole-3-carboxylate* (6a).** Following a general procedure,[13,47] a solution of TiCp$_2$Cl$_2$ (1.56 g, 6.27 mmol) in toluene (25 mL) was treated dropwise with LiMe solution (1.6 M, 7.9 mL in Et$_2$O, 12.6 mmol) at 0 °C under an argon atmosphere. After stirring for 1 h at 0 °C, saturated aqueous NH$_4$Cl solution was added. The organic layer was washed (water and brine), dried (Na$_2$SO$_4$) and filtered. The filtrate, which contained the Petasis reagent, was treated with lactone **5a** (650 mg, 1.26 mmol) and additional TiCp$_2$Cl$_2$ (15 mg) in a Schlenk flask. The resulting solution was heated at 80 °C for 16 h. The resulting mixture was allowed to cool to room temperature whereupon MeOH (1.8 mL), NaHCO$_3$ (50 mg) and water (18 μL) were added. The resulting mixture was heated at 40 °C for 2 h with stirring and then filtered through Celite. The filtrate was concentrated and chromatographed [silica, hexanes/ethyl acetate (3:1)] to afford a brown viscous liquid (357 mg, 55%): ^{1}H NMR δ 1.33 (t, J = 7.2 Hz, 3H), 1.75–1.91 (m, 4H), 1.97 (s, 3H), 2.81 (s, 2H), 3.54–3.59 (m, 4H), 3.93 (d, J = 3.0 Hz, 1H), 4.28 (q, J = 7.2 Hz, 2H), 4.42 (s, 4H), 4.53 (d, J = 3.0 Hz, 1H), 6.35 (d, J = 3.0 Hz, 1H), 7.23–7.32 (m, 11H), 8.52 (br, 1H); ^{13}C NMR δ 14.1, 14.6, 38.2, 39.3, 45.2, 59.8, 67.2, 73.2, 82.7, 99.1, 106.6, 116.9, 122.6, 127.7, 128.5, 132.8, 138.2, 149.7, 165.3, 166.0; ESI-MS obsd 516.2746, calcd 516.2744 [(M + H)$^+$, M = C$_{32}$H$_{37}$NO$_5$].

***(E)-Ethyl 5-((5-methylene-4,4-diphenyldihydrofuran-2(3H)-ylidene)methyl)-1H-pyrrole-3-carboxylate* (6b).** Following a general procedure,[13,47] a solution of TiCp$_2$Cl$_2$ (14.15 g, 56.85 mmol) in toluene (160 mL) was treated dropwise with LiMe solution (1.6 M, 71.1 mL in Et$_2$O, 113.7 mmol) at 0 °C under an argon atmosphere. The resulting mixture was stirred at 0 °C for 1 h, whereupon saturated aqueous NH$_4$Cl solution was added. The organic layer was washed (water and brine), dried (Na$_2$SO$_4$) and filtered. The filtrate, which contained the Petasis reagent,

was treated with lactone **5b** (4.40 g, 11.4 mmol) and additional TiCp$_2$Cl$_2$ (135 mg) in a Schlenk flask under argon. The resulting solution was heated at 80 °C for 16 h. The resulting mixture was allowed to cool to room temperature whereupon MeOH (20.0 mL), NaHCO$_3$ (500 mg) and water (0.20 mL) were added. The resulting mixture was heated at 40 °C for 2 h with stirring and then filtered through Celite. The filtrate was concentrated and chromatographed [silica, hexanes/ethyl acetate (4:1)] to afford a white solid (3.10 g, 71%): mp 144–146 °C; ^{1}H NMR δ 1.33 (t, J = 7.2 Hz, 3H), 3.63 (d, J = 1.8 Hz, 2H), 4.03 (d, J = 2.4 Hz, 1H), 4.27 (q, J = 7.2 Hz, 2H), 4.83 (d, J = 2.4 Hz, 1H), 5.80 (s, 1H), 6.35 (s, 1H), 7.23–7.34 (m, 11H), 8.52 (br, 1H); ^{13}C NMR δ 14.5, 43.6, 58.3, 59.9, 88.6, 92.4, 105.8, 117.4, 122.7, 127.1, 128.2, 128.4, 129.1, 143.4, 153.8, 165.3, 165.4; ESI-MS obsd 386.1753, calcd 386.1751 [(M + H)$^+$, M = C$_{25}$H$_{23}$NO$_3$].

2,2-Bis[2-(benzyloxy)ethyl]-8-carbethoxy-2,3-dihydro-1,5-dimethyldipyrrin (**7a**). Following a general procedure,[13,47] a solution of **6a** (350 mg, 0.680 mmol) in DMF (10 mL) was treated with 10% aqueous HCl (1.0 mL). After 30 min, NH$_4$OAc (1.05 g, 13.5 mmol) and Et$_3$N (1.9 mL, 14 mmol) were added, and the resulting mixture was stirred at 55 °C for 12 h. Then, the reaction was quenched by the addition of saturated aqueous KH$_2$PO$_4$ solution. Ethyl acetate (50 mL) was added, and the organic layer was washed (water), dried (Na$_2$SO$_4$) and concentrated. Column chromatography [silica, hexanes/ethyl acetate (3:1)] afforded a light yellow oil (**7a-Z**, 175 mg, 50%) and a light brown oil (**7a-E**, 105 mg, 30%). Data for **7a-Z**: ^{1}H NMR δ 1.35 (t, J = 7.2 Hz, 3H), 1.86–1.92 (m, 7H), 2.08 (s, 3H), 2.68 (s, 2H), 3.34–3.43 (m, 4H), 4.30 (q, J = 7.2 Hz, 2H), 4.38 (ABq, $\Delta\delta_{AB}$ = 0.3 Hz, J = 12.0 Hz, 4H), 6.57 (d, J = 3.0 Hz, 1H), 7.21–7.27 (m, 10H), 7.45 (dd, J = 3.0, 1.5 Hz, 1H), 11.9 (br, 1H); ^{13}C NMR δ 14.7, 16.1, 16.7, 37.0, 38.1, 53.0, 59.7, 66.8, 73.4, 106.7, 112.5, 115.9, 124.0, 127.7, 128.4, 134.9, 138.1, 147.7, 165.7, 182.4; ESI-MS obsd 515.2909, calcd 515.2904 [(M + H)$^+$, M = C$_{32}$H$_{38}$N$_2$O$_4$]. Data for **7a-E**: ^{1}H NMR δ 1.36 (t,

J = 7.2 Hz, 3H), 1.86–1.94 (m, 4H), 2.08 (s, 3H), 2.35 (s, 3H), 2.81 (s, 2H), 3.38–3.42 (m, 4H), 4.31 (q, *J* = 7.2 Hz, 2H), 4.38 (s, 4H), 6.62 (s, 1H), 7.23–7.35 (m, 11H), 8.55 (br, 1H); ^{13}C NMR δ 14.8, 16.0, 16.6, 38.0, 38.9, 55.4, 60.1, 67.1, 73.6, 108.6, 114.1, 117.6, 123.1, 127.8, 127.9, 128.6, 134.3, 138.2, 150.1, 165.3, 181.5; ESI-MS obsd 515.2919, calcd 515.2904 [(M + H)$^+$, M = $C_{32}H_{38}N_2O_4$].

Ethyl 5-((3,4-dihydro-5-methyl-4,4-diphenyl-2H-pyrrol-2-ylidene)methyl)-1H-pyrrole-3-carboxylate (7b). Following a general procedure,[13,47] a solution of **6b** (3.10 g, 8.05 mmol) in DMF (160 mL) was treated with 20% aqueous HCl (80.0 mL). After 30 min, NH$_4$OAc (12.40 g, 161.0 mmol) and Et$_3$N (22.44 mL, 161.0 mmol) were added. The resulting mixture was stirred at 55 °C for 12 h and then quenched by the addition of saturated aqueous KH$_2$PO$_4$ solution. Ethyl acetate (400 mL) was added, and the organic layer was washed (water), dried (Na$_2$SO$_4$) and concentrated. TLC analysis showed two components [silica, hexanes/ethyl acetate (1:1), R$_f$ values for **7b-Z** = 0.80 and **7b-E** = 0.12]. Column chromatography [silica, hexanes/ethyl acetate (1:1)] afforded a light yellow oil (**7b-Z**, 1.10 g, 36%) and a light brown oil (**7b-E**, 1.71 g, 55%). Data for **7b-Z**: ^{1}H NMR δ 1.35 (t, *J* = 7.2 Hz, 3H), 2.13 (s, 3H), 3.40 (s, 2H), 4.29 (q, *J* = 7.2 Hz, 2H), 5.94 (s, 1H), 6.49 (s, 1H), 7.20–7.45 (m, 11H), 11.15 (br, 1H); ^{13}C NMR δ 14.6, 18.4, 48.0, 59.7, 66.6, 106.4, 108.8, 116.4, 124.4, 127.0, 127.9, 128.7, 131.7, 143.7, 149.9, 165.3, 182.1; ESI-MS obsd 385.1907, calcd 385.1911 [(M + H)$^+$, M = $C_{25}H_{24}N_2O_2$]. Data for **7b-E**: ^{1}H NMR δ 1.31 (t, *J* = 7.2 Hz, 3H), 2.06 (s, 3H), 3.49 (d, *J* = 2.4 Hz, 2H), 4.26 (q, *J* = 7.2 Hz, 2H), 6.55 (s, 1H), 6.69 (s, 1H), 7.17–7.39 (m, 11H), 9.55 (br, 1H); ^{13}C NMR δ 14.5, 17.8, 47.5, 59.9, 68.5, 108.2, 109.2, 117.9, 123.8, 127.1, 127.9, 128.7, 130.5, 143.6, 153.3, 165.1, 181.2; ESI-MS obsd 385.1906, calcd 385.1911 [(M + H)$^+$, M = $C_{25}H_{24}N_2O_2$].

(Z)-2,2-Bis[2-(benzyloxy)ethyl]-8-carbethoxy-2,3-dihydro-1-(1,1-dimethoxymethyl)-5-

methyldipyrrin (**8a-Z**). Following a general procedure,[13,22] a solution of **7a-Z** (60 mg, 0.12 mmol) in 1,4-dioxane (10 mL) was treated with SeO_2 (39 mg, 0.36 mmol) and stirred at room temperature for 30 min. Ethyl acetate and water were then added, and the organic layer was washed (brine), dried and concentrated. The resulting crude solid was treated directly with $HC(OMe)_3$ (10 mL) and $TsOH·H_2O$ (7 mg, 0.04 mmol). After 12 h at room temperature, the reaction mixture was quenched by the addition of saturated aqueous $NaHCO_3$ solution followed by extraction with ethyl acetate. The organic layer was dried (Na_2SO_4), concentrated and chromatographed [silica, hexanes/ethyl acetate (4:1)] to afford a brown solid (38 mg, 57%): mp 131–132 °C; ^{1}H NMR δ 1.37 (t, J = 7.5 Hz, 3H), 1.92–2.09 (m, 7H), 2.78 (s, 2H), 3.36 (s, 6H), 3.38–3.45 (m, 4H), 4.28 (q, J = 7.5 Hz, 2H), 4.39 (s, 4H), 5.06 (s, 1H), 6.62 (s, 1H), 7.22–7.28 (m, 10H), 7.47 (dd, J = 2.8, 1.7 Hz, 1H), 11.80 (s, 1H); ^{13}C NMR δ 14.8, 16.4, 38.2, 38.9, 53.3, 54.8, 59.8, 67.3, 73.4, 102.6, 107.8, 116.1, 124.8, 127.8, 127.9, 128.5, 134.7, 138.3, 147.3, 165.7, 177.5; ESI-MS obsd 575.3109 calcd 575.3116 [$(M + H)^+$, M = $C_{34}H_{42}N_2O_6$].

(E)-2,2-Bis[2-(benzyloxy)ethyl]-8-carbethoxy-2,3-dihydro-1-(1,1-dimethoxymethyl)-5-methyldipyrrin (**8a-E**). Following a general procedure,[13,22] a solution of **7a-E** (90 mg, 0.17 mmol) in 1,4-dioxane (14 mL) was treated with SeO_2 (96 mg, 0.51 mmol) and stirred at room temperature for 2 h. Ethyl acetate and water were then added, and the organic layer was washed (brine), dried (Na_2SO_4) and concentrated. The resulting crude solid was treated directly with $HC(OMe)_3$ (15 mL) and $TsOH·H_2O$ (10 mg, 0.05 mmol). After 12 h at room temperature, the reaction mixture was quenched by the addition of saturated aqueous $NaHCO_3$ solution followed by extraction with ethyl acetate. The organic layer was dried (Na_2SO_4) and concentrated. Column chromatography [silica, hexanes/ethyl acetate (3:1)] afforded **8a-Z** (50 mg, 51%) and a light brown oil (**8a-E**, 12 mg, 12%). Data for **8a-E**: ^{1}H NMR δ 1.36 (t, J = 6.9 Hz, 3H), 1.99–2.01 (m, 4H), 2.36 (s, 3H),

2.89 (s, 2H), 3.36–3.49 (m, 10H), 4.31 (q, J = 6.9 Hz, 2H), 4.38 (s, 4H), 5.03 (s, 1H), 6.66 (s, 1H),

7.21–7.32 (m, 11H), 8.52 (br, 1H); ^{13}C NMR δ 14.6, 16.1, 37.9, 40.2, 54.9, 55.4, 59.9, 67.4, 73.3,

102.8, 109.2, 117.5, 123.4, 127.6, 127.8, 128.4, 133.8, 138.2, 149.3, 165.0, 176.0; ESI-MS obsd

575.3110, calcd 575.3116 [(M + H)$^+$, M = $C_{34}H_{42}N_2O_6$].

Ethyl 5-((3,4-dihydro-4,4-diphenyl-5-(1,1-dimethoxymethyl)-2H-pyrrol-2-ylidene)methyl)-1H-pyrrole-3-carboxylate (**8b**). Following a general procedure,[13,22] a solution of

7b-Z (1.04 g, 2.71 mmol) in 1,4-dioxane (180 mL) was treated with SeO$_2$ (0.902 g, 8.13 mmol)

and stirred at room temperature for 6 h. Ethyl acetate and water were then added, and the organic

layer was washed (brine), dried and concentrated. The resulting crude solid was treated directly

with HC(OMe)$_3$ (180 mL) and TsOH·H$_2$O (0.170 g, 0.89 mmol). After 12 h at room temperature,

the reaction mixture was quenched by the addition of saturated aqueous NaHCO$_3$ solution followed

by extraction with ethyl acetate. The organic layer was dried (Na$_2$SO$_4$) and concentrated. TLC

analysis showed two components [silica, hexanes/ethyl acetate (2:3), R$_f$ values for **8b-Z** = 0.5 and

8b-E = 0.16]. Column chromatography [silica, hexanes/ethyl acetate (2:3)] afforded a light brown

oil (**8b-Z**, 0.361 g, 30%) and a dark brown solid (**8b-E**, 0.301 g, 25%). Data for **8b-Z**: ^{1}H NMR

δ 1.34 (t, J = 7.2 Hz, 3H), 3.20 (s, 6H), 3.45 (s, 2H), 4.27 (q, J = 7.2 Hz, 2H), 4.97 (s, 1H), 6.08

(s, 1H), 6.54 (s, 1H), 7.24–7.48 (m, 11H), 11.00 (br, 1H); ^{13}C NMR δ 14.5, 48.5, 54.1, 59.7, 66.0,

98.92, 98.95, 109.7, 110.0, 116.5, 125.3, 127.2, 128.1, 128.6, 131.3, 143.5, 149.1, 165.1, 177.3;

ESI-MS obsd 445.2125 calcd 445.2122 [(M + H)$^+$, M = $C_{27}H_{28}N_2O_4$]. Data for **8b-E**: mp 188–

192 °C; ^{1}H NMR δ 1.31 (t, J = 7.2 Hz, 3H), 3.17 (s, 6H), 3.53 (d, J = 1.5 Hz, 2H), 4.27 (q, J = 7.2

Hz, 2H), 5.00 (s, 1H), 6.57 (s, 1H), 7.08 (s, 1H), 7.23–7.40 (m, 11H), 9.54 (br, 1H); ^{13}C NMR

δ 14.6, 48.4, 54.0, 59.9, 67.8, 98.8, 98.9, 108.9, 112.8, 118.2, 124.2, 127.2, 127.9, 128.1, 128.7,

128.8, 130.4, 143.6, 152.9, 164.9, 176.4; ESI-MS obsd 445.2121, calcd 445.2122 [(M + H)$^+$, M = C$_{27}$H$_{28}$N$_2$O$_4$].

Following a general procedure,[13,22] a solution of **7b-E** (1.71 g, 4.45 mmol) in 1,4-dioxane (310 mL) was treated with SeO$_2$ (1.48 g, 13.35 mmol) and stirred at room temperature for 2 h. Ethyl acetate and water were then added, and the organic layer was washed (brine), dried and concentrated. The resulting crude solid was treated directly with HC(OMe)$_3$ (310 mL) and TsOH·H$_2$O (0.280 g, 1.47 mmol). After 12 h at room temperature, the reaction mixture was quenched by the addition of saturated aqueous NaHCO$_3$ solution followed by extraction with ethyl acetate. The organic layer was dried (Na$_2$SO$_4$) and concentrated. TLC analysis showed two components [silica, hexanes/ethyl acetate (2:3), R$_f$ values for **8b-Z** = 0.5 and **8b-E** = 0.16]. Column chromatography [silica, hexanes/ethyl acetate (2:3)] afforded **8b-Z** (0.292 g, 15%) and **8b-E** (0.884 g, 45%).

8,8,18,18-Tetrakis[2-(benzyloxy)ethyl]-2,12-dicarbethoxy-5,15-dimethylbacteriochlorin (R-BC-Es^{2,12}Me^{5,15}). Following a general procedure,[13] a solution of **8a-Z** (40 mg, 69 µmol) in anhydrous CH$_2$Cl$_2$ (4.9 mL) was treated with DTBP (0.33 mL, 1.45 mmol) followed by TMSOTf (69 µL, 0.38 mmol). The reaction mixture was stirred at room temperature for 15 h, and then diluted with CH$_2$Cl$_2$ and washed with saturated aqueous NaHCO$_3$ solution. The organic layer was dried (Na$_2$SO$_4$), concentrated and chromatographed [silica, hexanes/ethyl acetate (4:1)] to afford a purple solid (7.0 mg, 18%): ^{1}H NMR δ −1.01 (s, 2H), 1.71 (t, J = 7.2 Hz, 6H), 2.69–2.78 (m, 8H), 3.32–3.35 (m, 8H), 3.57 (s, 6H), 4.05 (ABq, $\Delta\delta_{AB}$ = 0.09, J = 12.0 Hz, 8H), 4.43 (s, 4H), 4.76 (q, J = 7.2 Hz, 4H), 6.90–7.04 (m, 20H), 9.33 (d, J = 3.0 Hz, 2H), 9.67 (s, 2H); ^{13}C NMR δ 15.0, 19.9, 42.9, 45.4, 50.9, 61.1, 67.9, 73.1, 97.7, 109.0, 122.3, 123.4, 127.5, 127.6, 128.3, 134.6, 134.7,

138.3, 162.4, 166.0, 167.2; ESI–MS obsd 1023.5227, calcd 1023.5266 [(M + H)$^+$, M = C$_{64}$H$_{70}$N$_4$O$_8$]; λ_{abs} 362, 386, 549, 753 nm (CH$_2$Cl$_2$).

Following a general procedure,[13] a solution of **8a-E** (10 mg, 17 μmol) in anhydrous CH$_2$Cl$_2$ (1.2 mL) was treated with DTBP (0.08 mL, 0.4 mmol) followed by TMSOTf (18 μL, 96 μmol). The reaction mixture was stirred at room temperature for 15 h, and then diluted with CH$_2$Cl$_2$ and washed with saturated aqueous NaHCO$_3$ solution. The organic layer was dried (Na$_2$SO$_4$), concentrated and chromatographed [silica, hexanes/ethyl acetate (4:1)] to afford a purple solid (1 mg): MALDI–MS obsd 1022.5, [(M)$^+$, M = C$_{64}$H$_{70}$N$_4$O$_8$]; λ_{abs} 363, 551, 756 nm (CH$_2$Cl$_2$). The small scale precluded further analysis.

2,12-Dicarbethoxy-8,8,18,18-tetrakis(2-hydroxyethyl)-5,15-dimethylbacteriochlorin (HOR-BC-Es^{2,12}Me^{5,15}). Following a reported procedure,[56] a 6 mM solution of **R-BC-Es^{2,12}Me^{5,15}** (7.0 mg, 6.9 μmol) in anhydrous CH$_2$Cl$_2$ (1.2 mL) was treated with BCl$_3$ (1.0 M, 0.14 mL in CH$_2$Cl$_2$, 0.14 mmol) at –78 °C and stirred for 1 h at –78 °C. The dry ice–acetone bath was replaced by an ice bath, and mixture was stirred for 1 h. The reaction mixture was quenched by the addition of MeOH (0.2 mL) and then allowed to warm to room temperature. The mixture was concentrated and chromatographed [silica, CH$_2$Cl$_2$/MeOH (9:1)] to afford a purple solid (2.1 mg, 50%): ^{1}H NMR (DMSO-d_6; six protons corresponding to two methyl groups were overlapped with the solvent peak; four OH peaks were not observed) δ –1.05 (s, 2H), 1.64 (t, J = 7.2 Hz, 6H), 2.37–2.40 (m, 4H), 3.04–3.21 (m, 4H), 3.64 (s, 4H), 4.35 (s, 8H), 4.72 (q, J = 7.2 Hz, 4H), 9.44 (s, 2H), 9.61 (s, 2H); ESI-MS obsd 663.3390, calcd 663.3388 [(M + H)$^+$, M = C$_{36}$H$_{46}$N$_4$O$_8$]; λ_{abs} 362, 385, 549, 752 nm (CH$_2$Cl$_2$).

2,12-Dicarbethoxy-8,8,18,18-tetraphenylbacteriochlorin (Ph-BC-Es[2,12]). Following a general procedure,[13] a solution of **8b-Z** (0.614 g, 1.38 mmol) in anhydrous CH_2Cl_2 (77 mL) was treated with DTBP (3.10 mL, 13.8 mmol) followed by TMSOTf (1.58 mL, 6.90 mmol). The reaction mixture was stirred at room temperature for 18 h, then diluted with CH_2Cl_2 and washed with saturated aqueous $NaHCO_3$. The organic layer was dried (Na_2SO_4), concentrated and chromatographed [silica, hexanes/CH_2Cl_2 (1:1)] to give two bands (green and purple). The first band (green) was isolated and concentrated to afford the title compound as a green solid (6.8 mg, 1.3%). The second band (purple) afforded the 10-methoxybacteriochlorin **Ph-BC-Es[2,12]MeO[10]** as a purple solid (2.4 mg, 0.46%). Data for the title compound: ^{1}H NMR δ −1.58 (s, 2H), 1.49 (t, J = 7.2 Hz, 6H), 4.60 (q, J = 7.2 Hz, 4H), 5.33 (s, 4H), 7.22–7.32 (m, 12H), 7.48–7.51 (m, 8H), 8.86 (s, 2H), 9.22 (d, J = 2.4 Hz, 2H), 9.62 (s, 2H); ^{13}C NMR (100 MHz) δ 14.6, 55.6, 61.0, 64.7, 100.5, 102.7, 123.7, 126.6, 126.7, 128.5, 128.6, 133.6, 135.2, 148.8, 158.7, 165.3, 168.3; ESI-MS obsd 763.3279, calcd 763.3259 [$(M + H)^+$, M = $C_{50}H_{42}N_4O_4$]; λ_{abs} 357, 387, 525, 746 nm (CH_2Cl_2); 354, 383, 522, 741 nm (Et_2O). Data for **2,12-dicarbethoxy-10-methoxy-8,8,18,18-tetraphenylbacteriochlorin (Ph-BC-Es[2,12]MeO[10])**: ^{1}H NMR δ −1.43 (s, 1H), −1.21 (s, 1H), 1.48 (t, J = 6.9 Hz, 6H), 3.00 (s, 3H), 4.56–4.62 (m, 4H), 5.25 (s, 2H), 5.30 (s, 2H), 7.17–7.31 (m, 12H), 7.47–7.55 (m, 8H), 8.70 (s, 1H), 8.73 (s, 2H), 9.16 (s, 1H), 9.43 (s, 1H); ESI-MS obsd 792.3293, calcd 792.3306 [$(M)^+$, M = $C_{51}H_{44}N_4O_5$]; λ_{abs} 361, 383, 535, 734 nm (CH_2Cl_2); 357, 381, 529, 730 nm (Et_2O).

Photophysical studies. Spectral and photophysical studies of the three bacteriochlorins were carried out on dilute (μM) argon-purged samples at room temperature. Absorption spectra were acquired using a Shimadzu UV-1800 spectrometer. Static emission spectra were acquired using a Spex-Horiba Nanolog spectrofluorimeter with 2–4 nm excitation and detection bandwidths

and corrected for instrument spectral response. Fluorescence quantum yields are the average of values obtained relative to *meso*-tetraphenylporphyrin ($\Phi_f = 0.070$ in nondegassed toluene)[67] and 8,8,18,18-tetramethylbacteriochlorin ($\Phi_f = 0.14$ in degassed toluene).[59] The values for parent bacteriochlorin **Me-BC** and swallowtail bacteriochlorin **Ph-BC-Es^{2,12}MeO^{10}** are the same within experimental error as that obtained by absolute measurement using an integrating sphere (Quanti-Phi, Horiba). Singlet excited-state lifetimes were determined by using transient absorption (TA) spectroscopy employing ~100 fs excitation flashes from an ultrafast laser system (Spectra Physics) and acquisition of difference spectra (360–900 nm) using a white-light pulsed laser (~1 ns rise time) in 100-ps time bins with variable pump-probe spacing up to 0.5 ms (Ultrafast Systems, EOS). Transient absorption measurements employed excitation in the Q_x and Q_y bands. Time profiles of ΔA at ~1.5 nm spacing across the 380–800 nm region were analyzed at a number of individual wavelengths and also globally. Transient absorption studies were also used to measure the yield of $S_1 \rightarrow T_1$ intersystem crossing by comparing the extent of bleaching of the ground-state absorption bands due to T_1 at the asymptote of the S_1 decay versus the extent due to S_1 immediately after the excitation flash. Measurements in the Q_y region account for the contribution of both S_0 bleaching and S_1 stimulated emission to the S_1 feature.

Density functional theory calculations. DFT calculations were performed with Gaussian 09 version D.01. All calculations were in toluene using the polarizable continuum model (PCM). Molecular geometries were fully optimized using the hybrid B3LYP functional and basis set 6-31++G**.[68] Ground-state MOs were calculated at the optimized geometry using the B3LYP functional and basis set 6-31++G**. Single point TDDFT calculations were performed at the B3LYP/6-31++G** optimized geometry using the long range corrected wB97XD functional and basis set 6-31++G**. These calculations used Gaussian defaults with the exception of the

keywords SCF=(NoVarAcc, NoIntFock), GFInput POP=(Full, NBO) and TD(nStates=16). MO images were generated from Gaussian outputs using the Chemcraft program (http://www.chemcraftprog.com).

REFERENCES

1   H. Scheer, in *Chlorophylls and Bacteriochlorophylls: Biochemistry, Biophysics, Functions and Applications*, ed. B. Grimm, R. J. Porra, W. Rüdiger and H. Scheer, Springer, Dordrecht, The Netherlands, 2006, pp. 1–26.

2   M. Kobayashi, M. Akiyama, H. Kano and H. Kise, in *Chlorophylls and Bacteriochlorophylls: Biochemistry, Biophysics, Functions and Applications,* ed. B. Grimm, R. J. Porra, W. Rüdiger and H. Scheer, Springer, Dordrecht, The Netherlands, 2006, pp. 79–94.

3   Y. Chen, G. Li and R. K. Pandey, *Curr. Org. Chem.,* 2004, **8**, 1105–1134.

4   M. A. Grin, A. F. Mironov and A. A. Shtil, *Anti-Cancer Agents Med. Chem.*, 2008, **8**, 683–697.

5   C. Brückner, L. Samankumara and J. Ogikubo, in *Handbook of Porphyrin Science,* ed. K. M. Kadish, K. M. Smith and R. Guilard, World Scientific, Singapore, 2012, Vol. 17, pp 1–112.

6   M. Taniguchi and J. S. Lindsey, *Chem. Rev.,* 2017, **117**, 344–535.

7   T. G. Minehan and Y. Kishi, *Tetrahedron Lett.,* 1997, **38**, 6811–6814.

8   T. G. Minehan and Y. Kishi, *Tetrahedron Lett.,* 1997, **38**, 6815–6818.

9   T. G. Minehan and Y. Kishi, *Angew. Chem. Int. Ed.,* 1999, **38**, 923–925.

10   T. G. Minehan, L. Cook-Blumberg, Y. Kishi, M. R. Prinsep and R. E. Moore, *Angew. Chem. Int. Ed.,* 1999, **38**, 926–928.

11   W. Wang and Y. Kishi, *Org. Lett*., 1999, **1**, 1129–1132.

12   H.-J. Kim and J. S. Lindsey, *J. Org. Chem.,* 2005, **70**, 5475–5486.

13   Y. Liu and J. S. Lindsey, *J. Org. Chem.*, 2016, **81**, 11882–11897.

14   S. Zhang and J. S. Lindsey, J. S. ***J. Org. Chem.* 2017**, *82*, 2489–2504.

15   M. Krayer, M. Ptaszek, H.-J. Kim, K. R. Meneely, D. Fan, K. Secor and J. S. Lindsey, *J. Org. Chem.,* 2010, **75**, 1016–1039.

16   M. Krayer, E. Yang, J. R. Diers, D. F. Bocian, D. Holten and J. S. Lindsey, *New J. Chem.,* 2011, **35**, 587–601.

17   Z. Yu and M. Ptaszek, *Org. Lett.,* 2012, **14**, 3708–3711.

18   Z. Yu and M. Ptaszek, *J. Org. Chem.,* 2013, **78**, 10678–10691.

19   T. Harada, K. Sano, K. Sato, R. Watanabe, Z. Yu, H. Hanaoka, T. Nakajima, P. L. Choyke, M. Ptaszek and H. Kobayashi, *Bioconjugate Chem.,* 2014, **25**, 362–369.

20   Z. Yu, C. Pancholi, G. V. Bhagavathy, H. S. Kang, J. K. Nguyen and M. Ptaszek, *J. Org. Chem.,* 2014, **79**, 7910–7925.

21   F. F. de Assis, M. A. B. Ferreira, T. J. Brocksom and K. T. de Oliveira, *Org. Biomol. Chem.,* 2016, **14**, 1402–1412.

22 K. R. Reddy, E. Lubian, M. P. Pavan, H.-J. Kim, E. Yang, D. Holten and J. S. Lindsey, *New J. Chem.,* 2013, **37**, 1157–1173.

23 K. S. Suslick and T. J. Reinert, *J. Chem. Ed.*, 1985, **62**, 974–983.

24 J. P. Collman, *Acc. Chem. Res.*, 1977, **10**, 265–272.

25 J. P. Collman and L. Fu, *Acc. Chem. Res.*, 1999, **32**, 455–463.

26 K. E. Borbas, V. Chandrashaker, C. Muthiah, H. L. Kee, D. Holten and J. S. Lindsey, *J. Org. Chem.*, 2008, **73**, 3145–3158.

27 M. Liu, C.-Y. Chen, A. K. Mandal, V. Chandrashaker, R. B. Evans-Storms, J. B. Pitner, D. F. Bocian, D. Holten and J. S. Lindsey, *New J. Chem.,* 2016, 40, 7721–7740.

28 K. E. Borbas, C. Ruzié and J. S. Lindsey, *Org. Lett.*, 2008, **10**, 1931–1934.

29 N. Zhang, J. Jiang, M. Liu, M. Taniguchi, A. K. Mandal, R. B. Evans-Storms, J. B. Pitner, D. F. Bocian, D. Holten and J. S. Lindsey, *New J. Chem.,* 2016, **40**, 7750–7767.

30 S. Demmig and H. Langhals, *Chem. Ber.,* 1988, **121**, 225–230.

31 H. Langhals, S. Demmig and T. Potrawa, *J. Prakt. Chem.,* 1991, **333**, 733–748.

32 L. Feiler, H. Langhals and K. Polborn, *Liebigs Ann.*, 1995, 1229–1244.

33 H. Langhals, *Heterocycles,* 1995, **40**, 477–500.

34 H. Langhals, R. Ismael and O. Yürük, *Tetrahedron,* 2000, **56**, 5435–5441.

35 H. Langhals, *Helv. Chim. Acta*, 2005, **88**, 1309–1343.

36 P. Thamyongkit, M. Speckbacher, J. R. Diers, H. L. Kee, C. Kirmaier, D. Holten, D. F. Bocian and J. S. Lindsey, *J. Org. Chem.*, 2004, **69**, 3700–3710.

37 K. E. Borbas, P. Mroz, M. R. Hamblin and J. S. Lindsey, *Bioconjugate Chem.*, 2006, **17**, 638–653.

38 Z. Yao, K. E. Borbas and J. S. Lindsey, *New J. Chem.,* 2008, **32**, 436–451.

39 K. E. Borbas, H. L. Kee, D. Holten and J. S. Lindsey, *Org. Biomol. Chem.,* 2008, **6**, 187–194.

40 M. O. Senge In *The Porphyrin Handbook*, ed. K. M. Kadish, K. M. Smith and R. Guilard, Academic Press, San Diego, CA, 2000, Vol. 1, pp 239–347.

41 M. Taniguchi, H.-J. Kim, D. Ra, J. K. Schwartz, C. Kirmaier, E. Hindin, J. R. Diers, S. Prathapan, D. F. Bocian, D. Holten and J. S. Lindsey, *J. Org. Chem.,* 2002, **67**, 7329–7342.

42 P. A. Jacobi, H. L. Brielmann and S. I. Hauck, *Tetrahedron Lett.,* 1995, **36**, 1193–1196.

43 P. A. Jacobi, H. L. Brielmann and S. I. Hauck, *J. Org. Chem.,* 1996, **61**, 5013–5023.

44 P. A. Jacobi and H. Liu, *J. Org. Chem.,* 1999, **64**, 1778–1779.

45 P. A. Jacobi, S. Lanz, I. Ghosh, S. H. Leung, F. Löwer and D. Pippin, *Org. Lett.,* 2001, **3**, 831–834.

46 I. Ghosh and P. A. Jacobi, *J. Org. Chem.,* 2002, **67**, 9304–9309.

47   W. G. O'Neal, W. P. Roberts, I. Ghosh and P. A. Jacobi, *J. Org. Chem.,* 2005, **70**, 7243–7251.

48   W. G. O'Neal, W. P. Roberts, I. Ghosh, H. Wang and P. A. Jacobi, *J. Org. Chem.,* 2006, **71**, 3472–3480.

49   W. G. O'Neal and P. A. Jacobi, *J. Am. Chem. Soc.,* 2008, **130**, 1102–1108.

50   S. Ben Dror, I. Bronshtein, Y. Garini, W. G. O'Neal, P. A. Jacobi and B. Ehrenberg, *Photochem. Photobiol. Sci.,* 2009, **8**, 354–361.

51   S. Ben Dror, I. Bronshtein, H. Weitman, K. M. Smith, W. G. O'Neal, P. A. Jacobi and B. Ehrenberg, *Eur. Biophys. J.,* 2009, **38**, 847–855.

52   P. A. Jacobi, H. L. Brielmann, M. Chiu, I. Ghosh, S. I. Hauck, S. Lanz, S. Leung, Y. Li, H. Liu, F. Löwer, W. G. O'Neal, D. Pippin, E. Pollina, B. A. Pratt, F. Robert, W. P. Roberts, C. Tassa and H. Wang, *Heterocycles,* 2011, **82**, 1029–1081.

53   J. Holz, R. Stürmer, U. Schmidt, H.-J. Drexler, D. Heller, H.-P. Krimmer and A. Börner, *Eur. J. Org. Chem.,* 2001, 4615–4624.

54   K. C. Nicolaou, K. R. Reddy, G. Skokotas, F. Sato, X.-Y. Xiao and C.-K. Hwang, *J. Am. Chem. Soc.,* 1993, **115**, 3558–3575.

55   N. Nishizono, Y. Akama, M. Agata, M. Sugo, Y. Yamaguchi and K. Oda, *Tetrahedron,* 2011, **67**, 358–363.

56   J. Xie, M. Ménand and J.-M. Valéry, *Carbohydr. Res*., 2005, **340**, 481–487.

57   J. M. Schomaker, V. R. Pulgam and B. Borhan, *J. Am. Chem. Soc.,* 2004, **126**, 13600–13601.

58   M. Liu, M. Ptaszek, O. Mass, D. J. Minkler, R. D. Sommer, J. Bhaumik and J. S Lindsey, *New J. Chem.,* 2014, **38**, 1717–1730.

59   E. Yang, C. Kirmaier, M. Krayer, M. Taniguchi, H.-J. Kim, J. R. Diers, D. F. Bocian, J. S. Lindsey and D. Holten, *J. Phys. Chem. B*, 2011, **115**, 10801–10816.

60   C.-Y. Chen, E. Sun, D. Fan, M. Taniguchi, B. E. McDowell, E. Yang, J. R. Diers, D. F. Bocian, D. Holten and J. S. Lindsey, *Inorg. Chem.*, 2012, **51**, 9443–9464.

61   J. B. Birks, Photophysics of Aromatic Molecules; Wiley-Interscience, London, 1970, pp. 142−192.

62   J. M. Steed, T. A. Dixon and W. Klemperer, *J. Chem. Phys.*, 1979, **70**, 4940–4946.

63   M. Gouterman, *J. Chem. Phys.*, 1959, **30**, 1139–1161.

64   M. Gouterman, *J. Mol. Spectroscopy*, 1961, **6**, 138–163.

65   M. Gouterman In *The Porphyrins,* ed. D. Dolphin, Volume 3, Academic Press, New York, 1978, pp. 1–165.

66   N. Srinivasan, C. A. Haney, J. S. Lindsey, W. Zhang and B. T. Chait, *J. Porphyrins Phthalocyanines,* 1999, **3**, 283–291.

67   A. K. Mandal, M. Taniguchi, J. R. Diers, D. M. Niedzwiedzki, C. Kirmaier, J. S. Lindsey, D. F. Bocian and D. Holten, *J. Phys. Chem. A,* 2016, **120**, 9719–9731.

68   M. J. Frisch, G. W. Trucks, H. B. Schlegel, G. E. Scuseria, M. A. Robb, J. R. Cheeseman, G. Scalmani, V. Barone, B. Mennucci, G. A. Petersson, H. Nakatsuji, M. Caricato, X. Li, H. P. Hratchian, A. F. Izmaylov, J. Bloino, G. Zheng, J. L. Sonnenberg, M. Hada, M. Ehara, K. Toyota, R. Fukuda, J. Hasegawa, M. Ishida, T. Nakajima, Y. Honda, O. Kitao, H. Nakai, T. Vreven, J. A. Montgomery Jr., J. E. Peralta, F. Ogliaro, M. Bearpark, J. J. Heyd, E. Brothers, K. N. Kudin, V. N. Staroverov, R. Kobayashi, J. Normand, K. Raghavachari, A. Rendell, J. C. Burant, S. S. Iyengar, J. Tomasi, M. Cossi, N. Rega, J. M. Millam, M. Klene, J. E. Knox, J. B. Cross, V. Bakken, C. Adamo, J. Jaramillo, R. Gomperts, R. E. Stratmann, O. Yazyev, A. J. Austin, R. Cammi, C. Pomelli, J. W. Ochterski, R. L. Martin, K. Morokuma, V. G. Zakrzewski, G. A. Voth, P. Salvador, J. J. Dannenberg, S. Dapprich, A. D. Daniels, Ö. Farkas, J. B. Foresman, J. V. Ortiz, J. Cioslowski and D. J. Fox, Gaussian, Inc., Wallingford CT, 2009.

Chapter 6

Conclusions and Future Directions

The purpose of this research is to understand the photophysical behavior of tetrapyrroles with respect to both their environment and substituents. The longer range goals are to provide tunable absorption wavelengths for synthetic chromophores which are to be utilized in technologies such as organic dye photovoltaic cells, photodynamic therapy, synthetic photosynthesis, and other related applications. Below is a summation regarding the individual projects from this writing and possible future investigations.

Synthetic Oxobacteriochlorins

With the synthesis of simple oxo- and dioxobacteriochlorins the spectral gap between bacteriochlorins (near-infrared) and chlorins (red) absorption spectra has been tapped in a relatively simple synthesis. It illustrates that the properties of highly functionalized natural chlorins and bacteriochlorins are not solely based on the extensive functionalization. This bodes well for tuning hydroporphyrin macrocycles for red absorption in solar-energy and other applications. However, the modeling that could be used to direct design of new tetrapyrroles with more accurate tuning of the absorption spectra does not always accurately reflect the reality of the new spectrum. So far, first approximations regarding electron density in the four orbital model give an idea based on one-electron promotions among the four frontier MOs. The coupled changes in the B- and Q-bands are considered in the Time-Dependent Density Functional Theory (TDDFT) calculations. As yet, neither the four-orbital model nor the TDDFT calculations reproduce the actual spectrum. Therefore, work regarding the application of these calculations and simulations should be continued. That said, one of the motivations for this study was to produce a

bacteriochlorin with no auxochromes except for the oxo- groups to have a Q_y in the 60-700 nm region and in that succeeded. Work with the oxo groups and new auxochromes on both the x- and y-axis may give insights for fine tuning or for creating a coarse guideline for producing absorption spectra with Q_y absorptions at will.

Tolyporphin A

The initial interest in tolyporphin A was mainly to obtain the enzymes from the biosynthesis for use in syntheses of designer tetrapyrrole macrocycles. As tolyporphin A is of interest as a photosensitizer in living systems, an in-depth investigation of its photophysical parameters seemed prudent. And it was possible to compare it to the simpler oxo- and dioxo-bacteriochlorins discussed in Chapter 2. Because the spectral and photophysical properties of tolyporphin A and the synthetic oxobacteriochlorins seem to be relatively insensitive to widely differing solvent environments and the $S1$—T_1 intersystem crossing is such a large part of the S_1 decay, the next investigation should be a comparison of singlet oxygen generation in the various solvents for both the tolyporphin A and the oxobacteriochlorins. Then determine the photoactivity and the potential life of the photoactivity of tolyporphin A *in vivo*, again with the oxobacteriochlorins. If the 7,17-dioxobacteriochlorin behaves within reasonable step with the tolyporphin A, then more readily abundant source of photosensitizer may be at hand.

Biohybrids

The ability to add unnatural chromophores to light harvesting antennas provides sufficient future investigations to keep a dozen laboratories busy for the next decade. The investigation described in Chapter 4 was an important, but narrow, slice of the spectrum of experiments that can be run. Practically, the confirmation of the C-terminal positions providing as much or more

efficient energy transfer as the N-terminal positions may allow for slightly different chromophores to be attached to the β-peptide of the dyad. Particularly the +11 position lends itself to the possibility of attaching a panchromatic absorber with large groups attached to a porphyrin, such as a perylene-porphyrin with three perylenes attached to the porphyrin. The +11 is an attachment to the C-terminal of the β-peptide and extends beyond the bulk of the dyad. Not only does the +11 have one of the highest energy transfers, but it provides sufficient space for the perylene to rotate. This group, or other similar groups, would span the 400-8—nm range of the solar spectrum, approximately 60% of the photon flux density of the light emitted by our star. Other possibilities are to attach various unnatural chromophores that absorb in the NIR, but attached to the same β-peptide. As long as none of these substituents interfere with the helicity or the self-assembly into the dyads and oligomers, then there is a good chance of efficient energy transfer deeper into the NIR.

Swallowtail Bacteriochlorins

Should a more efficient synthetic set of pathways of the various swallowtails bacteriochlorins be developed that produce greater yields, then the ability to modify a bacteriochlorin to function better in its local environment would be useful. From water-soluble to lipophilic, these substituents at the β-pyrroline unit could provide access to a wide range of cell conditions and allow easier delivery to *in vivo* locations.